Delft University of Technology

Quadrotor Fault Tolerant Flight Control and Aerodynamic Model Identification

Sun, S.

DOI
10.4233/uuid:f0bdac3d-376d-4b24-9241-3a1e35731373

Publication date
2020

Document Version
Final published version

Citation (APA)
Sun, S. (2020). *Quadrotor Fault Tolerant Flight Control and Aerodynamic Model Identification*. [Dissertation (TU Delft), Delft University of Technology]. https://doi.org/10.4233/uuid:f0bdac3d-376d-4b24-9241-3a1e35731373

QUADROTOR FAULT TOLERANT FLIGHT CONTROL AND AERODYNAMIC MODEL IDENTIFICATION

QUADROTOR FAULT TOLERANT FLIGHT CONTROL AND AERODYNAMIC MODEL IDENTIFICATION

Dissertation

for the purpose of obtaining the degree of doctor
at Delft University of Technology
by the authority of the Rector Magnificus, Prof.dr.ir. T.H.J.J. van der Hagen,
chair of the Board for Doctorates
to be defended publicly on
Monday 14, December, 2020 at 18:00 o'clock

by

Sihao SUN

Master of Science in Aerospace Engineering,
Beihang University, China,
born in Harbin, China

This dissertation has been approved by the promotors

Composition of the doctoral committee:

Rector Magnificus,	chairperson
Prof. dr. G.C.H.E. de Croon,	Delft University of Technology, promotor
Dr. ir. C.C. de Visser,	Delft University of Technology, copromotor
Independent members:	
Prof. dr. ir. L.L.M. Veldhuis	Delft University of Technology
Prof. dr. ir. M. Wisse	Delft University of Technology
Prof. M. Lovera	Polytechnic University of Milan, Italy
Dr. D. Scaramuzza	University of Zurich, Switzerland
Dr. A. Franchi	University of Twente
Reserve member:	
Prof. dr. ir. J.M. Hoekstra,	Delft University of Technology

Keywords: Quadrotor, Safety, Modeling, Control

Printed by: Ridderprint

Front & Back: Sandra Tukker

ISBN 978-94-6384-181-8

An electronic version of this dissertation is available at
`http://repository.tudelft.nl/`.

To my beloved wife and parents

CONTENTS

SUMMARY

As Multi-rotor Unmanned Aerial Vehicles, or drones, are gradually becoming more popular in civilian applications, the safety of these flying machines becomes a significant concern. Such drones are powered by multiple rotors to generate lift and control torques. Hence, the failure of rotors can severely threaten their flying safety. Direct consequences of rotor failures are loss-of-control and a subsequent crash if no ad-hoc flight control method can take over. Such a method, built on the principles of Fault Tolerant Control (FTC), is thus essential to improving the safety of multi-rotor drones.

Fixed-pitch quadrotors are the simplest type of multi-rotor drones and have been extensively used in various applications thanks to their simplicity and higher energy efficiency. However, they suffer most from rotor failures since it requires a minimum of four fixed-pitch rotors to achieve full attitude control. Therefore, devising FTC algorithms for quadrotors presents a significant challenge.

As there have been many efforts to develop FTC for quadrotors flying in near-hover conditions, a primary objective of this thesis is further expanding the capability of FTC methods to high-speed conditions where significant aerodynamic effects arise that brings large model uncertainties to the control algorithm. The high-speed flight conditions can be, for instance, the cruising phase of a quadrotor (e.g., delivery drone).

Once rotor failure occurs, these aerodynamic effects can adversely impact the performance of FTC methods, and even drive the damaged quadrotor into upset conditions with abnormal attitude and angular rates. On the one hand, it is essential to improve state-of-art FTC methods withstanding significant aerodynamic effects as well as possible large initial disturbances. On the other hand, these aerodynamic effects need to be further investigated and modeled to facilitate the development of FTC in high-speed conditions. These two aspects constitute the two major parts of this thesis.

The first part of the thesis tackles the aerodynamic modeling problem of a damaged quadrotor in high-speed flight using an aerodynamic model identification approach. For a better understanding of high-speed aerodynamics of quadrotors, this study has identified a nominal gray-box model using the data from controlled flight tests in a large scale wind tunnel (Open Jet Facility, TU Delft). From the flight data, effects such as significant pitch-up moments, rotor-body interactions, and yaw moment variations are discovered and modeled, which are rarely discussed before. Apart from these secondary effects, thrust variations and rotor drag are captured as major aerodynamic effects. This gray-box model shows respective improvements of 20% and 80% on aerodynamic force and moment predictions in terms of model residuals in high-speed conditions compared to models only valid in low-speed conditions.

Unfortunately, we cannot directly generalize this gray-box model to rotor failure conditions, though it possesses high accuracy and sheds light on unknown aerodynamic effects. For this reason, a multi-body parametric model is established for predicting aerodynamic forces/moments of a quadrotor, which is not only valid in nominal conditions but also those with failure of an arbitrary number of rotors. This model separates the effect of each rotor and the airframe, and model parameters are estimated from flight data acquired in both nominal and damaged conditions. In order to improve the accuracy of data that are contaminated by the centrifugal force from the high-rate yaw motion in the rotor failure conditions, a novel data preprocessing approach is developed and analyzed. During the validation procedure, it is demonstrated that this model captures both primary and secondary aerodynamic effects, even those induced by high-speed airstream and yawing motion. The model is also implemented in a simulation environment to facilitate FTC design in the second part.

The second part of the thesis aims at developing robust FTC methods in the face of large aerodynamic and initial condition disturbances. For addressing the model uncertainties brought by significant aerodynamic effects in high-speed flight, the incremental nonlinear dynamic inversion (INDI) approach is implemented and developed in the occurrence of complete failure of one rotor (single-rotor-failure), and two opposing rotors (double-rotor-failure). In the latter case where the problem becomes underactuated, this study also analyzes the internal dynamics for defining an appropriate control output, which for the first time combines INDI with the output-redefinition technique in a real-life system. The proposed robust FTC has been validated in the wind tunnel by conducting high-speed controlled flights of a quadrotor with single-rotor-failure and double-rotor-failure conditions. These real-flight tests have shown the robustness of the method that outperforms a benchmark FTC approach. The quadrotor subjected to complete failure of two rotors can track trajectories in a wind of 5 m/s. Impressively, we have achieved flights at over 8 m/s, which is more than half of the maximum norminal flight speed of the tested quadrotor.

An upset-recovery FTC is also developed to deal with large initial disturbances. Imagine a quadrotor in an upside-down orientation along with a rotor failure; with the proposed FTC method, it can be recovered to the pre-failure orientation and altitude. In fact, this is an almost-globally convergent controller that can stabilize a damaged quadrotor from arbitrary initial orientations and a wide range of initial angular velocities. To this end, a novel control allocation approach is designed. This allocation method can effectively suppress the angular rate that hinders the recovery procedure, while providing rotor speed setpoints according to the outer-loop commands. For validation, a set of Monte Carlo simulations are conducted with the aerodynamic model identified in the first part of the thesis. It shows that more than 95% of flights could recover within 10 meters altitude loss from random initial conditions. In addition to validating the controller in simulations, real flights have been performed in the Cyberzoo, an in-door flight laboratory of TU Delft, where a quadrotor with only three rotors was randomly tossed into the air and finally recovered to a hovering state.

The research performed in this thesis leads to three recommendations. First, deteriorations of state estimates in such fast dynamics conditions are discovered, which may subsequently degrade the control performance. For alleviating this problem, fast-spinning and aerodynamic effects need to be considered for state estimation. After addressing this issue, one may conduct out-door experiments for fast-flight and upset recovery tests to further improve drone safety in a more realistic scenario. The second recommendation is to evaluate actuator-dynamic effects on the INDI approach, as it is believed to bring limitations to the proposed FTC methods. The degradation resulting from actuator dynamics may be alleviated by utilizing pseudo-control hedging (PCH), or generalizing methods addressing delays from linear systems to nonlinear. Last but not least, it is recommended to investigate the cause of these complex aerodynamic effects on a damaged quadrotor using static wind tunnel tests, computational fluid dynamics (CFD), and analytical approaches.

SAMENVATTING

Aangezien onbemande luchtvaartuigen met meerdere rotoren of drones geleidelijk aan populairder worden in civiele toepassingen, wordt de veiligheid van deze vliegmachines een groot aandachtspunt. Dergelijke drones worden aangedreven door meerdere rotoren om lift- en controlekoppels te genereren. Daarom kan het falen van rotoren hun vliegveiligheid ernstig in gevaar brengen. Directe gevolgen van rotorstoringen zijn controleverlies en een daaropvolgende crash als geen enkele ad-hoc-vluchtregelmethode het kan overnemen. Een dergelijke methode, gebouwd op de principes van Fault Tolerant Control (FTC), is dus essentieel om de veiligheid van drones met meerdere rotoren te verbeteren.

Quadrotors met vaste steek zijn het eenvoudigste type drones met meerdere rotoren en worden op grote schaal gebruikt in verschillende toepassingen dankzij hun eenvoud en hogere energie-efficiëntie. Ze hebben echter het meeste last van rotorstoringen, omdat er minimaal vier rotoren met vaste spoed nodig zijn om een volledige standcontrole te bereiken. Daarom is het bedenken van FTC-algoritmen voor quadrotors een grote uitdaging.

Aangezien er veel inspanningen zijn geleverd om FTC te ontwikkelen, voor quadrotors die vliegen in bijna zwevende omstandigheden, is een primaire doelstelling van dit proefschrift het verder uitbreiden van FTC-methoden in hogesnelheidsomstandigheden, waar aanzienlijke aerodynamische effecten optreden die grote modelonzekerheden veroorzaken in het controle algoritme. Een voorbeeld van deze omstandigheden is de kruisfase van een bezorgdrone.

Zodra een rotor defect is, kunnen deze aerodynamische effecten de prestaties van FTC-methoden nadelig beïnvloeden. Een beschadige quadrotor kan zelfs in een kritieke toestand komen met abnormale invalshoeken en hoeksnelheden. Enerzijds is het essentieel om "state-of-the-art"FTC-methoden te verbeteren, die significante aerodynamische effecten en mogelijk grote initiële verstoringen kunnen weerstaan. Anderzijds moeten deze aerodynamische effecten verder worden onderzocht en gemodelleerd om de ontwikkeling van FTC onder hoge snelheden te vergemakkelijken. Deze twee aspecten vormen de twee belangrijkste onderdelen van dit thesis.

Het eerste deel van het proefschrift behandelt het aerodynamische modelleringsprobleem van een beschadigde quadrotor tijdens een vlucht met hoge snelheid met behulp van een aerodynamische modelidentificatiebenadering. Voor een beter begrip van de hoge snelheids aerodynamica van quadrotors, heeft deze studie een nominaal "grey-box model"geïdentificeerd met behulp van de gegevens van gecontroleerde vluchttests in een windtunnel (Open Jet Facility, TU Delft). Uit de vluchtgegevens worden effecten zoals significante pitch-up-momenten, rotor-body interacties en giermomentvariaties ontdekt en gemodelleerd, die zelden eerder zijn besproken. Afgezien van deze secundaire effecten worden stuwkrachtvariaties en rotorweerstand opgevat als belangrijke aerodynamische effecten. Dit grijze doosmodel toont respectievelijke verbeteringen van 20% en 80% op aerodynamische kracht en momentvoorspellingen in termen van modelresiduen bij hoge snelheden ten opzichte van modellen die alleen geldig zijn bij lage snelheden.

Het "grey-box model"kan niet direct gegeneraliseerd worden naar omstandigheden met rotoruitval, ondanks de hoge nauwkeurigheid en licht werpt op onbekende aerodynamische effecten. Om deze reden is er een multi-body parametrisch model opgesteld voor het voorspellen van aerodynamische krachten / momenten van een quadrotor, die niet alleen geldig is in nominale omstandigheden maar ook wanneer een willkekeurig aantal rotors faalt. Dit model scheidt het effect van elke rotor en het frame. De modelparameters worden geschat op basis van vluchtgegevens die zijn verkregen in zowel nominale als beschadigde omstandigheden. Om de nauwkeurigheid te verbeteren van gegevens die zijn vervuild door de middelpuntvliedende kracht als gevolg van de hoge gierbeweging in de omstandigheden waarin de rotor faalt, wordt een nieuwe benadering voor het verwerken van gegevens ontwikkeld en geanalyseerd. Tijdens de validatieprocedure is aangetoond dat dit model zowel primaire als secundaire aerodynamische effecten opvangt, zelfs als deze worden veroorzaakt door snelle luchtstroom en gierende bewegingen. Het model is ook geïmplementeerd in een simulatieomgeving om het FTC-ontwerp in het tweede deel te facilitate.

Het tweede deel van het thesis is gericht op het ontwikkelen van robuuste FTC-methoden in het geval van grote aerodynamische en initiële conditiestoornissen. Voor het aanpakken van de modelonzekerheden, die worden veroorzaakt door significante aerodynamische effecten bij hogesnelheidsvluchten, wordt de incrementele niet-lineaire dynamische inversie (INDI) -benadering geïmplementeerd en ontwikkeld bij het optreden van volledig falen van één rotor (single-rotor-falen) en twee tegenoverliggende rotors (dubbele-rotor-falen). In het laatste geval waarin het probleem onderactueerd wordt, analyseert deze studie ook de interne dynamiek voor het definiëren van een geschikte controle-output, die voor het eerst INDI combineert met de output-herdefinitietechniek in een real-life systeem. De voorgestelde robuuste FTC is gevalideerd in de windtunnel door het uitvoeren van snelle gecontroleerde vluchten met een quadrotor die een gefaalde rotor had en een quadrotor met twee gefaalde rotoren. Deze echte vlucht test hebben de robuustheid van de methode aangetoond die beter presteert dan een "benchmark-FTC"benadering. De quadrotor die wordt onderworpen aan volledige uitval van twee rotoren, een traject volgen bij een wind van 5 m / s. Er zijn vluchten behaald met meer dan 8 m / s, wat meer is dan de helft van de maximale normale vliegsnelheid van de geteste quadrotor.

Er is ook een FTC algoritme voor het herstel van overstuur ontwikkeld om grote aanvankelijke verstoringen aan te pakken. Stel je een quadrotor voor, ondersteboven, in combinatie een rotorstoring. Met de voorgestelde FTC-methode kan deze worden hersteld naar de oriëntatie en hoogte vóór het falen. In feite is dit een bijna globaal convergente controller die een beschadigde quadrotor kan stabiliseren vanuit willekeurige initiële oriëntaties en een breed scala aan initiële hoeksnelheden. Daartoe wordt een nieuwe aanpak voor controletoewijzing ontworpen. Deze toewijzingsmethode kan de hoeksnelheid die de herstelprocedure belemmert effectief onderdrukken, terwijl de referentiepunten van de rotorsnelheid worden geleverd volgens de buitenste lus opdrachten. Ter validatie wordt een set Monte Carlo-simulaties uitgevoerd met het aerodynamische model dat in het eerste deel van het proefschrift is geïdentificeerd. Deze simulatie laat zien dat meer dan 95% van de vluchten zich binnen 10 meter hoogteverlies zou kunnen herstellen van willekeurige initiële omstandigheden. Naast het valideren van de controller in simulaties, zijn er echte vluchten uitgevoerd in de Cyberzoo, een in-door-vluchtlaboratorium van de TU Delft, waar een quadrotor met slechts drie rotors willekeurig in de lucht werd gegooid en uiteindelijk werd hersteld in een zwevende staat.

Het onderzoek in dit thesis leidt tot drie aanbevelingen. Ten eerste worden verslechteringen van toestandsschattingen in snelle dynamische omstandigheden ontdekt, die vervolgens de regelprestaties kunnen verslechteren. Om dit probleem te verhelpen, moeten snel draaiende en aerodynamische effecten in aanmerking worden genomen voor een schatting van de toestand. Nadat dit probleem is aangepakt, kan men buitenexperimenten uitvoeren voor snelle vlucht- en verstoorde hersteltests om de droneveiligheid verder te verbeteren in een realistischer scenario. De tweede aanbeveling is om de actuator-dynamische effecten op de INDI-benadering te evalueren, omdat er wordt aangenomen dat deze beperkingen met zich meebrengt voor de voorgestelde FTC-methoden. De achteruitgang als gevolg van de dynamiek van de actuator kan worden verlicht door gebruik te maken van pseudo-control hedging (PCH), of door generaliserende methoden die vertragingen van lineaire systemen naar niet-lineair aanpakken. Tenslotte wordt aanbevolen om de oorzaak van deze complexe aerodynamische effecten op een beschadigde quadrotor te onderzoeken met behulp van statische windtunneltests, computational fluid dynamics (CFD) en analytische benaderingen.

1

INTRODUCTION

Unmanned Aerial Vehicles (UAVs), or drones, have experienced dramatic developments in the last decades because of their great advantages and potentials, such as aerial photography, geographic mapping, precise agriculture, and express delivery. Meanwhile, new applications are still being discovered; hence the number of drones is projected to continue increasing in the future.

Along with the rapid development of drones, *safety* is always one of the major concerns. Crashing a drone could endanger infrastructure, and even worse, harm people on the ground, which is especially critical in applications above population-dense areas, such as package delivery [1] and drone light shows [2]. For some missions, crashing can cause even worse consequences, such as emergency medical deliveries [3], or an irreplaceable drone used for planetary explorations [4].

Among the various threats to safety, failure of the rotor system is a fundamental problem to be tackled. In order to achieve vertical take-off and landing, most drones are designed in configurations that are actuated by several (usually more than four) rotors with fixed-pitch blades (Fig. 1.1). They use the rotor system to generate both lift and control torques. For this reason, rotor failures can dramatically change the flight dynamics and threaten flying safety.

As the most commonly used and simplest multi-rotor drones, quadrotors are especially vulnerable to rotor failures because they lack rotor redundancy (Fig. 1.1a). The reason is that at a minimum of four actuators is required to maintain full control authority of thrust and three-axis attitude of a multi-rotor drone, with which its position within 3D space can be subsequently controlled. Obviously, introducing additional rotors is an appropriate solution for redundancy, which has indeed lead to the invention of other types of multi-rotor drones, such as hexarotors and octorotors (Fig. 1.1b). However, adding more rotors means higher cost, more complexity and hence more potential failure modes. In addition, owing to their significantly lower energy efficiency, they may potentially impact the environment after large-

Figure 1.1: Photos of two types of multi-rotor drones. a.) Quadrotor b.) Octorotor.

scale deployment [5].

Therefore, this thesis focuses on another promising solution, namely the Fault-Tolerant Control (FTC) algorithm, which is a flight controller running onboard of the drone. Just as its name implies, FTC helps a quadrotor to achieve controllable flights despite rotor failures without introducing mechanical adaptations. Instead, only software improvements are needed for the nominal flight controller. Thus this method can be easily deployed in existing platforms. With a well-designed FTC, a damaged quadrotor can perform a safe emergency landing, safely return to the base, or even accomplish the mission despite significant performance degradation.

1.1. QUADROTOR FAULT-TOLERANT CONTROL

A Fault-Tolerant Controller is able to achieve control objectives under both normal and abnormal conditions such as rotor failure. After the occurrence of rotor failures, the controller can be reconfigured according to the variation of the system dynamics, which is determined by the failure severity. Hence different control strategies are implemented in the following two distinct failure conditions. This section briefly reviews existing Fault-Tolerant Control (FTC) methods for quadrotors, and discusses the limitations of existing approaches.

1.1.1. PARTIAL ROTOR FAILURE

In general, partial rotor failure means the reduction of rotor effectiveness in generating the thrust and reaction torque. Partial rotor failure can be caused by electrical malfunctions of motors, or mechanical failures such as propeller blade damage as shown in Fig. 1.2.

With the knowledge of the rotor effectiveness reduction in the quadrotor model, various FTC methods can be designed. To begin with, a Proportional–Integral–Derivative (PID) controller with scheduled gains [6], fuzzy logics [7] and Model-Reference-Adaptive Control (MRAC) [8] have been developed successively. By parametrizing the rotor failure, Liu et al. designed a Linear-Parameter-Varying (LPV) controller [9]. Linear Quadratic Regulator (LQR) and Model Predictive Control (MPC)

Figure 1.2: Example of a quadrotor with partial rotor failure due to blade damage (red-dash line).

are also adopted and compared in [10, 11]. It is noteworthy that an independent Fault Detection and Diagnosis (FDD) module is required by these methods (e.g. [6, 9, 12]) to obtain the information of model variations.

More studies on partial failure problems, however, assume that the failure is unknown to the controller. The system dynamic change after the occurrence of rotor failure is regarded as disturbances to be rejected. Therefore, robust control methods such as Sliding Mode Control (SMC) have been extensively studied on this problem [13–19]. Other methods such as Backstepping [20], $\mathscr{L}1$ adaptive control [21], Active Disturbance Rejection Control (ADRC) [22] were employed on this problem as well. To improve the control performance, some pieces of research also estimate the reduced control effectiveness on-line [23, 24], which is more tightly coupled with the controller as compared with the FDD module mentioned earlier.

In reality, partial propeller damage can very likely cause rotor imbalance and subsequently lead to mechanical vibrations. These vibrations bring a significant amount of noise to the inertia measurement unit (IMU), which will potentially cause the controller's instability. Hence, when a propeller blade is severely bent or broken, the abovementioned partial FTC methods can be ineffective even though the damaged rotor can still generate a limited amount of thrust and torque. In this case, it is a better solution to switch off the damaged rotor and resort to FTC designed for a complete rotor failure condition.

1.1.2. COMPLETE ROTOR FAILURE

Naturally, scenarios with the complete failure of rotors are more hazardous, which could happen due to rotor detachment, or motor shut-off. Different from conditions with partial rotor failures, it is ineffective to increase the control input of the degraded rotor owning to its zero control effectiveness. Instead, an alternative control strategy is required.

For this control problem, seminal work was done by [26], where the authors demonstrated that sacrificing the stability in the yaw direction is inevitable while

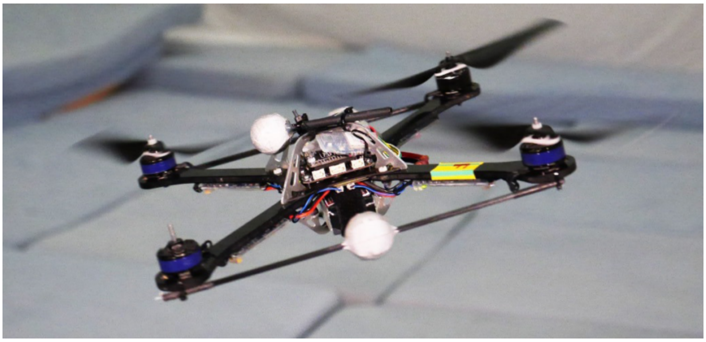

Figure 1.3: Controlled flight of a quadrotor subjected to complete failure of one rotor near hovering condition [25].

the full control of other states remains. As a consequence, the drone needs to spin with a non-zero yaw rate. In [27] and [28], authors solved the problem using a PID controller and a Backstepping approach respectively. Lu and van Kampen employed the Incremental Nonlinear Dynamic Inversion (INDI) approach, together with an FDD module [29]. Crousaz et al. applies the Sequential Linear Quadratic (SLQ) control under an iterative optimal control framework [30]. A geometric approach was proposed in [31] to conduct trajectory tracking control under the complete failure of one rotor. The works mentioned above, however, have only been validated in simulations. Hence their feasibility in real-life environments remains unknown, where the robustness against model uncertainties and computational efficiency have to be considered.

The first controlled flight of a quadrotor subjected to complete failure of one rotor and two opposing rotors was performed in [25]. In order to design the used linear control approach, a subsequent work of the author proposed the relaxed-hovering equilibrium showing the possibility of controlled flight with failure of one, two, or three rotors [32]. A vehicle with specially designed inertia properties has validated the principle with only one rotor remaining in [33]. Apart from classical linear control methods, a Linear Parameter Varying (LPV) control method was proposed by [34] to improve the stability during the accumulation phase of the yaw rate. Impressively, this work also performed low-speed flights in outdoor environments.

1.1.3. CHALLENGES IN QUADROTOR FTC

In reality, rotor failure could occur during high-speed flights, such as the cruising phase of a delivery drone. In such high-speed flight conditions, air inflow with respect to rotors and the air-frame brings significant aerodynamic disturbances, which can greatly deteriorate the FTC performance.

Table. 1.1 compares the existing work on the quadrotor FTC problem with ours. In theory, nonlinear methods considering model uncertainties can, to some extent, address these aerodynamic disturbances in high-speed flights. Unfortunately, they have not been validated in real life; their simulation validations also neglect these aerodynamic effects.

On the other hand, linear approaches have been tested in real flight validations (LQR [32] and LPV [34]) since they are relatively simple to implement. However, in order to establish equilibrium and linearized dynamics required by these linear approaches, they use a simple aerodynamic model, which can significantly differ from reality during high-speed flights. We refer to it as the "hovering-model", and Fig. 1.4 shows a substantial error of the hovering-model prediction on quadrotor pitch moment at 10 m/s forward flight. Such a model mismatch can harm the performance of these linear FTC approaches.

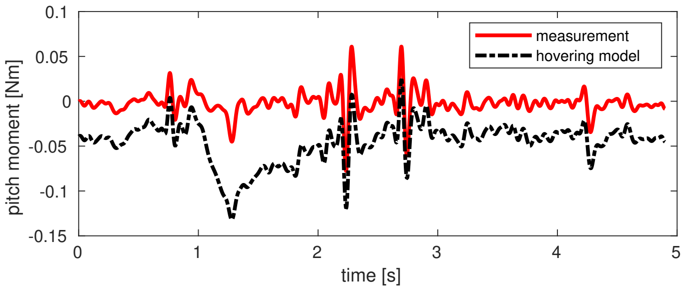

Figure 1.4: Comparison between the measured and model predicted pitch moment of a quadrotor during forward flight at 10m/s. The plot is captured from Fig.19.c in Chapter 2.

Therefore, a major challenge for current research is to design and validate an FTC method capable of high-speed flights of a quadrotor subjected to rotor failures under the disturbance of significant aerodynamic effects. The method has to be robust against significant model uncertainties while being simple and less computation demanding for real-time implementations.

Table 1.1: Comparison on Fault-Tolerant Control of Quadrotor under Complete Rotor Failure

Reference	Method	Nonlinear	Model uncertainty	Double rotor failure	Real flight	High-speed flight
Freddi *et al.* 2011 [26]	Feedback lineraization	✓				
Lanzon *et al.* 2014 [35]	Robust feedback linearization	✓	✓			
Lippiello *et al.* 2014[27]	Backstepping	✓		✓		
Lippiello *et al.* 2014 [27]	PID			✓		
Mueller *et al.* 2015 [32]	Linear quadratic programming (LQR)			✓	✓	
de Crousaz *at al.* 2015 [30]	Sequential linear programming (SLQ)			✓		
Lu *at al.* 2015 [29]	Incremental nonlinear dynamic inversion (INDI)	✓	✓			
Simha *at al.* 2017 [31]	Geometric control	✓	✓			
Stephan *at al.* 2018 [34]	Linear parameter-varying (LPV)			✓	✓	
Hou *at al.* 2020 [36]	Sliding mode control (SMC)	✓	✓			
This thesis (**Chapter 4**)	INDI	✓	✓		✓	✓
This thesis (**Chapter 5**)	INDI with output refinement	✓	✓	✓	✓	✓

1.2. DAMAGED QUADROTOR AERODYNAMICS MODELING

In addition to the controller design, the high-speed-induced aerodynamic effects need to be studied to improve the mathematical models of a damaged quadrotor. These models can be employed in the simulations for FTC design, or directly utilized by the FTC algorithms.

Aerodynamic modeling aims for establishing 3-degrees-of-freedom (3-DoF) forces and moments of a quadrotor subjected to complete rotor failures. Therefore, this section sheds some light on the aerodynamic effects of multi-rotor drones. Afterwards, model identification as the major methodology to develop the aerodynamic model will be briefly introduced.

1.2.1. AERODYNAMIC EFFECTS

Generally speaking, multi-rotor drones can be classified as rotorcraft. Hence a multi-rotor drone and a full-scale helicopter [37] share many similarities in aerodynamic properties, though a drone may have simplified characteristics because of the use of fixed-pitch rotors. In literature, the following effects have been identified:

- Thrust variations ([38–46]). As the name implies, this effect describes the variation of thrust during the translational motion compared with the hovering condition, which is caused by variations in the inflow of the rotor. A thrust model can be found in Fig. 1.5, which is obtained from momentum theory [41]. As the figure shows, both flight speed and the angle-of-attack influence the rotor thrust.

- Blade flapping ([38, 41, 47, 48]). During forward flight, the advancing blade has higher local air velocity and the other way around for the retreating blade. Hence the advancing blade generates a larger lift and flaps upwards while the retreating blade flaps downwards. This phenomena results in a static balance where the entire rotor disc tilts backward and sidewards (see Fig. 1.6). As a result, drag forces are generated as a projection of the tilted thrust vector in the rotor plane.

These two effects have been extensively studied since the advent of rotorcraft. With sufficient knowledge of the vehicle parameters, mathematical models with decent prediction performance can be obtained. For a multi-rotor drone, however, this is not sufficient yet to provide precise force and moment models due to the presence of the following effects:

- Aerodynamic moments on the rotor system [41, 49].

- Rotor-rotor, rotor-body interactions [50].

- Aerodynamic moments/forces on the airframe [51].

- Vortex-ring state [41, 52].

- Ground/ceiling effects [43].

Unfortunately, due to the absence of a thorough understanding of these effects, it is difficult to provide an accurate theoretical model. Instead, we can resort to a *phenomenological model* that relies on observations (data) rather than understanding underlying physics [53]. Notably, this thesis employs the model identification methodology to establish phenomenological aerodynamic models.

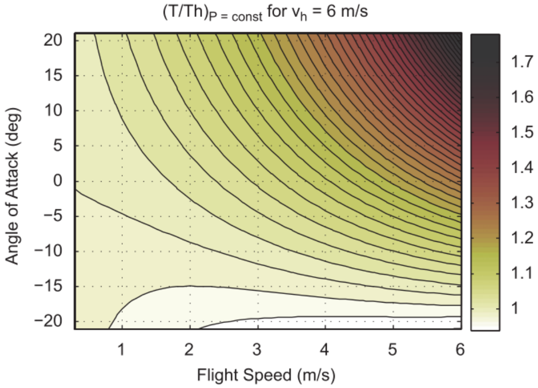

Figure 1.5: Thrust variation with respect to the hovering [41]. T and T_h indicates the thrust and hovering thrust, V_h represents the induced velocity.

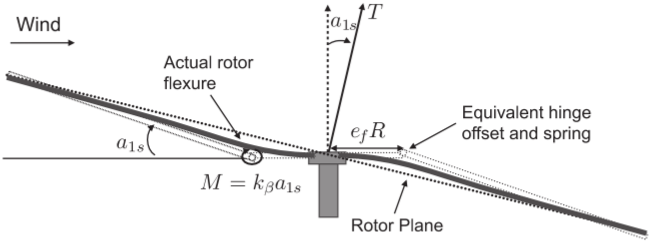

Figure 1.6: Blade flapping with stiff rotor vlades modeled as hinged blades with offset and spring [41].

1.2.2. IDENTIFICATION OF AERODYNAMIC MODEL

System Identification, is a methodology for determining or approximating the mathematical model of a dynamic system without complete knowledge of the underlying physics. Instead, the model is obtained by analyzing the input and output data of the dynamic system obtained from practical applications [54]. Deliberately designed experiments are important for obtaining consistent and accurate

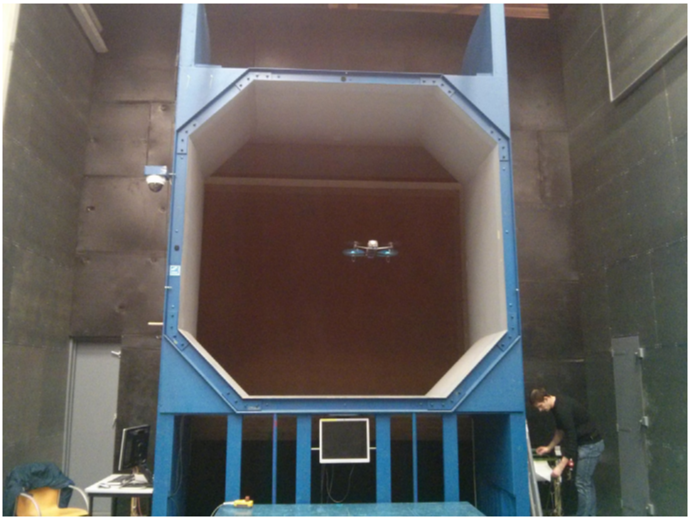

Figure 1.7: A quadrotor flying in a open jet wind-tunnel [57]

.

data sets for system identification. For drones, this means that real flight tests are always required (see e.g., [55]). The flight data can be obtained from various sources, such as measurements from onboard/external sensors, logging of the control commands. Before being fed into the identification algorithms, data preprocessing is often needed to alleviate the noise, eliminate the bias, synchronized measurements from different sources.

System identification algorithms also require sufficient excitations on the system to improve model versatility and accuracy [56]. For identifying a nonlinear global model of a drone, it is necessary to explore the flight envelope as much as possible while collecting data such that the identified model is valid in a wider operating regime. By providing carefully designed excitation sequences, colinearities in data sets can be reduced, resulting in lower parameter (co)variances when using parameter estimators. This can be achieved by performing different types of maneuvers in a wide range of flight speeds to explore the state space. Therefore, it is favorable to conduct flight experiments in a controlled environment for above purposes, such as a large-scale open jet wind-tunnel shown in Fig. 1.7.

Apart from data collection, the type of model structure is also essential. For aerodynamic model identification, the gray-box model structure is a popular choice since it fuses both the theoretical knowledge and data information when full knowledge of the aerodynamics is unattainable, as elaborated in Sec. 1.2.1. Different from generic black-box models (such as a neural network) identified directly from data, gray-box models utilize some physical understandings of the system. Thus, in general, they have higher accuracy in regimes where flight data is scarce.

1.2.3. CHALLENGES IN AERODYNAMIC IDENTIFICATION

As a central element in aerodynamic identification, flight data must be acquired from controllable flights in the high-speed condition where aerodynamic effects are apparent. This task is especially challenging with the occurrence of complete rotor failures, as standard controllers from literature are not adequate. For this reason, a novel FTC method needs to be devised to conduct real flights in the wind-tunnel, in spite of significant unknown aerodynamic disturbances.

Apart from the acquired flight data, selecting an appropriate model structure is of great importance. As a synthesis of both physical knowledge and data information, the identified model is ideally to be accurate in various flight conditions and vehicle configurations. However, accuracy and versatility are usually contradictory if data is limited. Hence a well-defined model structure is required, which captures primary aerodynamic effects by utilizing existing theories that are generally valid while effectively integrating data observations into the model for accuracy. Selecting such a model structure is still an open question for multi-rotor drone aerodynamic identifications.

1.3. THESIS GOAL AND RESEARCH APPROACH

1.3.1. GOAL OF THIS THESIS

In consideration of the need for a more real-life applicable fault-tolerant flight control method for quadcopter UAV, this thesis tackles the above-mentioned challenges on quadrotor FTC and aerodynamic modeling. Therefore, the main research goal of this thesis is defined as:

Research Goal

Establish aerodynamic models and devise control methods for a quadrotor drone subjected to complete failure of the rotor system in real-life environments with significant aerodynamic disturbances.

The main research goal can be split into two research questions. The first question is regard to the aerodynamic model identification:

Research Question I

How to establish aerodynamic models of a quadrotor subjected to complete failure of rotors in the high-speed flight regime using an aerodynamic model identification approach?

The second question is related to the fault-tolerant flight control methods:

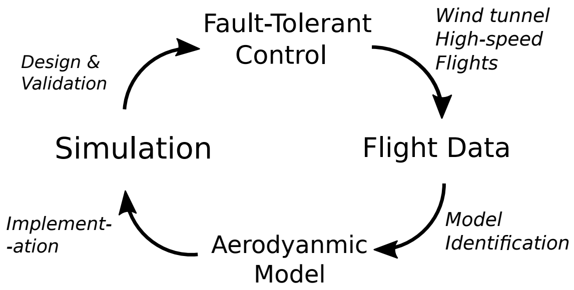

Figure 1.8: Iteration logic of the research.

Research Question II

How to devise a fault-tolerant control method for a quadrotor subjected to complete failure of rotors that is robust against significant aerodynamic effects?

1.3.2. RESEARCH APPROACH

In order to answer the defined research questions, this study will take an iterative research approach (Fig. 1.8). First, the aerodynamic model of a quadrotor in the nominal condition (without failure) will be identified from flight data using a benchmark control method [24]. The model provides deep insights into aerodynamic effects, and accelerates the development of the FTC method. Afterwards, the novel FTC method will be utilized to conduct high-speed flight of a quadrotor subjected to complete rotor failures in the wind tunnel. The flight data obtained, in turn, will be again employed to update the aerodynamic model in terms of both fidelity and versatility. The model is subsequently implemented in the simulation platform whereby the performance of FTC can be further tested and improved.

1.3.3. SCOPE AND LIMITATIONS

Since the failure of an entire rotor can significantly change the quadrotor dynamics, a Fault Detection and Diagnostics (FDD) module can be relatively simple to implement using, for example, an Extended Kalman Filter (EKF) or monitoring the motor currency. Hence a Fault Detection and Diagnostics (FDD) technique is not studied in this thesis, and the FTC is devised by assuming a predetermined rotor failure.

As mentioned in Sec. 1.3.2, the aerodynamic effects are studied for modeling purposes, instead of understanding the underlying physical mechanisms. Thus this thesis only provides limited reasoning about complex aerodynamics (such as wake interactions, vortex ring effects, etc.) instead of a systematic study of these phenomena using, for example, static wind-tunnel tests and particle image velocimetry

(PIV) techniques. Ground / ceiling effects are also excluded from the scope of this research since they rarely occur in the out-door high-speed flight scenario.

The term "robust" in the context of this thesis indicates the ability of a controller to be effective withstanding the model uncertainties / mismatch caused by aerodynamic effects. While improving robustness of the FTC method is our major goal, we are not leveraging modern "robust control methods" which is a well-known branch of the modern control theory, such as H-infinity [58] and sliding-mode control [59].

1.4. THESIS OUTLINE

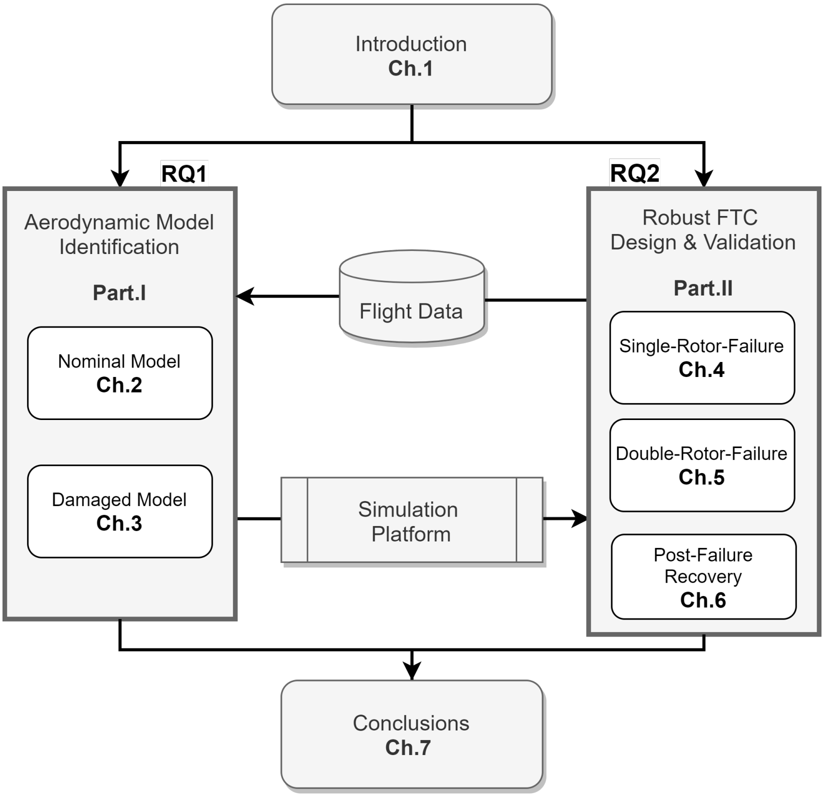

Figure 1.9: Overview of the thesis structure.

The research questions will be answered in the following chapters. Each chapter has been published in peer-reviewed journals and conference proceedings. As Fig. 1.9 presents, these chapters are divided into two parts. Part I focus on the aerodynamic model identification (RQ1). Part II presents the design and validation of a robust fault-tolerant controller under different conditions. The answers to the primary research questions will be concluded in the last chapter.

In **Chapter 2**, we use a controller from literature [24] to conduct a high-speed flight test of a quadrotor in a wind tunnel. With the flight data obtained, a gray-box aerodynamic model of a quadrotor without rotor failure is identified. In addition to capturing the major well-known aerodynamic effects such as blade flapping and thrust variation, the identified model also reveals the existence of aerodynamic moments on the rotor system and interactions between rotors. The identified gray-box model is then implemented in the simulation to help the design of the FTC.

Chapter 3 presents the work of identifying a gray-box multi-body aerodynamic model using the wind-tunnel flight data from Part.II. Inspired by the nominal model identified in Chapter 1, the 3-axis forces and moments of each rotor are considered in the model identification. Aerodynamic effects of the airframe are also taken into account, yielding a novel multi-body aerodynamic model. In addition to the flight data, static wind-tunnel tests of a single rotor are performed to extend the validity regime of the model.

Chapter 4 and **Chapter 5** present the work of designing the FTC methods for a quadrotor with complete loss of one rotor and two opposing rotors respectively. Both chapters employ the so-called incremental nonlinear dynamic inversion (INDI) technique to address aerodynamic disturbances and model uncertainties. Since the control problem is under-actuated when only two rotors remain, Chapter 5 sheds more light on the analysis of quadrotor internal dynamics for output-redefinition. Both FTCs are validated in high-speed flight tests in a wind tunnel to demonstrate significant robustness compared with the state-of-art [32]. Moreover, the flight data are subsequently used in Chapter 3 to identify the multi-body aerodynamic model.

By updating the simulation with the identified model from Chapter 3, a post-failure recovery controller is devised in **Chapter 6**. Apart from addressing disturbances associated with aerodynamics, the proposed controller also recovers the post-failure quadrotor from arbitrary initial attitude and angular rates. Monte-Carlo simulations using models from Chapter 3 are conducted to demonstrate the controller's capability of recovering a quadrotor with loss of a single rotor from random initial states while cruising at high speed.

REFERENCES

[1] K. Dorling, J. Heinrichs, G. G. Messier, and S. Magierowski, *Vehicle routing problems for drone delivery,* (IEEE, 2016) pp. 70–85.

[2] M. Waibel, B. Keays, and F. Augugliaro, *Drone shows: Creative potential and best practices*, Tech. Rep. (ETH Zurich, 2017).

[3] E. Ackerman and E. Strickland, *Medical delivery drones take flight in east africa,* IEEE Spectrum **55**, 34 (2018).

[4] M. Hassanalian, D. Rice, and A. Abdelkefi, *Evolution of space drones for planetary exploration: A review,* (Elsevier, 2018) pp. 61–105.

[5] J. K. Stolaroff, C. Samaras, E. R. O’ Neill, A. Lubers, A. S. Mitchell, and D. Ceperley, *Energy use and life cycle greenhouse gas emissions of drones for commercial package delivery,* Nature communications **9**, 1 (2018).

[6] A. Milhim, Y. Zhang, and C.-A. Rabbath, *Gain scheduling based pid controller for fault tolerant control of quad-rotor uav,* in *AIAA infotech@ aerospace 2010* (2010) p. 3530.

[7] M. H. Amoozgar, A. Chamseddine, and Y. Zhang, *Fault-tolerant fuzzy gain-scheduled pid for a quadrotor helicopter testbed in the presence of actuator faults,* (Elsevier, 2012) pp. 282–287.

[8] I. Sadeghzadeh, A. Mehta, Y. Zhang, and C.-A. Rabbath, *Fault-tolerant trajectory tracking control of a quadrotor helicopter using gain-scheduled pid and model reference adaptive control,* in *Annual Conference of the Prognostics and Health Management Society*, Vol. 2 (2011).

[9] Z. Liu, C. Yuan, and Y. Zhang, *Active fault-tolerant control of unmanned quadrotor helicopter using linear parameter varying technique,* Journal of Intelligent & Robotic Systems **88**, 415 (2017).

[10] B. Yu, Y. Zhang, I. Minchala, and Y. Qu, *Fault-tolerant control with linear quadratic and model predictive control techniques against actuator faults in a quadrotor uav,* in *2013 Conference on Control and Fault-Tolerant Systems (SysTol)* (IEEE, 2013) pp. 661–666.

[11] H. A. Izadi, Y. Zhang, and B. W. Gordon, *Fault tolerant model predictive control of quad-rotor helicopters with actuator fault estimation,* in *Proceedings of the 18th IFAC World Congress*, Vol. 18 (2011) pp. 6343–6348.

[12] Y. Zhang, A. Chamseddine, C. A. Rabbath, B. W. Gordon, C.-Y. Su, S. Rakheja, C. Fulford, J. Apkarian, and P. Gosselin, *Development of advanced fdd and ftc techniques with application to an unmanned quadrotor helicopter testbed,* Journal of the Franklin Institute **350**, 2396 (2013).

[13] F. Sharifi, M. Mirzaei, B. W. Gordon, and Y. Zhang, *Fault tolerant control of a quadrotor uav using sliding mode control,* in *2010 Conference on Control and Fault-Tolerant Systems (SysTol)* (IEEE, 2010) pp. 239–244.

[14] T. Li, Y. Zhang, and B. W. Gordon, *Passive and active nonlinear fault-tolerant control of a quadrotor unmanned aerial vehicle based on the sliding mode control technique,* (SAGE Publications Sage UK: London, England, 2013) pp. 12–23.

[15] L. Besnard, Y. B. Shtessel, and B. Landrum, *Quadrotor vehicle control via sliding mode controller driven by sliding mode disturbance observer,* Journal of the Franklin Institute **349**, 658 (2012).

[16] T. Li, Y. Zhang, and B. W. Gordon, *Passive and active nonlinear fault-tolerant control of a quadrotor unmanned aerial vehicle based on the sliding mode control technique,* Proceedings of the Institution of Mechanical Engineers, Part I: Journal of Systems and Control Engineering **227**, 12 (2013).

[17] A.-R. Merheb, H. Noura, and F. Bateman, *Active fault tolerant control of quadrotor uav using sliding mode control,* in *2014 International Conference on Unmanned Aircraft Systems (ICUAS)* (IEEE, 2014) pp. 156–166.

[18] A.-R. Merheb, H. Noura, and F. Bateman, *Design of passive fault-tolerant controllers of a quadrotor based on sliding mode theory,* International Journal of Applied Mathematics and Computer Science **25**, 561 (2015).

[19] F. Chen, K. Zhang, Z. Wang, G. Tao, and B. Jiang, *Trajectory tracking of a quadrotor with unknown parameters and its fault-tolerant control via sliding mode fault observer,* (SAGE Publications Sage UK: London, England, 2015) pp. 279–292.

[20] X. Zhang, Y. Zhang, C.-Y. Su, and Y. Feng, *Fault-tolerant control for quadrotor uav via backstepping approach,* in *48th AIAA Aerospace Sciences Meeting Including the New Horizons Forum and Aerospace Exposition* (2010) p. 947.

[21] D. Xu, J. F. Whidborne, and A. Cooke, *Fault tolerant control of a quadrotor using c 1 adaptive control,* International Journal of Intelligent Unmanned Systems (2016).

[22] Y. Guo, B. Jiang, and Y. Zhang, *A novel robust attitude control for quadrotor aircraft subject to actuator faults and wind gusts,* IEEE/CAA Journal of Automatica sinica **5**, 292 (2017).

[23] D. Höppener, *Actuator saturation handling using weighted optimal control allocation applied to an indi controlled quadcopter,* (2016).

[24] E. J. Smeur, Q. Chu, and G. C. de Croon, *Adaptive incremental nonlinear dynamic inversion for attitude control of micro air vehicles,* Journal of Guidance, Control, and Dynamics **39**, 450 (2016).

[25] M. W. Mueller and R. D'Andrea, *Stability and control of a quadrocopter despite the complete loss of one, two, or three propellers,* in *2014 IEEE international conference on robotics and automation (ICRA)* (IEEE, 2014) pp. 45–52.

[26] A. Freddi, A. Lanzon, and S. Longhi, *A feedback linearization approach to fault tolerance in quadrotor vehicles,* (Elsevier, 2011) pp. 5413–5418.

[27] V. Lippiello, F. Ruggiero, and D. Serra, *Emergency landing for a quadrotor in case of a propeller failure: A backstepping approach,* in *2014 IEEE/RSJ International Conference on Intelligent Robots and Systems* (IEEE, 2014) pp. 4782–4788.

[28] V. Lippiello, F. Ruggiero, and D. Serra, *Emergency landing for a quadrotor in case of a propeller failure: A pid based approach,* in *2014 IEEE International Symposium on Safety, Security, and Rescue Robotics (2014)* (IEEE, 2014) pp. 1–7.

[29] P. Lu and E.-J. van Kampen, *Active fault-tolerant control for quadrotors subjected to a complete rotor failure,* in *2015 IEEE/RSJ International Conference on Intelligent Robots and Systems (IROS)* (IEEE, 2015) pp. 4698–4703.

[30] C. De Crousaz, F. Farshidian, M. Neunert, and J. Buchli, *Unified motion control for dynamic quadrotor maneuvers demonstrated on slung load and rotor failure tasks,* in *2015 IEEE International Conference on Robotics and Automation (ICRA)* (IEEE, 2015) pp. 2223–2229.

[31] A. Simha, S. Vadgama, and S. Raha, *A geometric approach to rotor failure tolerant trajectory tracking control design for a quadrotor,* arXiv preprint arXiv:1704.00327 (2017).

[32] M. W. Mueller and R. D' Andrea, *Relaxed hover solutions for multicopters: Application to algorithmic redundancy and novel vehicles,* The International Journal of Robotics Research **35**, 873 (2016).

[33] W. Zhang, M. W. Mueller, and R. D'Andrea, *A controllable flying vehicle with a single moving part,* in *2016 IEEE International Conference on Robotics and Automation (ICRA)* (IEEE, 2016) pp. 3275–3281.

[34] J. Stephan, L. Schmitt, and W. Fichter, *Linear parameter-varying control for quadrotors in case of complete actuator loss,* Journal of Guidance, Control, and Dynamics **41**, 2232 (2018).

[35] A. Lanzon, A. Freddi, and S. Longhi, *Flight control of a quadrotor vehicle subsequent to a rotor failure,* Journal of Guidance, Control, and Dynamics **37**, 580 (2014).

[36] Z. Hou, P. Lu, and Z. Tu, *Nonsingular terminal sliding mode control for a quadrotor uav with a total rotor failure,* Aerospace Science and Technology **98**, 105716 (2020).

[37] R. C. Leishman, J. C. Macdonald, R. W. Beard, and T. W. McLain, *Quadrotors and accelerometers: State estimation with an improved dynamic model,* IEEE Control Systems Magazine **34**, 28 (2014).

[38] G. Hoffmann, H. Huang, S. Waslander, and C. Tomlin, *Quadrotor helicopter flight dynamics and control: Theory and experiment,* in *AIAA guidance, navigation and control conference and exhibit* (2007) p. 6461.

[39] P.-J. Bristeau, P. Martin, E. Salaün, and N. Petit, *The role of propeller aerodynamics in the model of a quadrotor uav,* in *2009 European control conference (ECC)* (IEEE, 2009) pp. 683–688.

[40] P. Pounds, R. Mahony, and P. Corke, *Modelling and control of a large quadrotor robot,* Control Engineering Practice **18**, 691 (2010).

[41] G. M. Hoffmann, H. Huang, S. L. Waslander, and C. J. Tomlin, *Precision flight control for a multi-vehicle quadrotor helicopter testbed,* Control engineering practice **19**, 1023 (2011).

[42] M. Orsag and S. Bogdan, *Influence of forward and descent flight on quadrotor dynamics,* Recent Advances in Aircraft Technology , 141 (2012).

[43] C. Powers, D. Mellinger, A. Kushleyev, B. Kothmann, and V. Kumar, *Influence of aerodynamics and proximity effects in quadrotor flight,* in *Experimental robotics* (2013) pp. 289–302.

[44] W. Khan and M. Nahon, *Toward an accurate physics-based uav thruster model,* IEEE/ASME Transactions on Mechatronics **18**, 1269 (2013).

[45] J. Svacha, K. Mohta, and V. Kumar, *Improving quadrotor trajectory tracking by compensating for aerodynamic effects,* in *2017 international conference on unmanned aircraft systems (ICUAS)* (IEEE, 2017) pp. 860–866.

[46] R. Gill and R. D'Andrea, *Propeller thrust and drag in forward flight,* in *2017 IEEE Conference on Control Technology and Applications (CCTA)* (IEEE, 2017) pp. 73–79.

[47] R. Mahony, V. Kumar, and P. Corke, *Multirotor aerial vehicles: Modeling, estimation, and control of quadrotor,* IEEE Robotics and Automation magazine **19**, 20 (2012).

[48] Y.-R. Tang and Y. Li, *Dynamic modeling for high-performance controller design of a uav quadrotor,* in *2015 IEEE International Conference on Information and Automation* (IEEE, 2015) pp. 3112–3117.

[49] D. Kaya and A. T. Kutay, *Aerodynamic modeling and parameter estimation of a quadrotor helicopter,* in *AIAA Atmospheric Flight Mechanics Conference* (2014) p. 2558.

[50] J. Luo, L. Zhu, and G. Yan, *Novel quadrotor forward-flight model based on wake interference,* AIAA Journal **53**, 3522 (2015).

[51] M. Schulz, F. Augugliaro, R. Ritz, and R. D'Andrea, *High-speed, steady flight with a quadrocopter in a confined environment using a tether,* in *2015 IEEE/RSJ International Conference on Intelligent Robots and Systems (IROS)* (IEEE, 2015) pp. 1279–1284.

[52] J. V. Foster and D. Hartman, *High-fidelity multi-rotor unmanned aircraft system (uas) simulation development for trajectory prediction under off-nominal flight dynamics,* in *17th AIAA Aviation Technology, Integration, and Operations Conference* (2017) p. 3271.

[53] T. Wilholt, *Explaining models: Theoretical and phenomenological models and their role for the first explanation of the hydrogen spectrum,* Foundations of Chemistry **7**, 149 (2005).

[54] L. Ljung, H. Hjalmarsson, and H. Ohlsson, *Four encounters with system identification,* European Journal of Control **17**, 449 (2011).

[55] M. Burri, J. Nikolic, H. Oleynikova, M. W. Achtelik, and R. Siegwart, *Maximum likelihood parameter identification for mavs,* in *2016 IEEE International Conference on Robotics and Automation (ICRA)* (IEEE, 2016) pp. 4297–4303.

[56] E. A. Morelli and V. Klein, *Aircraft system identification: theory and practice* (Sunflyte Enterprises Williamsburg, VA, 2016).

[57] E. J. Smeur, G. C. de Croon, and Q. Chu, *Cascaded incremental nonlinear dynamic inversion for mav disturbance rejection,* Control Engineering Practice **73**, 79 (2018).

[58] G. Zames, *Feedback and optimal sensitivity: Model reference transformations, multiplicative seminorms, and approximate inverses,* IEEE Transactions on automatic control **26**, 301 (1981).

[59] V. I. Utkin, *Sliding mode control design principles and applications to electric drives,* IEEE transactions on industrial electronics **40**, 23 (1993).

2

QUADROTOR GRAY-BOX MODEL IDENTIFICATION FROM HIGH-SPEED FLIGHT DATA

In this chapter, the aerodynamic effects on a quadrotor are studied by carrying out free flight tests in a large scale wind tunnel. The flight data reveal that complex aerodynamic interactions could appear and significantly influence the forces and moments acting on the quadrotor, which indicates the inaccuracy of state-of-art models established based on helicopter aerodynamic theory. To cope with this problem, gray-box models considering these effects are identified from flight data using a stepwise system identification approach, which combines both prior-knowledge of rotorcraft aerodynamic properties as well as data observations. Previous models introduced in the literature are compared with the gray-box models. Validation results show an 80% reduction of moment model residuals and 20% reduction of force model residuals.

Parts of this chapter have been published in:

S. Sun, C. C. de Visser, and Q. Chu, "Quadrotor Gray-Box Model Identification from High-Speed Flight Data," Journal of Aircraft., vol. 56, no. 2, pp. 645–661, Mar. 2019.

2.1. INTRODUCTION

Multi rotor drones are widely used currently as an efficient tool in multiple applications such as reconnaissance, package delivery, agriculture monitoring, filming and even personal transportation. Multi-rotor drones are equipped with individual rotors producing both propulsion and control power and frequently operate in non-hovering conditions in out-door environments. During flights with non-static incoming flow in these conditions, the aerodynamic characteristics of these rotors are different from those modeled in static conditions and considerable free-stream induced aerodynamic effects become apparent.

Drones are able to operate in conditions where additional aerodynamic effects occur without full knowledge of them due to the high update rates of sensors and robustness of the controller [1–3]. However, knowledge of these effects will be necessary for controllers capable of fully exploring the flight envelope [4, 5] such as high speed flights with aggressive maneuveres. Next to the controller enhancement, the modeling of these aerodynamic effects is also desirable of providing better attitude estimation [6] and refining the design process [7]. In addition, full knowledge of these aerodynamic effects is also required for high fidelity simulation platforms [8] and finally, global models need to be established for flight envelope computation [9], which is the main motivation for the current work.

The main subject of this research is the quadrotor, one of the simplest possible multi rotor drones. The aerodynamic effects acting on quadrotors can be summarized as the force variation and moment variation compared to that in the hovering condition without ground effect. Several discussions about these forces and moment variations are present in the literature.

Most literature sources focus on improving the thrust model. Ref. [10] , for instance, elaborate the cause of thrust variation during translational flight. The modeling process is mostly derived from helicopter aerodynamic theories. Ref. [4, 10, 11] use momentum theory to develop the model of relationships between thrust efficiency, flight speed, and the angle of attack. Thrust calculation of a single rotor according to blade element theory is adopted [12–15]. Momentum theory and blade element theory are also combined and a so-called blade element momentum (BEMT) theory is used to enhance the thrust model accuracy [16–18] .

Drag forces, which are mostly defined in the blade plane of multi-rotor drones, are also discussed in literature. The blade flapping effect is considered the main cause of drag force [10, 15, 19–21]. According to Ref. [12, 17, 19, 20], lift also induces an aerodynamic drag on the blade elements and generates a hub force perpendicular to the thrust. Besides the resistance caused by the rotor, the aerodynamic drag from the airframe is also considered [16], which is quadratic related to the flight speed.

Compared to forces, moment variations have received less attention in existing literature. The additional pitching moment due to the translational velocities is observed in the wind tunnel test presented in Ref. [22]. In the trim condition during forward flight, the aft rotors rotate faster than the front rotor. Damping effects [21], blade stiffness [11] and drag forces [21] are considered to cause these moments as well. The bare airframe itself may also generate a pitching moment [8]. To the best of the author's knowledge no high fidelity models of the aerodynamic moments exist in the literature.

Besides the forces and moments generated from individual propellers and airframe, rotor-rotor and airframe-rotor interaction effects are suspected to greatly influence the aerodynamic forces and moments. Ref. [13] shows that the interaction between multiple rotors deteriorates the total thrust from wind tunnel tests. Ref. [8] divides the forces and moments into propulsion, airframe and interaction units, and the research of interaction terms is still ongoing. Models considering the interaction effect have been made [7][23] based on physical theory and engineering assumptions, however, not validated with in-flight data. The actual effects of these interactions on thrust, drag and moments remain largely unknown, which should be investigated with free flight experiments.

The main contribution of this research is further revealing the effect of above interactions from flight data and establish accurate force and moment models taking account of these effects. To this end, multiple free flight tests have been carried out. Based on the data from these tests, it is shown that the interaction effects deteriorate the well-established thrust and drag model based on the first principles, and in addition demonstrate significant inaccuracies in the pitch and rolling moment predictions obtained with the broadly accepted quadrotor hovering model, i.e the distance of propellers times their thrust differences. Furthermore, it is shown that the yawing moment is strongly influenced by the incoming flow during high speed flight, which has not been discussed before.

We use a system identification approach to establish a high fidelity model of forces and moments which is valid in a larger flight envelope. Different from the first-principles modeling approach derived from helicopter aerodynamic theory, system identification methods are proper choice for modeling these complex interaction effects. Specifically, a gray-box model is established which combines the information from prior-physical knowledge of rotor-craft theory with experimental data obtained during high speed flight, and possesses both reliability of physical theory and accuracy of observation.

Several system identification techniques can be applied to establish nonlinear gray-box models, depending on the structure of the model, such as polynomial functions, multivariate spline-functions, neural networks, etc. Among them, a simple but effective piecewise polynomial structure is selected. A stepwise method is used for determining the model structure by selecting terms from a large set of candidate terms. This technique has been used in the past for full-scale aircraft system identification [24–26] but has never been seen used for determining the aerodynamic model of a quadrotor. The model structure candidates are determined from prior-knowledge of rotor-craft aerodynamic theories as well as preliminary assumptions. The stepwise method selects candidates into the model in a stepwise scheme according to their contributions to the current model.

The identified models are compared with state-of-art force models considering aerodynamic effects as well as moment models established in hovering conditions. The validation results reveal around 20% improvement in the accuracy of force model and more importantly, over 80% improvement in the moment model in terms of the residual root mean square (RMS) in non-hovering conditions. Although these models are specific to the Bebop platform, the methodologies can be generalized to other multi-rotor platforms.

The flight experiments are carried out in the Open Jet Facility (OJF), a large scale wind tunnel with a 3 meters aperture operated by the Delft University of Technology, as shown in Fig. 2.1. In contrast to static wind tunnel tests, free flights are performed in the OJF in order to negate the disturbance effect of a force balance and more importantly, to take dynamic motions into account. The wind tunnel provides 2.5 m by 2.5 m by 5.0 m space to carry out these flights. A large number of different flight maneuvers are made to fully excite the system and a maximum air speed up to 14 m/s is achieved. An of-the-shelf quadrotor (Parrot Bebop) running open-source autopilot (Paparazzi) is used in these flights. The standard build-in inertia measurement unit (IMU) running at 512 Hz and external motion capture systems (Optitrack) running at 360 Hz are sensor-fused for data acquisition [27].

Figure 2.1: Open Jet Facility (OJF), a large-scale wind tunnel, and the tested quadrotor.

A normalization method for modeling multi-rotor drones in terms of dimensionless coefficients is proposed in this research. The dimensionless aerodynamic coefficients and states are analogous to those used for single rotorcraft. Moment coefficients are for the first time introduced for quadrotor drones, taking into account their multi-rotor characteristics. The gray-box model established will be presented in dimensionless form as a mapping between dimensionless states and force (moment) coefficients. These dimensionless coefficients are also useful for revealing the interaction effects, and even for comparing the aerodynamic properties of different drone models.

The article is organized as follows. Chapter 2.2 introduces coordinate definition and hovering model definition. Chapter 2.3 depicts the stepwise method and provides definition of dimensionless aerodynamic coefficients and other dimensionless variables related to the model. Chapter 2.4 describes the flight test for this research and discusses the interaction effects observed from flight data. The identification process and results can be found in Chapter 2.5 and 2.6 respectively.

2.2. PRELIMINARY MODELING

A benchmark model is introduced in this chapter with the aim of further introducing the gray-box model and make comparisons between them. First, the two coordinate systems, in the form of the ground frame and the body frame, are defined (Fig. 2.2). For the ground frame, x_G is defined towards the wind tunnel nozzle, in order words, into the free stream; z_G is aligned with the gravity direction pointing downwards. The body frame is fixed to the vehicle with the center of gravity at the origin. x_B is aligned with the nose direction, y_B points to the right and z_B points against the thrust direction.

Airspeed, the flight speed with respect to the air stream, is defined as

$$\boldsymbol{V} = \boldsymbol{V}_g - \boldsymbol{V}_{wind} \tag{2.1}$$

where $\boldsymbol{V}_g$ and $\boldsymbol{V}_{wind}$ indicate ground speed and wind speed respectively. The projection of airspeed on the body frame is expressed as $\boldsymbol{V} = [u \quad v \quad w]^T$. Angle of attack α and sideslip angle β are defined as

$$\alpha = \arcsin(w/V) \qquad \beta = \arcsin(v/\sqrt{v^2 + u^2}) \tag{2.2}$$

where $V = ||\boldsymbol{V}||$. Note that since the quadrotor is able to hover and reverse, these two angles are singular when airspeed equals zero.

Rotor speeds (in rad/s) are expressed as $[\Omega_1 \quad \Omega_2 \quad \Omega_3 \quad \Omega_4]$ respectively. Fig. 2.2 shows the rotor index and their rotation directions of Parrot Bebop quadrotor, which is the object to be modeled in this Chapter.

For simplicity, the quadrotor is regarded as a rigid-body of which the translational and rotational dynamic equations can be written as

$$\dot{\boldsymbol{V}} + \boldsymbol{\Omega} \times \boldsymbol{V} = \boldsymbol{R}_{BG}\boldsymbol{g} + \boldsymbol{F}/m \tag{2.3}$$

$$\boldsymbol{I}_v\dot{\boldsymbol{\Omega}} + \boldsymbol{\Omega} \times \boldsymbol{I}_v\boldsymbol{\Omega} = \boldsymbol{M} + \boldsymbol{M}_{I_p} \tag{2.4}$$

where $\boldsymbol{g} = [0 \quad 0 \quad g]^T$ indicates the gravity vector expressed in the ground frame. $\boldsymbol{\Omega} = [p \quad q \quad r]^T$ represents the angular velocity expressed in the body frame. The

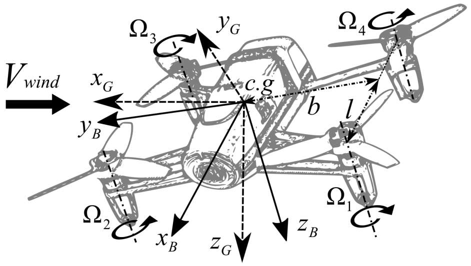

Figure 2.2: Coordinate systems definition and sketch of Parrot Bebop quadrotor.

aerodynamic forces and moments are denoted as $\boldsymbol{F}$ and $\boldsymbol{M}$ respectively, which are expressed in the body frame as well. $\boldsymbol{R}_{BG}$ is the rotational matrix from the ground frame to the body frame. $\boldsymbol{I}_v$ stands for the inertia matrix and m indicates the mass of the vehicle. $\boldsymbol{M}_{I_p}$ represents the moments due to gyroscopic effects and rotor spin-up torque; the later has been found significantly influence the Bebop quadrotor [28]

$$\boldsymbol{M}_{I_p} = \begin{bmatrix} qI_p(-\Omega_1 + \Omega_2 - \Omega_3 + \Omega_4) \\ pI_p(\Omega_1 - \Omega_2 + \Omega_3 - \Omega_4) \\ I_p(-\dot{\Omega}_1 + \dot{\Omega}_2 - \dot{\Omega}_3 + \dot{\Omega}_4) \end{bmatrix} \tag{2.5}$$

The positioning of a quadrotor in 3D space is controlled by changing its attitude and total thrust. The attitude can be changed by differential thrust. Specifically, rotor speed difference between front and aft rotors produces a pitching moment, while a rolling moment can be produced by differential thrust between left and right rotors. The rotor reaction torque is used to generate a yawing moment which the quadrotor uses to control its heading.

The emphasis of modeling is on the aerodynamic force vector $\boldsymbol{F}$ and the aerodynamic moment vector $\boldsymbol{M}$. Before establishing a gray-box model for $\boldsymbol{F}$ and $\boldsymbol{M}$, a hovering model that is only valid in hovering condition, is introduced as a benchmark for comparison

$$\boldsymbol{F}_h = \begin{bmatrix} 0 \\ 0 \\ -\kappa_0 \sum \Omega_i^2 \end{bmatrix} \tag{2.6}$$

$$\boldsymbol{M}_h = \begin{bmatrix} b\kappa_0(\Omega_1^2 + \Omega_2^2 - \Omega_3^2 - \Omega_4^2) \\ l\kappa_0(\Omega_1^2 - \Omega_2^2 - \Omega_3^2 + \Omega_4^2) \\ \tau_0(-\Omega_1^2 + \Omega_2^2 - \Omega_3^2 + \Omega_4^2) + \lambda_r r \end{bmatrix} \tag{2.7}$$

where l and b are geometry parameters of the quadrotor as Fig. 2.2 shows. κ_0, τ_0 and λ_r are constant coefficients. Note that the aerodynamic forces and moments are expressed in the body frame in this chapter. Therefore, the third component of $\boldsymbol{F}_h$ equals to the negative of the total thrust. Meanwhile, the first two components of

$\boldsymbol{F}_h$ equal zero, which means that rotor in-plane forces (i.e drag forces) are neglected.

However, significant in-plane drag has been found [6, 12, 17, 19] and thrust also varies with the flight speed beyond the hovering regime [11]. Furthermore, aerodynamic moments are found to be completely different from what the hovering model predicts. These studies indicate the importance of finding a model which is valid in a larger flight envelope.

In this chapter, a gray-box model is identified from high-speed free-flight data obtained in a wind tunnel. The aerodynamic effect of individual rotors, the rotor-rotor and rotor-airframe aerodynamic interactions in high-speed conditions are considered in this gray-box model as well.

2.3. METHODOLOGIES

2.3.1. NONDIMENSIONALIZATION

Dimensionless aerodynamic coefficients are convenient for comparisons between different conditions and platforms. For a single rotor, forces and moments can be normalized by rotor speed and reference area [8]. However, for multi-rotor aircraft such as quadrotors, determining the aerodynamic coefficient of each rotor could be impracticable using system identification approach since only joint forces are measurable by the 3-axis accelerometer located at the center of gravity. Furthermore, the local airspeed differs between rotors because of complex aerodynamic interactions, which makes the rotor-by-rotor modeling approach impractical.

In this research, a novel nondimensionalization approach is proposed which is based on an assumption that aerodynamic forces and moments are mainly generated by the rotor system. A geometric average of rotor speeds is used to represent the effect of multi-rotors

$$\bar{\Omega} = \sqrt{\frac{\sum_{i=1}^{N}\Omega_i^2}{N}} \tag{2.8}$$

where N is the number of rotors and equals 4 for quadrotor. In most cases, rotors are the same size with radius R. Afterwards, forces and moments acting on the entire vehicle can be normalized by the average rotor speed

$$C_z = \frac{F_z}{\rho(N\pi R^2)(R\bar{\Omega})^2}, \quad C_x = \frac{F_x}{\rho(N\pi R^2)(R\bar{\Omega})^2}, \quad C_y = \frac{F_y}{\rho(N\pi R^2)(R\bar{\Omega})^2} \tag{2.9}$$

$$C_l = \frac{M_x}{\rho b(N\pi R^2)(R\bar{\Omega})^2}, \quad C_m = \frac{M_y}{\rho b(N\pi R^2)(R\bar{\Omega})^2}, \quad C_n = \frac{M_z}{\rho b(N\pi R^2)(R\bar{\Omega})^2} \tag{2.10}$$

where b is the reference length chosen arbitrarily as long as it represents the geometry size of a specific vehicle. Since F_z is opposite to thrust which brings intuitive inconvenience, $T = -F_z$ is used as the total thrust force and $C_t = -C_z$ as the thrust coefficient. Note that T is interpreted as the joint of rotor thrust and drag force along the body vertical axis.

Translational and angular velocities, which have been found to significantly influence the abovementioned coefficients [10, 19], are normalized by

$$\mu_x = \frac{u}{\bar{\Omega}R}, \quad \mu_y = \frac{v}{\bar{\Omega}R}, \quad \mu_z = \frac{w}{\bar{\Omega}R} \tag{2.11}$$

$$\bar{p} = \frac{pb}{\bar{\Omega}R}, \quad \bar{q} = \frac{qb}{\bar{\Omega}R}, \quad \bar{r} = \frac{rb}{\bar{\Omega}R} \tag{2.12}$$

The horizontal component of the advance ratio $\mu = \sqrt{\mu_x^2 + \mu_y^2 + \mu_z^2}$, which is defined as $\mu_h = \sqrt{\mu_x^2 + \mu_y^2}$, is used to analyze interaction effects in this research. These dimensionless parameters are analogous to those used for single-rotor aircraft.

The rotor speeds are normalized by

$$\omega_i = \frac{\Omega_i}{\bar{\Omega}} \tag{2.13}$$

It is assumed that $\bar{\Omega} > 0$ always holds to avoid the singularity, because the status that all rotors are stopped is out of the scope of this work.

The moments for controlling attitude are produced by differential thrust from rotor speeds differences. Here three normalized inputs for roll, pitch and yaw controls are defined

$$u_p = (\omega_1^2 + \omega_4^2) - (\omega_2^2 + \omega_3^2) \tag{2.14}$$

$$u_q = (\omega_1^2 + \omega_2^2) - (\omega_3^2 + \omega_4^2) \tag{2.15}$$

$$u_r = -(\omega_1^2 + \omega_3^2) + (\omega_2^2 + \omega_4^2) \tag{2.16}$$

where signs and numbers are in accordance with the definition in Fig. 2.2, which may change for different types of quadrotor vehicles.

2.3.2. STEPWISE SYSTEM IDENTIFICATION

This section introduces the system identification approach applied to establish the gray-box model. Specifically, a regression method together with a model structure selection algorithm is used for determining mappings from dimensionless states to aerodynamic force and moment coefficients. The relation of model outputs to measurements satisfies

$$\boldsymbol{z} = \boldsymbol{y} + \boldsymbol{\epsilon} = \boldsymbol{A\theta} + \boldsymbol{\epsilon} \tag{2.17}$$

where $\boldsymbol{z} \in \mathbb{R}^N$ stands for N measured dimensionless forces and moments. $\boldsymbol{y} = \boldsymbol{A\theta}$ denotes model output and $\boldsymbol{\epsilon} \in \mathbb{R}^N$ vector indicates model residuals. $\boldsymbol{A} \in \mathbb{R}^{N\times p}$ is the regressor matrix with each column as a regressor which is an arbitrarily combination of independent variables. $\boldsymbol{\theta} \in \mathbb{R}^p$ stands for parameters of regressors to be estimated using , e.g Original Least Square (OLS) estimator

$$\hat{\boldsymbol{\theta}} = (\boldsymbol{A}^T \boldsymbol{A})^{-1} \boldsymbol{A}^T \boldsymbol{z} \tag{2.18}$$

where $\hat{\boldsymbol{\theta}}$ is the optimal parameter estimation that minimizes the sum of squares of the residual $\boldsymbol{\epsilon}$. The process of model structure selection is concerned with the choice of particular regressors in the $\boldsymbol{A}$ matrix.

In this chapter, two steps are taken in the model structure selection. The first step is defining a candidate regressors set using prior knowledge; the second step is selecting candidates using a selection algorithm.

A method to rigorously define candidate sets is introduced. Suppose $y(x_1, x_2, x_3)$ is a model with three independent variables and unknown model structure, the candidate set of y can be denoted by $\mathscr{S}(y)$. In this research, the model structures are in the form of polynomial functions. Now denote the basis of a dth order polynomial function of $\boldsymbol{x} = (x_1, x_2, x_3)$ as $P^d(\boldsymbol{x})$ and then the candidate set consisting of arbitrary polynomial terms can be defined. For example, if $\mathscr{S}(y) = \{P^2(x_1, x_2), P^2(x_1, x_2)x_3\}$, the candidate set of y contains regressors from $P^2(x_1, x_2) = \{x_1, x_2, x_3, x_1^2, x_2^2, x_1 x_2\}$ and from $P^2(x_1, x_2)x_3 = \{x_1 x_3, x_2 x_3, x_3 x_3, x_1^2 x_3, x_2^2 x_3, x_1 x_2 x_3\}$. Define the multiplication of two sets as a set containing non-repetitive products of elements from the two sets

$$\{a_1, a_2 ..., a_m\}\{b_1, b_2 ..., b_n\} = \{a_1 b_1, ... a_1 b_n, a_2 b_1, ..., a_2 b_n, ..., a_m b_1, ..., a_m b_n\} \tag{2.19}$$

Then $\mathscr{S}(y)$ can be expressed in a simplified form according to the law of association

$$\mathscr{S}(y) = \{P^2(x_1, x_2), P^2(x_1, x_2)x_3\} = \{P^2(x_1, x_2)\{1, x_3\}\} \tag{2.20}$$

A general formulation of $P^d(\boldsymbol{x})$ is

$$p^d(x_1, x_2, ..., x_n) = \{\prod_{i=1}^{n} x_i^{k_i} | 0 \le \sum_{i=1}^{n} k_i \le d,\ k_i \in \{0, 1, 2, ..., d\}\} \tag{2.21}$$

of which the total number of elements can be calculate by

$$\hat{d} = \frac{(d+n)!}{n!d!} \tag{2.22}$$

After determining the candidate set, a so-called (forward-backward) stepwise regression algorithm is applied to select regressors to build the model. The algorithm is summarized in the Appendix of this Chapter. Readers may refer [25] for more details.

2.4. DATA ACQUISITION AND ANALYSIS

2.4.1. EXPERIMENTAL SETUP

In order to identify force and moment models in high-speed flight regimes, free flights are performed in a large-scale wind tunnel for data acquisition. The tested quadrotor is Parrot Bebop without bumper attached, as Fig. 2.2 shows. The native autopilot of this off-the-shelf drone is replaced by Paparazzi [29], an open-source autopilot which runs at 512 Hz, and which is capable of performing aggressive maneuvers. Incremental Nonlinear Dynamic Inversion (INDI) guidance law and attitude controller have been programmed in Paparazzi [3, 28] to guarantee the position tracking performance against strong wind, which is essential for flight tests in our research. The quadrotor is equipped with a closed-loop Brushless DC motor controller; an MPU6050 Inertia Measurement Unit (IMU) including a 3-axis accelerometer and gyroscope. The inertia of Bebop is measured using the approach introduced in Ref. [30] with a percent error less than 5%. These parameters of tested quadrotor are listed in the Table 2.1

Flight tests are performed in the Open Jet Facility (OJF), a large-scale wind tunnel, operated by Delft University of Technology. The drone is controlled to maneuver in a confined area that is approximately 5.0 m long, 2.5 m wide and 2.5 m high. Wind speed is varied from 0 to 14 m/s with 2 m/s intervals to simulate flights at different airspeeds. An external motion capture system is applied to measure velocities and positions of the drone for indoor navigation. As Fig. 2.3 shows, five waypoints in the flight area are set to conduct flight maneuvers. To perform longitudinal maneuvers, the quadrotor can be controlled to track point A and B alternately. Similarly, waypoints C and D are set for performing lateral maneuver. To perform vertical maneuvers during forward flight, the drone is controlled to stay at point O and climb or descend with 2 m/s. Longitudinal, lateral and vertical maneuvers are conducted at varying heading angles denoted by ψ which are defined in Fig. 2.3; the heading angle is increased from 0 to 360° in steps of 45°. To identify the yawing moment model considering aerodynamic effects, yaw maneuvers are carried out at point O by changing ψ in steps of 45° both clockwise and counter-clockwise.

2.4.2. DATA PREPROCESSING

Flight data for system identification are collected by on-board and external sensors. Specifically, rotor speeds are observed by the motor controller, angular rates and specific forces are measured by gyroscope and accelerometer respectively. These measurements are logged on-board at 512 Hz. The external motion capturing system (10 × OptiTrack Prime 17 W cameras) measured the position of 6 markers fixed on the vehicle at 360 Hz, with a standard deviation less than 0.2 mm. Henceforth the quadrotor position, attitude and ground speed are derived from these marker positions and re-sampled to 512 Hz to align with on-board measurements.

Table 2.1: Inertia and geometric parameters of Parrot Bebop

m [kg]	I_x [kg · m^2]	I_y [kg · m^2]	I_z [kg · m^2]	I_{xz} [kg · m^2]	I_p [kg · m^2]	b [m]	l [m]	R [m]
0.389	0.000906	0.001242	0.002054	1.42E-05	3.39E-06	0.0775	0.0975	0.064

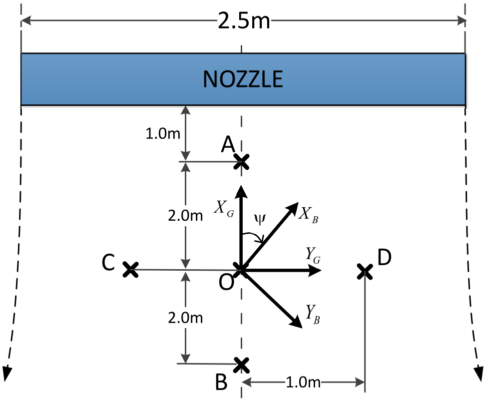

Figure 2.3: Top view diagram of flight maneuvres performed in the wind tunnel. Forward and backward flights are conducted by tracking point A and B by turns. Lateral flights are performed between C and D. Descend and ascend flights, yaw maneuvres are made at point O. The heading angle ψ is defined as the angle between x_B and x_G (clockwise positive).

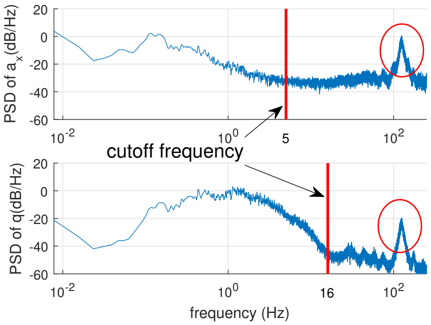

Figure 2.4: Power spectrum density (PSD) of accelerometer measurement and gyroscope measurement (acc_x and q) by Welch's method in Matlab. Cut-off frequencies are chosen as 5 Hz and 16 Hz respectively. Circled parts indicate the noise caused by an unbalanced rotor which is inevitable.

Measurements from the two sources have been fused using an Extended Kalman Filter (EKF) with the aim of calculating IMU bias [27]. The unbiased IMU measurements are further low-pass filtered by a 4th-order Butterworth lowpass filter. Power spectral density (PSD) of accelerometer and gyroscope measurements from one flight are plotted in Fig. 2.4. There is a resonance peak at around 120 Hz which is most likely caused by rotor imbalance (rotors rotate at around 7000 RPM = 117 Hz). Filter cut-off frequencies are chosen as 5 Hz and 16 Hz respectively, leading to a considerable noise reduction as shown in Fig. 2.5.

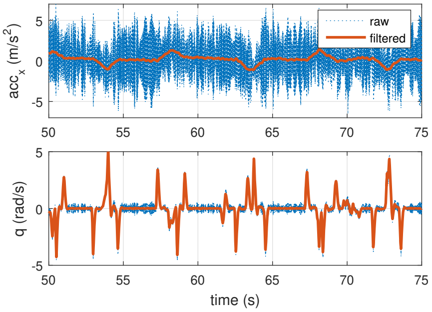

Figure 2.5: Comparison between raw and filtered measurements from accelerometer and gyroscope.

Finally, force and moment measurements are derived from the processed IMU data. The specific force times the mass of quadrotor equals the resultant non-gravitational force, namely $\boldsymbol{F}$. The moment $\boldsymbol{M}$ can be obtained from (2.4) where angular velocity $\boldsymbol{\Omega}$ is obtained from the processed gyroscope measurement.

2.4.3. COMPLEX AERODYNAMIC EFFECT

As outlined in the introduction, complex aerodynamic effects such as interactions between quadrotor components, have been clearly observed from the flight test data. These effects can significantly affect external forces and moments and has to be taken into account when creating a high fidelity model.

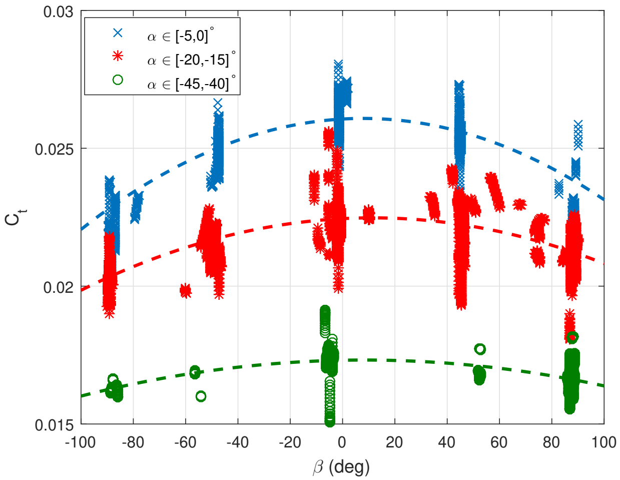

Figure 2.6: C_t vs. sideslip angle in different angle of attack.

Thrust coefficients C_t and corresponding sideslip angles β are shown in Fig. 2.6. These data are divided into three groups according to angles of attack α. The intervals of α are presented in the figure as well, while the interval of advance ratio is set as $\mu \in [0.1, 0.11]$ ($V \approx 5$ m/s). Note that only data within these intervals are plotted. Trend lines are also given for a better illustration of the C_t variation in different β. Apart from the vertical shift of C_t, the effect of β on C_t also varies with α. When α is negative with large absolute value, the mean value of C_t seems uncorrelated to β. As α is approaching zero, data with larger $|\beta|$ have smaller C_t, which could be interpreted as the thrust degradation caused by disturbance from the fuselage of Bebop quadrotor in high sideslip flights when the aft rotors are within the fuselage wake. In contrast, when α is decreased and becomes sufficient small, the aft rotors are outside the fuselage wake, therefore the sideslip angle does not influence the thrust coefficient. During the experiment, a clear shrill sound was produced while the aft rotors were obstructed by the fuselage, which can be regarded as another evidence that supports this hypothesis.

Fig. 2.7 presents the horizontal force coefficient defined as $C_h = \sqrt{C_x^2 + C_y^2}$ which indicates the total aerodynamic resistance projected on the x_B-y_B plane. The angle of attack is selected around -20° which is typical during forward flight. The distribution of data points with small sideslip angle ($|\beta| \in [0, 10]°$) shows an almost linear relationship between C_h and horizontal advance ratio μ_h. As sideslip angle grows, the drag coefficient also increases, and when $|\beta| \in [80, 90]°$ a quadratic tendency appears. This may be due to the fact that the fuselage of the Bebop has larger a projection area on y_B direction, as Fig. 2.2 shows.

Besides the sidesilp angle, the angle of attack also affects C_h. Since a large portion of the drag is produced by the rotors, thrust degradation caused by aerodynamic interactions can lead to induced drag reduction and subsequently decrease the total drag force. This drag reduction was not only observed in large sideslip angle but also straight forward flights when fuselage wake does not influence rotors. As can be seen in Fig. 2.8 where the sideslip angle is small ($\beta \in [-10,\ 10]°$), however C_h is found reduced when α is close to or above zero. This might be explained by the fact that the front rotors can obstruct the aft rotors and degraded their aerodynamic characteristics as well. Note that this drag force reduction is not obvious in the low-speed region since the flight speed is not high enough for this interaction. The drag force variance due to interactions should be considered as well in a high fidelity model.

Fig. 2.9 presents the pitching moment coefficient C_m versus the advance ratio μ at different sideslip angles. Significant differences can be found in different β intervals. For these data, pitch control u_q are chosen close to zero ($u_q \in [-0.05,\ 0]$) which means that almost no pitching moment is present in hovering condition because the front and aft rotors are nearly at the same speed. It is evident that the pitching moment increases significantly as the flight speed grows when $|\beta| \in [-10,\ 10]°$ compared to other sideslip angles. This pitch-up moment might be caused by blade flexibility [11] or interactions between rotors.

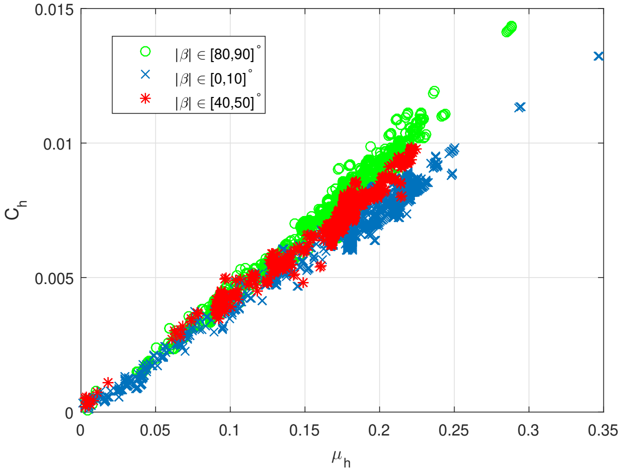

Figure 2.7: C_h vs. μ_h in different sideslip angle intervals. Plot shows that horizontal force coefficient varies with respect to sideslip angle.

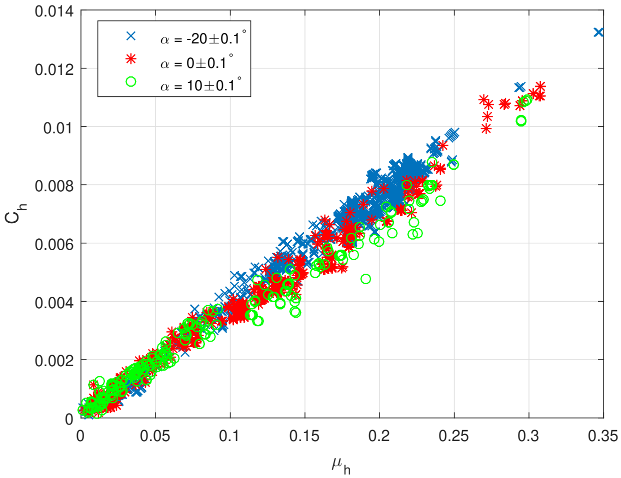

Figure 2.8: C_h vs. μ_h in different angles of attack when sideslip angle $\beta \in [-10,\ 10]^\circ$. A larger angle of attack can reduce the horizontal force coefficient.

The angle of attack is found to be positively related to the pitching moment during forward flight. Fig. 2.10 shows the data and trend lines of C_m versus α with $u_q \in [-0.01,\ 0.01]$ and $\beta \in [-10,\ 10]^\circ$. In these cases, the aft rotors and front rotors have almost the same rotor speeds. In general, C_m is positively correlated with the angle of attack indicating the longitudinal instability of a quadrotor. The slope is

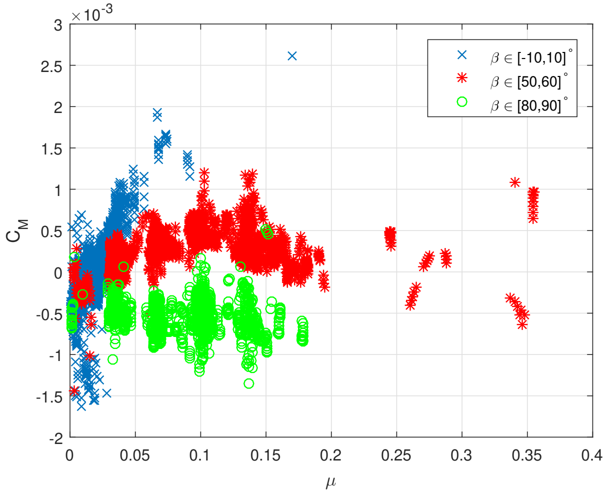

Figure 2.9: C_m in different sideslip angles when $u_q \in [-0.05, 0]$. Large nose up moment can be observed when sideslip angle is small ($\beta \in [-10, 10]°$).

larger with a higher advance ratio, which is consistent with results given by Fig. 2.9. More importantly, the C_m is almost always positive, indicating that a nose up aerodynamic moment appears in quadrotor forward flight even with a large negative angle of attack. This coincides with the result from Ref. [22] that the aft rotors need to rotate much faster than the front rotors in trim conditions. Similarly, for instance, flying to the right (with $\beta = 90°$) can produce a negative rolling moment which requires the left rotors to rotate faster in order to keep balance. This phenomenon is strongly present in the data; simple hovering models that neglect this effect will produce highly inaccurate moment predictions in fast flight regions.

The yawing moment is also found to be influenced by the sideslip angle. Notate the difference between the measured yawing moment and that calculated by the hovering model by ΔM_z, which is regarded as the additional yawing moment due to the aerodynamic effects.

$$\Delta M_z = M_z - [\tau_0(-\Omega_1^2 + \Omega_2^2 - \Omega_3^2 + \Omega_3^2) + \lambda_r r] \tag{2.23}$$

As is shown in Fig. 2.11, ΔM_z is negatively related to the sideslip angle in general. When $|\beta| < 40°$, ΔM_z is in the vicinity of zero. However its dispersion suddenly increases when $|\beta| > 40°$. At the same time, one aft rotor starts to be obstructed by the fuselage. The airframe-rotor aerodynamic interaction might occur in this situation as the cause of the sudden increased yawing moment.

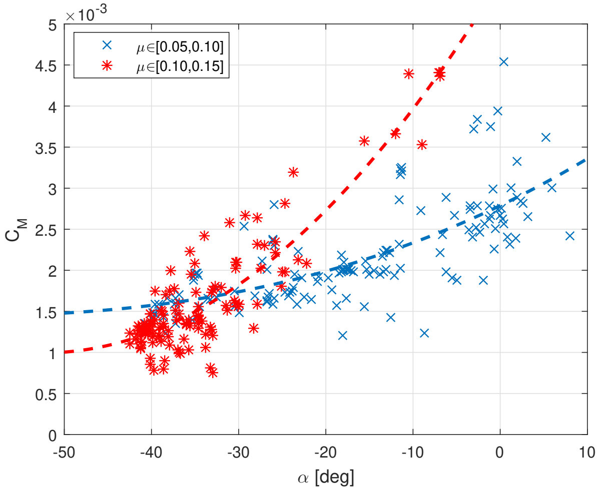

Figure 2.10: C_m vs. α in different advance ratio intervals with $u_q \in [-0.01,\ 0.01]$ and $\beta \in [-10,\ 10]°$.

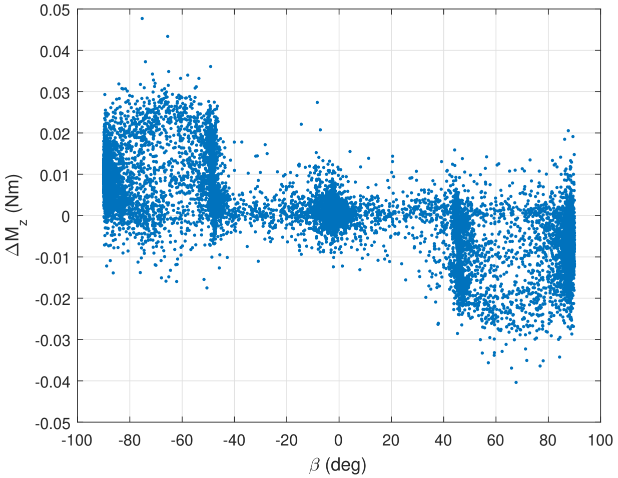

Figure 2.11: Additional aerodynamic yawing moment ΔM_z with respect to the hovering model. ΔM_z is negative related to the sideslip angle indicating that an aerodynamic moment related to β exists.

2.5. QUADROTOR MODEL STRUCTURE CANDIDATES

This section introduces the determination of candidate structure sets for the quadrotor dimensionless aerodynamic force and moment models, based on prior physical knowledge and observations. Then, the stepwise regression algorithm can be carried out to obtain the final model structure, which will be presented in a subsequent section.

2.5.1. FORCE MODEL CANDIDATES

F_x and F_y denote forces perpendicular to the thrust direction brought by aerodynamic resistance, of which the lift-induced drag and the blade flapping effect are the two major causes [6, 12, 19]. A widely accepted drag model of a single rotor is [6, 12]

$$F_{x,i} \propto u_i \Omega_i \tag{2.24}$$

where $F_{x,i}$ and u_i stand for the in-plane force and local velocity of the i_{th} rotor on the x_b direction respectively. In addition, as section 2.4.3 shows, airframe affects the drag force as well, especially at large sideslip angles. Therefore, the square of the velocity has been added into the drag model [16]. The drag force on x_B direction can thus be expressed as

$$F_x = \kappa_{d,1} \sum_{i=1}^{4} \Omega_i u_i + \kappa_{d,2} u^2 \tag{2.25}$$

where $\kappa_{d,1}$ and $\kappa_{d,2}$ are constants. Recall (2.8), (2.9) and 2.11), the normalized form of (2.25) can be obtained

$$C_x = C_{x,1}\mu_x + C_{x,2}\mu_x^2 \tag{2.26}$$

note that the rotor speed term $\sum_{i=1}^{4} \Omega_i$ in (2.25) disappears after normalization. This process needs to replace the arithmetic mean of rotor speeds by their geometrical mean, which does not lose accuracy in most flight conditions (0.8% relative error on average).

The above model can produce accurate predictions in most low-speed cases. However, it loses accuracy when interaction effects appear. For comparison with the gray-box model established in this research, the drag model in (2.26) is named the *reduced model*.

An additional term $C_{x,2,(\mu_x,|\mu_y|,\mu_z)}$, of which the exact structure is to be determined, is added to the reduced model. The variables in the subscript parentheses indicate the independent variables of $C_{x,2}$. A preliminary model structure of C_x can be

$$C_x = C_{x,1}\mu_x + C_{x,2,(\mu_x,|\mu_y|,\mu_z)} \tag{2.27}$$

Note that the $C_{x,2}\mu_x^2$ term is moved into the second term since it has a negligible effect in the flight regime as the data shows.

Recall the observation in the Section. 2.4.3; β, α and μ_h greatly influence the drag coefficient. Singularities in α and β, however, could occur in hovering conditions, therefore three components of the advance ratio are chosen as the independent variables. Absolute values of μ_y are used due to the symmetry of the quadrotor.

Similarly, for C_y we have

$$C_y = C_{y,1}\mu_y + C_{y,2,(|\mu_x|,\mu_y,\mu_z)} \tag{2.28}$$

The stepwise regression algorithm can be applied to determine the exact structure of the unknown parts of the above models. The candidate sets of C_x and C_y are chosen as

$$\mathscr{S}(C_x) = \{P^3(\mu_x, |\mu_y|, \mu_z)\} \tag{2.29}$$

$$\mathscr{S}(C_y) = \{P^3(|\mu_x|, \mu_y, \mu_z)\} \tag{2.30}$$

The terms μ_x and μ_y are always the first candidates to be tested by the model structure selection algorithm when assembling respectively the models for C_x and C_y.

F_z is derived by taking account of the thrust variation. In general, the thrust of the ith rotor with constant pitching angle can be expressed as [31]

$$T_i = \frac{\rho a B c \omega_i^2 R^3}{2}\left(\frac{\theta_r}{3} + \frac{(u_i^2 + v_i^2)\theta_r}{2\omega_i^2 R^2} + \frac{-w_i + v_{in,i}}{2\omega_i R}\right) \tag{2.31}$$

where a is the lift curve slope of the blade profile, B represents the number of blades, c is the blade chord length and θ_r stands for the rotor pitch angle. These parameters are related to rotor design and for quadrotors; they normally are all constants. $v_{in,i}$ indicates the induced velocity of the ith rotor.

A common way to model F_z is projecting the thrust of four rotors on the body frame and assuming that local velocities and induced velocities of the rotors are identical, yielding

$$F_z = -\sum_{i=1}^{4} T_i = \kappa_{t,1}\sum_{i=1}^{4}\Omega_i^2 + \kappa_{t,2}(u^2 + v^2) + \kappa_{t,3}(-w + v_{in})\sum_{i=1}^{4}\Omega_i \tag{2.32}$$

where $\kappa_{t,1}$, $\kappa_{t,2}$ and $\kappa_{t,3}$ are constants. (2.32) is the model structure adopted in several researches [13, 31]; it is indicated as the *reduced model* to compare against the new gray-box model. A dimensionless form of (2.32) can be calculated by substituting (2.8), (2.9), and (2.11) into (2.32), yielding

$$C_z = C_{z,0} + C_{z,1}(\mu_x^2 + \mu_y^2) + C_{z,2}(-\mu_z + \bar{v}_{in}) \tag{2.33}$$

where $C_{z,0}$, $C_{z,1}$ and $C_{z,2}$ are constants. $\bar{v}_{in}$ indicates the dimensionless induced velocity normalized by $\bar{\Omega}R$. The induced velocity $\bar{v}_{in}$ can be calculated by [4]

$$\bar{v}_{in} = \frac{C_{t,h}}{2\sqrt{\mu_x^2 + \mu_y^2 + (-\mu_z + \bar{v}_{in})^2}} \tag{2.34}$$

where $C_{t,h}$ is the thrust coefficient in the hover case which can be estimated accurately by conducting hovering flight experiments.

As mentioned earlier, interaction effects could degrade rotor thrust. This ef-

Table 2.2: Procedure of identifying the reduced model and the gray-box model

	Reduced model	Gray-box model
step 1	Data acquisition	
step 2	Determined structure	Define structure candidates $\mathscr{S}(y)$
step 3	Parameter estimation	Stepwise regression
Final model		

fect is not considered in the reduced model (2.32), not to mention other unknown complex aerodynamic effects and drag force on the z_B direction. The deviation of C_z from these effects is denoted by $C_{z,3}$. Flight speed, the difference between aft and front rotors, vehicle angular velocities could be the individual variables of this unknown part. Thus a gray-box model of C_z can be formalized as

$$C_z = C_{z,0} + C_{z,1}(\mu_x^2 + \mu_y^2) + C_{z,2}(-\mu_z + \bar{v}_{in}) + C_{z,3,(|\mu_x|,|\mu_y|,\mu_z,|u_p|,|u_q|,|u_r|,|p|,|q|,|r|)} \tag{2.35}$$

Henceforth the stepwise regression algorithm is applied to determine the structure of C_z, of which the candidate structure set is chosen as

$$\mathscr{S}(C_z) = \{P^4(|\mu_x|,|\mu_y|,\mu_z)\{1,|\bar{p}|,|\bar{q}|,|\bar{r}|,|u_p|,|u_q|,|u_r|\}\} \tag{2.36}$$

Note that $(\mu_x^2 + \mu_y^2)$ and $(-\mu_z + \bar{v}_{in})$ are regarded as fixed regressors that have been added in the model before the selection.

Both the reduced model and the gray-box model can be established using the system identification method. Table 2.2 briefly compares the procedures of establishing these models.

2.5.2. MOMENT MODEL CANDIDATES

Compared to the hovering case, additional aerodynamic moments can be produced during high-speed flight. First, the pitching moment could be a result of rotor resilience and the blade flapping effect [11]. Secondly, the vertical distance between rotor planes and the center of gravity also brings moments due to rotor drag [21]. Thirdly, angular rate (dynamic) damping term also contributes to the total aerodynamic moment [21]. Fourthly, as was observed from the flight test data, aerodynamic interactions may degrade the thrust of the aft rotors and lead to additional pitch up moments. All the above factors are related to advance ratio and angular rates.

Taking account of these possible effects, a lumped model of the pitching moment coefficient C_m could be expressed as

$$C_m = C_{m,(\mu_x,\mu_y,\mu_z,\bar{q},u_q)} \tag{2.37}$$

with advance ratio, dimensionless pitch rate and pitch input as independent variables.

Above pitch model neglects the influence of lateral variables u_p, u_r, p and r, which are of less effect on the pitching moment based on the flight data. However, μ_y is included in the model to handle the sideslip effect. To further simplify the candidate set, u_q and $\bar{q}$ are assumed linearly related to the pitching moment. Thus the lumped model (2.37) can be expressed as

$$C_m = C_{m,0,(\mu_x,|\mu_y|,\mu_z)} + C_{m,u_q,(\mu_x,|\mu_y|,\mu_z)}\, u_q + C_{m,q,(\mu_x,|\mu_y|,\mu_z)}\, \bar{q} \tag{2.38}$$

Based on the structure in (2.38), the candidate set of C_m is chosen as

$$\mathscr{S}(C_m) = \{P^5(\mu_x,\mu_z)P^2(|\mu_y|)\{1,\bar{q},u_q\}\} \tag{2.39}$$

The preliminary structure of the rolling moment model can be similarly determined as

$$C_l = C_{l,0,(|\mu_x|,\mu_y,\mu_z)} + C_{l,u_p,(|\mu_x|,\mu_y,\mu_z)}\, u_p + C_{l,p,(|\mu_x|,\mu_y,\mu_z)}\, \bar{p} \tag{2.40}$$

of which the regressors are selected from the candidate set

$$\mathscr{S}(C_l) = \{P^5(\mu_y,\mu_z)P^2(|\mu_x|)\{1,\bar{p},u_p\}\} \tag{2.41}$$

The yawing moment model is found to be much more complicated and u_r may not be linear to the model. Thus a preliminary structure is determined as

$$C_n = C_{n,(\mu_x,\mu_y,\mu_z,\bar{r},u_r)} \tag{2.42}$$

of which the candidate set is chosen as

$$\mathscr{S}(C_n) = \{P^5(\mu_x,\mu_y,\mu_z)P^3(\bar{r})P^3(u_r)\} \tag{2.43}$$

2.6. RESULTS

2.6.1. MODEL ESTIMATION RESULTS

After defining candidate structure sets, all force and moment models are determined by the stepwise regression algorithm. This section provides the estimation result of C_z since thrust is the biggest concern in most modeling tasks. Due to limited space, other models are provided in the Appendix of this Chapter.

The reduced model is found to be accurate in low-speed regions since the interaction effects are weak. Thus C_z is estimated with structure (2.33) when $\mu < 0.05$ (approximately $V < 2$ m/s). The result at this low-speed regime is listed in Table 2.3.

For the flight regime where $\mu > 0.05$, the complex aerodynamic effects become apparent and the gray-box model of $C_z$is established. The model structures and parameters are listed in Table 2.4. The state space is equally divided into three partitions according to the sideslip angle. On each partition, a gray-box model of C_z has been identified. The first column of the table lists the model structure which is ranked by the order of selection. The second column gives the values of corresponding parameters. The third column provides the decreasing normalized-root-mean-square (NRMS) of the model residual after the corresponding regressor is added into the model. In general, regressors at the top are the most significant, with significance becoming less moving towards the bottom of the list.

Fig. 2.12, 2.13 present the residuals of gray-box models on the entire estimation data sets. $1-\sigma$ intervals are given as well. In general, the residuals are confined to the interval. It also indicates that the gray-box model provides unbiased estimations because all residuals have a mean value closed to zero. Above properties demonstrate the validity of the model structure selected by the stepwise regression algorithm.

2.6.2. VALIDATION RESULTS

Gray-box models are validated using validation data which are separate from the estimation data but are collected from the same flights. For a better evaluation of these models, the validation outputs are chosen as forces and moments instead of their coefficients.

The force models are compared with the reduced models (2.25, 2.32) which have taken into account primary aerodynamic effects. The moment models, however, are compared with the hovering model because no mature reduced model for moment prediction can be found. Metrics of these models are given in Table 2.5 based on validation results.

Both gray-box and reduced model provide accurate F_x and F_y predictions. From the F_z metrics, it can be concluded that the gray-box model provides better thrust estimations. The RMS of the gray-box force model residuals are reduced by 20-30% on the whole. As for moment predictions, the hovering models (marked by an as-

Table 2.3: Estimation results of C_z model, $\mu \leq 0.05$

reg.	$\hat{\theta}$
1	5.020E-02
$\mu_x^2+\mu_y^2$	1.112E-01
$(\bar{v}_{in}-\mu_z)^2$	-9.420E-02
R2	0.953
NRMS	0.021

Table 2.4: Estimations result of C_z model, $\mu > 0.05$

$\lvert\beta\rvert \in [0,30]$			$\lvert\beta\rvert \in [30,60]$			$\lvert\beta\rvert \in [60,90]$		
reg.	$\hat{\theta}$	NRMS (%)	reg.	$\hat{\theta}$	NRMS (%)	reg.	$\hat{\theta}$	NRMS (%)
1	1.38E-01	8.636	1	2.20E-01	8.046	1	1.48E-01	8.759
$\mu_x^2+\mu_y^2$	-1.55E-01	8.487	$\mu_x^2+\mu_y^2$	-3.62E-01	7.487	$\mu_x^2+\mu_y^2$	-2.05E-01	8.533
$(\bar{v}_{in}-\mu_z)^2$	-4.00E-01	2.315	$(\bar{v}_{in}-\mu_z)^2$	-6.99E-01	2.142	$(\bar{v}_{in}-\mu_z)^2$	-4.48E-01	2.882
μ_z	-1.02E-01	2.070	μ_z	-2.91E-01	1.785	μ_z	-1.93E-01	2.575
$\lvert u_q\rvert\mu_z$	-2.28E-02	1.995	$\lvert u_p\rvert\lvert\mu_y\rvert$	-1.84E-02	1.723	$\lvert u_p\rvert\mu_z$	4.52E-02	2.418
$\lvert u_p\rvert\mu_z$	7.83E-02	1.952	$\lvert u_r\rvert\lvert\mu_y\rvert^2\mu_z^2$	3.22E+00	1.696	μ_z^3	1.08E+01	2.342
$\lvert u_p\rvert\mu_z^2$	5.88E-01	1.940	$\lvert u_q\rvert\lvert\mu_x\rvert$	1.19E-02	1.672	μ_z^4	3.70E+01	2.240
$\lvert u\rvert\mu_z^3$	3.48E+00	1.928	$\lvert\bar{r}\rvert\lvert\mu_y\rvert\mu_z^3$	1.34E+03	1.655	μ_z^2	5.82E-01	2.165
$\lvert u_q\rvert$	-3.11E-04	1.923	$\lvert u_p\rvert\lvert\mu_y\rvert^2\mu_z^2$	3.81E+00	1.650	$\lvert u_p\rvert\lvert\mu_y\rvert$	7.06E-03	2.148
R2	0.9503		R2	0.9580		$\lvert u_p\rvert\lvert\mu_y\rvert^3\lvert\mu_z\rvert$	-1.51E+00	2.139
						R2	0.9403	

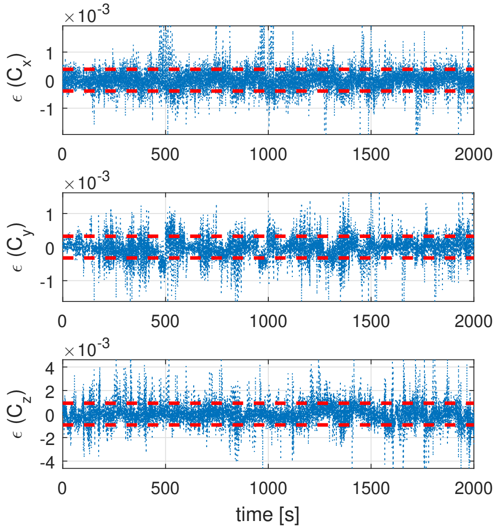

Figure 2.12: Residuals of force models compared with 1-σ interval.

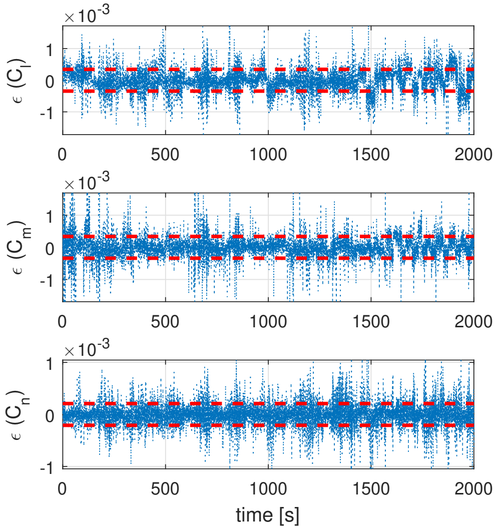

Figure 2.13: Residuals of moment models compared with 1-σ interval.

Table 2.5: Summary of validation results

	gray-box model			reduced or. hovering* model		
	Output corr.	R2	NRMS (%)	Output corr.	R2	NRMS (%)
F_z	0.9353	0.8636	2.10	0.8831	0.7650	3.03
F_x	0.9945	0.9889	1.54	0.9934	0.9861	1.70
F_y	0.9987	0.9975	1.05	0.9981	0.9961	1.32
M_x	0.7687	0.4847	2.06	0.1944*	-0.0201*	12.63*
M_y	0.8567	0.6883	1.23	0.4141*	-0.0524*	7.53*
M_z	0.8071	0.4873	5.19	0.4152*	0.1417*	13.81*

terisk) are almost invalid while the gray-box models can provide adequate results. Specifically, the RMS of residuals are reduced by over 80%. To make detailed comparison between above models, several figures are given below.

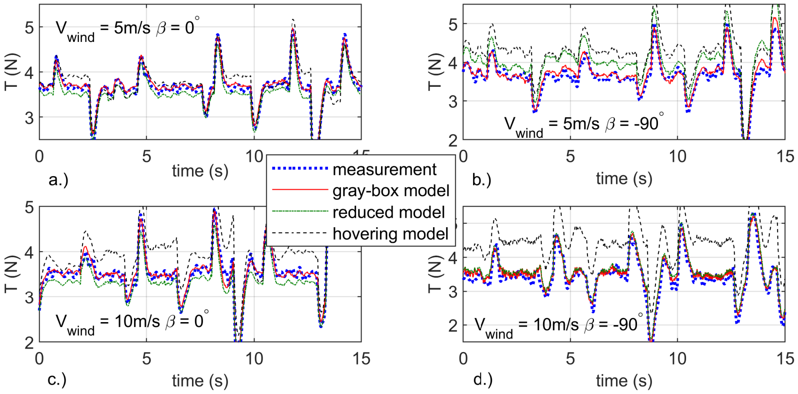

Figure 2.14: Validation results of the thrust model. The gray-box model (red solid) is compared with the reduced model(green dash-dot) and the hovering model (black dash). The left two figures illustrate flights when wind speeds are 5 m/s and 10 m/s and the sideslip angle is zero. The right two figures present flights when the sideslip angle is 90°. The gray-box model outperforms the other models in general.

Fig. 2.14 gives the validation result of F_z where thrust $T = -F_z$ is plotted for readability. Climbing and descending flights are performed at 5 m/s and 10 m/s airspeeds with $\beta = 0$ and $\beta = -90°$ respectively. It's clear that both the gray-box and the reduced model (2.32) outperform the hovering model, especially in the high-speed and large sideslip flight regime. It is evident that accuracy of the reduced model degrades beyond 5 m/s which could be caused by disturbances from the interactions of the Bebop fuselage with the airflow.

The drag model has been validated by forward and backward flights with different heading angles ψ. Fig. 2.15 shows the validation results of F_x. The reduced model (2.25) neglecting interaction effects are compared. Although both models

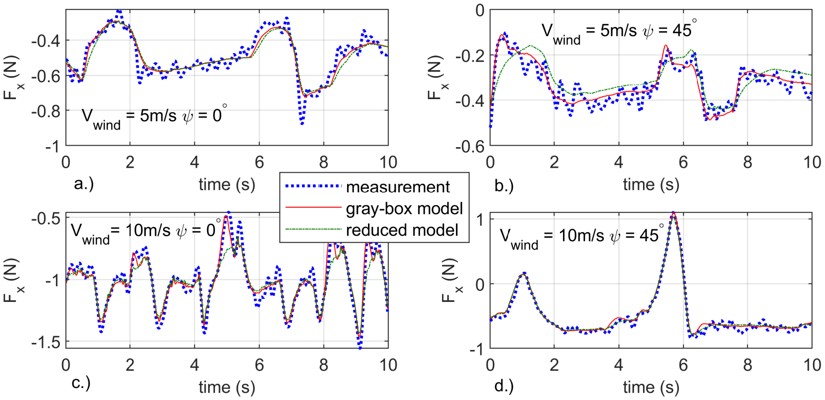

Figure 2.15: Validation results of the F_x model. The gray-box model (red solid line) is compared with the reduced model (green dash-dot). Forward and backward flights are performed for validation. The left two figures show flights with zero heading angle, i.e towards the wind tunnel outlet, while the heading angle is 45° in the right figures.

perform well in general, the gray-box model is more accurate in certain parts. For example, at $t = 5.0$ s and $t = 8.3$ s in the Fig. 2.15b, the gray-box provides accurate prediction while the reduced model produces relatively large errors. The angle of attack and the model residuals of this subplot are given in Fig. 2.16. It can be seen that the gray-box model outperforms the reduced model when the angle of attack is positive, which means that interactions between the front and aft rotors appear and the reduced model becomes less accurate.

Fig. 2.17 provides validation results of the F_y model. In flights with 90° heading angles, the quadrotor flew towards the left as what Fig. 2.3 illustrates. Again, as what is shown in Fig. 2.18, the gray-box model outperforms the reduced model at points when α is above zero. At $t = 12$ s when angle of attack is positive, a large error appears in predictions made by the reduced model, which does not take into account aerodynamic interaction effects.

Fig. 2.19 presents the validation result of pitching moment model. The gray-box model outperforms the hovering model as expected. During flights with $\psi = 0$, the prediction of the hovering model is almost always smaller than the measurements since the aft rotors need to rotate much faster than front rotors in the trim condition, which is in line with the observation given in Ref. [22]. This phenomena indicates that during forward flight, a significant pitch up moment appears which is not considered in the hovering model. As for the flights with $\psi = 45°$, although a large aerodynamic coupling exists due to large sideslip angles, the gray-box model can still provide accurate predictions. In addition, validation results of the M_x model are given in Fig. 2.20 showing the great advantage of the gray-box model.

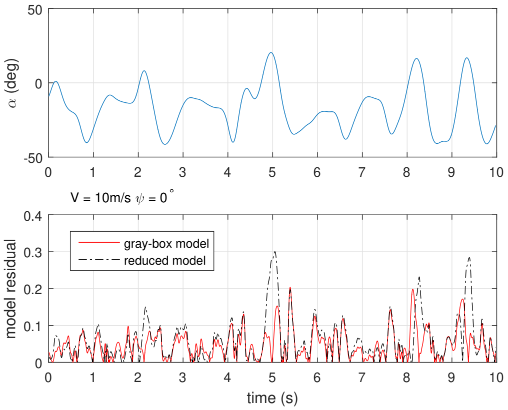

Figure 2.16: Time series of angle of attack at $V_{wind} = 10$ m/s and $\psi = 0$. The angle of attack is positive at $t = 5.0$ s and $t = 8.3$ s when errors in the reduced model for F_x appear.

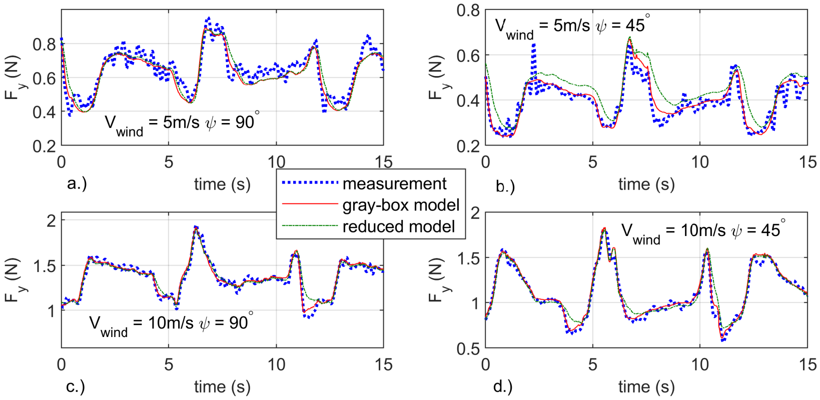

Figure 2.17: Validation results of the F_y model. The gray-box model (red solid line) is compared with the reduced model (green dash-dot). Forward and backward flights relative to the wind flow are performed. The left two figures present flights with 90° heading angle, i.e leftward flight against wind flow, while the heading angle is 45° in the right figures.

The model of the yawing moment M_z has been validated by yaw maneuvers and forward-backward maneuvers in the wind tunnel. The forward-backward maneuvers are carried out with $\psi = 45°$. As can be seen in Fig. 2.21, predictions from the gray-box model are more accurate than the hovering model. The residual of the hovering model increases as the flight speed grows and a constant bias appears in

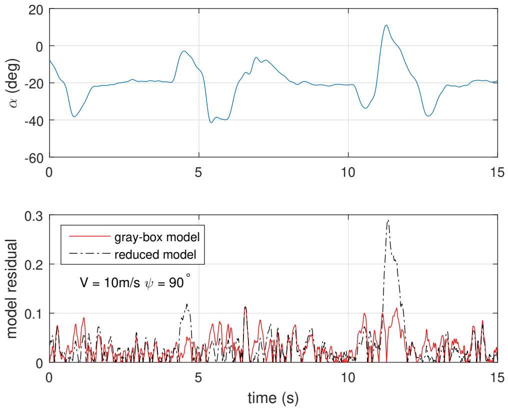

Figure 2.18: Time series of angle of attack in $V_{wind} = 10$ m/s and $\psi = 90°$. The angle of attack is positive at $t = 12.0$ s when errors of F_y reduced model appear.

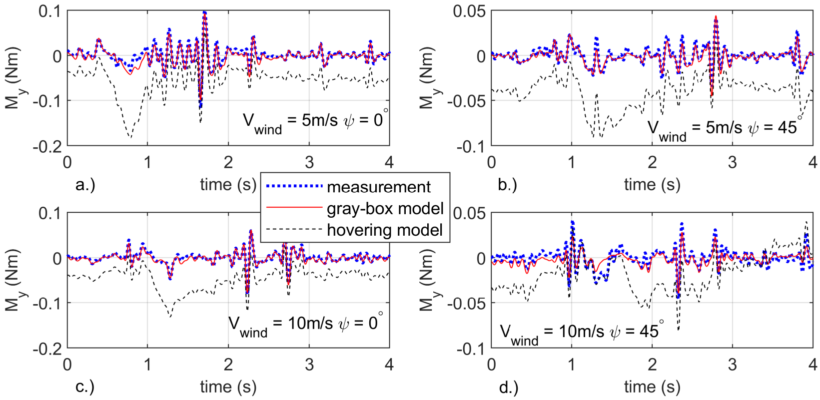

Figure 2.19: Validation result of pitching moment M_y model. The gray-box model (red solid) is compared with hovering model (black dash-dot). Forward and backward flights relative to the wind flow are used for validation. The left two figures show flights with zero heading angle, i.e towards the wind tunnel outlet, while heading angle is 45° in the right figures.

the Fig. 2.21d. In this case, the quadrotor flies with $\psi = 45°$, in other words, negative sideslip angle and additional positive yawing moment appear due to aerodynamic effects.

Finally, the gray-box models have been validated near the hovering condition and compared with the hovering models. As Fig. 2.22 shows, both types of models are accurate. Since aerodynamic resistance is small compared to the presented

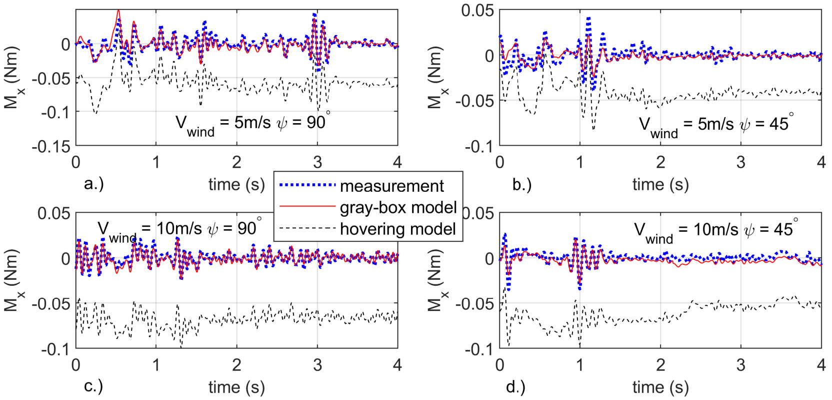

Figure 2.20: Validation result of rolling moment M_x model. The gray-box model (red solid) is compared with hovering model (black dash-dot). Forward and backward flights relative to the wind low are performed. The left two figures present flights with 90° heading angle, i.e leftward flight against wind flow, while the heading angle is 45° in the right figures.

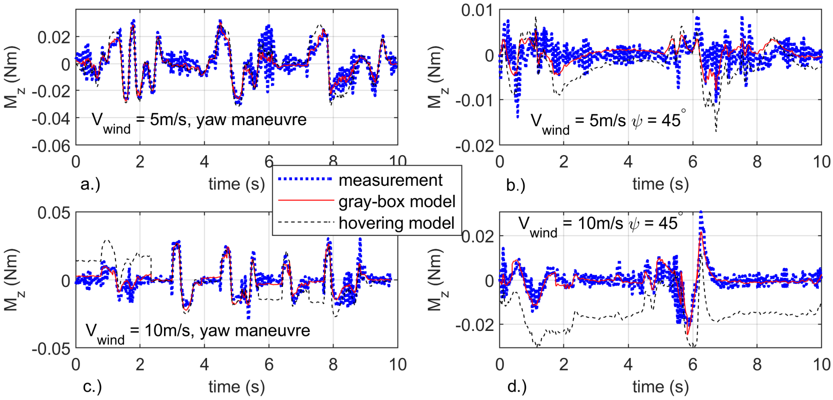

Figure 2.21: Validation results of the M_z model. The gray-box model (red solid) is compared with hovering model (black dash-dot). Yaw maneuvers are performed in the left two figures, with different flight speeds. Right two figures present data from forward and backward flights along the wind flow direction with 45° heading angle.

variables in the hovering condition, models of F_x and F_y are omitted in the plot.

The piecewise polynomial model in this research is discontinuous on the boundary of each section that might be unfavorable for some applications, though the discontinuity can be effectively weakened by increasing the number of model seg-

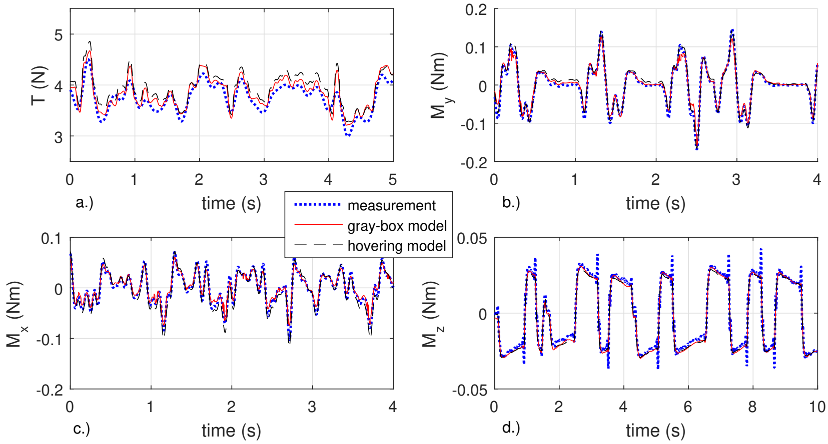

Figure 2.22: Validation results during hovering condition. Gray-box model (red solid) is compared with hovering model (green dash-dot). Both model possess enough accuracy in hovering condition.

ments. More advanced base functions such as multivariate splines may replace polynomials to guarantee the smoothness of the global model.

2.7. CONCLUSIONS

Gray-box models of a specific type of quadrotor considering aerodynamic interaction effects have been identified from flight data in a larger flight envelope with respect to the hovering condition. The identification process of this gray-box model consists of the information of phenomenological observation and prior-knowledge about rotorcraft aerodynamics. Therefore, this type of model possesses higher reliability in both high speed and low-speed flight regimes. Although the model structure and parameters are specific to the Bebop platform, the methodology including nondimensionalization, structure candidates and stepwise regression algorithm, can be generalized to other multi-rotor platforms.

The high-speed flight data have been collected in the wind tunnel. These flight data illustrate significant interaction effects which were rarely considered in the previous literature. The thrust reductions of the aft rotors that obstructed by the front rotors or airframe lead to variations of thrust, moment and even drag force acting on the quadrotor, which may inspire the drone manufacturer to revise their design. For instance, increase the power of aft actuators.

Since the data are obtained from flight tests instead of conventional static wind tunnel tests, and the forces and moments are measured indirectly from on-board and external navigation sensors, this process can also be applied in the open area instead of the wind tunnel. The motion capture system can be replaced by other navigation sensors, such as RTK-GPS, which can produce accurate velocity measurements. Thus the method introduced in this article can be repeated without wind tunnel equipment to establish accurate models in the interested flight regime.

However, on the other hand, a flight test is only able to explore a limited regime of the flight envelope, which is unfavorable for global model identification. The interaction effects can be only partially revealed by free flight data. Therefore, static wind tunnel tests with force balance are also suggested to carry out for global model identification as well as analyzing interaction effects in detail.

APPENDIX

A. STEPWISE REGRESSION ALGORITHM

The stepwise regression algorithm is summarized in the Algorithm 1.

Algorithm 1 Forward-backward Stepwise Regression Algorithm

```
Set initial regressor matrix $\boldsymbol{A}_0 = [1, 1, ..., 1]^T \in \mathbb{R}^N$
Set candidate set $\mathscr{S}(y) = \{\boldsymbol{\xi}_0,\ \boldsymbol{\xi}_1, ...,\ \boldsymbol{\xi}_q\}$ containing $q+1$ candidates
$k_{max} = 30;\ PSE_{tol} = 10^{-6};\ F_{out} = 4;\ k = 0$
$\boldsymbol{\epsilon}_0 = [\boldsymbol{I} - \boldsymbol{A}_0(\boldsymbol{A}_0^T\boldsymbol{A}_0)^{-1}\boldsymbol{A}_0^T]\boldsymbol{z}$
while $k \le k_{max}$ do
%Forward selection%
    $k = k + 1$
    for $i = 0, 1, ..., q$ do
        $\boldsymbol{\lambda}_i = \boldsymbol{\xi}_i - \boldsymbol{A}_{k-1}(\boldsymbol{A}_{k-1}^T\boldsymbol{A}_{k-1})^{-1}\boldsymbol{A}_{k-1}^T\boldsymbol{z}$
    end for
    $j = \text{argmax}_i\ corr(\boldsymbol{\lambda}_i, \boldsymbol{\epsilon}_{k-1})^\star$        ▷ %$corr(\boldsymbol{x}, \boldsymbol{y})$ stands for the correlation of $\boldsymbol{x}$ and $\boldsymbol{y}$%
    $\boldsymbol{A}_k = [\boldsymbol{A}_{k-1},\ \boldsymbol{\xi}_j]$
    $\hat{\boldsymbol{\theta}} = (\boldsymbol{A}_k^T\boldsymbol{A}_k)^{-1}\boldsymbol{A}_k\boldsymbol{z}$
    $\boldsymbol{\epsilon}_k = \boldsymbol{z} - \boldsymbol{A}_k\hat{\boldsymbol{\theta}}_k$
%Backward elimination%
    Assume there has been $p$ regressors added into $\boldsymbol{A}_k$
    for $i = 1, 2, ..., p$ do
        Define $\boldsymbol{A}_{k,i}$ as the reduced regressor matrix of $\boldsymbol{A}_k$ of which the $i$th regressor is eliminated
        $\hat{\boldsymbol{\theta}}_{k,i} = (\boldsymbol{A}_{k,i}^T\boldsymbol{A}_{k,i})^{-1}\boldsymbol{A}_{k,i}^T\boldsymbol{z}$
        $SS_R(\hat{\boldsymbol{\theta}}_k) = \hat{\boldsymbol{\theta}}_k\boldsymbol{A}_k^T\boldsymbol{z} - N\bar{z}^2$        ▷ %$\bar{z}$ stands for the mean of $\boldsymbol{z}$%
        $SS_R(\hat{\boldsymbol{\theta}}_{k,i}) = \hat{\boldsymbol{\theta}}_{k,i}\boldsymbol{A}_{k,i}^T\boldsymbol{z} - N\bar{z}^2$
        $s^2 = \boldsymbol{\epsilon}_k^T\boldsymbol{\epsilon}_k/(N - p - 1)$
        The F0-ratio of the $i$th regressor can be calculated by
        $F_{0,i} = [SS_R(\hat{\boldsymbol{\theta}}_k) - SS_R(\hat{\boldsymbol{\theta}}_{k,i})]/s^2$
    end for
    $l = \text{argmin}_i\ F_{0,i}$
    if $F_{0,l} < F_{out}$ then $\boldsymbol{A}_k = \boldsymbol{A}_{k,l}$
        $\hat{\boldsymbol{\theta}} = (\boldsymbol{A}_k^T\boldsymbol{A}_k)^{-1}\boldsymbol{A}_k\boldsymbol{z}$
        $\boldsymbol{\epsilon}_k = \boldsymbol{z} - \boldsymbol{A}_k\hat{\boldsymbol{\theta}}_k$
    end if
%Stopping criteria%
    $PSE = \frac{1}{N}\boldsymbol{\epsilon}_k^T\boldsymbol{\epsilon}_k + \frac{p}{N^2}\sum_{i=1}^N[\boldsymbol{z}(i) - \bar{z}]$
    if $PSE > PSE_{last}$ or $PSE \le PSE_{tol}$ or $l = j$ then
        break
    end if
    $PSE_{last} = PSE$
end while
$\boldsymbol{A}_k$ is the final regressors matrix (model structure), $\hat{\boldsymbol{\theta}}_k$ is the estimated parameters and $\boldsymbol{\epsilon}_k$ is the model residual.
```

B. ESTIMATED MODEL OF C_x, C_y, C_m, C_l AND C_n

The estimated aerodynamic coefficients are given in this appendix. Note that the model structure and corresponding parameters are only applicable to Parrot Bebop without bumpers.

Table 6: Estimation results of C_x model

	$\|\beta\| \in [0,30]^\circ$			$\|\beta\| \in [30,60]^\circ$			$\|\beta\| \in [60,90]^\circ$	
reg.	$\hat{\theta}$	NRMS (%)	reg.	$\hat{\theta}$	NRMS (%)	reg.	$\hat{\theta}$	NRMS (%)
1	4.182E-04	18.374	1	4.390E-04	22.466	1	5.007E-04	9.566
μ_x	-3.482E-02	1.327	μ_x	-3.684E-02	2.271	μ_x	-3.873E-02	3.067
$\mu_x\mu_z$	7.717E-02	1.232	$\|\mu_y\|^3$	7.354E-02	2.213	$\|\mu_y\|^3$	2.412E-02	2.983
$\mu_x\mu_z^2$	1.057E+00	1.157	$\mu_x\mu_z^2$	3.673E+00	2.190	μ_z	3.956E-03	2.960
$\mu_x\mu_z^3$	3.837E+00	1.119	$\mu_x\mu_z$	2.216E-01	2.111	μ_z^2	3.055E-02	2.915
$\mu_x^2\mu_z^2$	7.365E-01	1.101	$\mu_x\mu_z^3$	1.497E+01	1.929	$\mu_x\mu_z^2$	2.495E-01	2.904
μ_x^3	-2.883E-02	1.082	μ_x^3	6.234E-02	1.918	R2	0.9079	
μ_z^2	-2.073E-02	1.075	R2	0.9927				
R2	0.9966							

Table 7: Estimation result of C_y model

	$\|\beta\| \in [0,30]^\circ$			$\|\beta\| \in [30,60]^\circ$			$\|\beta\| \in [60,90]^\circ$	
reg.	$\hat{\theta}$	NRMS (%)	reg.	$\hat{\theta}$	NRMS (%)	reg.	$\hat{\theta}$	NRMS (%)
1	-1.79E-04	6.595	1	-1.98E-04	16.820	1	-1.23E-04	16.563
μ_y	-3.36E-02	2.771	μ_y	-3.54E-02	1.675	μ_y	-3.88E-02	1.283
$\mu_y\mu_z$	1.16E-01	2.718	$\|\mu_x\|\mu_y\mu_z$	2.56E-01	1.201	$\mu_y^3\mu_z$	4.41E-01	0.979
$\mu_x^2\mu_z^2$	9.29E-01	2.693	$\mu_y\mu_z^3$	4.64E+00	1.163	$\mu_y\mu_z^3$	1.41E+00	0.945
$\|\mu_x\|\mu_z^2$	-2.10E-01	2.677	$\mu_y\mu_z$	1.61E-01	1.141	$\mu_y\mu_z$	8.39E-02	0.877
$\|\mu_x\|$	5.45E-04	2.664	$\mu_y\mu_z^2$	1.57E+00	1.113	$\mu_y\mu_z^2$	7.41E-01	0.857
R2	0.8368		μ_y^3	-1.05E-01	1.089	μ_y^3	-7.01E-02	0.830
			$\|\mu_x\|$	1.14E-03	1.083	$\mu_y^2\mu_z^2$	1.12E-01	0.828
			R2	0.9959		R2	0.9975	

Table 8: Estimation result of C_n model, $\mu \leq 0.05$

reg.	$\hat{\theta}$	NRMS (%)
1	2.188E-05	13.930
$s(u_r)u_r^2$	2.032E-04	3.382
r	-3.317E-02	2.689
u_r	3.099E-04	2.492
$\mu_x^2 r$	3.271E+02	2.460
R2	0.9690	

Table 9: Estimation results of C_n model, $\mu > 0.05$

$\lvert\beta\rvert \in [0,30]^\circ$			$\lvert\beta\rvert \in [30,60]^\circ$			$\lvert\beta\rvert \in [60,90]^\circ$		
reg.	$\hat{\theta}$	NRMS (%)	reg.	$\hat{\theta}$	NRMS (%)	reg.	$\hat{\theta}$	NRMS (%)
1	5.470E-05	7.245	1	1.350E-05	7.120	1	2.202E-05	8.291
u_r	6.976E-04	3.446	u_r^3	-4.156E-05	5.883	u_r^3	3.320E-05	6.842
$u_r\mu_x$	-5.354E-04	3.353	$u_r\mu_x$	-3.286E-04	5.471	$\mu_x\mu_y$	-4.661E-02	6.280
$\mu_y\mu_z$	4.554E-02	3.276	$\mu_x\mu_y^3$	-2.113E-01	5.368	$s(u_r)u_r^2$	-7.975E-05	6.170
$s(r)\bar{r}^2$	-1.781E+00	3.244	μ_y^3	-2.595E-02	5.100	μ_y	-1.640E-03	5.702
R2	0.8060		$s(u_r)u_r^2$	3.005E-04	4.485	u_r	4.716E-04	5.445
			$\mu_x\mu_x$	1.349E-02	4.413	$s(\bar{r})\bar{r}^2$	-2.994E+00	5.366
			$s(\mu_y)\mu_y^2\mu_z$	2.348E-01	4.335	$\mu_x\mu_y\mu_z$	-1.210E-01	5.352
			$u_r\mu_z$	-4.223E-03	4.245	R2	0.5859	
			$s(\bar{r})\bar{r}^2u_r$	5.652E+01	4.188			
			$s(u_r)u_r\mu_z$	1.287E-03	4.156			
			$\mu_y\mu_z^2$	1.188E-01	4.141			
			R2	0.6652				

Table 10: Estimation result of C_m model, $\lvert\beta\rvert \in [0,45]^\circ$

$\lvert\beta\rvert \in [0,15]^\circ$			$\lvert\beta\rvert \in [15,30]^\circ$			$\lvert\beta\rvert \in [30,45]^\circ$		
reg.	$\hat{\theta}$	NRMS (%)	reg.	$\hat{\theta}$	NRMS (%)	reg.	$\hat{\theta}$	NRMS (%)
1	1.16E-04	6.247	1	5.36E-05	9.779	1	1.73E-05	5.456
u_q	4.44E-03	4.831	u_q	4.70E-03	6.682	u_q	5.01E-03	4.490
$u_q\mu_z$	-5.10E-02	4.589	$u_q\lvert\mu_y\rvert$	-5.31E-02	4.843	$u_q\lvert\mu_y\rvert$	-9.56E-02	4.150
μ_x	5.04E-02	4.414	μ_x	4.32E-02	3.473	$u_q\mu_y^2$	8.09E-01	3.168
μ_x^2	1.91E-02	4.019	$\mu_x^3\mu_z$	5.60E+00	3.093	μ_x	2.84E-02	2.988
μ_z	3.57E-02	3.375	$\mu_x^3\mu_y^2\mu_z$	-5.82E+02	2.857	$u_q\mu_z$	-6.23E-02	2.714
$\bar{q}$	-1.35E-01	3.205	$\mu_x\lvert\mu_y\rvert$	-4.29E-01	2.650	$\mu_x\mu_z^2$	-5.20E+00	2.360
μ_x^3	-1.27E+00	3.072	$u_q\mu_z$	-6.93E-02	2.512	$u_q\mu_y^2\mu_z$	2.90E+00	2.154
μ_x^4	2.87E+00	2.715	$\bar{q}$	-6.94E-02	2.147	$\mu_x\mu_z^3$	-2.82E+01	1.947
$u_q\mu_x^2\mu_z$	8.28E-01	2.500	$u_q\mu_z^2$	-3.25E-01	2.088	$\bar{q}$	-8.51E-02	1.768
$u_q\mu_z^3$	9.31E+00	2.410	R2	0.9521		$u_q\mu_x^3\mu_y^2\mu_z$	3.53E+02	1.718
$u_q\mu_z^4$	2.25E+01	2.301				$u_q\mu_z^3$	3.43E+00	1.619
$\mu_x^2\mu_z$	4.11E-01	2.234				$u_q\mu_x^2$	1.46E-01	1.513
$u_q\mu_x\mu_z^3$	-2.31E+01	2.178				$u_q\mu_x^2\mu_y^2$	-8.85E+00	1.431
$\mu_x^2\lvert\mu_y\rvert\mu_z^2$	1.90E+02	2.120				$\mu_y^2\mu_z^5$	-8.23E+02	1.407
$\mu_x\mu_y^2\mu_z^2$	-7.62E+02	2.088				R2	0.9393	
R2	0.8872							

Table 11: Estimation result of C_m model, $|\beta| \in [45, 90]^\circ$

$\|\beta\| \in [45,60]^\circ$			$\|\beta\| \in [60,75]^\circ$			$\|\beta\| \in [75,90]^\circ$		
reg.	$\hat{\theta}$	NRMS (%)	reg.	$\hat{\theta}$	NRMS (%)	reg.	$\hat{\theta}$	NRMS (%)
1	1.97E-04	3.290	1	-3.82E-05	4.779	1	-1.75E-04	3.590
u_q	4.17E-03	2.837	u_q	4.73E-03	3.767	u_q	3.67E-03	2.635
μ_z	3.00E-03	2.306	μ_x	5.52E-02	3.605	$\mu_y^2\mu_z$	1.57E-01	2.615
μ_x	3.74E-02	2.128	$\mu_x\mu_z^2$	-7.24E+00	3.400	$u_q\mu_z$	-9.03E-02	2.598
$\mu_x\|\mu_y\|\mu_z^2$	7.33E+00	1.995	$u_q\mu_z$	-7.10E-02	3.244	$u_q\mu_z^2$	-9.29E-01	2.562
$u_q\mu_x^2\|\mu_y\|$	2.42E+00	1.900	$\mu_x\|\mu_y\|$	-3.57E-01	3.100	$\mu_y^2\mu_z^3$	-2.56E+01	2.512
$u_q\mu_z$	-6.30E-02	1.845	$u_q\|\mu_y\|$	-2.66E-02	2.996	$u_q\|\mu_y\|\mu_z^4$	-2.17E+02	2.491
$\mu_x\bar{q}$	-8.64E-01	1.815	$\mu_x\|\mu_y\|\mu_z^2$	5.24E+01	2.800	μ_z	-2.44E-03	2.470
$u_q\|\mu_y\|\mu_z^2$	-3.67E+00	1.788	$\mu_x\mu_y^2\mu_z^2$	-1.02E+02	2.641	$\|\mu_y\|\mu_z^5$	2.41E+02	2.448
$\mu_x\mu_z^2$	-5.88E+00	1.706	$\mu_x^3\mu_y^2\bar{q}$	-9.88E+03	2.544	$u_q\mu_z^3$	1.49E+01	2.435
$u_q\mu_x^2\mu_z$	4.35E+00	1.653	$u_q\mu_z^2$	-3.92E-01	2.467	$u_q\mu_z^4$	1.14E+02	2.402
$u_q\mu_x^3\mu_y^2$	-5.76E+01	1.631	$\mu_x^3\|\mu_y\|\mu_z\bar{q}$	-1.77E+04	2.394	$u_q\|\mu_y\|$	-1.06E-02	2.370
$\mu_x\|\mu_y\|$	-1.03E-01	1.608	$\bar{q}$	-6.07E-02	2.360	$u_q\|\mu_y\|\mu_z^2$	6.79E+00	2.351
$\mu_x\mu_z^3$	-2.71E+01	1.550	$u_q\mu_y^2$	8.98E-02	2.334	$u_q\|\mu_y\|\mu_z$	2.45E-01	2.340
$u_q\|\mu_y\|$	-2.04E-02	1.517	$u_q\|\mu_y\|\mu_z$	3.12E-01	2.315	$\mu_y^2\mu_z^2$	-2.11E+00	2.307
$u_q\mu_x^3\mu_y^2\mu_z$	-5.26E+02	1.476	$u_q\mu_x$	-5.50E-03	2.257	$\|\mu_y\|\mu_z^4$	2.69E+01	2.298
$u_q\mu_x^2\|\mu_y\|\mu_z^2$	8.14E+01	1.438	$\mu_x\mu_y^2$	5.39E-01	2.236	μ_x	1.58E-03	2.292
$u_q\mu_y^2\mu_z^5$	-1.51E+03	1.425	$\mu_y^2\mu_z$	8.33E-02	2.185	R2	0.5958	
R2	0.8107		$u_q\|\mu_y\|\mu_z^2$	1.41E+00	2.163			
			$\mu_x\mu_z^3$	-5.46E+00	2.156			
			R2	0.7782				

Table 12: Estimation result of C_l model, $|\beta| \in [0, 45]^\circ$

$\|\beta\| \in [0,15]^\circ$			$\|\beta\| \in [15,30]^\circ$			$\|\beta\| \in [30,45]^\circ$		
reg.	$\hat{\theta}$	NRMS (%)	reg.	$\hat{\theta}$	NRMS (%)	reg.	$\hat{\theta}$	NRMS (%)
1	2.30E-04	2.940	1	1.28E-04	6.321	1	2.79E-04	6.603
u_p	5.40E-03	1.885	u_p	5.08E-03	3.693	u_p	3.86E-03	6.251
μ_y	-2.84E-02	1.825	μ_y	-1.93E-02	2.695	μ_y	-4.12E-02	5.089
$\|\mu_x\|\bar{p}$	-3.32E-01	1.789	$\mu_x^2\mu_y^3\mu_z$	-9.23E+02	2.186	$\mu_x^2\mu_y$	-2.51E+00	4.567
$\mu_x^2\mu_y$	5.08E-01	1.767	μ_y^2	2.56E-01	2.042	$\|\mu_x\|\mu_y$	5.41E-01	4.407
$u_p\|\mu_x\|$	-4.44E-02	1.726	$\|\mu_x\|\mu_y^4$	-1.80E+02	1.795	$\mu_y^3\mu_z$	2.03E+01	4.289
$u_p\mu_z$	-1.26E-02	1.685	$\bar{p}$	-3.72E-02	1.662	$\mu_x^2\mu_y^3$	4.74E+01	4.187
$u_p\mu_x^2$	1.47E-01	1.659	$\mu_z^2\bar{p}$	-8.79E+00	1.637	$\mu_z\bar{p}$	1.33E+00	4.048
$u_p\mu_x^2\mu_z^2$	-2.10E+00	1.629	R2	0.9282		$\|\mu_x\|\mu_y\mu_z^2$	1.54E+01	3.844
$u_p\mu_y$	-4.37E-02	1.607				$u_p\mu_y$	4.73E-03	3.768
$\mu_x^2\mu_y^2$	2.36E+01	1.584				$\mu_x^2\mu_z^5\bar{p}$	2.70E+05	3.741
$u_p\mu_y^2$	3.05E+00	1.550				$\bar{p}$	-4.30E-02	3.720
$u_p\mu_x^2\mu_y^3$	1.75E+03	1.537				$u_p\mu_z^2$	2.64E-02	3.704
$\mu_x^2\mu_y^4$	-8.40E+03	1.519				R2	0.6859	
$\mu_y^2\bar{p}$	-9.54E+01	1.510						
R2	0.7331							

Table 13: Estimation result of C_l model, $|\beta| \in [45, 90]^\circ$

$\lvert\beta\rvert \in [45, 60]^\circ$			$\lvert\beta\rvert \in [60, 75]^\circ$			$\lvert\beta\rvert \in [75, 90]^\circ$		
reg.	$\hat{\theta}$	NRMS (%)	reg.	$\hat{\theta}$	NRMS (%)	reg.	$\hat{\theta}$	NRMS (%)
1	3.16E-04	3.626	1	2.69E-04	6.058	1	3.34E-04	3.931
u_p	4.32E-03	3.551	u_p	4.37E-03	5.671	u_p	3.99E-03	3.751
μ_y	-3.45E-02	2.982	μ_y	-2.36E-02	4.600	μ_y	-2.24E-02	3.192
$\lvert\mu_x\rvert\mu_y^3\mu_z$	-2.93E+01	2.670	μ_y^3	2.12E-01	3.826	μ_y^3	1.34E-01	2.683
$\lvert\mu_x\rvert\mu_y$	4.44E-01	2.592	$\mu_y\mu_z^2$	2.37E+00	3.646	$\mu_y\mu_z^2$	1.35E+00	2.456
$\mu_x^2\mu_y$	-1.54E+00	2.512	$u_p\mu_y^2\mu_z^2$	-3.61E+00	3.473	$\mu_y^2\mu_z\bar{p}$	2.20E+01	2.350
$u_p\mu_z$	1.03E-02	2.475	$u_p\mu_y^2\mu_z$	-6.41E-01	3.369	$\bar{p}$	-5.43E-02	2.187
$\lvert\mu_x\rvert\mu_y^2$	-4.09E-02	2.438	$\mu_y^2\bar{p}$	-3.25E+00	3.291	$u_p\mu_z^4$	-4.51E+01	2.159
$\mu_y\mu_z^3$	-7.70E+00	2.414	$u_p\mu_z^5$	-1.66E+02	3.154	$u_p\mu_z^3$	-4.36E+00	2.129
$\lvert\mu_x\rvert\mu_y\mu_z^2$	-1.02E+01	2.382	$\mu_y^3\mu_z$	1.31E+00	3.124	μ_z	-2.81E-03	2.087
$\bar{p}$	-5.76E-02	2.352	$u_p\mu_z^4$	-2.39E+01	3.050	$u_p\mu_y^2$	4.01E-02	2.061
μ_y^3	-4.58E-01	2.325	$\mu_y\mu_z^3$	9.49E+00	2.965	$u_p\mu_z^5$	-1.31E+02	2.047
$u_p\mu_z^2$	9.37E-02	2.305	$u_p\mu_z^2$	-2.79E-01	2.922	$\mu_y\mu_z^3$	5.11E+00	2.008
$u_p\lvert\mu_x\rvert$	-1.96E-02	2.288	$u_p\mu_z^3$	-1.14E+00	2.907	$u_p\mu_y^4$	-3.73E-01	1.994
$u_p\mu_y^2$	6.65E-02	2.269	R2	0.7632		$u_p\mu_z^2$	-1.68E-01	1.975
$\mu_x^2\mu_y^2$	7.15E+00	2.262				μ_z^2	-2.23E-02	1.962
R2	0.6031					R2	0.7476	

REFERENCES

[1] D. Mellinger, N. Michael, and V. Kumar, *Trajectory Generation and Control For Precise Aggressive Maneuvers with Quadrotors,* in *Springer Tracts in Advanced Robotics*, Vol. 79 (2014) pp. 361–373.

[2] M. Hehn and R. Dandrea, *Real-Time Trajectory Generation for Quadrocopters,* IEEE Transactions on Robotics **31**, 877 (2015).

[3] E. J. Smeur, G. C. de Croon, and Q. Chu, *Cascaded incremental nonlinear dynamic inversion for mav disturbance rejection,* Control Engineering Practice **73**, 79 (2018).

[4] H. Huang, G. M. Hoffmann, S. L. Waslander, and C. J. Tomlin, *Aerodynamics and control of autonomous quadrotor helicopters in aggressive maneuvering,* in *Proceedings - IEEE International Conference on Robotics and Automation (ICRA)* (2009).

[5] K. Alexis, G. Nikolakopoulos, and A. Tzes, *Switching Model Predictive Attitude Control for a Quadrotor Helicopter Subject to Atmospheric Disturbances,* Control Engineering Practice **19**, 1195 (2011).

[6] R. C. Leishman, J. C. MacDonald, R. W. Beard, and T. W. McLain, *Quadrotors and Accelerometers: State Estimation with an Improved Dynamic Model,* IEEE Control Systems **34**, 28 (2014).

[7] T. Carroll, I.-R. E. George, and G. Bramesfeld, *Design Optimization of Small Rotors in Quad-Rotor Configuration,* in *54th AIAA Aerospace Sciences Meeting* (2016).

[8] J. V. Foster and D. Hartman, *High-Fidelity Multi-Rotor Unmanned Aircraft System (UAS) Simulation Development for Trajectory Prediction Under Off-Nominal Flight Dynamics,* in *17th AIAA Aviation Technology, Integration, and Operations Conference* (2017).

[9] Y. Zhang, C. C. de Visser, and Q. P. Chu, *Aircraft Damage Identification and Classification for Database-Driven Online Flight-Envelope Prediction,* Journal of Guidance, Control, and Dynamics **41**, 449 (2017).

[10] G. M. Hoffmann, H. Huang, S. L. Waslander, and C. J. Tomlin, *Quadrotor Helicopter Flight Dynamics and Control : Theory and Experiment,* American Institute of Aeronautics and Astronautics **4**, 1 (2007).

[11] G. M. Hoffmann, H. Huang, S. L. Waslander, and C. J. Tomlin, *Precision Flight Control for a Multi-Vehicle Quadrotor Helicopter Testbed,* Control Engineering Practice **19**, 1023 (2011).

[12] P. Martin and E. Salaün, *The true role of accelerometer feedback in quadrotor control,* in *2010 IEEE international conference on robotics and automation* (IEEE, 2010) pp. 1623–1629.

[13] D. Kaya and A. T. Kutay, *Aerodynamic modeling and parameter estimation of a quadrotor helicopter,* in *AIAA Atmospheric Flight Mechanics Conference*, June (2014).

[14] M. Orsag and S. Bogdan, *Influence of forward and descent flight on quadrotor dynamics,* Recent Advances in Aircraft Technology , 141 (2012).

[15] Y. R. Tang and Y. Li, *Dynamic Modeling for High-Performance Controller Design of a UAV Quadrotor,* in *2015 IEEE International Conference on Information and Automation* (2015) pp. 3112–3117.

[16] M. Schulz, F. Augugliaro, R. Ritz, and R. D'Andrea, *High-speed, steady flight with a quadrocopter in a confined environment using a tether,* in *2015 IEEE/RSJ International Conference on Intelligent Robots and Systems (IROS)* (IEEE, 2015) pp. 1279–1284.

[17] R. Gill and R. D'Andrea, *Propeller thrust and drag in forward flight,* in *2017 IEEE Conference on Control Technology and Applications (CCTA)* (IEEE, 2017) pp. 73–79.

[18] W. Khan and M. Nahon, *Toward an Accurate Physics-based UAV Thruster Model,* IEEE/ASME Transactions on Mechatronics **18**, 1269 (2013).

[19] R. Mahony, V. Kumar, and P. Corke, *Multirotor Aerial Vehicles: Modeling, Estimation, and Control of Quadrotor,* IEEE Robotics & Automation Magazine **19**, 20 (2012).

[20] P.-j. Bristeau, P. Martin, E. Salaun, and N. Petit, *The role of propeller aerodynamics in the model of a quadrotor UAV,* in *2009 European Control Conference (ECC)* (IEEE, 2009) pp. 683–688.

[21] P. Pounds, R. Mahony, and P. Corke, *Modelling and Control of a Large Quadrotor Robot,* Control Engineering Practice **18**, 691 (2010).

[22] C. R. Russell, J. Jung, G. Willink, and B. Glasner, *Wind tunnel and hover performance test results for multicopter uas vehicles,* (2016).

[23] J. Luo, L. Zhu, and G. Yan, *Novel Quadrotor Forward-Flight Model Based on Wake Interference,* AIAA Journal **53**, 3522 (2015).

[24] E. A. Morelli, *Global Nonlinear Aerodynamic Modeling Using Multivariate Orthogonal Functions,* Journal of Aircraft **32**, 270 (1995).

[25] V. Klein and E. A. Morelli, *Aircraft System Identification: Theory and Practice* (AIAA, Blacksburg, VA, 2006) p. 484, arXiv:arXiv:1011.1669v3 .

[26] T. Lombaerts, *Fault Tolerant Flight Control: A Physical Model Approach*, Ph.D. thesis, Delft Univ. of Technology, Delft, The Netherlands (2010).

[27] S. F. Armanini, M. Karásek, G. C. H. E. de Croon, and C. C. de Visser, *Onboard-/Offboard Sensor Fusion for High-Fidelity Flapping-Wing Robot Flight Data,* Journal of Guidance, Control, and Dynamics **40**, 2121 (2017).

[28] E. J. J. Smeur, Q. Chu, and Guido C. H. E. de Croon, *Adaptive Incremental Nonlinear Dynamic Inversion for Attitude Control of Micro Aerial Vehicles,* Journal of Guidance, Control, and Dynamics **39**, 450 (2016).

[29] *Wiki of paparazzi flight controller,* `https://github.com/paparazzi/paparazzi`, accessed: 2018-02-20.

[30] A. Mendes, E. van Kampen, B. Remes, and Q. Chu, *Determining moments of inertia of small uavs: A comparative analysis of an experimental method versus theoretical approaches,* in *AIAA Guidance, Navigation, and Control Conference* (2012) p. 4463.

[31] C. Powers, D. Mellinger, A. Kushleyev, B. Kothmann, and V. Kumar, *Influence of aerodynamics and proximity effects in quadrotor flight,* in *Experimental robotics* (2013) pp. 289–302.

3

AERODYNAMIC MODEL IDENTIFICATION OF A QUADROTOR SUBJECTED TO ROTOR FAILURES IN THE HIGH-SPEED FLIGHT REGIME

This chapter presents a high-fidelity aerodynamic model of a quadrotor in the high-speed flight, with the normal configuration, or subjected to rotor failures. A novel experimental setup, data processing and model identification procedure are developed. We first establish the thrust and torque model from static wind tunnel tests as the benchmark of the aerodynamic model, and then we further identify the in-plane forces, pitch and roll moments of each rotor from the free flight data obtained in a large scale open jet wind tunnel. The validation results show a decent model performance in predicting forces/moments, lateral forces effects and the quadrotor trimming curve, by comparing with the benchmark model.

Parts of this chapter have been published in:

S. Sun and C. de Visser, "Aerodynamic Model Identification of a Quadrotor Subjected to Rotor Failures in the High-Speed Flight Regime," IEEE Robotics and Automation Letters, vol. 4, no. 4, pp. 3868–3875, Oct. 2019.

1. INTRODUCTION

Since the advent of multi-rotor drones, the operating regimes have been extended from hovering to the high-speed conditions (e.g. delivery, drone racing, etc). This motivates researchers to establish reliable aerodynamic models of multi-rotor drones for various purposes, such as rejecting the wind disturbances[1], trajectory refinement[2], design optimization[3], etc.

There is an extensive body of literature discussing the aerodynamic effects on drones. The thrust variation [4–6] and blade flapping effects[7, 8] are mostly considered. They can to some extent precisely depict the major forces deviations in the fast flight comparing to the hovering condition. On the other hand, the aerodynamic moments of a single rotor have been discussed in, e.g. Ref. [9]. The difference between the advancing and retreating blade, and the blade flapping are found to be important in contributing to the moments [6]. The observation that the rear rotors require much higher rotational speed than front rotors during the trim condition demonstrates the existence of these aerodynamic moments [10, 11].

Due to limited knowledge of aerodynamic parameters, such as the Renold number of a small-sized rotor, the aforementioned effects are difficult to be modeled from merely physical insights. A more practical approach is using real data to identify the aerodynamic models. Thrust and drag models are mostly seen being identified for control synthesis (see, e.g., [12–14]). In comparison, aerodynamic moment models are more complex and identified in only a few pieces of research [11, 15], though these moments are found to be non-trivial especially in the high-speed regime. The model structures adopted in these methods, however, might not be effective for a drone with rotor failures.

In [16], we conducted flights of a quadrotor with complete loss of a rotor in the high-speed condition. Due to the fast spinning on the yaw direction, effects such as the lateral aerodynamic forces were observed. This motivates us to establish an aerodynamic model that could predict these effect and, at the same time, remain effective to quadrotors without failures.

Therefore, in this chapter, the high-speed flight data of a quadrotor with single-rotor-failure (SRF), diagonal double-rotor-failure (DRF) and no-failure (NF) are used for aerodynamic model identification, in combination with the wind tunnel static test of a single rotor. In this process, the following problems are resolved:

1. Establish a multi-body aerodynamic model by distinguishing between the rotor system and the airframe generated forces/moments, using only measurements from the inertial measurement unit (IMU) and the motion capturing system.

2. Precisely measure the forces on the center of gravity (c.g.) in the SRF / DRF configuration with the presence of centrifugal force due to the large yaw rate, and the displacement between c.g. and the IMU location.

3. Reconstruction of the local air velocities of the rotors considering attitude es-

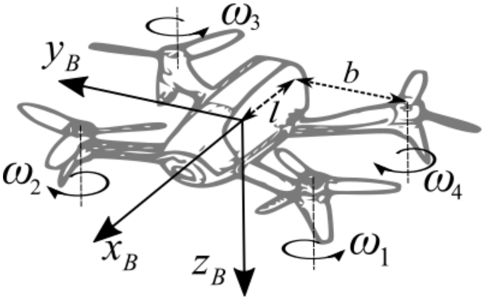

Figure 3.1: The tested quadrotor (Parrot Bebop2), the definition of the body frame, the rotor indices and the definition of l and b.

timation errors and reference frame displacements.

4. Select a model structure which ensures both accuracy and simplicity.

As the main contribution, a parametric model of a quadrotor 3-axis force/moment is consequently established which is generally applicable to either low/high-speed flight conditions and to either configuration with/without rotor failures. In addition, the effects such as the lateral forces in SRF and DRF configurations are also captured by the proposed model during the validation procedure. As a consequence, this model can be used in a wide variety of applications such as improving the controller performance while confronting significant wind flow or complete actuator failures.

This chapter is organized as follows. Section 3 introduces the central equations and methodologies of the identification procedure. Section 5 details the experimental setups. The data processing is discussed by Section 4. The selection of model structures and the identification method is described in Section 5. In Section 6, the proposed model is validated in both rotor failure and non-failure cases.

2. METHODOLOGY

The coordinate systems are first of all introduced. The inertial frame $\{O_I, x_I, y_I, z_I\}$ is originated at a fixed point on the ground. For wind tunnel tests, we define x_I as pointing against the wind flow, y_I pointing right side perpendicular to the wind flow, and z_I aligning with the gravity. The body frame $\{O_B, x_B, y_B, z_B\}$ is originated at the center of gravity with x_B pointing forwards, y_B pointing rightwards, and z_B aligning with the thrust vector but pointing downwards. In the following context, the superscript I and B indicate the coordinate system on which a vector is projected; the subscript i indicates the variable of the ith rotor; the subscript x, y, and z indicate the projection of a vector on the corresponding axis. The drone used for identification is a modified Parrot Bebop2 as is shown in Fig. 3.1, where the geometric parameters b and l, and the rotor index definition, are also presented.

Recall the translational and rotational dynamic equations of a quadrotor as

$$\dot{\boldsymbol{V}}^B + \boldsymbol{\Omega}^B \times \boldsymbol{V}^B = \boldsymbol{L}_{BI}(\boldsymbol{g}^I - \dot{\boldsymbol{V}}_w^I) + \boldsymbol{F}^B/m \tag{3.1}$$

$$\boldsymbol{I}_v^B \dot{\boldsymbol{\Omega}}^B + \boldsymbol{\Omega}^B \times \boldsymbol{I}_v^B \boldsymbol{\Omega}^B + (\boldsymbol{\Omega}^B \times \sum \boldsymbol{I}_p^B \boldsymbol{\omega}_i^B + \sum \boldsymbol{I}_p^B \dot{\boldsymbol{\omega}}_i^B) = \boldsymbol{M}^B \tag{3.2}$$

where $\boldsymbol{V}^B = [u,\ v,\ w]^T$ is the translational velocity of the center of gravity (c.g.) with respect to the airflow, as is projected on the body frame. $\boldsymbol{V}_w^I$ is the wind velocity with respect to the inertial frame. $\boldsymbol{\Omega}^B = [p,\ q,\ r]^T$ is the vehicle's angular velocity with respect to the inertial frame, which is projected in the body frame. The symbol m, $\boldsymbol{I}_v$ and $\boldsymbol{I}_p$ respectively indicate the total mass, moment of inertia of the entire vehicle and of the rotor. $\boldsymbol{L}_{BI}$ is the rotational matrix from the inertial frame to the body frame. $\boldsymbol{\omega}_i^B$ is the angular rate vector of the ith rotor with respect to the inertial frame which is expressed as $\boldsymbol{\omega}_i^B = \boldsymbol{\Omega}^B + [0,\ 0,\ s_{n,i}\omega_i]^T$, where ω_i is the angular rate of the ith rotor with respect to the body frame. $s_{n,i}$ indicates the rotational direction of the ith rotor such that 1 indicates clockwise rotation; for Parrot Bebop2, we have

$$s_n = [-1,\ 1,\ -1,\ 1] \tag{3.3}$$

The external forces and moments projection on the body frame, denoted by $\boldsymbol{F}^B$ and $\boldsymbol{M}^B$, are composed of control forces/moments and other aerodynamic effects on both rotor systems and the airframe, which is to be determined in this chapter. They can be expressed as follows

$$\begin{bmatrix} \boldsymbol{F}^B \\ \boldsymbol{M}^B \end{bmatrix} = \begin{bmatrix} F_x \\ F_y \\ F_z \\ M_x \\ M_y \\ M_z \end{bmatrix} = \begin{bmatrix} \sum F_{x,i} \\ \sum F_{y,i} \\ -\sum T_i \\ \sum s_{l,i} b T_i + \sum M_{x,i} \\ \sum s_{m,i} l T_i + \sum M_{y,i} \\ \sum s_{l,i} b F_{x,i} + \sum s_{m,i} l F_{y,i} + \sum M_{z,i} \end{bmatrix} + \begin{bmatrix} \boldsymbol{F}_f^B \\ \boldsymbol{M}_f^B \end{bmatrix} + a \tag{3.4}$$

where $\boldsymbol{F}_f^B$ and $\boldsymbol{M}_f^B$ indicate the 3-axis forces and moments generated by the airframe. $\boldsymbol{F}_i^B = [F_{x,i},\ F_{y,i},\ F_{z,i}]^T$ and $\boldsymbol{M}_i^B = [M_{x,i},\ M_{y,i},\ M_{z,i}]^T$ stand for the 3-axis forces and moments from the ith rotor. By convention, the z_B directions force of each rotor $F_{z,i}$ is replaced by the thrust T_i. Vectors s_l and s_m indicate the direction that each rotor contributes to rolling and pitching; they are

$$s_l = [1,\ -1,\ -1,\ 1],\ s_m = [1,\ 1,\ -1,\ -1] \tag{3.5}$$

In this research, the thrust T_i and the z_B direction moment of each rotor $M_{z,i}$ (rotor drag torque by convention) are directly measured during the static test conducted in the wind tunnel, using an off-the-shelf rotor test stand. With T_i and $M_{z,i}$ independently measured instead of identified from the flight data, the aerodynamics on the air-frame can be more accurately estimated (see [11] otherwise). The remaining part of the model, namely the in-plane forces $F_{x,i}$, $F_{y,i}$, the pitch/roll moments $M_{y,i}$, $M_{x,i}$ of each rotor, and the forces/moments from the airframe are identified using the flight data. They are functions of ω_i and the local air velocity of the ith rotor denoted by $\boldsymbol{V}_i^B = [u_i,\ v_i,\ w_i]^T$.

The thrust of the rotor i is expressed as

$$T_i = C_{t,i}\rho(\pi R^2)(\omega_i R)^2 \tag{3.6}$$

and the drag torque of the rotor i is expressed as

$$M_{z,i} = s_{n,i}C_{q,i}\rho(\pi R^3)(\omega_i R)^2 \tag{3.7}$$

where ρ is the air density and R is the radius of the rotor. The model of thrust and torque of each rotor will be given in the dimensionless form (C_t and C_q) to increase the generality of this model to drones with different sizes. Define the symbol $|\cdot|$ as the L^2 norm of a vector. Then the $C_{t,i}$ and $C_{q,i}$ can be further characterized as functions of advance ratio J and the angle of attack α, which are defined as

$$J_i = \frac{|\boldsymbol{V}_i|}{\omega_i R},\ \ \alpha_i = \sin^{-1}(w_i/|\boldsymbol{V}_i|) \tag{3.8}$$

3. EXPERIMENTAL SETUP

3.1. STATIC WIND TUNNEL TEST

The static wind tunnel test of a single rotor has been carried out using an off-the-shelf rotor test stand (RCbenchmark series 1580), as Fig. 3.2 shows. The thrust and the drag torque of a Bebop2 rotor have been measured at the frequency of 4 Hz.

During the static wind tunnel test, the angle of attack α varies from -90 to 90 degrees with steps of 15 degrees. The wind speed changes from 0 to 14 m/s in steps of 2 m/s. At each test point, the reference revolutions per minute (RPM) starts from 3000 to 12000 in steps of 1000 RPM. In negative angles of attack, the rotor is mounted such that the thrust pulls the test bench and generate a negative force measurement; on the contrary, the rotor is reversed and push the test bench in the positive angles of attack setups.

The model of C_t and C_q can then be established from (3.6) and (3.7). A 5th order polynomial model is used to fit the data as is shown in Fig. 3.3. The parameters $\boldsymbol{K}_{Ct}$ and $\boldsymbol{K}_{Cq}$ are given in the Appendix of this Chapter. Note that the unit of α is radian.

$$C_t = \mathbf{Q}\boldsymbol{K}_{Ct},\ C_q = \mathbf{Q}\boldsymbol{K}_{Cq} \tag{3.9}$$

$$\begin{aligned}\mathbf{Q} = \ & [1,\ J,\ J^2,\ J^3,\ J^4,\ J^5,\ J\alpha,\ J^2\alpha,\ J^3\alpha,\ J^4\alpha,\\ & J\alpha^2,\ J^2\alpha^2,\ J^3\alpha^2,\ J\alpha^3,\ J^2\alpha^3,\ J\alpha^4]\end{aligned}$$

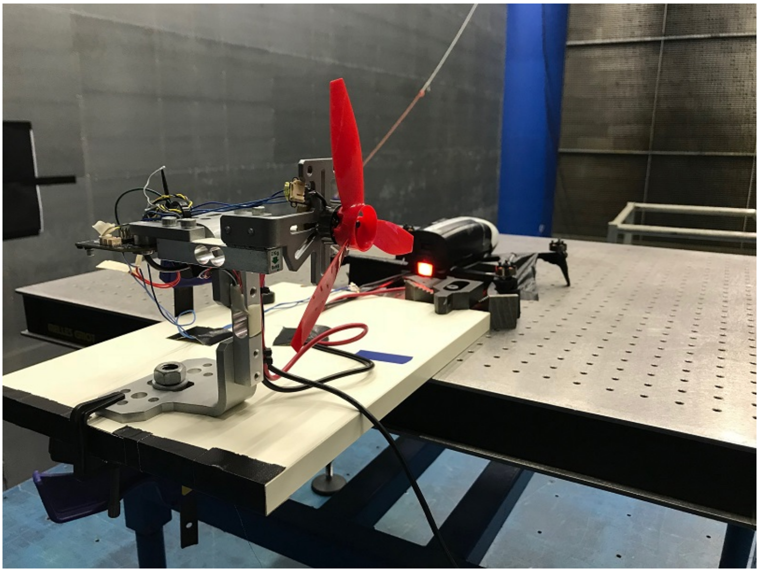

Figure 3.2: Setup of the static wind tunnel test of a Bebop2 rotor.

3.2. FLIGHT TEST

Since the test bench is only able to measure the thrust and drag torque of rotors, the flight data can be then utilized to identify the rest forces/moments of the rotor and the aerodynamics of the airframe. The flight test has been carried out in the Open Jet Facility (OJF), a large-scale wind tunnel with the aperture of 2.85 m.

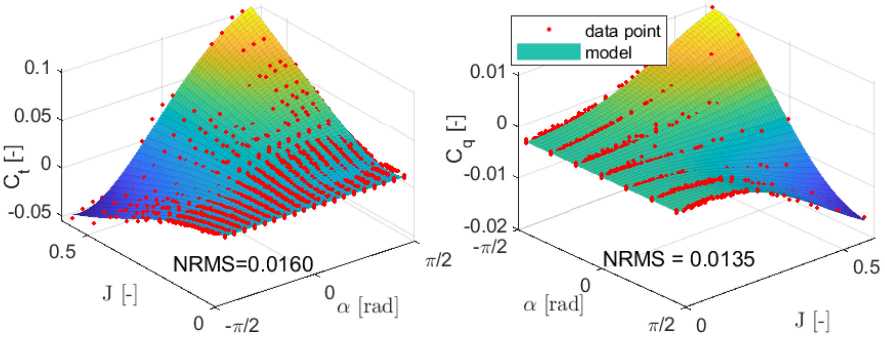

Figure 3.3: Model of C_t and C_q in different angles of attack and advance ratios, together with the normalized root mean square (NRMS) of the model residuals.

Table 3.1: Inertial and geometric properties of the tested quadrotor.

parameter	value	unit
m_{NF}	0.510	kg
$m_{\mathrm{DRF/SRF}}$	0.410	kg
$\boldsymbol{I}^B_{v,\mathrm{NF}}$	diag(1.92, 1.85, 3.34)$\times 10^{-3}$	kgm^2
$\boldsymbol{I}^B_{v,\mathrm{DRF/SRF}}$	diag(1.45, 1.26, 2.52)$\times 10^{-3}$	kgm^2
$\boldsymbol{I}^B_p$	diag(4.2, 4.2, 8.0)$\times 10^{-6}$	kgm^2
b, l, R	0.115, 0.088, 0.075	m

There is a set of motion capturing system (OptiTrack) including 12 cameras providing the position measurement of the four markers attached to the drone in 120 Hz, with the RMS error less than 0.2 mm. The measurement is transmitted to the on-board autopilot to provide necessary indoor position and velocity information of the drone.

The rest of the measurements are obtained using the on-board sensors at 512 Hz. The implemented IMU is a built-in MPU-6050 MEMS which provides the angular velocity and specific force measurements. The noise performance is 0.005 deg$\cdot$ s^{-1}/$\sqrt{\mathrm{Hz}}$ for the gyroscope and 400 μg/$\sqrt{\mathrm{Hz}}$ for the accelerometer. More details can be found in [17]. The IMU ground calibration is conducted to take into account the bias from angular displacements from the IMU to the body frame [18]. An Extended Kalman Filter (EKF) is applied to fuse the OptiTrack and the IMU measurements to obtain the attitude estimation of the body frame. A built-in Brushless DC (BLDC) motor controller on the Parrot Bebop2 measures the rotational speed of each rotor in RPM. The on-board sensor measurements are re-sampled to 120 Hz to synchronize with the OptiTrack measurements.

The flights in three types of configurations are carried out. The no-failure (NF) configuration has been tested in various flight speeds from 0 to 16 m/s, with heading angle towards the nozzle. Next, one or two rotors are removed from the drone to test the single-rotor-failure (SRF) and double-rotor-failure (DRF) configurations. In order to achieve higher flight speed in the rotor failure conditions, the weight of the drone is reduced by lightening the battery. The incremental nonlinear dynamic inversion (INDI) method has been applied to control the drone in SRF case in the wind tunnel. Details about the method can be found in [16]. The controller of a quadrotor in the DRF configuration will be introduced in an upcoming report.

In the SRF and DRF configuration, the drone fast spins on the yaw direction at about 20 rad/s. By making use of this effect, the in-plane force of the rotor can be easily extracted from the damping on the yaw direction. In these two configurations, the drone is able to reach up to 9 m/s flight speed. The measured inertial and geometric properties of the tested quadrotor in different falure conditions are listed in Table 6.1.

4. DATA PREPROCESSING

4.1. FORCE AND MOMENT MEASUREMENT

The specific force acting on the IMU, denoted by $\boldsymbol{a}^B$, can be obtained from the unbiased accelerometer measurement after the ground calibrations. However, for the high-rate spinning quadrotor, a horizontal supporting force is acting on the accelerometer to compensate for the centrifugal force caused by the displacement between the c.g. and the IMU location. Roughly speaking, this (normalized) centrifugal force can reach about 1 m/s^2 with displacement less than 3 mm.

Although this displacement, denoted by $\boldsymbol{d}_{ca}^B$, can be inconsistent in different flights and too minute to measure, it can be estimated from the flight data. According to [18], the real external force acting on the c.g. is

$$\frac{1}{m}\begin{bmatrix} F_x \\ F_y \end{bmatrix} = \begin{bmatrix} a_x \\ a_y \end{bmatrix} - \begin{bmatrix} -(q^2+r^2) & pq-\dot{r} & pr+\dot{q} \\ pq+\dot{r} & -(r^2+p^2) & qr-\dot{p} \end{bmatrix} \boldsymbol{d}_{ca}^B \tag{3.10}$$

An approximation is made that the external horizontal force is zero during the relaxed hovering flight [19]:

$$F_x = F_y = 0$$

Then $\boldsymbol{d}_{ca}^B$ can be estimated by a Least Square estimator using (3.10). After knowing the estimation $\hat{\boldsymbol{d}}_{ca}^B$, we can in turn obtain the measurement of $\boldsymbol{F}^B$ on c.g. as follows

$$\frac{1}{m}\boldsymbol{F}_{\text{mea}}^B = \boldsymbol{a}^B - \frac{d\boldsymbol{\Omega}^B}{dt} \times \hat{\boldsymbol{d}}_{ca}^B - \boldsymbol{\Omega}^B \times (\boldsymbol{\Omega}^B \times \hat{\boldsymbol{d}}_{ca}^B) \tag{3.11}$$

The original measured specific force and the corrected specific force are compared as shown in Fig. 3.4a.

The moment measurement $\boldsymbol{M}_{\text{mea}}^B$ can be obtained using (6.4), with the knowledge of inertial properties given in Table 6.1. It is worth noting that, for SRF/DRF configurations, the gyroscopic moments from rotors cannot be neutralized by counter-rotating propellers due to the loss of rotors. Therefore, $\boldsymbol{I}_p^B$ is estimated by making a CAD model to ensure the accuracy of the estimation of the gyroscopic moment. The accelerometer measured $\boldsymbol{a}^B$, the gyroscopic measured $\boldsymbol{\Omega}^B$ and the BLDC measured ω_i are bi-directionally filtered by a 4th order Butterworth filter with 15 Hz cut-off frequency.

4.2. VELOCITY RECONSTRUCTION

The air velocity of c.g., namely $\boldsymbol{V}^B$, and the local air velocity each rotor $\boldsymbol{V}_i^B$ should be characterized as independent variables of the proposed model. However, the slight displacement from the motion capturing system measured reference point to the IMU location could bring nonnegligible effects on these air-velocities due to the spinning motion in the SRF/DRF configurations.

The velocity of c.g. with respect to the airflow can be measured indirectly by

$$\boldsymbol{V}^B = \boldsymbol{\Omega}^B \times (\boldsymbol{d}^B_{oa} - \boldsymbol{d}^B_{ca}) + \boldsymbol{L}_{BI}(\boldsymbol{V}^I_o - \boldsymbol{V}^I_w) \tag{3.12}$$

where $\boldsymbol{V}^I_o$ is the velocity measured by the OptiTrack; $\boldsymbol{d}^B_{oa}$ is the displacement from the OptiTrack measured point to the IMU location. $\boldsymbol{d}^B_{ca}$ is the displacement from IMU location to c.g., which can be estimated using the method given in Sec. 4.1.

Similarly, the local air-velocity of the ith rotor can be measured indirectly by

$$\boldsymbol{V}^B_i = \boldsymbol{\Omega}^B \times (\boldsymbol{d}^B_{oa} + \boldsymbol{d}^B_{ai}) + \boldsymbol{L}_{BI}(\boldsymbol{V}^I_o - \boldsymbol{V}^I_w) \tag{3.13}$$

where $\boldsymbol{d}^B_{ai}$ represents the displacement from the IMU to the center of the ith rotor, which is consistent and can be measured accurately.

From the practical standpoint, $\boldsymbol{d}^B_{oa}$ in (3.12) and (3.13) can be variable in different experiments. Here we introduce a method to determine $\boldsymbol{d}^B_{oa}$ using the flight data. The velocity of IMU with respect to the inertial frame can be expressed as

$$\boldsymbol{V}^B_a = \boldsymbol{L}_{BI}\boldsymbol{V}^I_o + \boldsymbol{\Omega}^B \times \boldsymbol{d}^B_{oa} \tag{3.14}$$

By taking derivative of both sides of the above equation and projecting on the body frame, we have

$$\boldsymbol{a}^B + \boldsymbol{L}_{BI}(\boldsymbol{g}^I - \dot{\boldsymbol{V}}^I_o) = (\dot{\boldsymbol{\Omega}}^B_\times + \boldsymbol{\Omega}^B_\times\boldsymbol{\Omega}^B_\times)\boldsymbol{d}^B_{oa} \tag{3.15}$$

where $\boldsymbol{\Omega}_\times$ denotes the skew-symmetric matrix such that $\boldsymbol{\Omega}_\times \boldsymbol{v} = \boldsymbol{\Omega} \times \boldsymbol{v}$ for any $\boldsymbol{v} \in \mathbb{R}^3$. We hereby use $\hat{\boldsymbol{L}_{BI}}$ to represents the estimated rotational matrix from the EKF. Then the estimation of $\boldsymbol{d}^B_{oa}$, denoted by $\hat{\boldsymbol{d}}^B_{oa}$, can be obtained by

$$\hat{\boldsymbol{d}}^B_{oa} = (\dot{\boldsymbol{\Omega}}^B_\times + \boldsymbol{\Omega}^B_\times\boldsymbol{\Omega}^B_\times)^{-1}\left[\boldsymbol{a}^B + \hat{\boldsymbol{L}_{BI}}(\boldsymbol{g}^I - \dot{\boldsymbol{V}}^I_o)\right] \tag{3.16}$$

Subsequently, the air-velocities can be obtained from (3.12) and (3.13). For demonstration, the local air-velocity of the 1st rotor during a set of flight with SRF configuration are plotted in Fig. 3.4. It shows that the horizontal velocity estimation is quite different after considering the effect of $\boldsymbol{d}^B_{oa}$, because the yaw rate is over 20 rad/s during this flight.

The estimated rotational matrix $\hat{\boldsymbol{L}_{BI}}$, however, can be deviated from the real value due to the orientation difference between the OptiTrack measurements and the body frame. We hereby define the estimation error as $\Delta\boldsymbol{L}_{BI}$ for quantification, such that

$$\boldsymbol{L}_{BI} = (\boldsymbol{I}_{3\times3} - \Delta\boldsymbol{L}_{BI})\hat{\boldsymbol{L}_{BI}} \tag{3.17}$$

By substituting (3.16) and (3.17) into (3.15), we have

$$(\dot{\boldsymbol{\Omega}}^B_\times + \boldsymbol{\Omega}^B_\times\boldsymbol{\Omega}^B_\times)\Delta\boldsymbol{d}^B_{oa} = \Delta\boldsymbol{L}_{BI}\hat{\boldsymbol{L}_{BI}}(\boldsymbol{g}^I - \frac{d\boldsymbol{V}^I_o}{dt}) \tag{3.18}$$

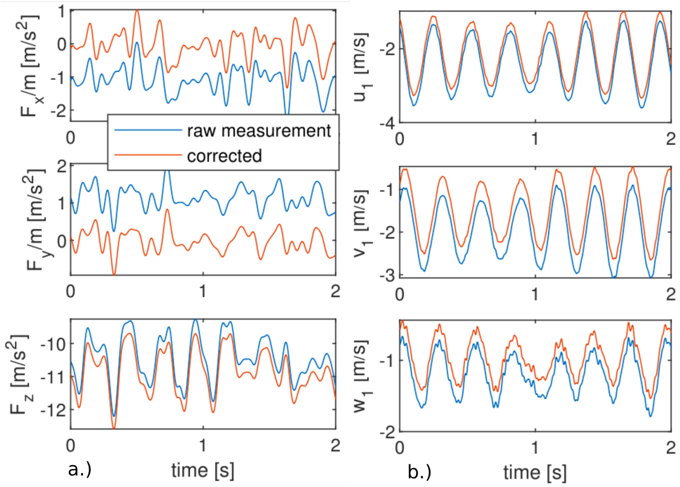

Figure 3.4: a.) Comparison between the accelerometer measured external force before and after the correctness considering $\boldsymbol{d}_{ca}^B$, where $\hat{\boldsymbol{d}}_{ca}^B = [1.8, -2.7,\ 0.4]^T$mm. b.) The local air-velocity estimation of a rotor before and after correction considering $\boldsymbol{d}_{oa}^B$, where $\hat{\boldsymbol{d}}_{oa}^B = [23.4,\ 1.5,\ 23.8]^T$mm.

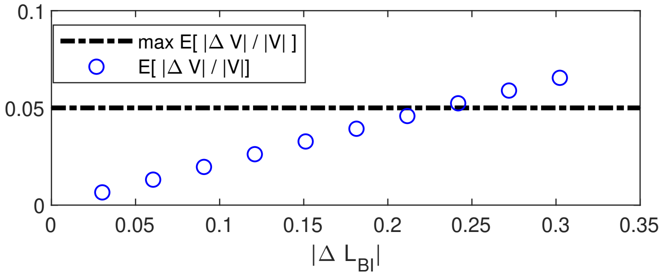

Figure 3.5: Average relative error of velocity ($E[|\Delta \boldsymbol{V}|/|\boldsymbol{V}|]$) versus the attitude estimation error represented by $|\Delta \boldsymbol{L}_{BI}|$. The velocity error grows with the increase of $|\Delta \boldsymbol{L}_{BI}|$.

where $\Delta \boldsymbol{d}_{oa}^B = \hat{\boldsymbol{d}}_{oa}^B - \boldsymbol{d}_{oa}^B$ is the estimation error of $\boldsymbol{d}_{oa}^B$. By substituting $\Delta \boldsymbol{d}_{oa}^B$ and (3.17) into (3.12) and (3.13), we can derive the estimation error of velocities due to the error of the attitude estimation:

$$\Delta \boldsymbol{V}^B = \Delta \boldsymbol{V}_i^B = \boldsymbol{\Omega}_\times^B \Delta \boldsymbol{d}_{oa}^B + \Delta \boldsymbol{L}_{BI} \hat{\boldsymbol{L}}_{BI} (\boldsymbol{V}_o^I - \boldsymbol{V}_w^I) \tag{3.19}$$

Fig. 3.5 demonstrates the average relative error of velocity $E[|\Delta \boldsymbol{V}|/|\boldsymbol{V}|]$ versus the L^2 norm of $\Delta \boldsymbol{L}_{BI}$ using (3.19) where the other variables in (3.19) are from a set of flight data. It is clear that the velocity estimation error grows with the increase of $|\Delta \boldsymbol{L}_{BI}|$.

If we set the maximum velocity relative error as 5%, for example, $|\Delta \boldsymbol{L}_{BI}|$ need to be smaller than 0.22, which is easy to fulfil for most attitude estimators.

5. MODEL IDENTIFICATION

In this section, the aerodynamic model is identified from the preprocessed data. A parametric model is established with model structures predefined in the form of polynomials based on physical insight. Compared with the non-parametric model, the parametric model is less tend to overfit and requires less computational effort. By virtue of these advantages, it has been widely used in the aircraft model identification applications (see, e.g., [18]).

First of all, a simplified model structure of the in-plane forces and the pitch/roll moments of a single is derived. Most of the multi-rotor vehicles employ fixed-pitch rotors with elasticity. Due to the imbalanced lift between the advancing and retreating blades with the existence of airspeed, the tip-path-plane tilts backward and sideways with respect to the air stream. This brings several consequences. First of all, the thrust has a projection on the rotor plane and contributes to the in-plane force [8]. Secondly, due to the resilience of the rotor blade, the pitch and roll moments are generated with respect to the rotor hub [6, 9]. The latter is usually omitted because of the symmetric property of the quadrotor. However, these moments have to be taken in to account with the occurrence of rotor failures.

The identified model is usually valid within the test regime covering the flight data. To improve the validity of the model for extrapolation, the structure should be chosen as simple as possible while capturing the major effects.

For the ith rotor, define a 2-D vector named horizontal advance ratio and its perpendicular vector as

$$\boldsymbol{\mu}_i = [u_i,\ v_i]^T/\omega_i R,\ \ \boldsymbol{\mu}_i^{\perp} = [-v_i,\ u_i]^T/\omega_i R \tag{3.20}$$

Usually $\frac{1}{2}|\boldsymbol{\mu}_i|^2 \ll 1$, then a simple model of the rotor flapping angle can be expressed as [8]

$$\begin{aligned} \boldsymbol{\beta} &= -\boldsymbol{\mu}_i A_{1,c}/(1-\tfrac{1}{2}|\boldsymbol{\mu}_i|^2) \approx -\boldsymbol{\mu}_i A_{1,c} \\ \boldsymbol{\beta}^{\perp} &= -\boldsymbol{\mu}_i^{\perp} s_{n,i} A_{1,s}/(1-\tfrac{1}{2}|\boldsymbol{\mu}_i^{\perp}|^2) \approx -\boldsymbol{\mu}_i^{\perp} s_{n,i} A_{1,s} \end{aligned} \tag{3.21}$$

where $A_{1,c}$ and $A_{1,s}$ are constants. Vectors $\boldsymbol{\beta}$ and $\boldsymbol{\beta}^{\perp}$ contain the information about flapping angles along and perpendicular to the incoming flow. The norms of both vectors indicate the magnitude of the flapping angle as the elements indicate the flapping direction expressed in the $x_B - y_B$ plane.

By assuming that the flapping angles are small and using (3.6), the in-plane forces of the ith rotor due to the blade-flapping effect can be approximated by

$$\begin{bmatrix} F_{x,i} \\ F_{y,i} \end{bmatrix} \approx T_i(\boldsymbol{\beta}+\boldsymbol{\beta}^{\perp}) = C_{t,i}\pi R^3 \rho \omega_i \begin{bmatrix} -A_{1,c}u_i + A_{1,s}s_{n,i}v_i \\ -A_{1,c}v_i - A_{1,s}s_{n,i}u_i \end{bmatrix} \tag{3.22}$$

We assume a constant $C_{t,i}$ for simplicity of the model, then (3.22) can be re-written as

$$\begin{bmatrix} F_{x,i} \\ F_{y,i} \end{bmatrix} = k_1 \begin{bmatrix} u_i \omega_i \\ v_i \omega_i \end{bmatrix} + k_2 \begin{bmatrix} v_i s_{n,i} \omega_i \\ -u_i s_{n,i} \omega_i \end{bmatrix} \tag{3.23}$$

where k_1 and k_2 are parameters to be identified.

The roll/pitch moment of a single rotor can be caused by two major effects: The elastic moment due to the blade flapping [6], and the in-plane force generated moment with respect to the c.g.. Therefore, we assume that the moment aligns with the rotor plan tilted direction and a simplified model structure is selected as

$$\begin{bmatrix} M_{x,i} \\ M_{y,i} \end{bmatrix} = k_3 \begin{bmatrix} -v_i \omega_i \\ u_i \omega_i \end{bmatrix} + k_4 \begin{bmatrix} u_i s_{n,i} \omega_i \\ v_i s_{n,i} \omega_i \end{bmatrix} \tag{3.24}$$

In the high-speed flight, the forces and moments from the airframe become apparent and are modeled as

$$\boldsymbol{F}_f = \frac{1}{2}\rho|\boldsymbol{V}|^2 S[C_x,\ C_y,\ C_z]^T \tag{3.25}$$

$$\boldsymbol{M}_f = \frac{1}{2}\rho|\boldsymbol{V}|^2 Sb[C_l,\ C_m,\ C_n]^T \tag{3.26}$$

where $S = 4lb$ is defined as the reference area; C_x to C_n are modeled as functions of air-velocity of the c.g.. These coefficients need to capture most of the aerodynamic effects on the airframe. Therefore, the model structure of these coefficients are selected as follows. First of all, define the normalized velocities as

$$[\bar{u},\ \bar{v},\ \bar{w}]^T = \frac{[u,\ v,\ w]^T}{\sqrt{u^2+v^2+w^2}} = [\frac{u}{|\boldsymbol{V}|},\ \frac{v}{|\boldsymbol{V}|}\ \frac{w}{|\boldsymbol{V}|}]^T \tag{3.27}$$

To prevent singularity, define

$$[\bar{u},\ \bar{v},\ \bar{w}]^T = [0,\ 0,\ 0]^T, \text{when } |\boldsymbol{V}| = 0 \tag{3.28}$$

Noting that $\bar{w}$ can be analogous to the angle of attack while $\bar{v}$ is analogous to the side-slip angle of a fixed-wing aircraft. Normalizing the velocity could prevent extrapolation of the model and increase its stability.

Then the model structures of these aerodynamic coefficients are selected as follows

$$\begin{bmatrix} C_x \\ C_y \\ C_z \\ C_l \\ C_m \\ C_n \end{bmatrix} = \begin{bmatrix} \operatorname{sgn}(\bar{u})\left[|\bar{u}|,\ \bar{u}^2\right]\boldsymbol{K_x} \\ \operatorname{sgn}(\bar{v})\left[|\bar{v}|,\ \bar{v}^2\right]\boldsymbol{K_y} \\ \operatorname{sgn}(\bar{w})\left[|\bar{w}|,\ \bar{w}^2\right]\boldsymbol{K_z} \\ \operatorname{sgn}(\bar{v})[|\bar{v}|,\ \bar{v}^2,\ |\bar{v}|\bar{w},\ |\bar{v}|^3,\ \bar{v}^2\bar{w},\ |\bar{v}|\bar{w}^2]\boldsymbol{K_l}/b \\ \operatorname{sgn}(\bar{u})[|\bar{u}|,\ \bar{u}^2,\ |\bar{u}|\bar{w},\ |\bar{u}|^3,\ \bar{u}^2\bar{w},\ |\bar{u}|\bar{w}^2]\boldsymbol{K_m}/b \\ \operatorname{sgn}(\bar{u})\operatorname{sgn}(\bar{v})[|\bar{v}|,\ \bar{v}^2,\ |\bar{v}|\bar{u},\ |\bar{v}|^3,\ \bar{v}^2\bar{u},\ |\bar{v}|\bar{u}^2]\boldsymbol{K_n}/b \end{bmatrix} \tag{3.29}$$

$$= \mathbf{P}\left[\boldsymbol{K_x}^T,\ \boldsymbol{K_y}^T,\ \boldsymbol{K_z}^T,\ \boldsymbol{K_l}^T,\ \boldsymbol{K_m}^T,\ \boldsymbol{K_n}^T\right]^T$$

where $\boldsymbol{K_x}$ to $\boldsymbol{K_n}$ are arrays of parameters to identify. This model structure is selected to capture the major aerodynamic effects while minimizing the number of terms in the model to facilitate estimation. For instance, the C_x is found to be mostly affected by u and should be zero while the drone is conducting vertical ($\bar{w} = \pm 1,\ \bar{u} = \bar{v} = 0$) and sidewards ($\bar{v} = \pm 1,\ \bar{u} = \bar{w} = 0$) maneuvers. Therefore, C_x model is selected as a second order polynomial of $\bar{u}$. Similarly, C_m is known to be affected by the angle of attack and side-slip angle [20]. Then we use $\bar{w}$ and $\bar{u}$ to capture the effect of these angles, and at the same time, guarantee that the pitch moment should be zero while doing vertical and sideways maneuvers. To cope with the symmetry of the drone, the absolute value of $\bar{u}$ and the sign function $\operatorname{sgn}(\cdot)$ are implemented. The model structure information is then summarized in the matrix $\mathbf{P}$ in (3.29).

Consequently, substituting (3.23)-(3.26) and (3.29) into (3.4) yields a model that is linear in parameters

$$\boldsymbol{Y} = \boldsymbol{A}\boldsymbol{K} + \boldsymbol{\epsilon} \tag{3.30}$$

where $\boldsymbol{\epsilon}$ is the model residual, and $\boldsymbol{A}$, $\boldsymbol{K}$ and $\boldsymbol{Y}$ are given in (3.31). Note that T_i and $M_{z,i}$ in $\boldsymbol{Y}$ are not measured but calculated from the static test obtained model using (3.6) and (3.7).

$$\boldsymbol{A} = \left[\begin{array}{llll:l} \sum u_i\omega_i & \sum v_i s_{n,i}\omega_i & 0 & 0 & \\ \sum v_i\omega_i & -\sum u_i s_{n,i}\omega_i & 0 & 0 & \\ 0 & 0 & 0 & 0 & \\ 0 & 0 & -\sum v_i\omega_i & \sum s_{n,i}u_i\omega_i & \frac{1}{2}\rho|\boldsymbol{V}|^2 S\,\mathbf{P} \\ 0 & 0 & \sum u_i\omega_i & \sum s_{n,i}v_i\omega_i & \\ \sum(bs_{l,i}u_i + ls_{m,i}v_i)\omega_i & \sum(bs_{l,i}v_i - ls_{m,i}u_i)s_{n,i}\omega_i & 0 & 0 & \end{array}\right],$$

$$\begin{gathered} \boldsymbol{Y} = [F_x,\ F_y,\ F_z + \sum T_i,\ M_x - \sum s_{l,i}bT_i,\ M_y - \sum s_{n,i}lT_i,\ M_z - \sum M_{z,i}]^T, \\ \boldsymbol{K} = [k_1,\ k_2,\ k_3,\ k_4,\ \boldsymbol{K_x}^T,\ \boldsymbol{K_y}^T,\ \boldsymbol{K_z}^T,\ \boldsymbol{K_l}^T,\ \boldsymbol{K_m}^T,\ \boldsymbol{K_n}^T]^T \end{gathered} \tag{3.31}$$

With N measurement samples, the regressor matrix $\mathbf{A}$ and the total output $\boldsymbol{Z}$ are defined as

$$\boldsymbol{G} = [\boldsymbol{A}_1^T, \ldots,\ \boldsymbol{A}_N^T]^T,\ \boldsymbol{Z} = [\boldsymbol{Y}_1^T, \ldots \boldsymbol{Y}_N^T]^T \tag{3.32}$$

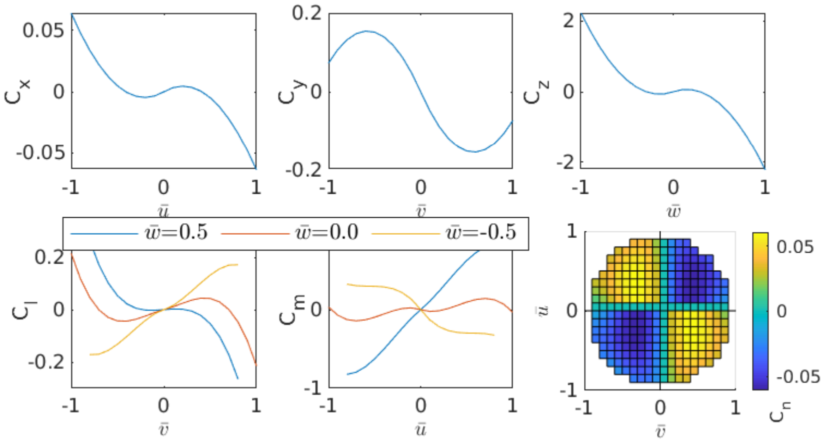

Figure 3.6: The aerodynamic coefficients model of the airframe identified from the flight data.

Since the forces and moments have different orders of magnitude, a weight least square (WLS) estimator is applied:

$$\boldsymbol{K} = (\boldsymbol{G}^T \boldsymbol{W} \boldsymbol{G})^{-1} \boldsymbol{G}^T \boldsymbol{W} \boldsymbol{Z} \tag{3.33}$$

The weighting matrix is select to be

$$\boldsymbol{W} = \mathrm{diag}(\overbrace{1,1,1,200,200,200,...,1,1,1,200,200,200}^{N\times 6}) \tag{3.34}$$

which indicates that the moments measurements have larger weighting because of their smaller magnitude compared to the forces.

The key parameters in the model are listed in Appendix of this Chapter. Based on (3.23) and (3.24), apart from the in-plane force along the coming flow, there exists a force that is right side perpendicular to the coming flow. A pitch up moment and a roll moment to the left are also generated. Fig. 3.6 presents the aerodynamic coefficients of the airframe. The force related coefficients are negatively related to the normalized speeds, which is in line with the physics view. In addition, the moment models present aerodynamic instabilities of the airframe. For instance, the pitch up moment grows with the increase of angle of attack.

6. MODEL VALIDATION

Several sets of flight data in SRF and norminal configurations are compared with the preceding model to show its validity. Note that these data are independent from those used for model estimation. For comparison, a commonly used lumped parameters model ([7, 19]), in combine with the T_i and $M_{z,i}$ model obtained during the static wind tunnel test of this research, is introduced as the benchmark

$$\begin{gathered} F_x = c_1 u + c_2 u^2,\ F_y = c_3 v + c_4 v^2,\ F_z = -\sum T_i, \\ M_x = \sum b s_{l,i} T_i + c_5 p^2,\ M_y = \sum l s_{m,i} T_i + c_6 q^2, \\ M_z = \sum M_{z,i} + c_7 r^2 \end{gathered} \tag{3.35}$$

where c_1-c_7 are constants, T_i and $M_{z,i}$ are obtained from (3.6) and (3.7) using the rotor C_t and C_q data obtained from the static wind tunnel test.

Case 1: One set of flight data with SRF configuration is used for validating the aerodynamic forces/moments. In this flight, the left-back rotor (rotor 4) is removed and the drone spins at the yaw rate $r \approx -20$ rad/s. Fig. 3.7 presents the aerodynamic predictions using two models, together with their normalized root mean square error (NRMS). Both models perform well at $V = 2$ m/s whereas the proposed model performs better at $V = 8$ m/s when aerodynamic effects become apparent.

Case 2: Define the lateral force perpendicular to the free stream as

$$F_{\text{lateral}} = [0,\ 1,\ 0]\boldsymbol{L}_{IB}[F_x,\ F_y, 0]^T \tag{3.36}$$

Noting that $F_{\text{lateral}} = 0$ for NF case with zero side-slip. However, as was observed in a previous research [16], this lateral force is non-zero for the spinning quadrotor with single rotor failure.

The direction of this lateral force is also correlated to the yaw rate direction. Specifically, a positive yaw rate ($r > 0$) leads to a lateral force towards the right with respect to the flight direction; a negative yaw rate could lead to a force to the left. This is probably due to the speed up of the rotor behind the airframe with respect to the air stream that brings larger in-plane force than the other rotors. Fig. 3.8 compares the measured F_{lateral} and both the proposed model and the benchmark, together with trend lines illuminating the model performance. It is obvious that the proposed model can well predict this effect, while the lateral force can be hardly captured by the benchmark model.

Case 3: Apart from the cases with rotor failures, the model also needs to be effective for the quadrotor in the no-failure configuration. This is validated by calculating the longitudinal trim curve using the models and comparing with the measurement. The longitudinal trim curve of a quadrotor was defined in [21] as the rotor speeds and the pitch angle during the level flight at different airspeed. The trim curve reveals that the rear rotors should rotate faster than front rotors during the forward flight. As Fig. 3.9 shows, the proposed model can capture this effect and fit the measured data in the whole range of airspeed, despite slight mismatch at 2 - 8 m/s. In comparison, this distinction cannot be captured by the benchmark model, and the data fitting is unsatisfactory.

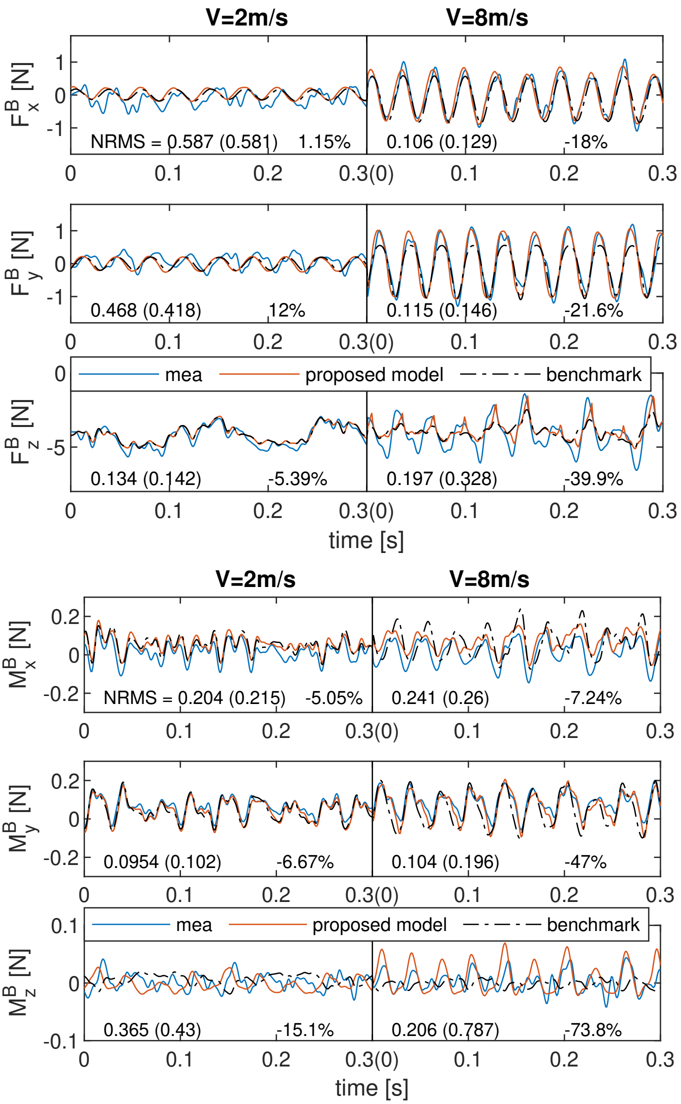

Figure 3.7: Validation result of $\boldsymbol{F}^B$ and $\boldsymbol{M}^B$ with the SRF configuration at the airspeed of 2 m/s and 8 m/s. The normalized RMS (NRMS) is given for both the proposed model and the benchmark model (in parentheses), together with the percentage change of the NRMS.

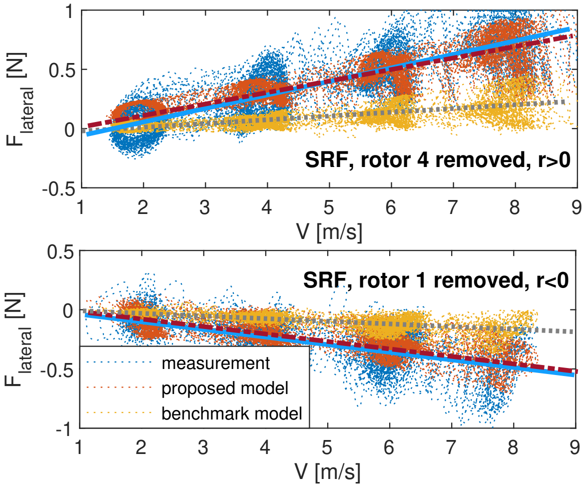

Figure 3.8: Aerodynamic force perpendicular to the air velocity (considered positive to the right with respect to the air velocity). Comparison among the measurement (blue), the proposed model (red) and the benchmark model (yellow), of which trend lines are given in blue-solid, red-dash-dot and gray-dot respectively.

7. CONCLUSIONS

In this research, the aerodynamic force/moment model of a quadrotor has been identified in the high-speed flight regime. A multi-body parametric model is selected to balance between accuracy and simplicity, and the model is versatile to fit different flight conditions. To cope with fast spinning motion in rotor failure configurations, a novel correction method for specific force and velocity measurements has been developed considering the location mismatch among IMU, c.g. and the reference point of the motion capturing system. The proposed model has been validated in both nominal cases and with rotor failures. The comparison also shows advantages with respect to the lumped parameters benchmark model, particularly in the high-speed flight regime.

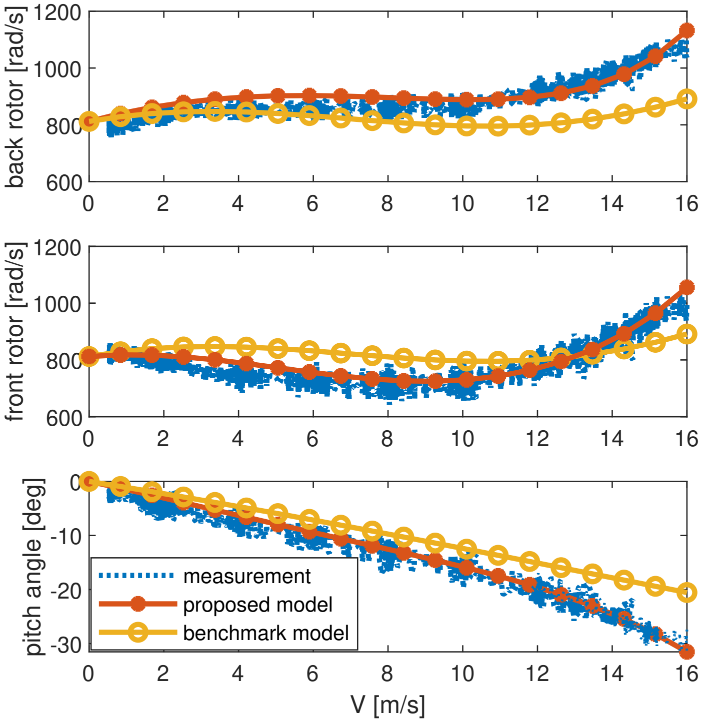

Figure 3.9: Rotor speeds and pitch angle during the level forward flight at different flight speeds with the nominal configuration. Comparison between the model prediction and the flight data.

APPENDIX

The parameters of the proposed model for a Bebop2 quadrotor are given as follows. Readers may access the model in MATLAB script via `https://bitbucket.org/SihaoSun/bebop2_aerodynamic_model`. The model is valid when the airspeed $V \in [0,\ 16]$ m/s. Model beyond this range may have deficient accuracy.

$$
\begin{aligned}
[k_1,\ k_2,\ k_3,\ k_4] &= [-3.96,\ 2.29,\ 0.464, -0.0966] \times 10^{-5} \\
\boldsymbol{K_x} &= [3.00, -8.92]^T \times 10^{-2} \\
\boldsymbol{K_y} &= [-0.509,\ 0.400]^T \\
\boldsymbol{K_z} &= [0.838, -2.85]^T \\
\boldsymbol{K_l} &= [1.17, -0.0498,\ 1.69, -2.65,\ 6.24, -4.57]^T \times 10^{-2} \\
\boldsymbol{K_m} &= [-8.46,\ 27.6,\ 10.2, -19.4,\ 3.62,\ 1.98]^T \times 10^{-2} \\
\boldsymbol{K_n} &= [-3.07,\ 7.59, -1.34, -4.51,\ 1.55, -0.572]^T \times 10^{-2} \\
\boldsymbol{K}_{Ct} &= [\ 0.0156,\ -0.0552,\ 0.684,\ -2.24,\ 3.05, -1.52, \\
&\quad -0.0145,\ 0.457,\ -0.525,\ 0.233,\ -0.0258,\ 0.0401, \\
&\quad -0.0116,\ -0.00223,\ -0.0225,\ 0.00336]^T \\
\boldsymbol{K}_{Cq} &= [\ -0.00227, -0.00113,\ 0.00368, -0.101,\ 0.226, \\
&\quad -0.146, -0.00305, -0.00748, -0.111,\ 0.121,\ 0.00336, \\
&\quad 0.00363, -0.00729,\ 0.00116,\ 0.00257, -0.000681]^T
\end{aligned}
$$

REFERENCES

[1] S. Waslander and C. Wang, *Wind disturbance estimation and rejection for quadrotor position control,* in *AIAA Infotech@ Aerospace conference and AIAA unmanned Unlimited conference* (2009) p. 1983.

[2] S. Kim, D. Falanga, and D. Scaramuzza, *Computing the Forward Reachable Set for a Multirotor Under First-Order Aerodynamic Effects,* IEEE Robotics and Automation Letters **3**, 2934 (2018).

[3] T. Carroll, I.-R. E. George, and G. Bramesfeld, *Design optimization of small rotors in quad-rotor configuration,* in *54th AIAA Aerospace Sciences Meeting* (2016) p. 1788.

[4] H. Huang, G. Hoffmann, S. Waslander, and C. Tomlin, *Aerodynamics and control of autonomous quadrotor helicopters in aggressive maneuvering,* in *2009 IEEE International Conference on Robotics and Automation* (IEEE, 2009) pp. 3277–3282.

[5] G. Hoffmann, H. Huang, S. Waslander, and C. Tomlin, *Quadrotor helicopter flight dynamics and control: Theory and experiment,* in *AIAA guidance, navigation and control conference and exhibit* (2007) p. 6461.

[6] G. M. Hoffmann, H. Huang, S. L. Waslander, and C. J. Tomlin, *Precision flight*

control for a multi-vehicle quadrotor helicopter testbed, Control Engineering Practice **19**, 1023 (2011).

[7] M. Schulz, F. Augugliaro, R. Ritz, and R. D'Andrea, *High-speed, steady flight with a quadrocopter in a confined environment using a tether,* in *2015 IEEE/RSJ International Conference on Intelligent Robots and Systems (IROS)* (IEEE, 2015) pp. 1279–1284.

[8] R. Mahony, V. Kumar, and P. Corke, *Multirotor Aerial Vehicles: Modeling, Estimation, and Control of Quadrotor,* IEEE Robotics & Automation Magazine **19**, 20 (2012).

[9] P. Bristeau, P. Martin, E. Salaun, and N. Petit, *The role of propeller aerodynamics in the model of a quadrotor UAV,* in *2009 European Control Conference (ECC)* (IEEE, 2009) pp. 683–688.

[10] C. R. Russell, J. Jung, G. Willink, and B. Glasner, *Wind tunnel and hover performance test results for multicopter uas vehicles,* (2016).

[11] S. Sun, C. C. de Visser, and Q. Chu, *Quadrotor gray-box model identification from high-speed flight data,* Journal of Aircraft **56**, 645 (2019).

[12] M. Burri, J. Nikolic, H. Oleynikova, M. W. Achtelik, and R. Siegwart, *Maximum likelihood parameter identification for mavs,* in *2016 IEEE International Conference on Robotics and Automation (ICRA)* (IEEE, 2016) pp. 4297–4303.

[13] J. Svacha, K. Mohta, and V. Kumar, *Improving quadrotor trajectory tracking by compensating for aerodynamic effects,* in *2017 International Conference on Unmanned Aircraft Systems (ICUAS)* (IEEE, 2017) pp. 860–866.

[14] J.-M. Kai, G. Allibert, M.-D. Hua, and T. Hamel, *Nonlinear feedback control of quadrotors exploiting first-order drag effects,* IFAC-PapersOnLine **50**, 8189 (2017).

[15] D. Kaya and A. T. Kutay, *Aerodynamic modeling and parameter estimation of a quadrotor helicopter,* in *AIAA Atmospheric Flight Mechanics Conference* (2014) p. 2558.

[16] S. Sun, L. Sijbers, X. Wang, and C. de Visser, *High-speed flight of quadrotor despite loss of single rotor,* IEEE Robotics and Automation Letters **3**, 3201 (2018).

[17] *TDK invensense MPU-6050,* `https://www.invensense.com/products/motion-tracking/6-axis/mpu-6050/`, accessed: 2010-09-30.

[18] E. A. Morelli and V. Klein, *Aircraft system identification: theory and practice* (Sunflyte Enterprises Williamsburg, VA, 2016).

[19] M. W. Mueller and R. D'Andrea, *Relaxed hover solutions for multicopters: Application to algorithmic redundancy and novel vehicles,* The International Journal of Robotics Research **35**, 873 (2016).

[20] J. V. Foster and D. Hartman, *High-fidelity multi-rotor unmanned aircraft system (uas) simulation development for trajectory prediction under off-nominal flight dynamics,* in *17th AIAA Aviation Technology, Integration, and Operations Conference* (2017) p. 3271.

[21] S. Sun and C. C. de Visser, *Quadrotor safe flight envelope prediction in the high-speed regime: A monte-carlo approach,* in *AIAA Scitech 2019 Forum* (2019) p. 0948.

4

HIGH-SPEED FLIGHT OF QUADROTOR DESPITE LOSS OF A SINGLE ROTOR

In this chapter, a multi-loop hybrid nonlinear controller is designed to achieve high-speed flight of a damaged quadrotor with complete loss of a single rotor. By fully making use of sensor measurements, the model dependency of this control method is reduced, which is conducive to handling disturbance from unknown aerodynamic effects. This controller is tested on a quadrotor vehicle with one rotor completely removed in the high-speed condition. Free flights are performed in the Open Jet Facility (OJF), a large-scale wind tunnel. Over 9 m/s flight speed is reached for the damaged quadrotor in these tests. In addition, several high-speed spin-induced aerodynamic effects are discovered and analyzed.

Parts of this chapter have been published in:

S. Sun, L. Sijbers, X. Wang, and C. de Visser, "High-Speed Flight of Quadrotor Despite Loss of a Single Rotor," IEEE Robotics and Automation Letters., vol. 3, no. 4, pp. 3201–3207, Oct. 2018.

1. INTRODUCTION

Multi-rotor aerial robots have the potential to be widely used in outdoor environments such as package delivery, construction monitoring, fire protection, etc. In these circumstances, vehicles usually operate in high-speed conditions where aerodynamic effects become apparent. On the other hand, owing to their task importance and safety regards, there are large demands on their ability to tolerate structural and sensor faults during the mission. To improve their resilience under both fault cases and high-speed flight conditions is a central concern for future applications.

Among these multi-rotor drones, the quadrotor excels in its structural simplicity and has been found to be more energy efficient as a delivery tool [1]. However, without actuator redundancy, this kind of vehicle suffers most from actuator failures. Several literature sources have proposed fault-tolerant controllers in terms of actuator failures for a quadrotor. Most researchers discussed the problem with partial actuator failure in the scheme of robust control or adaptive control by regarding failures as model uncertainties [2–5].

Cases in which rotors are entirely missing have been discussed as well. Lanzon et al. revealed that the damaged quadrotor can be stabilized after giving up yaw control and spins around a certain axis [6]. Lippiello et al. used a strategy that transformed a damaged quadrotor into a bi-rotor after which the backstepping and PID controllers were applied [7, 8]. Lu and van Kampen proposed a three loop controller using nonlinear control methods in conjunction with an active diagnose module [9]. Above algorithms were only validated in simulations. Mueller and D'Andrea came up with a relaxed hovering solution about which the quadrotor can be stabilized using a linear control method [10, 11], such as Linear Quadratic Regulator (LQR). This control scheme has been validated in real flight tests.

Above controllers were tested in the simulation environment or low-speed flight conditions. However, critical faults such as complete loss of efficiency in an actuator could occur while the quadrotor is cruising at high speeds at which aerodynamic effects are non-negligible. Fault-tolerant control of a severely damaged quadrotor in these circumstances has not been researched to the best of our knowledge.

The main contribution of this research is revealing the possibility of continuing high-speed cruising flight instead of a forced landing of a quadrotor of which one actuator has completely failed. A 3-loop nonlinear controller, which was initially proposed in [9], is improved in this research to achieve high-speed flight in the wind tunnel. The main feature of this cascaded controller is the usage of Incremental Nonlinear Dynamic Inversion (INDI) control in the inner loop, of which robustness to external disturbances and model uncertainties has been verified both theoretically [12] and practically [13, 14]. By virtue of the reduced model dependency of this sensor-based nonlinear controller, no model based relaxed equilibrium solutions [10] are needed and the designing process can be simplified.

Fast forward flight tests with speeds of over 9 m/s (approximately 50% of the nominal quadrotor maximum speed) have been achieved in the wind tunnel as

Figure 4.1: Figure of Open Jet Facility and the spinning quadrotor during flight.

Fig. 4.1 shows. For the first time, this has allowed systematic flight test experiments in regions of the flight envelope that have not been reachable using existing controllers. This, in turn, has led to the discovery of new high-speed spin-induced aerodynamics effects that when harnessed correctly could further improve the performance of a damaged quadrotor.

This chapter is organized as follows: Section 2 introduces the dynamic model of quadrotors. Section 3 provides the procedure of controller design. Section 4 validates the controller in a low-speed flight. High-speed flight test and analyses of aerodynamic effects are given in Section 5.

2. MODEL DESCRIPTION

The inertial frame, denoted by $\mathscr{F}_I$, is defined as the reference coordinate system fixed to the ground. x_I, y_I point along and perpendicular to the wind flow respectively; z_I points to the ground. The tested quadrotor in this research is Parrot Bebop2 shown in Fig. 4.2. The body frame is defined fixed to the quadrotor with x_B pointing forward, y_B pointing right and z_B is the opposite of the thrust vector. For notational simplicity, the superscript 'B'and 'I' indicate the coordinate system on which the vector is projected; the subscripts 'x', 'y' and 'z' indicate the components of a 3 dimensional vector.

As shown in Fig. 4.2, ω_{1-4} denote rotor speeds with respect to $\mathscr{F}_B$; b and l are geometric parameters.

The equations of motion of a quadrotor based on six-dimensional rigid body dynamics is given as [15]

$$\dot{\boldsymbol{\xi}} = \boldsymbol{v} \tag{4.1}$$

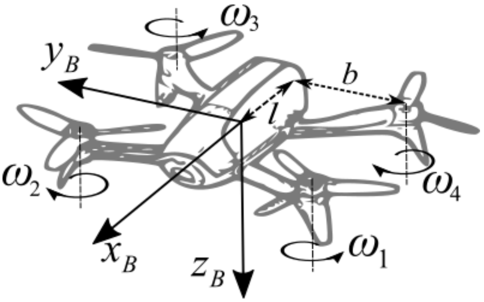

Figure 4.2: Body-fixed frame definition and graphic of Parrot Bebop2.

$$m\dot{\boldsymbol{v}} = m\boldsymbol{g} + \boldsymbol{L_{IB}}\boldsymbol{F} \tag{4.2}$$

$$\dot{\boldsymbol{L}}_{\boldsymbol{IB}} = \boldsymbol{L_{IB}}\tilde{\boldsymbol{\Omega}} \tag{4.3}$$

$$\boldsymbol{I_v}\dot{\boldsymbol{\Omega}} = -\tilde{\boldsymbol{\Omega}}\boldsymbol{I_v}\boldsymbol{\Omega} + \boldsymbol{M} \tag{4.4}$$

where $\boldsymbol{\xi}$, $\boldsymbol{v}$ indicate position and velocity respectively. $\boldsymbol{\Omega} = [p \quad q \quad r]^T$ represents the angular rate of quadrotor. The tilde superscript indicates the cross product (i.e. $\tilde{\boldsymbol{\Omega}}\boldsymbol{I_v} = \boldsymbol{\Omega} \times \boldsymbol{I_v}$). m and $\boldsymbol{I_v}$ denote mass and inertia of the vehicle. $\boldsymbol{L_{IB}}$ is the rotation matrix from $\mathscr{F}_B$ to $\mathscr{F}_I$. $\boldsymbol{g}$ is the gravity vector. $\boldsymbol{F}$ and $\boldsymbol{M}$ represent the resultant force and moment acting on the quadrotor, including the control force and moment generated by rotors.

Without loss of generality, we assume the left back rotor (ω_4) is removed and define the control input $\boldsymbol{u}$ as

$$\boldsymbol{u} = [\omega_1^2 \quad \omega_2^2 \quad \omega_3^2]^T \tag{4.5}$$

Therefore, a general expression of the resultant force and moment can be [16]

$$\boldsymbol{F} = \boldsymbol{F}_a + \boldsymbol{G_F}\boldsymbol{u} \tag{4.6}$$

$$\boldsymbol{M} = \boldsymbol{M}_a + \boldsymbol{M}_g + \boldsymbol{G_M}\boldsymbol{u} \approx \boldsymbol{M}_a + \boldsymbol{G_M}\boldsymbol{u} \tag{4.7}$$

where $\boldsymbol{M}_g$ is the rotor induced gyroscopic moment and is found to be negligible. $\boldsymbol{F_a}$ and $\boldsymbol{M_a}$ indicate the external aerodynamic force and moment which are influenced by the airspeed, aerodynamic angles, angular rates, and complex interaction effects that are difficult to model accurately. In static hovering, $\boldsymbol{F_a}$ and $\boldsymbol{M_a}$ can be neglected and subsequently (5.5) and (5.6) become linear.

The expressions of the constant matrix $\boldsymbol{G_F}$ and $\boldsymbol{G_M}$ are

$$\boldsymbol{G_F} = \begin{bmatrix} 0 & 0 & 0 \\ 0 & 0 & 0 \\ in-\kappa_0 & -\kappa_0 & -\kappa_0 \end{bmatrix}, \ \boldsymbol{G_M} = \begin{bmatrix} b\kappa_0 & -b\kappa_0 & -b\kappa_0 \\ l\kappa_0 & l\kappa_0 & -l\kappa_0 \\ \tau_0 & -\tau_0 & \tau_0 \end{bmatrix} \tag{4.8}$$

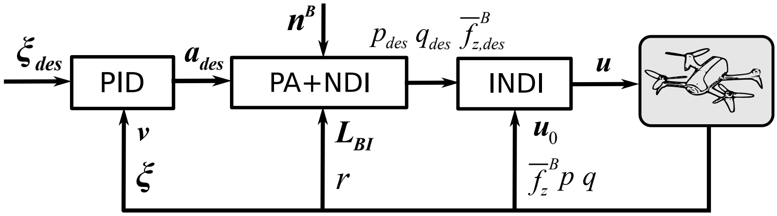

Figure 4.3: Control structure of the three-loop nonlinear controller.

where κ_0 and τ_0 are force and torque coefficients respectively and can be identified using hovering flight data.

3. CONTROLLER DESIGN

A three loop controller is designed to achieve position control based on the time scale-separation assumption. Fig. 4.3 illustrates the controller which includes a position control loop using PID method, an attitude control loop using the primary-axis Nonlinear Dynamic Inversion (PA+NDI) and a control allocation loop using the Incremental Nonlinear Dynamic Inversion (INDI) method.

3.1. POSITION CONTROL LOOP

The outer loop is a PID controller using acceleration as virtual input

$$\begin{aligned}\boldsymbol{a_{des}} = k_p(\boldsymbol{\xi_{des}} - \boldsymbol{\xi}) + k_d(\dot{\boldsymbol{\xi}}_{\boldsymbol{des}} - \boldsymbol{v}) + k_i \int(\boldsymbol{\xi_{des}} - \boldsymbol{\xi})dt,\\ (k_p,\ k_d,\ k_i > 0)\end{aligned} \tag{4.9}$$

The addition of integral term will compensate the constant bias brought by aerodynamic drag.

3.2. PRIMARY-AXIS ATTITUDE CONTROL LOOP

A primary-axis based attitude loop controller is designed in this section to calculate the desired angular rates p_{des} and q_{des} from $\boldsymbol{a_{des}}$.

After the removal of a single rotor, the quadrotor subsequently spins around a certain axis due to the fact that the yawing moment balance is broken [6]. The primary axis, denoted by $\boldsymbol{n}$, was introduced in [11] and defined as a unit vector about which the damaged quadrotor rotates and points at the average thrust direction in the relaxed hover solution [10]. This vector is fixed to the body frame $\mathscr{F}_B$ and can be chosen arbitrarily. If $\boldsymbol{n}$ is designed to be aligned with the instant thrust direction ($n^B_x = n^B_y = 0$) as shown in Fig. 4.4a, the drone spins without wobbling. An alternative way is letting $n^B_x, n^B_y > 0$ which is more energy efficient for the drone with the left back rotor removed [11], and the drone wobbles consequently as Fig. 4.4b shows. In addition, the following constraint should be imposed

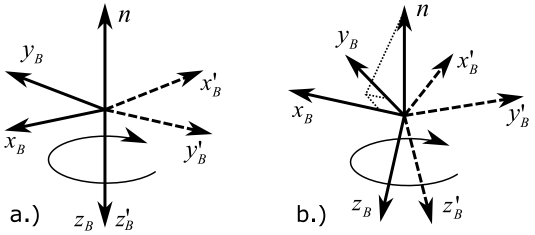

Figure 4.4: a.) $\boldsymbol{n}$ is aligned with the instant thrust direction ($\boldsymbol{n}^B = [0\ 0\ -1]^T$). b.) $\boldsymbol{n}$ is not parallel with the instant thrust direction and the drone wobbles consequently ($\boldsymbol{n}^B \neq [0\ 0\ -1]^T$).

$$-n_z^B \geq m||\boldsymbol{g}||/T_{max} \tag{4.10}$$

where T_{max} denotes the available total thrust.

The task of the attitude controller is to align the direction of the primary axis $\boldsymbol{n}$ with the desired acceleration $\boldsymbol{a_{des}}$. To this end, a normalized vector pointing at a desired specific force direction is defined as $\boldsymbol{n_{des}}$ and is calculated by

$$\boldsymbol{n_{des}} = \frac{\boldsymbol{a_{des}} - \boldsymbol{g}}{||\boldsymbol{a_{des}} - \boldsymbol{g}||} \tag{4.11}$$

The expression of $\boldsymbol{n_{des}}$ in $\mathscr{F}_I$ is denoted by $\boldsymbol{n^I_{des}}$ and similarly, superscript B indicates the vector expressed in $\mathscr{F}_B$. The main idea of this attitude control loop is to let $\boldsymbol{n^B_{des}}$ track $\boldsymbol{n^B}$ by manipulating quadrotor angular rates. A nonlinear dynamic inversion (NDI) method is used to achieve this tracking, by taking the derivative of $\boldsymbol{n^B_{des}}$, we have

$$\begin{aligned} \boldsymbol{\dot{n}^B_{des}} &= d(\boldsymbol{L_{BI}} \boldsymbol{n^I_{des}})/dt \\ &= \boldsymbol{\dot{L}_{BI}} \boldsymbol{n^I_{des}} + \boldsymbol{L_{BI}} \boldsymbol{\dot{n}^I_{des}} \\ &= -\boldsymbol{\tilde{\Omega}} \boldsymbol{n^B_{des}} + \boldsymbol{L_{BI}} \boldsymbol{\dot{n}^I_{des}} \\ &= \boldsymbol{\tilde{n}^B_{des}} \boldsymbol{\Omega} + \boldsymbol{L_{BI}} \boldsymbol{\dot{n}^I_{des}} \end{aligned} \tag{4.12}$$

For notational simplicity, we define

$$\boldsymbol{n^B_{des}} = [h_1 \quad h_2 \quad h_3]^T \tag{4.13}$$

thus (4.12) can be expanded as

$$\begin{bmatrix} \dot{h}_1 \\ \dot{h}_2 \\ \dot{h}_3 \end{bmatrix} = \begin{bmatrix} 0 & -h_3 & h_2 \\ h_3 & 0 & -h_1 \\ -h_2 & h_1 & 0 \end{bmatrix} \begin{bmatrix} p \\ q \\ r \end{bmatrix} + \boldsymbol{L_{BI}} \boldsymbol{\dot{n}^I_{des}} \tag{4.14}$$

Since the matrix $\boldsymbol{\tilde{n}^B_{des}}$ is singular and cannot be inverted, a subsystem $[h_1 \quad h_2]^T$

is to be stabilized. This is similar to the process introduced in [9], whereas the $\boldsymbol{n}^{\boldsymbol{B}}_{\boldsymbol{des}} = [h_1 \quad h_2 \quad h_3]^T$ is defined as the state and the primary axis $\boldsymbol{n}^{\boldsymbol{B}} = [n^B_x \quad n^B_y \quad n^B_z]^T$ is defined as reference in our method. This distinction is important since the original method shows inability to stabilize the drone due to measurement noise and model uncertainty in the experiment. Note that $\sqrt{h_1^2 + h_2^2 + h_3^2} = 1$, therefore an accurate tracking of h_1 and h_2 to their reference value (the first two components of $\boldsymbol{n}^{\boldsymbol{B}}$) will also guarantee the tracking of h_3. Thus a subspace system is separated from (4.14) yielding

$$\begin{bmatrix} \dot{h}_1 \\ \dot{h}_2 \end{bmatrix} = \begin{bmatrix} 0 & -h_3 \\ h_3 & 0 \end{bmatrix} \begin{bmatrix} p \\ q \end{bmatrix} + \begin{bmatrix} h_2 \\ -h_1 \end{bmatrix} r + \hat{\dot{\boldsymbol{n}}}^{\boldsymbol{I}}_{\boldsymbol{des}} \tag{4.15}$$

where $\hat{\dot{\boldsymbol{n}}}^{\boldsymbol{I}}_{\boldsymbol{des}}$ is composed of the x and y component of $\boldsymbol{L_{BI}} \dot{\boldsymbol{n}}^{\boldsymbol{I}}_{\boldsymbol{des}}$.

Now, replace the left-hand side of (4.15) by the virtual input $\boldsymbol{\nu_{out}}$, we have

$$\begin{bmatrix} p_{des} \\ q_{des} \end{bmatrix} = \begin{bmatrix} 0 & 1/h_3 \\ -1/h_3 & 0 \end{bmatrix} \left(\boldsymbol{\nu_{out}} - \begin{bmatrix} h_2 \\ -h_1 \end{bmatrix} r - \hat{\dot{\boldsymbol{n}}}^{\boldsymbol{I}}_{\boldsymbol{des}} \right) \tag{4.16}$$

where

$$\boldsymbol{\nu_{out}} = \begin{bmatrix} \dot{n}^B_x + k_x(n^B_x - h_1) \\ \dot{n}^B_y + k_y(n^B_y - h_2) \end{bmatrix} \qquad (k_x, k_y > 0) \tag{4.17}$$

Note that $\dot{n}^B_x$ and $\dot{n}^B_y$ are zero since the primary axis is fixed to the vehicle.

In the attitude controller (4.16), only pitch and roll rate are assigned (p_{des} and q_{des}). The yaw rate r is measured on-board and used as a state information for the controller. This property is essential for achieving high speed flight because the yaw rate is found to vary with the flight speed and the heading angle as Section 5 shows. It is worth noting that a nominal drone with zero or small yaw rate may also use this method in conjunction with an individual yaw controller.

The magnitude of the desired acceleration should be determined by thrust which is computed using the same method introduced in [10].

$$n^B_z \bar{f}^B_{z,des} \boldsymbol{n_{des}} = \boldsymbol{a_{des}} - \boldsymbol{g} \tag{4.18}$$

where $\bar{f}^B_{z,des} = -T_{des}/m$ indicates the desire specific force on the z_B.

3.3. CONTROL ALLOCATION LOOP

The control allocation loop converts p_{des}, q_{des} and $\bar{f}^B_{z,des}$ to the rotor speed commands. With the existence of both fast spinning and high speed inflow, the aerodynamic effects significantly influence the rotational dynamics of the quadrotor [16]. Since the moment from the aerodynamics (the abovementioned $\boldsymbol{M}_a$) is difficult to model, a model based control allocation method may be impractical. On the other hand, the Incremental Nonlinear Dynamic Inversion (INDI) method is applicable to this problem [12, 13]. Consider a general system $\dot{\boldsymbol{x}} = \boldsymbol{f}(\boldsymbol{x}, \boldsymbol{u})$ with the output $\boldsymbol{y} = \boldsymbol{Cx}$.

Then the dynamics of the output $\boldsymbol{y}$ can be expressed in an incremental form as

$$\begin{aligned}\dot{\boldsymbol{y}} &= \boldsymbol{C}\dot{\boldsymbol{x}} = \boldsymbol{C}\boldsymbol{f}(\boldsymbol{x},\boldsymbol{u}) \\ &= \boldsymbol{C}\dot{\boldsymbol{x}}_{\mathbf{0}} + \boldsymbol{C}\frac{\partial \boldsymbol{f}}{\partial \boldsymbol{x}}\Big|_{\mathbf{0}}\Delta\boldsymbol{x} + \boldsymbol{C}\frac{\partial \boldsymbol{f}}{\partial \boldsymbol{u}}\Big|_{\mathbf{0}}\Delta\boldsymbol{u} + \boldsymbol{C}\mathcal{O}(\Delta\boldsymbol{x}^2,\Delta\boldsymbol{u}^2) \\ &= \dot{\boldsymbol{y}}_{\mathbf{0}} + \hat{\boldsymbol{G}}\Delta\boldsymbol{u} + \boldsymbol{\epsilon}\end{aligned} \tag{4.19}$$

where $\Delta\boldsymbol{x} = \boldsymbol{x} - \boldsymbol{x}_{\mathbf{0}}$, $\Delta\boldsymbol{x} = \boldsymbol{u} - \boldsymbol{u}_{\mathbf{0}}$ and $\boldsymbol{y}_{\mathbf{0}}$, $\boldsymbol{u}_{\mathbf{0}}$ stand for the measured output and input at the last sample when system states are $\boldsymbol{x}_{\mathbf{0}}$. The matrix $\hat{\boldsymbol{G}}$ is an estimation of the control effectiveness matrix $\boldsymbol{C}\frac{\partial \boldsymbol{f}}{\partial \boldsymbol{u}}\big|_{\mathbf{0}}$. The residual, $\boldsymbol{\epsilon}$, includes three elements: the $\boldsymbol{C}(\frac{\partial \boldsymbol{f}}{\partial \boldsymbol{u}}\big|_{\mathbf{0}} - \hat{\boldsymbol{G}})\Delta\boldsymbol{u}$ term which comes from the estimation error of the control effectiveness matrix, the $\boldsymbol{C}\frac{\partial \boldsymbol{f}}{\partial \boldsymbol{x}}\big|_{\mathbf{0}}\Delta\boldsymbol{x}$ term and the Taylor expansion remainder $\boldsymbol{C}\mathcal{O}(\Delta\boldsymbol{x}^2,\Delta\boldsymbol{u}^2)$.

For a Bebop2 quadrotor with the left back rotor removed, define the system output as $\boldsymbol{y} = [p \quad q \quad \int \bar{f}_z^B dt]^T$, where $\bar{f}_z^B$ denotes the specific force on z_B direction which can be measured by the accelerometer. The incremental form of $\dot{\boldsymbol{y}}$ is

$$\begin{aligned}\dot{\boldsymbol{y}} = \dot{\boldsymbol{y}}_{\mathbf{0}} + \hat{\boldsymbol{G}}\Delta\boldsymbol{u} + \boldsymbol{\epsilon} &= \begin{bmatrix}\dot{p}_0 & \dot{q}_0 & \bar{f}_{z,0}^B\end{bmatrix}^T \\ &+ \begin{bmatrix} b\kappa_0/I_{vx} & -b\kappa_0/I_{vx} & -b\kappa_0/I_{vx} \\ l\kappa_0/I_{vy} & l\kappa_0/I_{vy} & -l\kappa_0/I_{vy} \\ -\kappa_0/m & -\kappa_0/m & -\kappa_0/m \end{bmatrix}(\boldsymbol{u} - \boldsymbol{u}_{\mathbf{0}}) + \boldsymbol{\epsilon}\end{aligned} \tag{4.20}$$

where $\boldsymbol{u}$ is defined in the (4.5); p_0, q_0 and $\bar{f}_{z,0}^B$ are the last measured angular rate and specific force. The $\hat{\boldsymbol{G}}$ matrix is estimated using (4.8) and assuming $I_{vxy} = 0$. Recall (5.4) to (5.6), the major effects of the coupling term $-\tilde{\boldsymbol{\Omega}}\boldsymbol{I}_v\boldsymbol{\Omega}$, the aerodynamic force $\boldsymbol{F}_a$ and moment $\boldsymbol{M}_a$ are included in the $\dot{\boldsymbol{y}}_0$, which can be obtained from sensor measurements instead of accurate models. By virtue of the high sampling frequency of the sensors (512 Hz for the Bebop2), the influence of $\boldsymbol{\epsilon}$ becomes negligible, thus can be omitted [12].

Particularly, $\dot{\boldsymbol{y}}_{\mathbf{0}}$ is obtained by taking derivative of the gyroscope and accelerometer measurements. The considerable noise of these measurements is reduced by a first-order low-pass filter [13]. To compensate the lag introduced by the filter, the input measurement $\boldsymbol{u}_{\mathbf{0}}$ needs to be filtered with the same cut-off frequency to maintain synchronization between input increment and measured rotation accelerations. This process introduces the filtered measurements $\dot{\boldsymbol{y}}_{\boldsymbol{f}}$ and $\boldsymbol{u}_{\boldsymbol{f}}$ to replace $\dot{\boldsymbol{y}}_{\mathbf{0}}$ and $\boldsymbol{u}_{\mathbf{0}}$ in the (4.20). Finally, the desired rotor speed command can be obtained by

$$\boldsymbol{u} = \hat{\boldsymbol{G}}^{-1}(\boldsymbol{v}_{\boldsymbol{in}} - \dot{\boldsymbol{y}}_{\boldsymbol{f}}) + \boldsymbol{u}_{\boldsymbol{f}} \tag{4.21}$$

where

$$\boldsymbol{v}_{\boldsymbol{in}} = \begin{bmatrix} \dot{p}_{des} + k_1(p_{des} - p) \\ \dot{q}_{des} + k_2(q_{des} - q) \\ \bar{f}_{z,des}^B + k_3\int(\bar{f}_{z,des}^B - \bar{f}_z^B)dt \end{bmatrix} \quad (k_1, k_2, k_3 > 0) \tag{4.22}$$

To satisfy the time-scale separation assumption, the gains in the inner loop should

Table 4.1: Parameter of the tested quadrotor (light weighted Bebop2)

parameter	value	unit
m	0.0.410	kg
l	0.088	m
b	0.115	m
$\boldsymbol{I}_{vx}$	1.67×10^{-3}	kgm^2
$\boldsymbol{I}_{vy}$	1.38×10^{-3}	kgm^2
$\boldsymbol{I}_{vz}$	2.82×10^{-3}	kgm^2

be larger than the outer loop gains yielding

$$\min\{k_1, k_2, k_3\} > \max\{k_x, k_y\} \tag{4.23}$$

4. VALIDATION

In order to validate the above nonlinear controller first without significant aerodynamic effects, low-speed flight tests are carried out in the Cyberzoo, an indoor flight test field operated by the Delft University of Technology. The inertia and geometry parameters of the tested quadrotor, Parrot Bebop2, are listed in Table 6.1. To alleviate the effects of actuator saturation, the quadrotor is lightened by removing the camera and a lighter weight battery is used. The processor is a Parrot P7 dual-core CPU Cortex 9. The onboard sensor is MPU6050 for accelerometers and gyroscope with 512Hz sampling rate. Other hardware information about this type of drone can be found in [17]. An open source autopilot, Paparazzi [18], is modified to run the algorithm. An external motion capturing system (Optitrack) is operated at 120Hz and provides the position measurements of 6 reflecting markers fixed to the drone. The position of the center of gravity, velocity and attitude are then derived from these measurements and are transmitted to the on-board controller via WiFi.

In the flight tests, the drone was controlled to track a certain trajectory as shown in Fig. 4.5a. As compared to the linear controller adopted in [6], no prior-calculated solutions are required. To illustrate the advantage of the nonlinear controller, the primary axis was set to change at 7s from $\boldsymbol{n^B} = [0.1 \quad 0.1 \quad -1.00]^T$ to $\boldsymbol{n^B} = [0.2 \quad 0.2 \quad -0.96]^T$ without any prior calculation and using the same set of gains. As a consequence, the reference value of h_1 and h_2 changed from 0.1 to 0.2 which can be clearly seen in the Fig. 4.5b. The p_{des}, q_{des} calculated from (4.16) and the measured p and q are presented in Fig. 4.5c. The slight errors of tracking on p and q can be observed and subsequently lead to the tracking errors of h_1 and h_2. As a consequence, the orientation of the primary axis $\boldsymbol{n^I}$ oscillated about the $\boldsymbol{n^I_{des}}$ as Fig. 4.6 shows. However, the average thrust can still align with the $\boldsymbol{n^I_{des}}$ and subsequently guarantee position control. The average thrust direction is calculated by implementing a

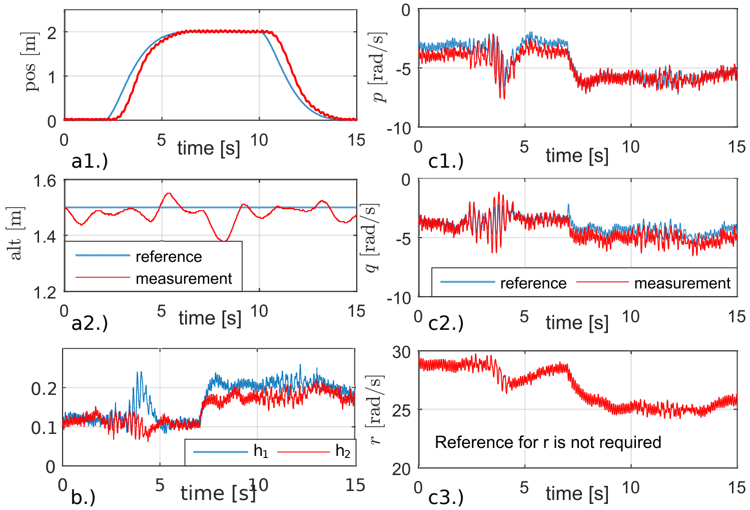

Figure 4.5: a.) Reference trajectory and the measured position. b.) Time series of h_1, h_2. The reference value of them changed from 0.1 to 0.2 at t=7s. c.) Reference value of pitch rate, roll rate and measurement value of angular rates. The reference and real values changed at t=7s when primary axis is changed.

forward-backward low-pass filter on the primary axis $\boldsymbol{n}^{\boldsymbol{I}}$ with 2Hz cut-off frequency.

The measured yaw rate r is also given in Fig. 4.5c. A positive yaw rate stands for a clockwise spinning direction. It is obvious that the yaw rate reduced after the primary axis is changed since a more tilted primary axis leads to a larger wobbling angle and a smaller spinning rate [11].

5. WIND TUNNEL FLIGHT TEST

To validate the controller in the high-speed condition and reveal the aerodynamic effects acting on the spinning quadrotor, flight tests have been carried out in the Open Jet Facility (OJF), a large scale wind tunnel with a 3 m by 3 m aperture as Fig. 4.1 shows. The external motion capturing system is also mounted in the OJF, which contains 12 cameras providing an area of 2 m × 2 m × 3 m for consistent tracking of the drone. The other experimental settings are same as those introduced in Section 4. The damaged quadrotor is controlled to track a way point 1.5 m away from the wind tunnel nozzle. The wind speed is initialized from 0 m/s and increased in steps of 1 m/s until the drone crashes. Both clockwise and counterclockwise rotating rotors are disabled leading to different spinning directions of the quadrotor. As a result, the drone is able to maintain stable flight until the wind speed reaches over 9 m/s, which is approximately 50% of the maximum flight speed in nominal

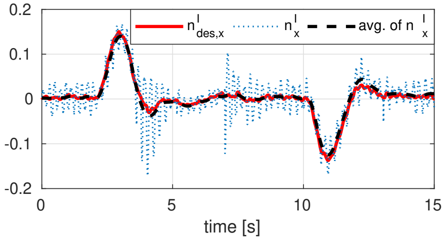

Figure 4.6: Time series of the desired primary axis direction $n^I_{x,des}$, the real direction of primary axis n^I_x, and the average value of n^I_x. Although the primary axis oscillates around $n^I_{x,des}$, its average value is perfectly aligned with it, which ensures desirable position tracking performance.

case.

Fig. 4.7a demonstrates the 3-D trajectory of a single flight the left back rotor removed and $\boldsymbol{n^B} = [0.2\ 0.2\ -0.96]^T$. Fig. 4.7d shows the wind speed from the time when the drone starts to be stabilized at the way point until it crashes due to the violent aerodynamic effects. Fig. 4.7b presents the time history of the rotor speeds of which the level of fluctuation grows with the wind speed, which can be interpreted as the effect of aerodynamics. Saturation of the actuator occurs and its severity increased with higher wind speeds as is shown in Fig. 4.7c. When the speed is higher than 5 m/s, two propellers reached saturation. The drone finally crashed when three remaining actuators reached their limit. Therefore, the actuator saturation is suspected to be the main reason for the loss of control.

5.1. EFFECT OF AERODYNAMIC MOMENT

In order to analyze the aerodynamic effects, two variables are introduced. The airspeed, denoted by V, indicates the relative speed between the drone and the coming flow and can be calculate by

$$V = ||\boldsymbol{v} - \boldsymbol{V}_{wind}|| \tag{4.24}$$

where $\boldsymbol{V}_{wind}$ represents the vector of wind velocity. The heading angle of the drone, denoted by ψ, is considered to be pointing towards the nozzle (against the wind) when $\psi = 0$.

From the high-speed flight data, the effect of the aerodynamic moment $\boldsymbol{M_a}$ is found to be considerable. This leads to a significant distinction from the hovering conditions. To estimate this aerodynamic moment, the resultant moment $\boldsymbol{M}$ is calculated by (5.4) using the method introduced in [16]. Subsequently, $\boldsymbol{M}_a$ can be calculated from (5.6).

It is indicated that the aerodynamic induced rolling and pitching moment denoted by $M_{a,x}$ and $M_{a,y}$ are highly correlated to the heading angle ψ. Fig. 4.8b shows

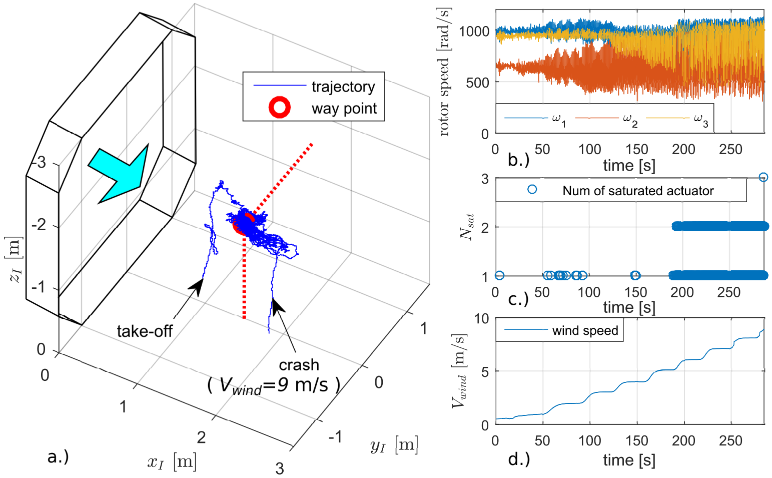

Figure 4.7: a.) 3D trajectory in a single wind tunnel flight test and the way point to be tracked. b.)Time series of rotor speed. c.) The number of saturated actuator. d.) Time series of the wind speed. In this flight, the rotor #4 was removed. The drone crashed at around 9 m/s when all three rotors reached their speed limits.

the value of $M_{a,x}$ and $M_{a,y}$ at different heading angles from the data including 20 rotations at airspeed of 4 m/s. The magnitude of these moments are considerable with respect to the size and inertia of Bebop2 quadrotor. To stabilize the quadrotor under these heading angle related moments, the rotor speeds are found to vary with the heading angle as presented in Fig. 4.8a accounting for the vast fluctuation of the rotor speeds in the high-speed condition as shown in Fig. 4.7b. By contrast, in the hovering condition without significant aerodynamic effects, the rotor speeds are supposed to keep constant in one rotation.

As is shown in Fig. 4.8c, the rotor speed fluctuation also lead to the variation of the yaw rate. For ex, a yaw rate reduction occurs at the airspeed of 4 m/s and 6 m/s from $\psi = 110°$ to $\psi = 200°$ while ω_2 is increasing and ω_3 is decreasing. The airspeed also influences the mean value of the yaw rate. As the wind speed increased from 0 m/s to 4 m/s, a dramatic drop-off appears which can be caused by the mis-tracking of the primary-axis due to the aerodynamic moment. The primary axis is not perfectly tracked in these conditions, nevertheless, the average thrust can still align with the desired acceleration direction to maintain the position tracking, as was analyzed in Section 4.

5.2. NECESSITY OF APPLYING ROBUST NONLINEAR CONTROLLER

According to the assumption and flight validation results presented in [10], the resultant moment acting on the quadrotor in the hovering condition can be ex-

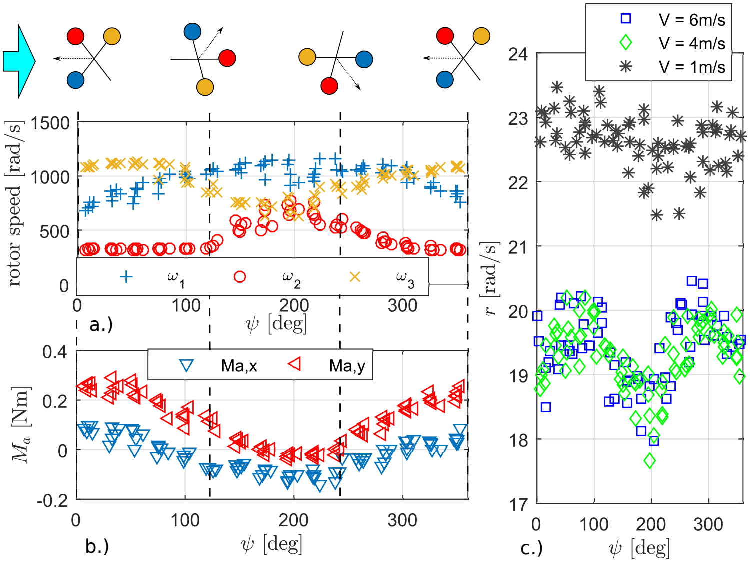

Figure 4.8: a.) Rotor speeds vary significantly with the heading angle, plotted data are with $V = 4$ m/s containing 20 revolutions. b.) Aerodynamic rolling moment $M_{a,x}$ and $M_{a,y}$ acting on the quadrotor. c.)Comparison of the yaw rate in different flight speeds. Yaw rate varies with the heading angle when $V > 0$ m/s.

pressed as

$$\boldsymbol{M} = [0 \quad 0 \quad -\gamma]^T r + \boldsymbol{G_M u} \tag{4.25}$$

where $\gamma > 0$ is the yaw damping coefficient. It is clear that near hovering conditions, the resultant moment is linear to the states and control inputs. Thus knowing the information of the $\boldsymbol{G_M}$ matrix and the yaw damping coefficient γ, a linear controller such as the Linear Quadratic Regulator (LQR) can be well designed[10, 11].

On the other hand, in the high-speed flight conditions, the resultant moment $\boldsymbol{M}$ is highly nonlinear with respect to the speed, angular rate, and heading angle on the basis of the flight data and literature about rotor aerodynamic characteristics[19–21], yielding

$$\boldsymbol{M} = \boldsymbol{M_a}(V, \psi, \boldsymbol{\Omega}) + \boldsymbol{G_M u} \tag{4.26}$$

For this reason, designing a satisfying gain-scheduling controller requires an accurate model of $\boldsymbol{M_a}(V, \psi, \boldsymbol{\Omega})$, which is difficult to obtain. Even if true, a large number of set points and gain (matrices) need to be computed and tuned at different V, ψ and $\boldsymbol{\Omega}$, which is possible but impractical.

In comparison, the INDI controller has two significant advantages. First, the aerodynamic model is not required since the effects of $\boldsymbol{M_a}$ are included in the $\dot{\boldsymbol{y}}_0$ term in (4.19). Secondly, only a small number of gains $(k_x, k_y, k_1, k_2, k_3)$ need to be tuned. We believe that other nonlinear/robust controllers are also applicable, to some extend, by knowing the model of $\boldsymbol{M_a}$ or regarding it as an external disturbance.

5.3. AERODYNAMIC FORCE MODEL

The simplified aerodynamic force model can be identified from the flight data for further analyzing the performance of the damaged quadrotor, such as the maximum flight speed and range, etc.

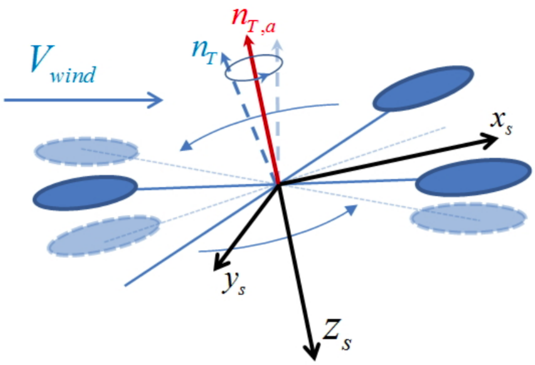

Figure 4.9: The definition of the stabilization frame. $\boldsymbol{n}_T$ indicates the instant thrust direction and $\boldsymbol{n}_{T,a}$ indicates the average thrust direction.

Since the quadrotor spins at a high rate (approximately 20 rad/s), we introduce the stabilization frame, denoted by $\mathscr{F}_S$, to describe the forces acting on the entire spinner. As Fig. 4.9 illustrates, z_S points against the average direction of the thrust vector; x_S lies in the plane formed by the gravity and the airspeed and points against the airspeed direction; y_S is perpendicular to the $O_S x_S z_S$ plane and points to the left. The motion capturing system is used to measure the specific forces acting on the quadrotor by differentiating measured velocities. Because of the slight misalignment between the rotation center and the rigid body center interpreted by the motion capturing system, the measured velocity oscillates with the spinning frequency of the quadrotor. A low-pass filter with cut-off frequency lower than the spinning frequency is applied to the measured velocity to obtain $\boldsymbol{v_f}$ and the estimated specific force can be calculated by

$$\bar{\boldsymbol{f}} = d\boldsymbol{v_f}/dt - \boldsymbol{g} \tag{4.27}$$

Two sets of flight data are plotted in Fig. 4.10 showing the airspeed versus specific forces which are expressed in $\mathscr{F}_S$. The index of the removed rotor is the only difference between these two flights, where the case without right back rotor is plotted in green and left back in red. As a consequence, the damaged quadrotor losing its left back rotor spins clockwise (from the top view) and vise versa.

Fig. 4.10a shows the specific force along x_S, i.e. $\bar{f}_x^B$, which can be interpreted as the drag. A linear relationship between V and $\bar{f}_x^B$ can be clearly seen. Note that this linear relationship also holds for the nominal quadrotor [22], indicating the spinning motion may bring high-frequency force deviation on the drone but the linear trend still holds. For two damage types with different spinning directions, the slope remains the same. Therefore, a linear model can be identified to predict the drag specific force in the form of

$$\bar{f}_x^s = C_x V \tag{4.28}$$

where C_x is the drag coefficient.

As Fig. 4.10b shows, the lateral force appears and its direction varies with the spinning direction. For anticlockwise rotation, the lateral force is slightly positive when flight speed is smaller than 3.5 m/s and then become negative as flight speed increases. On the other hand, the data from clockwise rotation shows a nearly opposite pattern. The asymmetric configuration of the spinning quadrotor under fault condition can be the major cause of this lateral force. Therefore, the lateral specific force can be modeled as

$$\bar{f}_y^s = \mathrm{sign}(r)(C_{y,1} V + C_{y,2} V^2) \tag{4.29}$$

Flight data with the right back rotor removed are used for identifying the C_x, $C_{y,1}$ and $C_{y,2}$ using a Least Square estimator. The model is verified using the data with left back rotor removed as Fig. 4.10 shows. The drag coefficients of the tested Bebop2 quadrotor are listed in Table 4.2.

Table 4.2: Identified drag / lateral force coefficients of the spinning damaged Bebop2

C_x [s^{-1}]	$C_{y,1}$ [s^{-1}]	$C_{y,2}$ [m^{-1}]
0.306	0.129	-0.0339

6. CONCLUSIONS

A 3-loop nonlinear controller is designed and tested on a quadrotor with one rotor removed. High-speed flight tests are carried out systematically in the wind tunnel. The new control scheme possesses robustness against complex aerodynamic effects brought by both fast translational and fast spinning motion of a damaged quadrotor. The research shows that quadrotors with severe actuator damage can continue high-speed missions instead of having to immediately abort.

Several high-speed spinning-induced aerodynamic effects have been discovered. Rotor speeds and the yaw rate which are constant in the hovering conditions are found to vary with the heading angle in the high-speed flight. Aerodynamic moments are observed to significantly increase the nonlinearity of the system. Aerodynamic forces, especially the lateral force induced by the spinning motion, are observed and modeled. Understanding of these effects could further help to improve

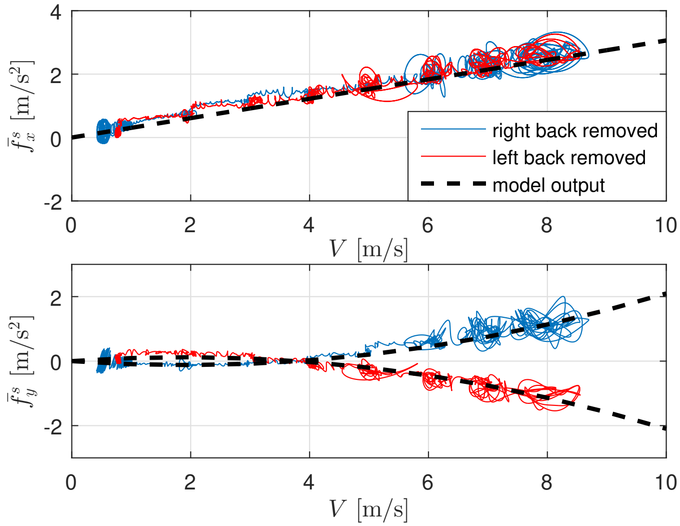

Figure 4.10: a.) Specific force projecting on the stability coordinate system. The drag force $\bar{f}_x^s$ is linear with the flight speed. b.) The lateral-force $\bar{f}_y^s$ is positive related to the flight speed and its direction varies with the quadrotor spinning direction. Model identified from the data with the right-back rotor removed are compared in the black dash line.

the performance of a damaged quadrotor and increase its fault tolerance which is essential for a broader acceptance of multi-rotor drones by the public.

REFERENCES

[1] J. K. Stolaroff, C. Samaras, E. R. O'Neill, A. Lubers, A. S. Mitchell, and D. Ceperley, *Energy use and life cycle greenhouse gas emissions of drones for commercial package delivery,* Nature Communications **9**, 409 (2018).

[2] L. Besnard, Y. B. Shtessel, and B. Landrum, *Quadrotor vehicle control via sliding mode controller driven by sliding mode disturbance observer,* Journal of the Franklin Institute **349**, 658 (2012).

[3] T. Li, Y. Zhang, and B. W. Gordon, *Passive and active nonlinear fault-tolerant control of a quadrotor unmanned aerial vehicle based on the sliding mode control technique,* Proceedings of the Institution of Mechanical Engineers. Part I: Journal of Systems and Control Engineering **227**, 12 (2013).

[4] A. R. Merheb, H. Noura, and F. Bateman, *Design of passive fault-tolerant controllers of a quadrotor based on sliding mode theory,* International Journal of Applied Mathematics and Computer Science **25**, 561 (2015).

[5] Y. Zhang, A. Chamseddine, C. Rabbath, B. Gordon, C.-Y. Su, S. Rakheja, C. Fulford, J. Apkarian, and P. Gosselin, *Development of advanced FDD and FTC techniques with application to an unmanned quadrotor helicopter testbed,* Journal of the Franklin Institute **350**, 2396 (2013).

[6] A. Lanzon, A. Freddi, and S. Longhi, *Flight control of a quadrotor vehicle subsequent to a rotor failure,* Journal of Guidance, Control, and Dynamics **37**, 580 (2014).

[7] V. Lippiello, F. Ruggiero, and D. Serra, *Emergency landing for a quadrotor in case of a propeller failure: A backstepping approach,* in *2014 IEEE/RSJ International Conference on Intelligent Robots and Systems (IROS)* (IEEE, 2014) pp. 4782–4788.

[8] V. Lippiello, F. Ruggiero, and D. Serra, *Emergency landing for a quadrotor in case of a propeller failure: A pid based approach,* in *2014 IEEE International Symposium on Safety, Security, and Rescue Robotics (2014)* (IEEE, 2014) pp. 1–7.

[9] P. Lu and E.-J. van Kampen, *Active fault-tolerant control for quadrotors subjected to a complete rotor failure,* in *2015 IEEE/RSJ International Conference on Intelligent Robots and Systems (IROS)* (IEEE, 2015) pp. 4698–4703.

[10] M. W. Mueller and R. D'Andrea, *Relaxed hover solutions for multicopters: Application to algorithmic redundancy and novel vehicles,* The International Journal of Robotics Research **35**, 873 (2016).

[11] M. W. Mueller and R. D'Andrea, *Stability and control of a quadrocopter despite the complete loss of one, two, or three propellers,* in *2014 IEEE International Conference on Robotics and Automation (ICRA)* (IEEE, 2014) pp. 45–52.

[12] X. Wang, E. J. Van Kampen, Q. Chu, and P. Lu, *Stability analysis for incremental nonlinear dynamic inversion control,* in *AIAA Guidance, Navigation, and Control Conference, 2018*, 210039 (2018).

[13] E. J. J. Smeur, Q. Chu, and G. C. H. E. de Croon, *Adaptive incremental nonlinear dynamic inversion for attitude control of micro air vehicles,* Journal of Guidance, Control, and Dynamics **39**, 450 (2016).

[14] E. J. Smeur, G. C. de Croon, and Q. Chu, *Gust disturbance alleviation with Incremental Nonlinear Dynamic Inversion,* in *2016 IEEE/RSJ International Conference on Intelligent Robots and Systems (IROS)* (IEEE, 2016) pp. 5626–5631.

[15] R. Mahony, V. Kumar, and P. Corke, *Multirotor aerial vehicles: modeling, estimation, and control of quadrotor,* IEEE Robotics & Automation Magazine **19**, 20 (2012).

[16] S. Sun, R. Schilder, and C. C. de Visser, *Identification of quadrotor aerodynamic model from high speed flight data,* in *2018 AIAA Atmospheric Flight Mechanics Conference* (2018) p. 0523.

[17] *Wiki of parrot bebop,* `https://wiki.paparazziuav.org/wiki/Bebop` (), accessed: 2018-06-30.

[18] *Wiki of paparazzi flight controller,* `https://github.com/paparazzi/paparazzi` (), accessed: 2018-02-20.

[19] G. M. Hoffmann, H. Huang, S. L. Waslander, and C. J. Tomlin, *Precision flight control for a multi-vehicle quadrotor helicopter testbed,* Control Engineering Practice **19**, 1023 (2011).

[20] P.-j. Bristeau, P. Martin, E. Salaun, and N. Petit, *The role of propeller aerodynamics in the model of a quadrotor UAV,* in *2009 European Control Conference (ECC)* (IEEE, 2009) pp. 683–688.

[21] W. Johnson, *Helicopter theory* (Courier Corporation, 1980) pp. 1–64.

[22] R. C. Leishman, J. C. MacDonald, R. W. Beard, and T. W. McLain, *Quadrotors and accelerometers: state estimation with an improved dynamic model,* IEEE Control Systems **34**, 28 (2014).

5

INCREMENTAL NONLINEAR FAULT-TOLERANT CONTROL OF A QUADROTOR WITH COMPLETE LOSS OF TWO OPPOSING ROTORS

In order to further expand the flight envelope of quadrotors under actuator failures, we design a nonlinear sensor-based fault-tolerant controller to stabilize a quadrotor with failure of two opposing rotors in the high-speed flight condition (> 8m/s). The incremental nonlinear dynamic inversion (INDI) approach which excels in handling model uncertainties is adopted to compensate for the significant unknown aerodynamic effects. The internal dynamics of such an underactuated system are been analyzed, and subsequently stabilized by re-defining the control output. The proposed method is also applicable to single-rotor-failure and no-failure flight conditions. For validation, flight tests have been carried out in a large-scale open jet wind tunnel. The position of a damaged quadrotor can be controlled in the presence of significant wind disturbances. A linear quadratic regulator (LQR) approach from the literature is compared to demonstrate the advantages of the proposed nonlinear method in the windy and high-speed flight condition.

Parts of this chapter have been accepted by:

S. Sun, X. Wang, Q. Chu, and C. de Visser, "Incremental Nonlinear Fault-Tolerant Control of a Quadrotor with Complete Loss of Two Opposing Rotors," IEEE Transactions on Robotics.

1. INTRODUCTION

Multi-rotor drones have demonstrated their ability in a large variety of applications such as surveillance, delivery, and recreation. Due to the potential growth of the drone market in the coming decades, safety issues are of critical concern. Apart from sensor redundancies, and improving operational regulations, fault-tolerant control (FTC) is a key to improving safety in the face of unexpected structural and actuator failures.

Among different types of multi-rotor drones, quadrotors excel in their structural simplicity. However, they suffer more from actuator damages due to a lack of actuator redundancy. Partial damage on the rotors could result in the reduction of control effectiveness, which has been extensively studied in the literature (e.g., [1–4]). A more challenging problem is the complete loss of one or more rotors. Various control methodologies addressing this problem have been proposed and validated in simulations (e.g., [5–10]).

In-flight validations have been achieved by several pieces of research where linear control methods were mostly adopted, such as linear quadratic regulator (LQR) [11], proportional-integral-derivative (PID) control [12] and linear parameter varying (LPV) control [13]. The relaxed hovering solution proposed by [14] indicates that the hovering flight of a quadrotor is possible with a loss of up to three rotors. With a specially designed configuration, a vehicle with only a single rotor is tested using LQR with actuator saturations taken into account [15] .

The aforementioned literature assumes that the drone is operated around the hovering condition and only limited aerodynamic effects are considered such as the rotational damping [13, 14]. However, in out-door applications, significant aerodynamic forces/moments on the quadrotor are present due to fast cruising speed and large wind disturbances [16, 17]. The system nonlinearity also becomes more significant due to the complex variation of rotor aerodynamic characteristics in high-speed conditions. Therefore, designing a high-speed capable robust nonlinear controller is essential for expanding the flight envelope of a quadrotor subjected to rotor failures, and increasing its robustness against wind disturbances.

Incremental nonlinear dynamic inversion (INDI) is a sensor-based nonlinear control approach that makes use of sensor measurements to reduce its model dependency, thereby improving its robustness against model uncertainties. This approach has been adopted by the aviation industry in several applications, such as the control of fixed-wing aircraft [18], spacecrafts [19], helicopters [20] and multi-rotor drones [21–23]. In [24], we made use of the INDI controller to control a quadrotor with a single rotor failure in the wind tunnel. The control method has shown its advantage in providing robustness to large aerodynamic disturbances while simplifying gain tuning, and eliminating the need to calculate an equilibrium for linear control design.

However, the INDI controller relies on a dynamic inversion step. This step requires the number of inputs to be no less than the number of outputs. For a quadrotor with only two opposing rotors remain, the attitude control problem becomes under-actuated where the direct inversion is inapplicable. For this reason, we need to redesign the original control outputs of a quadrotor such as the thrust and attitudes. This subsequently results in several internal dynamics of which the stability needs to be guaranteed. The selection of the outputs ensuring stable internal dynamics has been addressed on some under-actuated control problems, e.g., wheeled mobile robots [25], quadrotor position control [26], and the attitude control of space aircraft [27].

The main theoretical contributions of this research are twofold: (1) A detailed analysis of the internal dynamics of quadrotors with complete loss of two opposing rotors; (2) A subsequent novel robust fault-tolerant control method implementing the INDI approach. The controlled quadrotor thereby suffers less from model uncertainties caused by significant aerodynamic effects during high-speed flight.

To validate the proposed controller, flight tests of a quadrotor with failure of two opposing rotors have been performed in an open jet wind tunnel. With limited information on the model, the controller is able to stabilize the damaged quadrotor in wind of over 8 m/s, which is more than half of its nominal maximum flight speed. This could significantly increase the safety of quadrotors by expanding the flight envelope under actuator failure conditions. With slight adaptation, the same control scheme can be used on a quadrotor with a single rotor failure for which the internal dynamics are proved to be inherently stable. A benchmark approach (LQR) has been compared to demonstrate the advantage of the proposed controller in the high-speed and windy flight conditions.

This chapter is organized as follows. Sec. 2 provides information on the quadrotor model and the reduced attitude control. Sec. 3 introduces the INDI controller and Sec. 4 directly provides the detailed controller design for a quadrotor with failure of two opposing rotors. Sec. 5 elaborates on the selection of control outputs and the stability of internal dynamics. Sec. 6 generalizes the proposed method to the single-rotor-failure and the nominal conditions. Finally, Sec. 5 and Sec. 8 demonstrate the flight test results in low-speed and high-speed flight conditions respectively.

2. PROBLEM FORMULATION

2.1. QUADROTOR KINEMATIC AND DYNAMIC MODEL

There are two coordinate systems considered in this work. The inertial frame $\mathscr{F}_{\mathscr{I}} = \{O_I, \boldsymbol{x}_I, \boldsymbol{y}_I, \boldsymbol{z}_I\}$, is fixed to the ground, with $\boldsymbol{x}_I$, $\boldsymbol{y}_I$ and $\boldsymbol{z}_I$ pointing to the north, east and aligning with the local gravity. The body frame $\mathscr{F}_{\mathscr{B}} = \{O_B, \boldsymbol{x}_B, \boldsymbol{y}_B, \boldsymbol{z}_B\}$ is fixed to the vehicle, with the origin located at the center of mass. As Fig. 1 shows, we assume the quadrotor has a symmetric fuselage, which is a common configuration for many commercially available quadrotors. As a convention, we define $\boldsymbol{x}_B$ points forward, $\boldsymbol{z}_B$ points downwards such that the drone inertia is symmetric with respect to the $\boldsymbol{x}_B - \boldsymbol{z}_B$ plane, and $\boldsymbol{z}_B$ is parallel with the thrust direction. $\boldsymbol{y}_B$ thus points rightwards to render $\mathscr{F}_{\mathscr{B}}$ a right-handed coordinate system. In the following context, the superscript $[\cdot]^I$ and $[\cdot]^B$ indicate the coordinate system in which a vector is expressed.

The equations of motion of a quadrotor are formulated as follows:

$$\dot{\boldsymbol{P}}^I = \boldsymbol{V}^I \tag{5.1}$$

$$m_v \dot{\boldsymbol{V}}^I = m_v \boldsymbol{g}^I + \boldsymbol{R}\boldsymbol{F}^B \tag{5.2}$$

$$\dot{\boldsymbol{R}} = \boldsymbol{R}\boldsymbol{\Omega}^B_\times \tag{5.3}$$

$$\boldsymbol{I_v}\dot{\boldsymbol{\Omega}}^B = -\boldsymbol{\Omega}^B_\times \boldsymbol{I_v}\boldsymbol{\Omega}^B + \boldsymbol{M}^B \tag{5.4}$$

where $\boldsymbol{P}^I = [X,\ Y,\ Z]^T$ and $\boldsymbol{V}^I = [V_x,\ V_y,\ V_z]^T$ represent the position and the velocity of the center of mass in $\mathscr{F}_{\mathscr{I}}$; m_v is the vehicle gross mass and $\boldsymbol{I_v}$ denotes the inertia matrix of the vehicle including rotors. $\boldsymbol{g}$ is the local gravity vector. $\boldsymbol{R} \in \mathrm{SO}(3)$ indicates the rotational matrix from $\mathscr{F}_{\mathscr{B}}$ to $\mathscr{F}_{\mathscr{I}}$. The angular velocity is expressed as $\boldsymbol{\Omega}^B = [p\ q\ r]^T$ where p, q and r denote pitch rate, roll rate and yaw rate respectively. $\boldsymbol{\Omega}_\times$ is the skew symmetric matrix such that $\boldsymbol{\Omega}_\times \boldsymbol{a} = \boldsymbol{\Omega} \times \boldsymbol{a}$ for any vector $\boldsymbol{a} \in \mathbb{R}^3$.

The variables $\boldsymbol{F}^B$ and $\boldsymbol{M}^B$ denote the resultant force and moment on the center of mass respectively, projected on $\mathscr{F}_{\mathscr{B}}$. For a quadrotor with thrust parallel to the $\boldsymbol{z}_B$ axis and rotor directions shown in Fig. 5.1, we have

$$\boldsymbol{F}^B = \begin{bmatrix} 0 \\ 0 \\ -\bar{\kappa}\sum_{i=1}^4 \omega_i^2 \end{bmatrix} + \boldsymbol{F}_a \tag{5.5}$$

$$\begin{aligned} \boldsymbol{M}^B \quad &= \bar{\kappa} \begin{bmatrix} b\sin\beta & -b\sin\beta & -b\sin\beta & b\sin\beta \\ b\cos\beta & b\cos\beta & -b\cos\beta & -b\cos\beta \\ \sigma & -\sigma & \sigma & -\sigma \end{bmatrix} \begin{bmatrix} \omega_1^2 \\ \omega_2^2 \\ \omega_3^2 \\ \omega_4^2 \end{bmatrix} \\ &+ \begin{bmatrix} I_p q(\omega_1 - \omega_2 + \omega_3 - \omega_4) \\ -I_p p(\omega_1 - \omega_2 + \omega_3 - \omega_4) \\ I_p(\dot{\omega}_1 - \dot{\omega}_2 + \dot{\omega}_3 - \dot{\omega}_4) \end{bmatrix} + \begin{bmatrix} 0 \\ 0 \\ -\gamma r \end{bmatrix} + \boldsymbol{M}_a \end{aligned} \tag{5.6}$$

where $\bar{\kappa}$ is a thrust coefficient valid in the hovering condition; σ is a constant ratio between the thrust coefficient and drag coefficient of the rotor; b and β are geometry parameters as Fig. 5.1 shows. Note that $\beta \in (0, \pi/2)$ for a quadrotor. $\boldsymbol{\omega}_i^B = [0,\ 0,\ \omega_i]$ is the angular speed of the ith rotor with respect to the body. I_p denotes the moment of inertia of each rotor about the rotational axis. Note that this model assumes that $||\boldsymbol{\Omega}|| << ||\boldsymbol{\omega}_i||$, thus the magnitude of rotor angular speed with respect to the air is approximated by ω_i. Symbol $||\cdot||$ is defined as the L^2 norm of a vector. γ in (5.6) indicates the aerodynamic yaw damping coefficient [11, 13].

In the high-speed flight condition, there are significant aerodynamic effects such as thrust variation [28], rotor in-plane force [29], rotor moment and airframe aerodynamic [30]. These additional aerodynamic related forces and moments are then expressed as $\boldsymbol{F}_a$ and $\boldsymbol{M}_a$ in (5.5) and (5.6). They are regarded as model uncer-

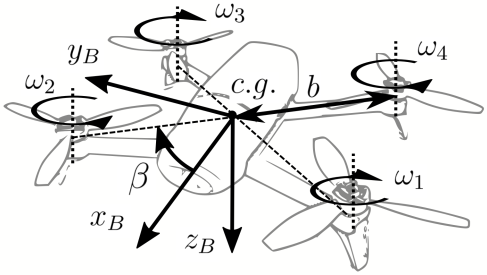

Figure 5.1: Definition of geometry parameters, rotor index and directions, and the body frame $\mathscr{F}_{\mathscr{B}}$.

tainties that need to be compensated for by the robustness of the control method.

2.2. REDUCED ATTITUDE CONTROL

The concept of reduced attitude control [31] has been adopted by [14] in the quadrotor fault tolerant control problem. We hereby briefly introduce the concept.

For a quadrotor with complete rotor failures, the full state equilibrium becomes unattainable. This is due to the incapacity of the remaining rotors to generate zero yaw moment while producing necessary thrust. As a consequence, the vehicle spins around the yaw axis. And the attitude control is reduced to a thrust vector pointing problem without considering the yaw angle.

Define a unit vector $\boldsymbol{n}$ fixed to $\mathscr{F}_{\mathscr{B}}$ where $\boldsymbol{n}^B = [n_x^B,\ n_y^B,\ n_z^B]^T$. For a quadrotor with double rotor failures, choosing $\boldsymbol{n}^B = [0,\ 0,\ -1]^T$ is most energy-efficient [11] where $\boldsymbol{n}$ aligns with the instantaneous thrust direction. Define another unit vector $\boldsymbol{n}_d$ as the reference of $\boldsymbol{n}$, which is calculated by the position controller or manually given by remote control. Then aligning $\boldsymbol{n}_d$ with $\boldsymbol{n}$ (or vise versa) becomes the primary task of the attitude controller. Therefore, we introduce the following relaxed attitude kinematic equation:

$$\dot{\boldsymbol{n}}_d^B = -\boldsymbol{\Omega}_\times \boldsymbol{n}_d^B + \boldsymbol{R}^T \dot{\boldsymbol{n}}_d^I \tag{5.7}$$

With the expressions $\boldsymbol{n}_d^B = [h_1,\ h_2,\ h_3]^T$ and $\boldsymbol{R}^T \dot{\boldsymbol{n}}_d^I = [\lambda_1,\ \lambda_2,\ \lambda_3]^T$, the expanded formula of (5.7) can be given as:

$$\begin{bmatrix} \dot{h}_1 \\ \dot{h}_2 \\ \dot{h}_3 \end{bmatrix} = \begin{bmatrix} 0 & r & -q \\ -r & 0 & p \\ q & -p & 0 \end{bmatrix} \begin{bmatrix} h_1 \\ h_2 \\ h_3 \end{bmatrix} + \begin{bmatrix} \lambda_1 \\ \lambda_2 \\ \lambda_3 \end{bmatrix} \tag{5.8}$$

The alignment of $\boldsymbol{n}$ and $\boldsymbol{n}_d$ thus can be achieved by controlling h_1 and h_2 to track n_x^B and n_y^B respectively. To be specific, with the selection of $\boldsymbol{n}^B = [0,\ 0,\ -1]^T$, h_1 and h_2 need to be stabilized to zero. The other selections of $\boldsymbol{n}^B$ may be considered for the case with single rotor failure, which has been discussed in [11, 14].

The challenge of the problem is conducting relaxed attitude control of a quadrotor with only two opposing rotors remain in the presence of significant model uncertainties $\boldsymbol{F}_a$ and $\boldsymbol{M}_a$, for instance, in high-speed flight conditions where significant aerodynamic effects become apparent. To achieve this goal, we employ a sensor-based nonlinear control method to be described in Sec. 3. The detailed implementation of this method will be provided in Sec. 4.

3. METHODOLOGY

Incremental nonlinear dynamic inversion (INDI) is a sensor-based nonlinear control approach. The approach stems from nonlinear dynamic inversion (NDI) control. INDI reduces the model dependencies of NDI by replacing non-input related model terms with direct sensor measurements, or sensor measurement derived quantities, thereby greatly improving robustness against model uncertainties.

For aircraft systems, including nominal quadrotors, each sub-problem (e.g., the attitude and rate control loops) is fully actuated without internal dynamics to be analyzed [3, 18, 21]. However, for a quadrotor with double rotor failures, the number of control inputs is less than the required output in a conventional cascaded control setup, yielding internal dynamics that have to be stabilized. In the following context, the generalized INDI control considering internal dynamics will be briefly reviewed. Readers may refer to [32] and [33] for further details.

Consider a nonlinear input affine system

$$\begin{aligned}\dot{\boldsymbol{x}} &= \boldsymbol{f}(\boldsymbol{x}) + \boldsymbol{G}(\boldsymbol{x})\boldsymbol{u}\\ \boldsymbol{y} &= \boldsymbol{h}(\boldsymbol{x})\end{aligned} \tag{5.9}$$

where $\boldsymbol{f} : \mathbb{R}^n \to \mathbb{R}^n$ and $\boldsymbol{h} : \mathbb{R}^n \to \mathbb{R}^l$ are smooth vector fields. $\boldsymbol{G} : \mathbb{R}^n \to \mathbb{R}^{n\times m}$ is a function mapping with smooth vector fields as columns. The number of outputs is not larger than the number of inputs (i.e., $l \le m$). There exists a nonlinear transformation $\boldsymbol{T} : \mathbb{R}^n \to \mathbb{R}^n$ such that the states $\boldsymbol{x}$ can be transformed to the normal form including internal states $\boldsymbol{\eta}$ and external states $\boldsymbol{\xi}$:

$$\begin{bmatrix} \boldsymbol{\eta} \\ \boldsymbol{\xi} \end{bmatrix} = \begin{bmatrix} \boldsymbol{\phi}(\boldsymbol{x}) \\ \boldsymbol{\theta}(\boldsymbol{x}) \end{bmatrix} = \boldsymbol{T}(\boldsymbol{x}) \tag{5.10}$$

where

$$\boldsymbol{\theta}(\boldsymbol{x}) = [\boldsymbol{\theta}_1(\boldsymbol{x}),\ \boldsymbol{\theta}_2(\boldsymbol{x}), ...,\ \boldsymbol{\theta}_l(\boldsymbol{x})]^T \tag{5.11}$$

with

$$\boldsymbol{\theta}_i(\boldsymbol{x}) = [h_i(\boldsymbol{x}),\ L_f h_i(\boldsymbol{x}), ..., L_f^{\rho_i - 1} h_i(\boldsymbol{x})],\ i = 1, 2, ..., l \tag{5.12}$$

where $h_i(\boldsymbol{x})$ indicates the ith element in the vector field $\boldsymbol{h}$. The notation $L_f^{\rho_i} h_i(\boldsymbol{x})$ indicates the ρ_ith order Lie derivative of the function h_i with respect to the vector fields $\boldsymbol{f}(\boldsymbol{x})$ [33]. ρ_i indicates the relative degree of the ith output y_i.

By defining $\bar{\rho} = \Sigma_1^l \rho_i$ as the sum of relative degrees of each output, one can define the transformation $\boldsymbol{\phi}(\boldsymbol{x}) = [\phi_1(\boldsymbol{x}),\ \phi_2(\boldsymbol{x}),\ ...,\ \phi_{n-\bar{\rho}}(\boldsymbol{x})]$. The selection of $\boldsymbol{\phi}(\boldsymbol{x})$ is not unique, but has to satisfy the following condition:

$$\frac{\partial \phi_i}{\partial \boldsymbol{x}} \boldsymbol{G}(\boldsymbol{x}) = 0, \qquad i = 1, 2, ..., n - \bar{\rho} \tag{5.13}$$

namely the first-order derivative of $\boldsymbol{\eta}$ as defined per (5.10) does not include control input $\boldsymbol{u}$. The nonlinear transformation $\boldsymbol{T}(\boldsymbol{x})$ is a diffeomorphism (i.e., smooth and invertible) in the domain of interest.

As a consequence, the problem is transformed to the normal form

$$\begin{aligned} \dot{\boldsymbol{\eta}} &= \boldsymbol{f}_\eta(\boldsymbol{\eta}, \boldsymbol{\xi}) \\ \dot{\boldsymbol{\xi}} &= \boldsymbol{A_c}\boldsymbol{\xi} + \boldsymbol{B_c}[\boldsymbol{\alpha}(\boldsymbol{x}) + \mathscr{B}(\boldsymbol{x})\boldsymbol{u}] \\ \boldsymbol{y} &= \boldsymbol{C_c}\boldsymbol{\xi} \end{aligned} \tag{5.14}$$

where the triplet $(\boldsymbol{A_c}, \boldsymbol{B_c}, \boldsymbol{C_c})$ is a canonical form representation of l chains of ρ_i integrators $(i = 1, 2, ..., l)$; $\boldsymbol{\alpha}: \mathbb{R}^n \to \mathbb{R}^l$ and $\mathscr{B}: \mathbb{R}^n \to \mathbb{R}^{l \times m}$ are mappings determined by the system (5.9). Subsequently, the output dynamics can be represented as

$$\boldsymbol{y}^{(\boldsymbol{\rho})} = \boldsymbol{\alpha}(\boldsymbol{x}) + \mathscr{B}(\boldsymbol{x})\boldsymbol{u} \tag{5.15}$$

where $\boldsymbol{y}^{(\boldsymbol{\rho})} = [y_1^{(\rho_1)},\ y_2^{(\rho_2)}, ...,\ y_l^{(\rho_l)}]^T$. The NDI control law is designed as

$$\boldsymbol{u}_{\text{ndi}} = \mathscr{B}(\boldsymbol{x})^+ (\boldsymbol{\nu} - \boldsymbol{\alpha}(\boldsymbol{x})) \tag{5.16}$$

where superscript $[\cdot]^+$ indicates the Moore-Penrose inverse of the matrix; $\boldsymbol{\nu} \in \mathbb{R}^n$ is called the pseudo-input. With a full knowledge of $\boldsymbol{\alpha}(x)$ and $\mathscr{B}(\boldsymbol{x})$, control law (5.16) yields the closed loop dynamics

$$\boldsymbol{y}^{(\boldsymbol{\rho})} = \boldsymbol{\nu} \tag{5.17}$$

For a command tracking problem with reference output $\boldsymbol{y}_{\text{ref}} \in \mathbb{R}^l$ that is $\boldsymbol{\rho}$th order differentiable, selecting

$$\boldsymbol{\nu} = -\boldsymbol{K}(\boldsymbol{\xi} - \boldsymbol{\xi}_{\text{ref}}) + \boldsymbol{y}_{\text{ref}}^{(\boldsymbol{\rho})} \tag{5.18}$$

ensures that the reference output is being tracked asymptotically, where the gains $\boldsymbol{K}$ is selected such that $\boldsymbol{A_c} - \boldsymbol{B_c}\boldsymbol{K}$ is Hurwitz. The reference $\boldsymbol{\xi}_{\text{ref}}$ is denoted as

$$\begin{aligned} \boldsymbol{\xi}_{\text{ref}} &= [\boldsymbol{\psi}_1,\ \boldsymbol{\psi}_2, ..., \boldsymbol{\psi}_l]^T, \\ \boldsymbol{\psi}_i &= [y_{\text{ref},i},\ y_{\text{ref},i}^{(1)}, ..., y_{\text{ref},i}^{(\rho_i - 1)}],\ i = 1, 2, ..., l \end{aligned} \tag{5.19}$$

In reality, the nonlinear model dependent terms $\boldsymbol{\alpha}(\boldsymbol{x})$ and $\mathscr{B}(\boldsymbol{x})$ are almost impossible to be obtained due to inevitable model uncertainties. In view of this, we take the first-order Taylor series expansion of (5.15) around the condition at the last sensor sampling moment $t - \Delta t$ (denoted by subscript $[\cdot]_0$), then (5.15) becomes [32]

$$\begin{aligned} \boldsymbol{y}^{(\boldsymbol{\rho})} &= \boldsymbol{\alpha}(\boldsymbol{x}) + \mathscr{B}(\boldsymbol{x})\boldsymbol{u} \\ &= \boldsymbol{y}_0^{(\boldsymbol{\rho})} + \mathscr{B}(\boldsymbol{x}_0)\Delta\boldsymbol{u} + \left.\frac{\partial[\boldsymbol{\alpha}(\boldsymbol{x}) + \mathscr{B}(\boldsymbol{x})\boldsymbol{u}]}{\partial \boldsymbol{x}}\right|_0 \Delta\boldsymbol{x} + \mathscr{O}(\Delta\boldsymbol{x}^2) \\ &\triangleq \boldsymbol{y}_0^{(\boldsymbol{\rho})} + \mathscr{B}(\boldsymbol{x}_0)\Delta\boldsymbol{u} + \boldsymbol{\delta}(\boldsymbol{x}, \Delta t) \end{aligned} \tag{5.20}$$

where $\Delta\boldsymbol{u} = \boldsymbol{u} - \boldsymbol{u}_0$, $\Delta\boldsymbol{x} = \boldsymbol{x} - \boldsymbol{x}_0$. Design the incremental nonlinear dynamic inversion (INDI) control as

$$\bar{\boldsymbol{u}}_{\text{indi}} = \hat{\mathscr{B}}(\boldsymbol{x}_0)^+(\boldsymbol{\nu} - \boldsymbol{y}_0^{(\boldsymbol{\rho})}) + \boldsymbol{u}_0 \tag{5.21}$$

where $\boldsymbol{\nu}$ is selected as per (5.18), while $\hat{\mathscr{B}}$ is the estimated control effectiveness matrix. As a result, the closed-loop tracking error ($\boldsymbol{e} = \boldsymbol{y} - \boldsymbol{y}_{\text{ref}}$) dynamics are $\dot{\boldsymbol{e}} = (\boldsymbol{A}_c - \boldsymbol{B}_c\boldsymbol{K})\boldsymbol{e} + \boldsymbol{B}_c\boldsymbol{\varepsilon}_{\text{indi}}$, where $\boldsymbol{\varepsilon}_{\text{indi}}$ is the residual error caused by model uncertainties. The boundedness of $\boldsymbol{\varepsilon}_{\text{indi}}$ and $\boldsymbol{e}$ has been proved in [34].

5

In INDI control, the model information of $\boldsymbol{\alpha}(\boldsymbol{x})$ is not needed for implementation, which greatly reduces the effort of modeling. The control effectiveness matrix $\hat{\mathscr{B}}$ is relatively easier to be estimated offline or identified online [21]. Apart form its reduced model dependency, INDI control also has enhanced robustness as compared to its classical NDI counterpart [34].

Due to the measurement noise, the variables $\boldsymbol{x}_0$, $\boldsymbol{y}_0$ can be low-pass filtered in practice. To synchronize the time delay caused by these filters, $\boldsymbol{u}_0$ also need to be filtered with the same cut-off frequency [21]. We use subscript $[\cdot]_f$ to denote the filtered variables (e.g., $\boldsymbol{x}_0 \to \boldsymbol{x}_f$, $\boldsymbol{y}_0 \to \boldsymbol{y}_f$ and $\boldsymbol{u}_0 \to \boldsymbol{u}_f$). Consequently, the INDI control law becomes

$$\boldsymbol{u}_{\text{indi}} = \hat{\mathscr{B}}(\boldsymbol{x}_f)^+(\boldsymbol{\nu} - \boldsymbol{y}_f^{(\boldsymbol{\rho})}) + \boldsymbol{u}_f \tag{5.22}$$

We will elaborate on applying the INDI control law (5.22) to the quadrotor control problem in the following sections.

4. CONTROLLER DESIGN

The detailed design process of the controller for a quadrotor with complete failure of two opossing rotors is presented in this section. In general, we use a cascaded controller with two loops (Fig. 5.2), where INDI is applied in the inner-loop for compensating model uncertainties ($\boldsymbol{M}_a$, $\boldsymbol{F}_a$).

4.1. OUTER-LOOP DESIGN

The outer-loop contains a horizontal position controller that computes the acceleration command from the reference horizontal position denoted by X_{ref} and Y_{ref}. Due to the linear property of translational kinematics, a linear method such as a PID controller can be employed. In addition, the reference altitude Z_{ref} needs to be

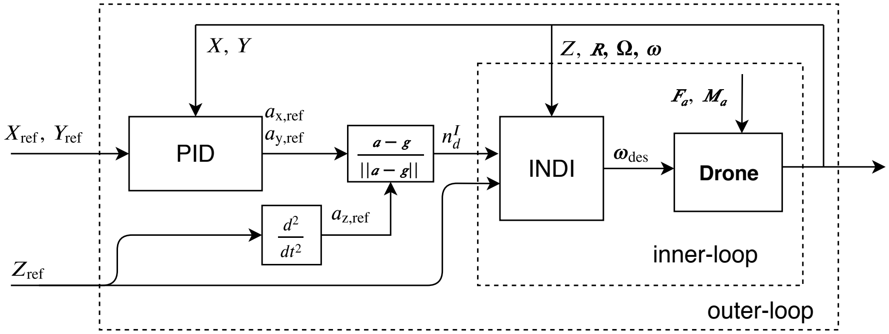

Figure 5.2: The two-loops cascaded control scheme using PID as outer-loop position control and INDI as inner-loop altitude / attitude control.

second-order differentiable. Therefore, we have

$$\boldsymbol{a}_{\text{ref}} = \begin{bmatrix} -k_p e_x - k_d \dot{e}_x - k_i \int e_x dt \\ -k_p e_y - k_d \dot{e}_y - k_i \int e_y dt \\ \ddot{Z}_{\text{ref}} \end{bmatrix} \tag{5.23}$$

where $e_x = X - X_{\text{ref}}$, $e_y = Y - Y_{\text{ref}}$ denote the horizontal position errors in $\mathscr{F}_{\mathscr{I}}$; control gains k_p, k_i and k_d are positive. Then $\boldsymbol{n}_d$ for reduced attitude control (see Sec. 2) can be calculated by

$$\boldsymbol{n}_d = \frac{\boldsymbol{a}_{\text{ref}} - \boldsymbol{g}}{||\boldsymbol{a}_{\text{ref}} - \boldsymbol{g}||} \tag{5.24}$$

It is possible to replace (5.23) by more sophisticated position controllers to obtain $\boldsymbol{a}_{\text{ref}}$, which will not be elaborated in this research.

4.2. INNER-LOOP DESIGN

The altitude control is included in the inner-loop controller since the altitude reference Z_{ref} is related to rotor thrust which contains model uncertainties $\boldsymbol{F}_a$. Consequently, the inner-loop is a combination of altitude and attitude control using the INDI approach.

States for the inner-loop control are defined as $\boldsymbol{x}_{\text{in}} = [h_1,\ h_2,\ p,\ q,\ r,\ Z,\ V_z]^T$. There are two different scenarios for a quadrotor with two opposite rotor failures. If only rotor 1 and 3 remain functional, we define the control input as

$$\boldsymbol{u} = [u_1,\ u_2]^T \triangleq [\omega_1^2,\ \omega_3^2]^T,\ \ s_l = 1 \tag{5.25}$$

If only rotor 2 and 4 remain, then

$$\boldsymbol{u} = [u_1,\ u_2]^T \triangleq [\omega_2^2,\ \omega_4^2]^T,\ \ s_l = -1 \tag{5.26}$$

where $s_l \in \{-1,\ 1\}$ is a parameter indicating the type of failure.

Since the product of inertia is negligible compared with the moment of inertia for a typical quadrotor, we can assume a diagonal inertia matrix $\boldsymbol{I_v} = \mathrm{diag}(I_x,\ I_y,\ I_z)$. Thus the state equations for the inner-loop states $\boldsymbol{x}$ can be derived from (5.4) and (5.7), yielding

$$\begin{bmatrix} \dot{Z} \\ \dot{V}_z \\ \dot{h}_1 \\ \dot{h}_2 \\ \dot{p} \\ \dot{q} \\ \dot{r} \end{bmatrix} = \begin{bmatrix} V_z \\ g + F_{a,z} - R_{33}\bar{\kappa}(u_1 + u_2)/m_v \\ h_3 p - h_1 r + \lambda_2 \\ -h_3 q + h_2 r + \lambda_1 \\ A_x r q - 2a_x q\bar{\omega} s_n + M_{a,x} + s_l G_p(u_1 - u_2) \\ A_y r p + 2a_y p\bar{\omega} s_n + M_{a,y} + G_q(u_1 - u_2) \\ A_z pq - \gamma r/I_z + M_{a,z} - s_n G_r(u_1 + u_2) \end{bmatrix} \tag{5.27}$$

where

$$A_x = (I_y - I_z)/I_x,\ A_y = (I_z - I_x)/I_y,\ A_z = (I_x - I_y)/I_z \tag{5.28}$$

$$a_x = I_p/I_x,\ a_y = I_p/I_y,\ g = ||\boldsymbol{g}|| \tag{5.29}$$

where R_{33} in (5.27) represens the entry at the third row and the third column of the matrix $\boldsymbol{R}$; $\bar{\omega}$ is the average angular rate of the remaining rotors; $s_n \in \{-1,\ 1\}$ indicates the handedness of the remaining rotors with 1 clockwise and -1 counterclockwise. G_p, G_q and G_r are control effectiveness on angular accelerations, where

$$G_p = \bar{\kappa}\sin\beta/I_x,\ \ G_q = \bar{\kappa}\cos\beta/I_y,\ \ G_r = \sigma\bar{\kappa}/I_z \tag{5.30}$$

Normally, $|G_r| << \min\{|G_p|, |G_q|\}$. Note that state equations (5.27) are nonlinear and contain model uncertainties ($F_{a,z}$, $M_{a,x}$, $M_{a,y}$ and $M_{a,z}$). The following content in this section designs the INDI control law (5.22) for this specific problem.

CONTROL OUTPUT DEFINITION

Since there are only two inputs remain, we can select a maximum of two variables as control outputs. To guarantee altitude tracking, we choose the first output as

$$y_1 = Z \tag{5.31}$$

The second output have to be associated with the reduced attitude control. Recall that in Sec. 2.2, $\boldsymbol{n}$ needs to align with $\boldsymbol{n}_d$ by manipulating the vehicle attitude, and h_1 and h_2 of (5.8) need to converge to zero. We hereby introduce a new coordinate system $\mathscr{F}_{\mathscr{S}} = \{O_S, \boldsymbol{x}_S, \boldsymbol{y}_S, \boldsymbol{z}_S\}$ that is fixed with respect to the body frame. As Fig. 5.3 illustrates, $\mathscr{F}_{\mathscr{S}}$ is generated by rotating the body frame about $\boldsymbol{z}_B$. The rotation angle is denoted as χ.

The second output y_2 is then defined as the projection of $\boldsymbol{n}_d$ on $\boldsymbol{x}_S$. In other words, y_2 becomes a linear combination of h_1 and h_2 scheduled by the angle χ:

$$y_2 = h_1\cos\chi + h_2\sin\chi \tag{5.32}$$

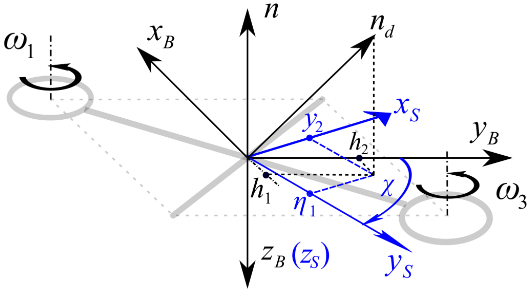

Figure 5.3: Definition of $\mathscr{F}_{\mathscr{S}}$, y_2, η_1 and χ when rotor 2 and rotor 4 are removed.

Meanwhile, the projection of $\boldsymbol{n}_d$ on $\boldsymbol{y}_S$ that is perpendicular to the second output y_2 remains uncontrolled (see Fig. 5.3). We will elaborate in Sec. 5 that this variable, denoted by η_1, is one of the internal states to be stabilized by properly selecting the angle χ.

Due to the symmetric property of a quadrotor, we can determine χ by selecting its absolute value, using the following relationship:

$$\chi = s_l|\chi| \tag{5.33}$$

It is noteworthy that $|\chi|$ is associated with the control performance, which can be analogous to physically informed control gains. The selection of $|\chi|$ will be further discussed in Sec. 5.

CONTROL EFFECTIVENESS ESTIMATION

After defining the outputs we can take second order derivative of both y_1 and y_2, yielding

$$\begin{aligned}\ddot{y}_1 &= g + F_{a,z} - R_{33}\bar{\kappa}(u_1+u_2)/m_v \\ &= \alpha_1 + B_1(u_1+u_2)\end{aligned} \tag{5.34}$$

$$\begin{aligned}\ddot{y}_2 &= \ddot{h}_1\cos\chi + \ddot{h}_2\sin\chi \\ &= \alpha_2(\boldsymbol{x},\chi) + B_2(u_1-u_2)\end{aligned} \tag{5.35}$$

where α_2 can be calculated from (5.27) whereupon includes nonlinear terms and model uncertainties. B_1 and B_2 are control effectiveness on y_1 and y_2 respectively:

$$B_1 = -\bar{\kappa}R_{33,f}/m_v \tag{5.36}$$

$$\begin{aligned}B_2 &= s_l h_{3,f}(G_p\sin\chi - G_q\cos\chi) \\ &= -\frac{h_{3,f}\bar{\kappa}b\sin\beta}{I_x\cos\zeta}\sin(\zeta-|\chi|)\end{aligned} \tag{5.37}$$

where ζ is a positive virtual angle defined as

$$\zeta = \tan^{-1}\left(\frac{I_x}{I_y}\cot\beta\right) \tag{5.38}$$

Now, from (5.34) and (5.35), the estimated control effectiveness matrix in (5.22) can be described as

$$\hat{\mathscr{B}}(\boldsymbol{x}_f) = \begin{bmatrix} B_1 & B_1 \\ B_2 & -B_2 \end{bmatrix} \tag{5.39}$$

The estimation error of $\hat{\mathscr{B}}$ mainly stems from the error of m_v, I_x, I_y, and $\bar{\kappa}$. Note that the filtered variables $R_{33,f}$ and $h_{3,f}$ are used in (5.36) and (5.37) because $\hat{\mathscr{B}}$ is a function of $\boldsymbol{x}_f$ as per (5.22).

Remark 1: As indicated by (5.35) and (5.37), the system has the largest control effectiveness on y_2 when $|\sin(\zeta - |\chi|)| = 1$. On the contrary, the control effectiveness becomes zero when $\sin(\zeta - |\chi|) = 0$. Small control effectiveness leads to large control input command and subsequently deteriorates the control performance with the presence of actuator position and rate limit. Therefore, we enforce the effectiveness on y_2 to be greater than the minimum of G_p and G_q, which yields the following constraint on $|\chi|$:

$$r_B(|\chi|) \triangleq \frac{|B_2(|\chi|)|}{\min\{|G_p|, |G_q|\}} \geq 1 \tag{5.40}$$

In addition, the following constraints are made to prevent $B_1 = B_2 = 0$, which is rather easy to fulfill:

- $R_{33,f} \neq 0$: the thrust direction does not remain in the horizontal plane of $\mathscr{F}_{\mathscr{I}}$.
- $h_{3,f} \neq 0$: $\boldsymbol{n}_d$ is not perpendicular to the current thrust direction ($-\boldsymbol{z}_B$).

SECOND DERIVATIVE OF THE OUTPUT

$\ddot{\boldsymbol{y}}_f = [\ddot{y}_{1,f},\ \ddot{y}_{2,f}]^T$ in (5.22) can be obtained by directly taking the second-order derivative of filtered outputs. This, however, is prone to be detrimentally affected by measurement noise. Therefore, we can approximate $\ddot{y}_{1,f}$ by:

$$\ddot{y}_{1,f} = \ddot{Z}_f = \dot{V}_{z,f} \simeq a_{z,f} R_{33,f} + g \tag{5.41}$$

where $a_{z,f}$ is the projection of the filtered accelerometer measurement on $\boldsymbol{z}_B$.

$\ddot{y}_{2,f}$ can be obtained by numerically differentiating filtered $\dot{y}_2$. The latter can be derived from (5.8) and (5.32):

$$\dot{y}_2 = \cos\chi(-h_3 q + h_2 r + \lambda_1) + \sin\chi(h_3 p - h_1 r + \lambda_2) \tag{5.42}$$

PSEUDO-INPUT DEFINITION

The last step is to define the pseudo-input $\boldsymbol{v}$ as per (5.18). As presented in (5.34) and (5.35), the control input $\boldsymbol{u}$ appears after taking the second derivative of both y_1

and y_2. Thus the system relative degrees are $\rho_1 = \rho_2 = 2$. According to (5.11) and (5.12), there are four external states:

$$[\xi_1,\ \xi_2,\ \xi_3,\ \xi_4]^T = \left[y_1,\ \dot{y}_1,\ y_2,\ \dot{y}_2\right]^T = \begin{bmatrix} Z \\ V_z \\ h_1\cos\chi + h_2\sin\chi \\ (-h_3 q + h_2 r + \lambda_1)\cos\chi + (h_3 p - h_1 r + \lambda_2)\sin\chi \end{bmatrix} \tag{5.43}$$

For this problem, the output reference is defined as

$$\boldsymbol{y}_{\text{ref}} = [Z_{\text{ref}},\ h_{1,\text{ref}}\cos\chi + h_{2,\text{ref}}\sin\chi]^T = [Z_{\text{ref}},\ 0]^T \tag{5.44}$$

Then, by substituting (5.43) and (5.44) into (5.18), we obtain the pseudo-input

$$\boldsymbol{\nu} = \begin{bmatrix} -k_{z,p}(\xi_1 - Z_{\text{ref}}) - k_{z,d}(\xi_2 - \dot{Z}_{\text{ref}}) + \ddot{Z}_{\text{ref}} \\ -k_{a,p}\xi_3 - k_{a,d}\xi_4 \end{bmatrix} \tag{5.45}$$

with positive gains $k_{z,p},\ k_{z,d},\ k_{a,p},\ k_{a,d}$ to be tuned.

Eventually, the control effectiveness $\hat{\mathscr{B}}$, $\ddot{\boldsymbol{y}}$ and $\boldsymbol{\nu}$ is substituted into (5.22) to obtain $\boldsymbol{u}_{\text{indi}}$. The rotor speed command of the remaining rotors can be subsequently calculated using (5.25) or (5.26).

5. STABILITY ANALYSIS OF INTERNAL DYNAMICS

For the attitude/altitude inner-loop, internal states that need to be analyzed regarding their stability properties. As (5.32) shows, the selection of χ is of great importance for influencing the internal dynamics, which will be elaborated in this section.

5.1. RELAXED TRIMMING EQUILIBRIUM

The relaxed trimming equilibrium is an extension of the relaxed hovering equilibrium [14] to the high-speed flight regime where the aerodynamic drag becomes apparent. Note that the term trimming indicates the condition at a constant forward flight velocity. As Fig. 5.4a shows, the quadrotor spins about the axis $\boldsymbol{n}$ which represents the average thrust in a single revolution. In the relaxed trimming equilibrium, this averaged thrust is balanced with the average drag force (denoted by $\boldsymbol{F}_{a,xy}$) and the gravity. If we assume the constancy of $\boldsymbol{M}_a$ and $\boldsymbol{F}_{a,z}$ in (5.27), we have

$$\boldsymbol{x}_{\text{in}} = \bar{\boldsymbol{x}}_{\text{in}} = [\bar{h}_1,\ \bar{h}_2,\ \bar{p},\ \bar{q},\ \bar{r},\ \bar{Z},\ \bar{V}_z]^T \tag{5.46}$$

Specifically, if $\boldsymbol{n}^B = [0,\ 0,\ -1]^T$, we have

$$\bar{h}_1 = \bar{h}_2 = \bar{p} = \bar{q} = 0 \tag{5.47}$$

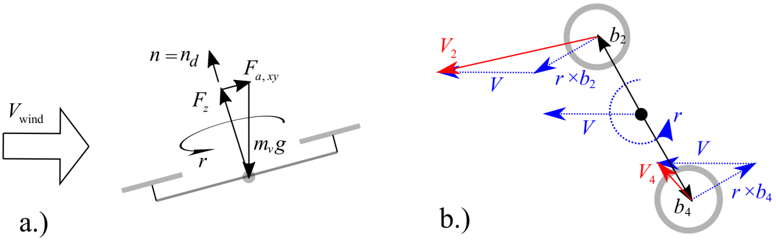

Figure 5.4: a.) Illustration of the force equilibrium at the relaxed trimming equilibrium. b.) The local velocities of the remaining rotors are different due to the high angular and translational speed of the drone (rotor 2 and 4 remain).

In practice, $\boldsymbol{M}_a$ and $\boldsymbol{F}_a$ are non-stationary. Thus variables h_1, h_2, p, q and r normally oscillate about the equilibrium. Nevertheless, as was analysed in [24], the average thrust direction remain unchanged as long as the reduced attitude h_1 and h_2 are bounded. The variation of yaw rate r is also relatively small compared to $\bar{r}$. We therefore assume the constancy of r in the following analysis.

Due to the spinning motion around the yaw axis during forward flight, the local airspeed and angle of attack of each rotor can be different (see Fig. 5.4b). The difference of local airspeed leads to the variation of thrust coefficient κ of each remaining rotor [30]. The rotor speeds, therefore, vary with the heading angle and the variation grows with the flight speed.

5.2. INTERNAL DYNAMICS

The internal dynamics are analyzed around the relaxed-trimming equilibrium. The following assumptions are further made to derive the internal states.

Assumption 1: $\boldsymbol{F}_a$ and $\boldsymbol{M}_a$ are independent from the control input $\boldsymbol{u}$.

Assumption 2: The attitude reference $\boldsymbol{n}_d^I$ is slowly time-varying, thus $\dot{\boldsymbol{n}}_d^I = [\lambda_1, \lambda_2, \lambda_3]^T \simeq 0$.

Assumption 3: The average rotor speed $\bar{\omega}$ is considered as a constant that is independent from the control input $\boldsymbol{u}$.

Note that *Assumption 3* holds because of the near-constancy of the resultant thrust during the trimming condition, which has been verified from the flight data. But this assumption is invalid during aggressive thrust variation, such as vertical maneuvers. Nevertheless, the flight experiments given in Sec. 5 will demonstrate that the internal dynamics are still stable during vertical maneuvers.

Since $\boldsymbol{x}_{\text{in}}$ has seven states in total and there are four external states as per (5.43), we need to determine three internal states. The selection of internal states is not unique as long as the condition (5.13) is satisfied, namely the first-order derivatives of $\boldsymbol{\eta}$ do not include $\boldsymbol{u}$. Based on the above assumptions, we hereby make the following choices for the internal states:

$$\begin{bmatrix} \eta_1 \\ \eta_2 \\ \eta_3 \end{bmatrix} = \begin{bmatrix} -h_1 \sin\chi + h_2 \cos\chi \\ q\cos\zeta - s_l p \sin\zeta \\ r + s_n \mu V_z \end{bmatrix} \tag{5.48}$$

where

$$\mu = m_v \sigma / h_3 \tag{5.49}$$

and ζ is defined as per (5.38). Note that the first internal state η_1 is the projection of $\boldsymbol{n}_d$ on $\boldsymbol{y}_S$ axis as illustrated in Fig. 5.3. Substituting (5.47) into (5.48) gives the internal state at relaxed hovering equilibrium $\bar{\boldsymbol{\eta}} = \boldsymbol{\phi}(\bar{\boldsymbol{x}}_{\text{in}}) = [0,\ 0,\ \bar{r} + s_n \mu \bar{V}_z]^T$.

Proposition 1: The internal dynamics of the inner-loop system are locally asymptotically stable at the relaxed trimming equilibrium $\bar{\boldsymbol{x}}_{\text{in}}$ if and only if $\chi = s_l|\chi|$ is selected such that every eigenvalue of the following $\boldsymbol{A}_1$ matrix has strictly negative real part:

$$\boldsymbol{A}_1 = \frac{s_l}{\sin(|\chi| - \zeta)} \begin{bmatrix} -\bar{r}\cos(|\chi| - \zeta) & 1 \\ -\bar{r}\Lambda & \Delta \end{bmatrix} \tag{5.50}$$

where

$$\Lambda = (A_x \bar{r} - 2a_x \bar{\omega} s_n)\sin^2\zeta + (A_y \bar{r} + 2a_y \bar{\omega} s_n)\cos^2\zeta \tag{5.51}$$

$$\Delta = -(A_x \bar{r} - 2a_x \bar{\omega} s_n)\sin\zeta \sin|\chi| + (A_y \bar{r} + 2a_y \bar{\omega} s_n)\cos\zeta\cos\chi \tag{5.52}$$

Proof. The transformation $[\boldsymbol{\eta},\ \boldsymbol{\zeta}]^T = \boldsymbol{T}(\boldsymbol{x})$ expressed as (5.43) and (5.48) is a diffeomorphism if $h_3 \sin(\zeta - |\chi|) \neq 0$. The inverse transformation $\boldsymbol{x} = \boldsymbol{T}^{-1}([\boldsymbol{\xi},\ \boldsymbol{\eta}])$ thus can be obtained as

$$\begin{bmatrix} Z \\ V_z \\ h_1 \\ h_2 \\ p \\ q \\ r \end{bmatrix} = \begin{bmatrix} \xi_1 \\ \xi_2 \\ \xi_3 \cos\chi - \eta_1 \sin\chi \\ \xi_3 \sin\chi + \eta_1 \cos\chi \\ \frac{h_3 s_n s_l(\xi_4 \cos\zeta + \eta_2 \cos\chi) + (m_v \sigma \xi_2 - \eta_3 h_3) s_l \eta_1 \cos\zeta}{h_3^2 s_n \sin(|\chi| - \zeta)} \\ \frac{h_3 s_n(\xi_4 \sin\zeta + \eta_2 \sin|\chi|) + (m_v \sigma \xi_2 - \eta_3 h_3)\eta_1 \sin\zeta}{h_3^2 s_n \sin(|\chi| - \zeta)} \\ (\eta h_3 - m_v \sigma \xi_2)/(h_3 s_n) \end{bmatrix} \tag{5.53}$$

Then the dynamic equation of the internal states is derived as

$$\dot{\boldsymbol{\eta}} = \tilde{\boldsymbol{f}}_\eta(\boldsymbol{x}; \chi) = \tilde{\boldsymbol{f}}_\eta(\boldsymbol{T}^{-1}(\boldsymbol{\eta}, \boldsymbol{\xi}); \chi) = \boldsymbol{f}_\eta(\boldsymbol{\eta}, \boldsymbol{\xi}; \chi) \tag{5.54}$$

A sufficient condition of the local stability of internal dynamics can be established via the notion of the zero dynamics [27]:

$$\dot{\boldsymbol{\eta}} = \boldsymbol{f}_\eta(\boldsymbol{\eta}, 0; \chi) \tag{5.55}$$

By substituting (5.53) into (5.55), we have:

$$\dot{\eta}_1 = \frac{\eta_2 s_n h_3^2 - \eta_1\eta_3\cos(|\chi|-\zeta)h_3}{h_3 s_n s_l \sin(|\chi|-\zeta)} \tag{5.56}$$

$$\dot{\eta}_2 = \frac{\begin{array}{c}\sin\zeta(-2a_x\bar{\omega} + A_x\eta_3)(\eta_1\eta_3\sin\zeta - \eta_2 h_3 s_n \sin|\chi|) \\ -\cos\zeta(2a_y\bar{\omega} + A_y\eta_3)(\eta_1\eta_3\cos\zeta - \eta_2 h_3 s_n\cos\chi)\end{array}}{s_l h_3 \sin(|\chi|-\zeta)} \tag{5.57}$$

$$\dot{\eta}_3 = \begin{array}{c} g m_v \sigma / h_3 - s_n \eta_3 \gamma / s_n \\ -\frac{s_l A_z(\eta_1\eta_3\cos\zeta - \eta_2 h_3 s_n \cos\chi)(\eta_1\eta_3\sin\zeta - \eta_2 h_3 s_n \sin|\chi|)}{h_3^2 \sin(|\chi|-\zeta)^2}\end{array} \tag{5.58}$$

According to the first Lyapunov criterion, the equilibrium of the nonlinear system is asymptotically stable if the linearized system is asymptotically stable [33]. At the relaxed trimming equilibrium, the internal states are $\bar{\boldsymbol{\eta}} = [0,\ 0,\ \bar{r} + s_n\mu\bar{V}_z]^T$, and the local linearized system is derived from (5.56)-(5.58) as

$$\begin{bmatrix} \dot{\eta}_1 \\ \dot{\eta}_2 \\ \dot{\eta}_3 \end{bmatrix} = \begin{bmatrix} \boldsymbol{A}_1 & \mathbf{O}_{2\times 1} \\ 0 & -\gamma/I_z \end{bmatrix} \left(\begin{bmatrix} \eta_1 \\ \eta_2 \\ \eta_3 \end{bmatrix} - \bar{\boldsymbol{\eta}} \right) \tag{5.59}$$

where $\boldsymbol{A}_1$ is expressed as per (5.50). Note that the yaw damping γ is positive definite and the system matrix of (5.59) is block diagonal. Therefore, if $\boldsymbol{A}_1$ is Hurwitz, namely every eigenvalue of $\boldsymbol{A}_1$ has strictly negative real part, then the linear system (5.59) is asymptotically stable. Subsequently the local asymptotic stability of the internal dynamics is satisfied. □

One may approximate $\bar{r}$ and $\bar{\omega}$ from (5.27) with $\boldsymbol{M}_a$ and $\boldsymbol{F}_a$ neglected:

$$\bar{r} = -s_n m_v g\sigma/\gamma,\ \bar{\omega} = \sqrt{\frac{m_v g}{2\bar{\kappa}}} \tag{5.60}$$

Remark 2: From (5.50) and (5.60) we have

$$\mathrm{Re}\left(\boldsymbol{\lambda}_{\boldsymbol{A}_1}(s_l s_n,\ |\chi|)\right) = -\mathrm{Re}\left(\boldsymbol{\lambda}_{\boldsymbol{A}_1}(-s_l s_n,\ |\chi|)\right) \tag{5.61}$$

where $\boldsymbol{\lambda}_{\boldsymbol{A}_1}$ denotes eigenvalues of $\boldsymbol{A}_1$. Note that for a specific quadrotor, the value of $s_l s_n$ is identical under both failure scenarios indicated by (5.25) and (5.26). Therefore, we can further conclude from (5.61) that $\boldsymbol{\lambda}_{\boldsymbol{A}_1}$, i.e. the stability property of internal dynamics, remain invariant despite the failure type if $|\chi|$ is fixed.

5.3. CASE STUDY: SELECTION OF $|\chi|$

As previous analysis presents, parameter $|\chi|$ need to be selected such that : (1) The matrix $\boldsymbol{A}_1$ in (5.50) is Hurwitz for stable internal dynamics. (2) Condition (5.40) is satisfied for an acceptable control effectiveness on y_2.

In this section, we conduct a case study on a specific type of quadrotor, a modified Parrot Bebop2, in the simulation to demonstrate the effect of $|\chi|$ on the overall

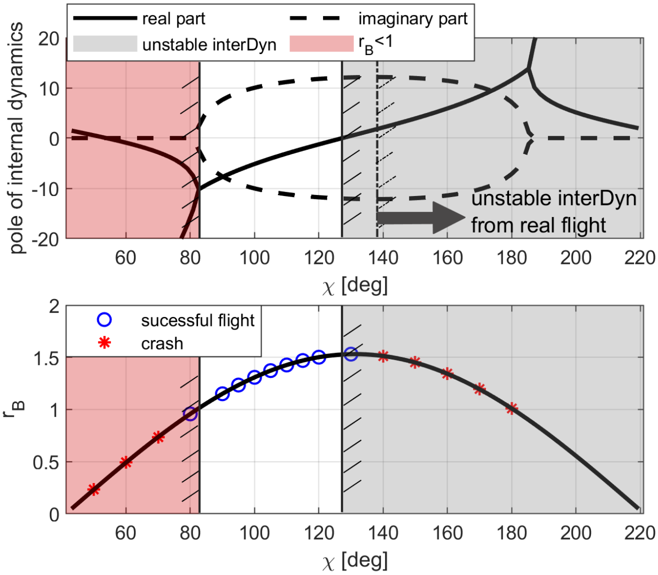

Figure 5.5: Poles of matrix $\boldsymbol{A}_1$ and r_B varying with $|\chi| \in (\zeta, \zeta+\pi)$. The unshadded area is the permitted region of $|\chi|$. Tests in the simulation are marked in the bottom plot with different symbols indicating if the flight succeeds. Unstable internal dynamic region obtained from real flight data in is shown in the top plot, which slightly moves rightward indicating a larger admissible region of $|\chi|$. Though $\boldsymbol{A}_1$ is stable in the area shaded red, crash still occurs because of $r_B < 1$ that violates the constraint (5.40).

controller performance. The inertial and geometric property of this quadrotor is listed in Table 6.1. Without loss of generality, we assume rotor 2 and 4 are removed ($s_n = -1$, $s_l = 1$, $\chi = |\chi|$). Thus from (5.60), we have $\bar{r} = 26.4$ rad/s, $\bar{\omega} = 1015$ rad/s.

The top plot in Fig. 5.5 shows the poles of $\boldsymbol{A}_1$ versus $|\chi| \in (\zeta, \zeta+\pi)$. Note that $|\chi| = \zeta + k\pi$ $(k \in \mathbb{Z})$ causes singularity as (5.50) shows. The shadded gray area represents positive real part of poles that render unstable internal dynamics. The bottom plot in Fig. 5.5 presents $r_B(|\chi|)$ as given in (5.40) with different $|\chi|$. The shaded red represents the violation of the constraint $r_B \geq 1$.

In the simulation, the quadrotor is commanded to transfer from $X = 0$ to $X = 3$ m at $t = 1$ s. Various selections of $|\chi|$ are tested and given in the bottom plot of Fig. 5.5. The flights within the unshaded area succeed in conducting the transfer maneuver, whereas most of those in the shaded area failed.

Three tests in the simulation with respective $|\chi|$ equal to 70, 105, and 140 degrees are further demonstrated. Fig. 5.6 shows the time series of output y_2, internal state η_1, and $u_1 - u_2$ of these three flights. When $|\chi| = 105$ deg, the transition is successful where both y_2 and internal states η_1 converge to zero. As $|\chi| = 70$ deg, the

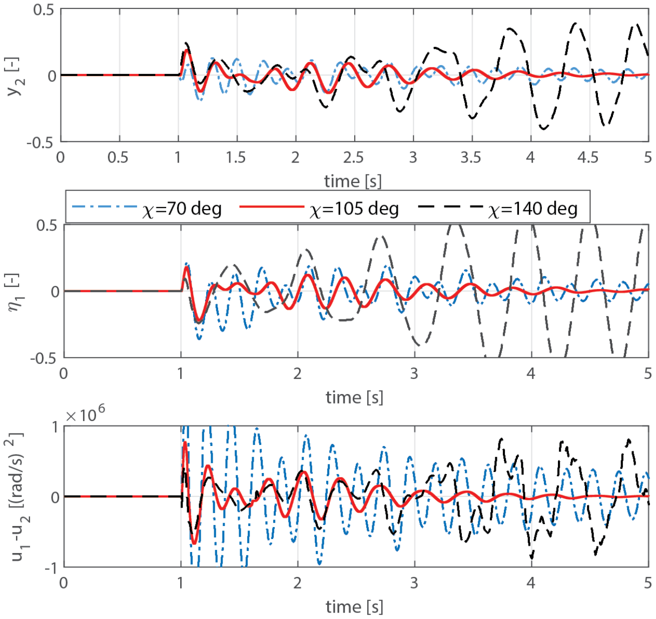

Figure 5.6: Time series of y_2, η_1, and $u_1 - u_2$ of three tests with different $|\chi|$ in the simulation. A step-input of position command is given at $t = 1$ s.

violation of constraint $r_B \le 1$ leads to a small control effectiveness $\hat{B}_2$. As a result, $u_1 - u_2$ significantly oscillates during the maneuver and the drone crashed due to limited actuator dynamics. On the other hand, when $|\chi| = 140$ deg, the internal dynamics are unstable and divergent oscillation of η_1 occurs that makes the drone crash.

6. GENERALIZATION TO OTHER FAILURE CONDITIONS

In this section, the inner-loop control scheme introduced in Sec. 4 is generalized to a quadrotor with complete loss of a single rotor, or without rotor failure (nominal condition).

6.1. SINGLE ROTOR FAILURE

INTERNAL DYNAMICS ANALYSIS

For a quadrotor with a single rotor failure, there are three permitted inputs. Therefore, three outputs can be defined. Similar to the double-rotor-failure condition, one output is defined as the altitude:

$$y_1 = Z \tag{5.62}$$

The other two outputs are related to the reduced attitude control:

$$y_2 = h_1 - n_x^B \tag{5.63}$$

$$y_3 = h_2 - n_y^B \tag{5.64}$$

To align the body fixed unit vector $\boldsymbol{n}^B = [n_x^B,\ n_y^B,\ n_z^B]^T$ with the reference $\boldsymbol{n}_d^B = [h_1,\ h_2,\ h_3]^T$, the preceding y_2 and y_3 should be stabilized to zero.

The relative degrees of the inner-loop system are $\rho_1 = \rho_2 = \rho_3 = 2$ from (5.27). Therefore, the external states are

$$\begin{bmatrix} \xi_1 \\ \xi_2 \\ \xi_3 \\ \xi_4 \\ \xi_5 \\ \xi_6 \end{bmatrix} = \begin{bmatrix} y_1 \\ \dot{y}_1 \\ y_2 \\ \dot{y}_2 \\ y_3 \\ \dot{y}_3 \end{bmatrix} = \begin{bmatrix} Z \\ V_z \\ h_1 - n_x^B \\ -h_3 q + h_2 r \\ h_2 - n_y^B \\ h_3 p - h_1 r \end{bmatrix} \tag{5.65}$$

Note that $\boldsymbol{x}_{\text{in}} \in \mathbb{R}^7$ and there are 6 external states, the only internal state can be selected as

$$\eta_1 = r + \mu_1 V_z + \mu_2 p + \mu_3 q \tag{5.66}$$

where μ_1, μ_2, μ_3 are calculated such that $\dot{\eta}_1$ does not include the control input. These coefficients are constant and related to the handedness of the remaining rotors.

After some tedious algebra, the zero dynamics can be calculated as

$$\dot{\eta}_1 = -\frac{\gamma}{\Theta}\eta_1 + \frac{\Pi}{h_3\Theta^2}\eta_1^2 + g\mu_1 \tag{5.67}$$

where

$$\Theta = n_x^B \mu_2 / h_3 + n_y^B \mu_3 / h_3 + 1 \tag{5.68}$$

$$\Pi = A_z n_x^B n_y^B / h_3 + A_x n_y^B \mu_2 + A_y n_x^B \mu_3 \tag{5.69}$$

Particularly, when $n_x^B = n_y^B = 0$, namely the drone spins about it thrust direction, we have

$$\dot{\eta}_1 = -\gamma(\eta_1 - \bar{\eta}_1) \tag{5.70}$$

Since the yaw damping $\gamma > 0$, the internal state η_1 at the equilibrium $\bar{\eta}_1$ is stable.

CONTROL LAW

The above analysis demonstrates that the stability of internal dynamics with the selection of outputs in (5.62)-(5.64). After selecting the control outputs, the same control scheme presented in Fig. 5.2 can be applied for the single rotor failure condition. Without loss of generality, we assume that rotor 4 is removed, then we have

$$\boldsymbol{u} = [\omega_1^2,\ \omega_2^2,\ \omega_3^2]^T \tag{5.71}$$

Table 5.1: Parameters of the tested quadrotor.

par.	value	unit	par.	value	unit
I_x	$1.45e^{-3}$	kg· m^2	m_v	0.410	kg
I_y	$1.26e^{-3}$	kg· m^2	b	0.145	m
I_z	$2.52e^{-3}$	kg· m^2	β	52.6	deg
I_p	$8.00e^{-6}$	kg· m^2	γ	$1.50e^{-3}$	N·m·s
$\bar{\kappa}$	$1.90e^{-6}$	kg· m^2	σ	0.01	m

With the same procedure introduced in Sec. 4, the control law for a quadrotor subjected to a single rotor failure can be obtained using (5.22), where

$$\boldsymbol{\nu} = \begin{bmatrix} -k_{z,p}(\xi_1 - Z_{\text{ref}}) - k_{z,d}(\xi_2 - \dot{Z}_{\text{ref}}) + \ddot{Z}_{\text{ref}}) \\ -k_{a,p}\xi_3 - k_{a,d}\xi_4 \\ -k_{a,p}\xi_5 - k_{a,d}\xi_6 \end{bmatrix} \tag{5.72}$$

$$\ddot{\boldsymbol{y}}_f = [\dot{a}_{z,f}/R_{33,f},\ \ddot{h}_{1,f},\ \ddot{h}_{2,f}]^T \tag{5.73}$$

The control effectiveness matrix $\hat{\mathscr{B}}$ can be estimated using (5.5) and (5.6):

$$\hat{\mathscr{B}}(\boldsymbol{x}_f) = \begin{bmatrix} -\bar{\kappa}R_{33,f}/m_v & -\bar{\kappa}R_{33,f}/m_v & -\bar{\kappa}R_{33,f}/m_v \\ -\bar{\kappa}b\sin\beta & \bar{\kappa}b\sin\beta & \bar{\kappa}b\sin\beta \\ \bar{\kappa}b\cos\beta & \bar{\kappa}b\cos\beta & -\bar{\kappa}b\cos\beta \end{bmatrix} \tag{5.74}$$

6.2. WITHOUT ROTOR FAILURE

For a multi-rotor drone with more than three actuators, such as a nominal quadrotor or a hexacopter, there are four or more permitted control inputs. We can then introduce the fourth output related to the yaw control:

$$y_4 = r \tag{5.75}$$

An independent yaw controller can be appended to provide the reference yaw rate r_{ref}, such as a PD controller:

$$r_{\text{ref}} = -k_{p,\psi}e_\psi - k_{d,\psi}\dot{e}_\psi \tag{5.76}$$

where e_ψ is the yaw angle tracking error; $k_{p,\psi}$ and $k_{d,\psi}$ are positive gains.

Note that the rotor angular acceleration $\dot{\omega}_i$ may deteriorate the yaw control performance while implementing this approach. Interested readers are referred to [21] to tackle this problem for a nominal quadrotor.

Table 5.2: Control gains.

outer	k_p [s^{-2}]	k_i [s^{-3}]	k_d [s^{-1}]	
-loop	1.0	0.1	1.0	
inner	$k_{a,p}$ [s^{-2}]	$k_{a,d}$ [s^{-1}]	$k_{z,p}$ [s^{-2}]	$k_{z,d}$ [s^{-1}]
-loop	50	30	15	10

7. EXPERIMENTAL VALIDATION

The proposed control method has been validated on a modified Parrot Bebop2 drone with a lighter battery and camera module removed. The geometric and moment of inertia properties are given in Table 6.1. During the flight test, a motion capturing system (OptiTrack) with 12 cameras provided the position measurements of the 4 markers attached to the drone at 120 Hz. The inertial measurement unit (IMU) measured the angular rates (from gyroscope) and the specific force (from the accelerometer) at 512 Hz. A built-in brushless DC (BLDC) motor controller controled the rotor speeds of each propeller, and also measured the rotor rotational rates in RPM at 512 Hz. Subsequently, an Extended Kalman Filter (EKF) was implemented to estimate the position, velocity of the center of mass, and the attitude of the body frame. The proposed controller and the EKF were run onboard at 500 Hz with the original processor Parrot P7 dual-core CPU Cortex 9. The control gains are given in Table 5.2.

7.1. FLIGHTS WITH DOUBLE AND SINGLE ROTOR FAILURE

The first set of flights tested the 3-D trajectory tracking of the quadrotor without wind disturbance. Fig. 5.7 presents snapshots of the tested quadrotor with double/single rotor failure within 0.3 s. In Fig. 5.8, the reference position together with the measured position of the quadrotor with double/single rotor failure are given.

Without loss of generality, we removed the rotor 1 and rotor 3 for the double rotor failure case. Fig. 5.9a shows the second output y_2 and the first internal state η_1.

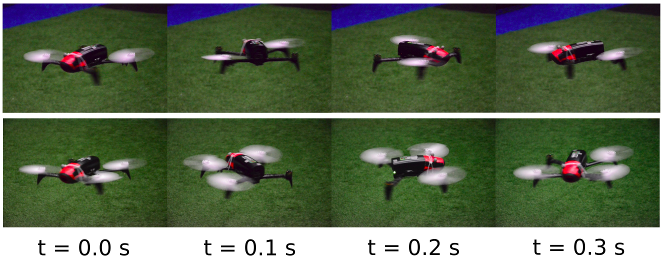

Figure 5.7: Snapshot of the tested Bebop2 subjected to failures of rotor 1 & 3 (upper row), and subjected to failure of rotor 3 (bottom row).

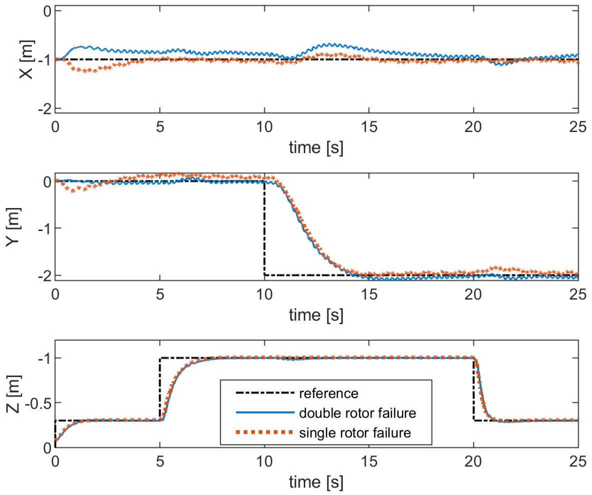

Figure 5.8: Position tracking task under windless condition. The double-rotor-failure condition (blue solid line) and single rotor failure condition (red dash line) to track the reference position (black dot dash line).

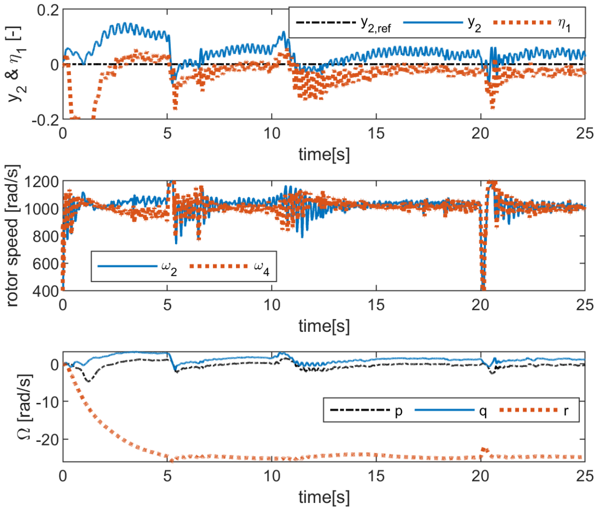

Figure 5.9: Variables during the position tracking flight test with failures of rotor 1 and rotor 3. From top to bottom are: the output y_2 and internal state η_1; the angular speed measurements of the rotor 2 and rotor 4; the angular rates measurements.

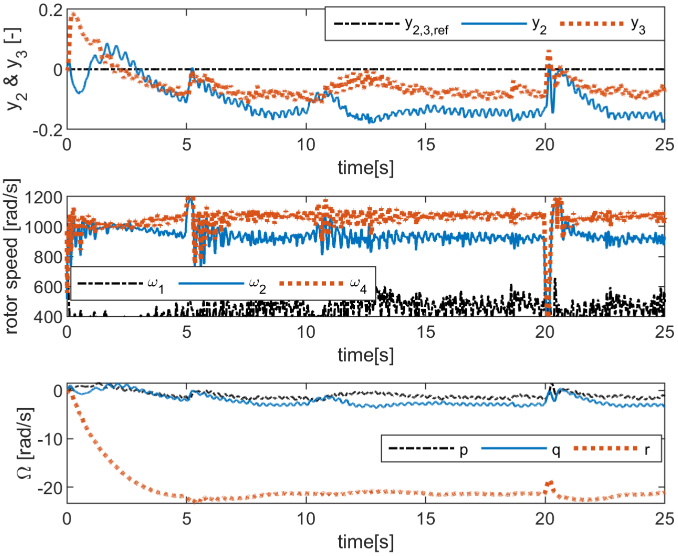

Figure 5.10: Variables during the position tracking flight test with failure of rotor 3. From top to bottom are: the output y_2 and y_3; the angular speed measurements of the rotor 1, 2, and 4; the angular rates measurements.

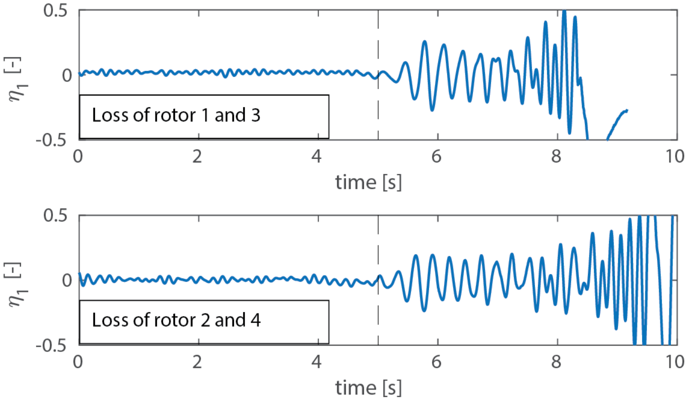

Figure 5.11: Internal state η_1 in with different selection of $|\chi|$. Before $t = 5$ s, $|\chi| = 90$ deg is selected which leads to stable internal dynamics in both conditions. After $t = 5$ s, $|\chi|$ is changed to 180 deg and the internal dynamics become unstable.

As is introduced in Sec. 4, they represent the reduced attitude and need to converge to zero. Despite the misalignment during the take-off maneuver at the first 3 seconds, a slight tracking error of y_2 is observed which is presumably due to the bias of the center of mass. In this flight, $|\chi| = 90$ deg was selected for stable internal dynamics. Consequently, the internal state η_1 was confined around zero. Fig. 5.9b shows the angular speeds of rotor 2 and 4 that remained almost constant at $\bar{\omega} = 1000$ rad/s during the horizontal maneuvers, which was in-line with the *Assumption* 3. A yaw rate at about −25 rad/s shown in Fig. 5.9c indicates the fast spinning motion of the damaged quadrotor.

With the same controller and the same set of gains, the condition with single rotor failure was also tested. The rotor 3 was removed in this test. As is shown in Fig. 5.10a, the internal state η_1 is replaced by the third output y_3 because of the addition of one rotor compared to the double-rotor-failure condition. The reference $y_{2,\text{ref}} = y_{3,\text{ref}} = 0$ was employed in this flight that required the rotor 1 (the one diagonal to the failed rotor) to generate no force. However, due to the lower saturation of rotor 1 presented in Fig. 5.10b, a constant tracking error of y_2 and y_3 are observed. In spite of these attitude tracking errors, the drone under both single/double rotor failure cases were able to track the position commands.

7.2. EFFECT OF χ IN THE DOUBLE-ROTOR-FAILURE CONDITION

The quadrotor in the double-rotor-failure condition was tested in the hover region with different sets of $|\chi|$ to experimentally demonstrate its effect on the stability of the internal dynamics. Fig. 5.11 shows the internal state η_1 during a hovering flight where the parameter $|\chi|$ was initialized at 90 deg which would lead to stable internal dynamics. At $t = 5$ s, $|\chi|$ was changed to 180 deg during the flight

Figure 5.12: Snapshot of the tested quadrotor in the wind tunnel, with removal of rotor 1 and 3.

and the internal state became unstable. This complies with the prediction from *Proposition 1*.

It is noteworthy that the stable region boundary moves slightly to the right compared to the theoretical prediction, as is shown in Fig. 5.5. As a consequence, the admissible region of $|\chi|$ becomes larger. The difference might come from the omission of the aerodynamic damping on pitch and roll rate while conducting internal dynamic analysis.

8. VALIDATIONS IN A WIND TUNNEL

To validate the robustness against unmodeled aerodynamic forces and moments in the high-speed flight regime, flight tests have been carried out in the Open Jet Facility (OJF), a large scale wind tunnel with an aperture of 2.85 meters (see Fig. 5.12). The parameter $|\chi| = 105$ deg that lies roughly in the center of its admissible region is selected, as Fig. 5.5 illustrates.

The linear quadratic regulator (LQR) is selected as the baseline for comparison in the wind tunnel. This method has been validated in practice in a milestone research paper [14]. The same set of gains from this chapter were implemented for comparison. Specifically, the cost on control inputs was set to one; the cost on the reduced attitude was set to 20 and the cost on angular rates was set to zero. Since a different drone was used, the time constant of the first-order actuator model is set as 30 ms that differs from the literature. Both INDI and LQR used the same outer-loop control gains as given in Table. 5.2.

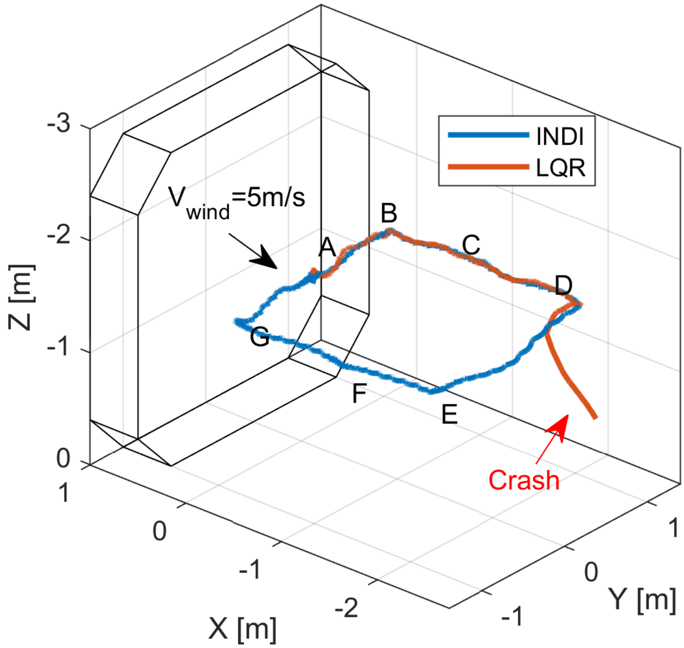

Figure 5.13: 3D trajectories of the damaged quadrotor under $V_{\text{wind}} = 5$ m/s, where A to G represent the setpoints. INDI finished the trajectory tracking task while LQR failed during the transition from setpoint D to E.

Table 5.3: Maximum flight speed of the INDI and LQR controller with various control gains. Q for LQR indicates the cost on the reduced attitude.

INDI			LQR	
$k_{a,p}$ [s^{-2}]	$k_{a,d}$ [s^{-1}]	$V_{\max}$ [m/s]	Q [−]	$V_{\max}$ [m/s]
5	1	7.8	1	4.6
10	2	8.3	3	5.9
50*	30*	8.8	10	5.2
100	30	8.2	20*	5.1
200	50	7.8	30	6.3

*Gains for the trajectory tracking task.

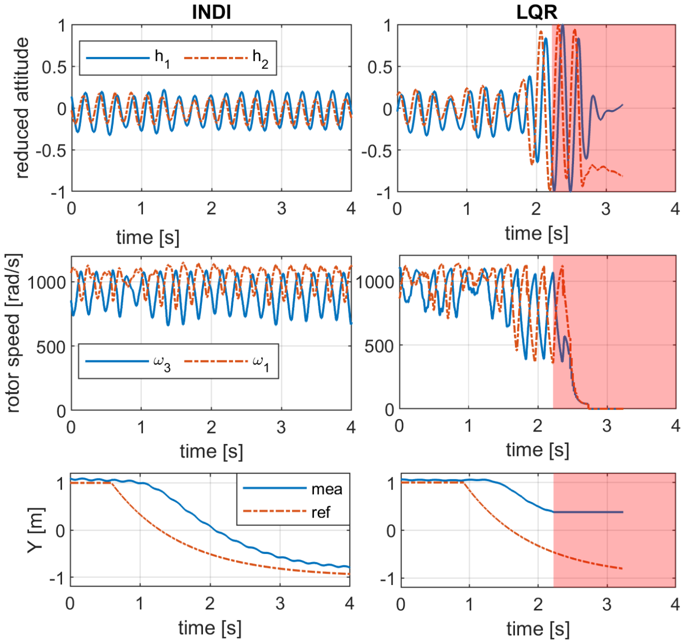

Figure 5.14: Reduced attitude, rotor speeds and lateral position Y of the quadrotor during the transition from setpoint D to E. The reduced attitude of the drone controlled by LQR became unstable, before the loss of OptiTrack measurement shaded in red, and eventually crashed. In comparison, the drone controlled by the INDI approach succeed to finish this maneuver.

8.1. TRAJECTORY TRACKING TASK

A trajectory tracking task was performed under a wind flow of 5 m/s. The wind flow was along the negative direction of the $\boldsymbol{x}_I$ axis. Fig. 5.13 plots the trajectories using INDI and LQR respectively. The drone tracked setpoints A to G in sequence every 3 seconds. In addition, the step reference positions (X_{ref} and Y_{ref}) were smoothed by a first-order filter with a time constant 1 s. As Fig. 5.13 shows, both methods successfully tracked the setpoints before point D. However, the LQR approach failed during the transition from setpoint D to E, which was perpendicular to the wind flow.

Fig. 5.14 compares states between the two approaches in this period. From the plotted data, we can find that the reduced attitudes of both methods were bounded before conducting the maneuver, despite oscillations of reduced attitude and rotor speeds caused by the wind flow and yaw motion. During the maneuver from point D to E, the reduced attitude of the LQR approach diverged from zero (the linearization point). The instability of the inner-loop attitude control caused the failure of trajectory tracking and eventually lead to a crash.

For LQR, the rotor speed commands (i.e. the control input) were naturally amplified (at around $t = 2$ s in the mid-right plot of Fig. 5.14) to stabilize the reduced attitudes (h_1 and h_2) as they were diverging from the equilibrium (top-right plot). These increase of control input may destabilize the system in the presence of nonlinearities and model uncertainties caused by the wind flow. By contrast, the INDI approach used the second-order derivative of the reduced attitude ($\boldsymbol{y}_f^{(\boldsymbol{\rho})}$ in (5.22)) to compensate for the model uncertainties. The nonlinearities are also handled by the feedback linearization step of INDI. Thereby the reduced attitude can be stabilized without drastically increasing the control input.

8.2. MAXIMUM FLIGHT SPEED TEST

To explore the maximum flight speed of a quadrotor under the failure of two opposing rotors, maximum speed flight tests were conducted using both INDI and LQR. During the entire flight, the drone was hovering at a setpoint located in front of the wind tunnel ($\boldsymbol{P}_{\text{ref}} = [0,\ 0,\ -1.5]^T$). The wind speed was gradually increased from $V_{\text{wind}} = 0$ to a V_{max} until the drone crashed.

Table. 5.3 compares the maximum flight speed achieved by the two approaches with different set of gains. Similarly to the trajectory tracking task in the preceding section, INDI outperforms the LQR approach in terms of maximum flight speed. Be that as it may, the drone controlled by LQR was still stabilized at relatively high-speeds thanks to the inherent stabilizing property of feedback control.

Fig. 5.15 shows the time series of position, η_1, y_2, rotor speeds and wind speed during a flight controlled by INDI, where the drone crashed at $V_{\text{wind}} = 8.8$ m/s when $t = 107$ s. The variations of η_1, y_2 and rotor speeds significantly increased with the wind speed. Despite the gradual increase of the oscillation, the internal state η_1 was bounded near zero and subsequently ensured successful position tracking.

To investigate the cause of loss-of-control of INDI, Fig. 5.16 shows the close-up of Fig. 5.15 during the last 7 seconds before the crash. In addition to the rotor speed

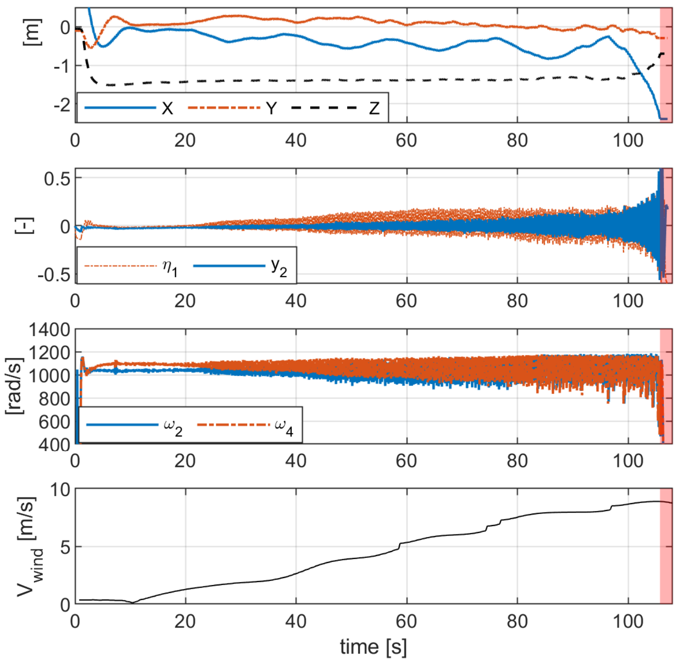

Figure 5.15: Variables during the wind-tunnel maximum flight speed test of INDI. From top to bottom are: positions of the drone; the internal state η_1 and the output y_2; the angular speed of the remaining rotor (rotor 2 & 4); the time series of the wind speed which gradually increased until the loss-of-control happened. The red area represents loss of OptiTrack measurement.

measurements, the rotor speed commands are also plotted. From the reduction of X in the top plot, we can find that the quadrotor was blown away from the setpoint along the wind flow. Meanwhile, the increase of Z indicates the continues reduction of the altitude in this process. These phenomena are believed caused by the saturation of motors under wind resistance, which can be clearly seen in the bottom two plots of Fig. 5.16. In addition to the motor saturation, the control input lag due to motor dynamics can be observed, which may cause the gradual divergence of η_1 ad y_2 in the second plot of Fig. 5.16. We hence infer that the motor capacity (bandwidth and power limit) is a major limiting factor of the maximum flight speed.

8.3. HIGH-SPEED FLIGHT WITH IMPERFECT STATE ESTIMATIONS

Since the ultimate goal of this work is improving drone safety during the high-speed flight in outdoor environments, preliminary validations of the proposed method using imperfect state estimations have been conducted in the wind-tunnel. The

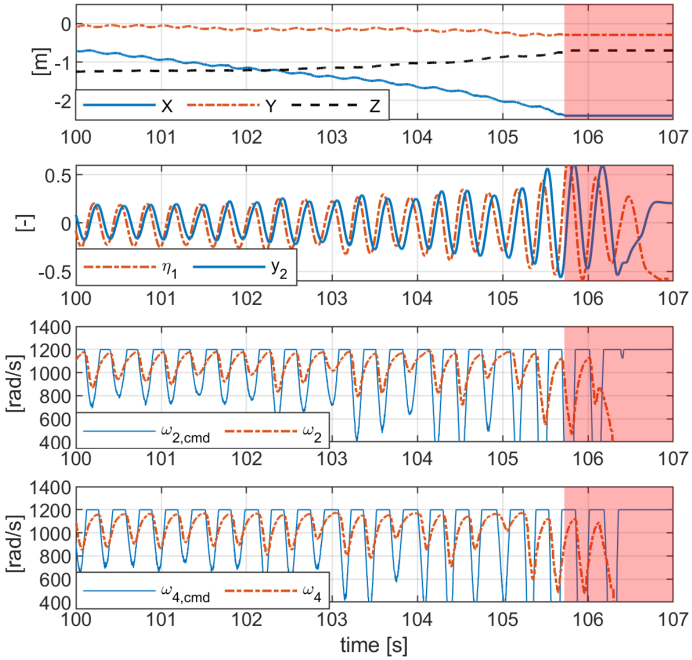

Figure 5.16: Close-up of the variables of Fig. 5.15 during last 7 seconds before the crash. The red area represents loss of OptiTrack measurement.

sampling rate of the motion capturing system was reduced from 120 Hz to 10 Hz to simulate GPS-like update rates. Only position measurements were transmitted to the onboard flight controller. A complementary filter [35] was implemented by fusing the measurements from the IMU and the magnetometer, to provide attitude estimates.

In this setting, the INDI controlled drone achieved controlled flight at 8.4 m/s inside the wind tunnel, indicating robustness to significant attitude estimation errors. These errors can be seen in Fig. 5.17, which compares the pitch and roll angles from the onboard complementary filter with the ground truth obtained with the OptiTrack system at three different flight speeds. As a consequence, the tracking errors of the reduced attitude were greater using the onboard complementary filter, especially at 0m/s and 5m/s as Fig. 5.18 shows. Note that the increase of tracking error was less apparent at 8m/s where the drone was near the flight envelope boundary, because the controller performance was not only degraded by imperfect state estimations, but also motor limitations.

We hypothesize that the degradation of the complementary filter is caused by the strong aerodynamic forces and centrifugal forces measured by the accelerom-

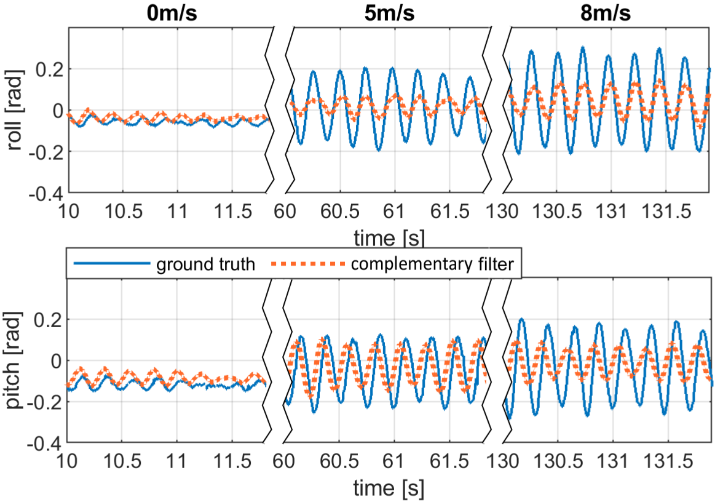

Figure 5.17: Comparison of pitch and roll estimations between the complementary filter and the ground truth in different flight speeds demonstrating degradation of the compensatory filter at these condition.

eters. Improving the accuracy of the state estimator at high flight speeds and high angular rate conditions is out of the scope of this work, but it is a highly recommended future research.

9. CONCLUSIONS

In this research, an incremental nonlinear fault-tolerant control method is developed for a quadrotor subjected to complete loss of two opposing rotors. The internal dynamics of this under-actuated control problem is analyzed. Thereby a criterion is given to select proper control outputs that guarantee the stability of internal dynamics, which has been validated in both simulations and flight tests. The control scheme can be generalized to a nominal quadrotor, or one with the loss of a single rotor.

The proposed method uses the incremental nonlinear dynamic inversion (INDI) approach to control the selected outputs. The INDI approach replaces non-input related model terms with sensor measurements, which reduces the model dependencies and consequently increases the robustness against wind disturbances in the high-speed flight regime. Flight tests of a quadrotor with complete loss of two opposing rotors are conducted in an open jet wind tunnel. In the presence of significant aerodynamic effects, the control method is able to stabilize the quadrotor at over 8.0 m/s. Compared with the linear quadratic regulator (LQR) approach, the proposed method was found to have better robustness against model uncertainties

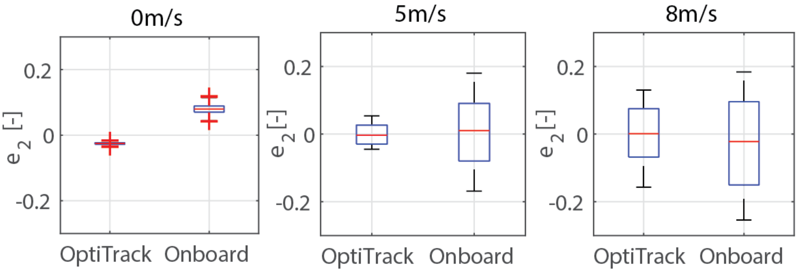

Figure 5.18: Boxplots comparing the tracking error of y_2, denoted by e_2, between flights with OptiTrack aided attitude estimation and those with onboard complementary filter, in different flight speeds.

brought by the significant aerodynamic effects.

Flights with imperfect state estimations from onboard sensors have been conducted. Flight data in the high-speed regime with onboard sensors reveal the adverse effects of aerodynamics on the state estimation. Future work is recommended to focus on improving the attitude estimation using onboard sensors by taking into account the effect of aerodynamics and high angular rate motion on the state estimator.

REFERENCES

[1] T. Li, Y. Zhang, and B. W. Gordon, *Passive and active nonlinear fault-tolerant control of a quadrotor unmanned aerial vehicle based on the sliding mode control technique,* Proceedings of the Institution of Mechanical Engineers, Part I: Journal of Systems and Control Engineering **227**, 12 (2013).

[2] L. Besnard, Y. B. Shtessel, and B. Landrum, *Quadrotor vehicle control via sliding mode controller driven by sliding mode disturbance observer,* Journal of the Franklin Institute **349**, 658 (2012).

[3] X. Wang, S. Sun, E.-J. van Kampen, and Q. Chu, *Quadrotor fault tolerant incremental sliding mode control driven by sliding mode disturbance observers,* Aerospace Science and Technology **87**, 417 (2019).

[4] X. Wang, E.-J. van Kampen, and Q. Chu, *Quadrotor fault-tolerant incremental nonsingular terminal sliding mode control,* Aerospace Science and Technology **95**, 105514 (2019).

[5] A. Lanzon, A. Freddi, and S. Longhi, *Flight control of a quadrotor vehicle subsequent to a rotor failure,* Journal of Guidance, Control, and Dynamics **37**, 580 (2014).

[6] V. Lippiello, F. Ruggiero, and D. Serra, *Emergency landing for a quadrotor in case*

of a propeller failure: A backstepping approach, in *2014 IEEE/RSJ International Conference on Intelligent Robots and Systems* (IEEE, 2014) pp. 4782–4788.

[7] V. Lippiello, F. Ruggiero, and D. Serra, *Emergency landing for a quadrotor in case of a propeller failure: A pid based approach,* in *2014 IEEE International Symposium on Safety, Security, and Rescue Robotics (2014)* (IEEE, 2014) pp. 1–7.

[8] P. Lu and E.-J. van Kampen, *Active fault-tolerant control for quadrotors subjected to a complete rotor failure,* in *2015 IEEE/RSJ International Conference on Intelligent Robots and Systems (IROS)* (IEEE, 2015) pp. 4698–4703.

[9] Y. V. Morozov, *Emergency control of a quadrocopter in case of failure of two symmetric propellers,* Automation and Remote Control **79**, 463 (2018).

[10] C. de Crousaz, F. Farshidian, M. Neunert, and J. Buchli, *Unified motion control for dynamic quadrotor maneuvers demonstrated on slung load and rotor failure tasks,* in *2015 IEEE International Conference on Robotics and Automation (ICRA)* (IEEE, 2015) pp. 2223–2229.

[11] M. W. Mueller and R. D'Andrea, *Stability and control of a quadrocopter despite the complete loss of one, two, or three propellers,* in *2014 IEEE International Conference on Robotics and Automation (ICRA)* (IEEE, 2014) pp. 45–52.

[12] A.-R. Merheb, H. Noura, and F. Bateman, *Emergency control of ar drone quadrotor uav suffering a total loss of one rotor,* IEEE/ASME Transactions on Mechatronics **22**, 961 (2017).

[13] J. Stephan, L. Schmitt, and W. Fichter, *Linear parameter-varying control for quadrotors in case of complete actuator loss,* Journal of Guidance, Control, and Dynamics **41**, 2232 (2018).

[14] M. W. Mueller and R. D'Andrea, *Relaxed hover solutions for multicopters: Application to algorithmic redundancy and novel vehicles,* The International Journal of Robotics Research **35**, 873 (2016).

[15] W. Zhang, M. W. Mueller, and R. D'Andrea, *A controllable flying vehicle with a single moving part,* in *2016 IEEE International Conference on Robotics and Automation (ICRA)* (IEEE, 2016) pp. 3275–3281.

[16] C. Russell, J. Jung, G. Willink, and B. Glasner, *Wind tunnel and hover performance test results for multicopter UAS vehicles,* Annual Forum Proceedings - AHS International (2016).

[17] S. Sun, C. C. de Visser, and Q. Chu, *Quadrotor Gray-Box Model Identification from High-Speed Flight Data,* Journal of Aircraft **56**, 645 (2019).

[18] S. Sieberling, Q. Chu, and J. Mulder, *Robust flight control using incremental nonlinear dynamic inversion and angular acceleration prediction,* Journal of guidance, control, and dynamics **33**, 1732 (2010).

[19] P. Acquatella, W. Falkena, E.-J. van Kampen, and Q. P. Chu, *Robust nonlinear spacecraft attitude control using incremental nonlinear dynamic Inversion. AIAA Guidance, Navigation, and Control Conference,* (2012).

[20] P. Simplício, M. Pavel, E.-J. van Kampen, and Q. Chu, *An acceleration measurements-based approach for helicopter nonlinear flight control using Incremental Nonlinear Dynamic Inversion,* Control Engineering Practice **21**, 1065 (2013).

[21] E. J. Smeur, Q. Chu, and G. C. de Croon, *Adaptive incremental nonlinear dynamic inversion for attitude control of micro air vehicles,* Journal of Guidance, Control, and Dynamics **39**, 450 (2016).

[22] E. J. Smeur, G. C. de Croon, and Q. Chu, *Gust disturbance alleviation with Incremental Nonlinear Dynamic Inversion,* in *2016 IEEE/RSJ International Conference on Intelligent Robots and Systems (IROS)* (IEEE, 2016) pp. 5626–5631.

[23] E. Tal and S. Karaman, *Accurate tracking of aggressive quadrotor trajectories using incremental nonlinear dynamic inversion and differential flatness,* IEEE Transactions on Control Systems Technology (2020).

[24] S. Sun, L. Sijbers, X. Wang, and C. de Visser, *High-speed flight of quadrotor despite loss of single rotor,* IEEE Robotics and Automation Letters **3**, 3201 (2018).

[25] X. Yun and Y. Yamamoto, *Internal dynamics of a wheeled mobile robot,* in *Proceedings of 1993 IEEE/RSJ International Conference on Intelligent Robots and Systems (IROS '93),* Vol. 2 (IEEE, 1993) pp. 1288–1294.

[26] F. Lewis, A. Das, and K. Subbarao, *Dynamic inversion with zero-dynamics stabilisation for quadrotor control,* IET Control Theory Applications **3**, 303 (2009).

[27] E. M. Wallner and K. H. Well, *Attitude Control of a Reentry Vehicle with Internal Dynamics,* Journal of Guidance, Control, and Dynamics **26**, 846 (2003).

[28] G. M. Hoffmann, H. Huang, S. L. Waslander, and C. J. Tomlin, *Precision flight control for a multi-vehicle quadrotor helicopter testbed,* Control Engineering Practice **19**, 1023 (2011).

[29] R. Mahony, V. Kumar, and P. Corke, *Multirotor aerial vehicles: Modeling, estimation, and control of quadrotor,* IEEE Robotics and Automation magazine **19**, 20 (2012).

[30] S. Sun and C. de Visser, *Aerodynamic model identification of a quadrotor subjected to rotor failures in the high-speed flight regime,* IEEE Robotics and Automation Letters **4**, 3868 (2019).

[31] N. A. Chaturvedi, A. K. Sanyal, and N. H. McClamroch, *Rigid-body attitude control,* IEEE control systems magazine **31**, 30 (2011).

[32] X. Wang, E.-J. van Kampen, Q. Chu, and P. Lu, *Stability Analysis for Incremental Nonlinear Dynamic Inversion Control,* Journal of Guidance, Control, and Dynamics **42**, 1116 (2019).

[33] H. K. Khalil, *Nonlinear Systems* (Prentice-Hall, 2002).

[34] X. Wang, E.-J. van Kampen, Q. Chu, and P. Lu, *Incremental Sliding-Mode Fault-Tolerant Flight Control,* Journal of Guidance, Control, and Dynamics **42**, 244 (2019).

[35] R. Mahony, T. Hamel, and J.-M. Pflimlin, *Nonlinear complementary filters on the special orthogonal group,* IEEE Transactions on Automatic Control **53**, 1203 (2008).

6

UPSET RECOVERY CONTROL FOR QUADROTORS SUBJECTED TO A COMPLETE ROTOR FAILURE FROM LARGE INITIAL DISTURBANCES

In this chapter, we will introduce a novel fault-tolerant controller that is able to recover a quadrotor from arbitrary initial orientations and angular velocities, despite the complete failure of a rotor. This cascaded control method includes a position/altitude controller, an almost-global convergence attitude controller, and a control allocation method based on quadratic programming. As a major novelty, a constraint of undesirable angular velocity is derived and fused into the control allocator, which significantly improves the recovery performance. For validation, we have conducted a set of Monte-Carlo simulation to test the reliability of the proposed method of recovering the quadrotor from arbitrary initial attitude/rate conditions. In addition, real-life flight tests have been performed. The results demonstrate that the post-failure quadrotor can recover after being casually tossed into the air.

Parts of this chapter have been published in:

S. Sun, M. Baert, B. A. S. van Schijndel, and C. de Visser, "Upset Recovery Control for Quadrotors Subjected to a Complete Rotor Failure from Large Initial Disturbances," In 2020 IEEE International Conference on Robotics and Automation (ICRA) (pp. 4273-4279). IEEE.

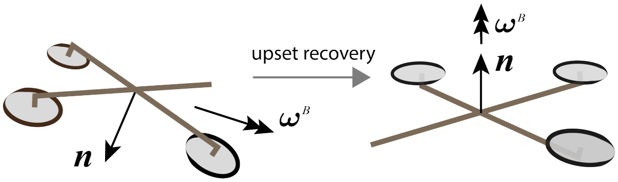

Figure 6.1: Illustration of the upset recovery problem where $\boldsymbol{n}$ indicates the total thrust direction and $\boldsymbol{\omega}^B$ indicates the vehicle angular velocity.

1. INTRODUCTION

In recent years, multi-rotor aerial vehicles have received a lot of attention. These aerial vehicles are usually unmanned robots that can perform various tasks, in some cases without human intervention. Multi-rotors are mainly used outdoors for agricultural purposes, architecture and construction, delivery, emergency services, media purposes or to monitor and conserve the environment. As these vehicles will become more involved in daily life, safety can not be overlooked.

One of the most common multi-rotors is the quadrotor due to its simplicity and energy efficiency [1]. As the name implies, a quadrotor has four rotors positioned in a rectangular profile on the vehicle. However, because this vehicle is not overactuated, this type of multi-rotor suffers most from an actuator failure and might not be able to continue its mission or worse, might not be able to land safely.

1.1. FAULT-TOLERANT CONTROL

Fault-tolerant control (FTC) for quadrotors has been the subject of various literature sources. Some research is focused on the partial damage of a rotor [2, 3], while other research considers the complete loss of one or multiple rotors. A solution to the case of a complete loss of a rotor is presented in [4] where the author proposes to give up on yaw control to maintain control over the other states. An analytical solution under the complete loss of one, two or three propellers are given in [5, 6]. A PID and a backstepping approach focusing on an emergency landing in case of failure is presented in [7, 8] respectively. A fault-tolerant controller using incremental nonlinear dynamic inversion (INDI) is given in [9] where fault detection is also implemented. To improve the robustness of the controller, [10] employs a nonsingular terminal sliding mode control (NTSMC) to this fault-tolerant control problem.

The validations in practice are carried out by [5] using the linear quadratic regulator (LQR) around the proposed analytical equilibrium. To improve the stability under various yaw rates, the study in [11] employs a linear parameter varying (LPV) controller. In [12], a quadrotor with loss of single rotor controlled by INDI is shown able to fly in high-speed conditions despite significant aerodynamic disturbances.

1.2. UPSET RECOVERY

Upset recovery is a technique extensively studied for improving aviation safety [13, 14]. The upset condition is defined as "any uncommanded or inadvertent event with an abnormal aircraft attitude, angular rate, acceleration, airspeed, or flight trajectory [15]", such as aircraft stall that directly leads to loss-of-control [16]. In comparison, upset of a multi-rotor drone is rarely heard by virtue of its relatively high control effectiveness in full flight envelope. For example, a quadrotor can easily perform aerobatic maneuvers [17].

However, due to the significant maneuverability reduction, a quadrotor with single-rotor-failure can easily enter an upset condition. For instance, as Fig. 6.1 shows, a post-failure quadrotor may be upside down and fast rotating before the FTC is triggered, because of strong wind disturbances and delay of the fault detection module. At this moment, existing FTC methods could fail owing to multiple reasons, such as violation of linearization assumptions, actuator saturations, etc. Therefore, an improved FTC method is required to address the upset recovery problem.

1.3. CONTRIBUTIONS

As the main contribution, this research proposes a controller which has the ability to recover a quadrotor with complete loss of a rotor from an arbitrary attitude and a wide range of initial angular velocities. Then the method can subsequently steer the damaged drone to a designated position and altitude. This cascaded control method is composed of three parts: a control allocator that tracks the angular acceleration command while suppressing the undesirable angular rate, an attitude controller with an almost-global attraction region, and a position controller subordinate to the former two parts.

The control method has been validated in a real-life environment where the quadrotor was randomly tossed into the air and recovers thereafter. A set of Monte-Carlo simulations have been also performed to test the performance of the controller from a wide range of initial conditions. It is shown that the proposed method can significantly improve the quadrotor safety after rotor failures despite large initial disturbances.

2. PROBLEM FORMULATION

2.1. NOTATION

The inertial frame is represented by the north-east-down coordinate system. The body frame is originated at the c.g. of the vehicle with the forward-right-down convention, as is shown in Fig. 6.2. Throughout the chapter, we use lower-case boldface symbols to denote vectors, upper-case boldface symbols for matrices and non-boldface symbols for scalars. A 3-D vector with superscript $[\cdot]^B$ indicates that the vector is expressed in the body frame, otherwise in the inertial frame. Operator diag$(\cdot)$ indicates a diagonal matrix with element $(\cdot)$ as diagonal entries.

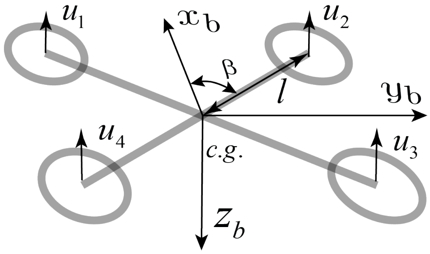

Figure 6.2: Definition of the body frame, the geometric parameters β and l, the index of control inputs.

2.2. 6-DOF MODEL OF A QUADROTOR

The quadrotor is powered by four independently controlled rotors to produce necessary lift and control moments. Fig. 6.2 shows the definition of the body frame, and the rotor index of a quadrotor. The state equations of a quadrotors can be composed of the following 6-DoF rigid body kinematics and dynamic equations [18]:

$$\dot{\boldsymbol{\xi}} = \boldsymbol{v} \tag{6.1}$$

$$\dot{\boldsymbol{R}} = \boldsymbol{R}\boldsymbol{\omega}^B_\times \tag{6.2}$$

$$m\dot{\boldsymbol{v}} = m\boldsymbol{g} + \boldsymbol{R}(\boldsymbol{f}^B_c + \boldsymbol{f}^B_a) \tag{6.3}$$

$$\boldsymbol{I}^B_v\dot{\boldsymbol{\omega}}^B + \boldsymbol{\omega}^B \times \boldsymbol{I}^B_v\boldsymbol{\omega}^B = \boldsymbol{m}^B_c + \boldsymbol{m}^B_a + \boldsymbol{m}^B_g \tag{6.4}$$

where $\boldsymbol{\xi} = [x,\ y,\ z]^T$ and $\boldsymbol{v} = [v_x,\ v_y,\ v_z]^T$ indicate the position and velocity respectively. $\boldsymbol{R} \in \mathrm{SO}(3)$ is the rotational matrix of the quadrotor from the body frame to the inertial frame. Therefore, for any vector $\boldsymbol{e} \in \mathbb{R}^3$, we have $\boldsymbol{e} = \boldsymbol{R}\boldsymbol{e}^B$. The angular velocity of the body frame w.r.t the inertial frame is expressed as $\boldsymbol{\omega}^B = [\omega_x,\ \omega_y,\ \omega_z]^T$, where $\boldsymbol{\omega}^B_\times$ is the skew symetric matrix such that $\boldsymbol{\omega}_\times\boldsymbol{a} = \boldsymbol{\omega} \times \boldsymbol{a}$ for any $\boldsymbol{a} \in \mathbb{R}^3$. The vehicle mass and inertia are denoted by m and $\boldsymbol{I_v}^B$ respectively and $\boldsymbol{g}$ denotes the gravity vector. The control forces $\boldsymbol{f}^B_c$ and moments $\boldsymbol{m}^B_c$ are produced by rotors. A simplified model of forces and moments generated by rotors are expressed as

$$\boldsymbol{f}^B_c = [0,\ 0,\ \boldsymbol{G}_t\boldsymbol{u}]^T, \quad \boldsymbol{m}^B_c = \boldsymbol{G}_m\boldsymbol{u} \tag{6.5}$$

where $\boldsymbol{u} = [u_1,\ u_2,\ u_3,\ u_4]^T$ and u_i is the force produced by rotor i (see Fig. 6.2). Note that $0 \le \boldsymbol{u}_{\mathrm{min}} \le \boldsymbol{u} \le \boldsymbol{u}_{\mathrm{max}}$. When complete failure of rotor i occurs, we have $u_{\mathrm{min},i} = u_{\mathrm{max},i} = 0$. $\boldsymbol{G}_m$ is a mapping from rotor generated forces to control moments and $\boldsymbol{G}_t$ is the mapping from rotor generated forces to the total thrust. For a quadtrotor that the thrust of each rotor is parallel with the $\boldsymbol{z}_b$ axis, we have

$$\boldsymbol{G}_t = [-1, -1, -1, -1] \tag{6.6}$$

$$\boldsymbol{G}_m = \mathrm{diag}(l\sin\beta,\ l\cos\beta,\ s\sigma)\begin{bmatrix} 1 & -1 & -1 & 1 \\ 1 & 1 & -1 & -1 \\ 1 & -1 & 1 & -1 \end{bmatrix} \tag{6.7}$$

where l and β are geometric parameters as shown in Fig. 6.2. σ is the torque thrust ratio of the rotor, s is a sign variable determined by the rotating direction of the rotor.

The force model given by (6.5) neglects the variation of thrust stem from quadrotor translational motions with respect to the airflow. Therefore, an aerodynamic force term $\boldsymbol{f}_a^B$ is added in (6.3), so as the term $\boldsymbol{m}_a^B$ in (6.4). The gyroscopic moment, denoted by $\boldsymbol{m}_g^B$, is caused by the rotation of rotors with respect to the body frame. For the current research, we omit $\boldsymbol{f}_a^B$, $\boldsymbol{m}_a^B$ and $\boldsymbol{m}_g^B$ in the controller design whereas they are included in the simulation presented in Sec.4.

2.3. QUADROTOR UPSET RECOVERY PROBLEM

A quadrotor has four independently powered rotors, such that the thrust, pitch, roll and yaw channels can be totally decoupled. This characteristic, however, can be different when a single rotor failure occurs. A most commonly used strategy is by giving up the yaw control and keep the rest which is more essential for maintaining the desired position and altitude [4]. This requires the post-failure vehicle to enter a so-called *relaxed-hovering condition* [6] in which the drone spins about an average thrust direction whilst the position of the spinning center and the altitude maintain constant. By slightly changing the direction and amount of the reference thrust, the average position and altitude of the post-failure quadrotor can be controlled.

Driving a quadrotor with a single rotor failure to the relaxed-hovering condition from arbitrary initial attitude, angular rates, and positions, is defined as the quadrotor upset recovery problem.

3. METHODOLOGY

The major challenge of the recovery problem is threefold. First of all, we need to design an almost-global (excluding finite singularities) reduced attitude controller to drive the vehicle orientation to the relaxed-hovering condition from large initial attitude deviation. Secondly, with the complete failure of a rotor, the quadrotor system only has three remaining constraint inputs. Hence it requires a novel control allocation approach to address input constraints while preventing the drone from entering upset conditions. Last but not least, a hedging of position/altitude loop need to be designed to coordinate with the aforementioned attitude controller and the control allocation method. A cascaded framework of the proposed controller is given as Fig. 6.3 shows.

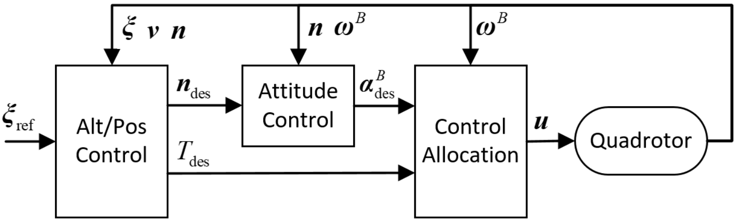

Figure 6.3: Diagram of the proposed control method.

3.1. ALTITUDE AND POSITION CONTROL

The position and altitude control, namely the outer-loop control, is designed as a cascaded P+PI controller as follows

$$\boldsymbol{v}_{\text{des}} = \boldsymbol{K}_{p,\text{pos}}(\boldsymbol{\xi}_{\text{ref}} - \boldsymbol{\xi}) \tag{6.8}$$

$$\boldsymbol{a}_{\text{des},0} = \boldsymbol{K}_{p,\text{vel}}(\boldsymbol{v}_{\text{des}} - \boldsymbol{v}) + \boldsymbol{K}_{i,\text{vel}} \int (\boldsymbol{v}_{\text{des}} - \boldsymbol{v})\text{d}t - \boldsymbol{g} \tag{6.9}$$

where $\boldsymbol{\xi}_{\text{ref}}$ is the reference position; $\boldsymbol{K}_{p,\text{pos}}$, $\boldsymbol{K}_{p,\text{vel}}$ and $\boldsymbol{K}_{i,\text{vel}}$ are 3×3 positive diagonal gain matrices. The acceleration reference is then obtained by

$$\boldsymbol{a}_{\text{des}} = \text{diag}(1/\epsilon,\ 1/\epsilon,\ 1)\boldsymbol{a}_{\text{des},0} \tag{6.10}$$

where

$$\epsilon = \max\left(\sqrt{a^2_{x,\text{des},0} + a^2_{y,\text{des},0}}/a_{z,\text{des},0}\tan\theta_1\ ,\ 1\right) \tag{6.11}$$

Then we can obtain the desired thrust direction

$$\boldsymbol{n}_{\text{des}} = \boldsymbol{a}_{\text{des}}/||\boldsymbol{a}_{\text{des}}|| \tag{6.12}$$

Note that the transform (6.10) guarantees that the angle between $\boldsymbol{n}_{\text{des}}$ and the reverse of gravity $-\boldsymbol{g}$ is confined by angle θ_1. Limiting this desired thrust direction can prevent aggressive spatial maneuvers during recovery.

Now we use θ to denote the angle between current thrust direction $\boldsymbol{n}$ and $-\boldsymbol{g}$

$$\theta = \arccos(-\boldsymbol{g}\cdot\boldsymbol{n}/||\boldsymbol{g}||) \tag{6.13}$$

Then the original thrust command can be obtained by

$$T_{\text{des},0} = -m\cdot a_{z,\text{des}}/\cos\theta \tag{6.14}$$

However, this method may deteriorate the attitude loop performance. Consider when the drone is upside down where $\theta \geq 90$ deg, (6.14) gives a negative thrust command; or when $\theta = 90$ deg, (6.14) leads to singularity. For this reason, a scaling factor

β is introduced which is scheduled by the total incline angle θ, yielding

$$\beta = \frac{\theta_2 - \min(\max(\theta,\, \theta_1),\, \theta_2)}{\theta_2 - \theta_1} \tag{6.15}$$

where $\theta_1 < \theta_2$ are predetermined parameters (see Table. 6.2). Finally the total thrust command is obtained by

$$T_{\text{des}} = -\beta \cdot m \cdot a_{z,\text{des}} / \cos(\min(\theta,\, \theta_1)) \tag{6.16}$$

3.2. ATTITUDE CONTROL

The attitude controller calculates the the angular rate command in order to control the thrust orientation $\boldsymbol{n}$ to $\boldsymbol{n}_{\text{des}}$. Now introduce the total incline angle ρ as the angle from $\boldsymbol{n}_{\text{des}}$ to $\boldsymbol{n}$, where

$$\rho = \arccos(\boldsymbol{n}_{\text{des}} \cdot \boldsymbol{n}) \tag{6.17}$$

Define the instant rotation vector $\boldsymbol{n}_c$ perpendicular to both $\boldsymbol{n}_{\text{des}}$ and $\boldsymbol{n}$, we have

$$\boldsymbol{n}_c = \boldsymbol{n} \times \boldsymbol{n}_{\text{des}} / \sin\rho \tag{6.18}$$

The reference angular rate can be consequently obtained

$$\boldsymbol{\omega}^B_{\text{des}} = k_{p,\text{att}} \cdot \rho \boldsymbol{R}^T \boldsymbol{n}_c \tag{6.19}$$

where $k_{p,\text{att}}$ is a positive gain. Then the angular acceleration reference can be obtained by a proportional controller with a feed-forward term

$$\boldsymbol{\alpha}^B_{\text{des}} = \boldsymbol{K}_{p,\text{rate}}(\boldsymbol{\omega}^B_{\text{des}} - \boldsymbol{\omega}^B) + \dot{\boldsymbol{\omega}}^B_{\text{des}} \tag{6.20}$$

Note that (6.18) becomes singular when $\boldsymbol{n}$ and $\boldsymbol{n}_{\text{des}}$ are collinear. Thus the attitude control presented above could result in the almost-global reduced attitude stabilization [19] with exception of two special points, namely $\rho \in \{0,\, \pi\}$. In practice, when singularity occurs, we can simply set $\boldsymbol{n}_c$ as an arbitrary unit vector perpendicular to $\boldsymbol{n}$.

3.3. CONTROL ALLOCATION

The control allocation step solves the desired thrust of each rotor, namely $\boldsymbol{u}$, using the desired angular acceleration $\boldsymbol{\alpha}^B_{\text{des}}$ and the total thrust command T_{des} as calculated above. Now, we use $\boldsymbol{\mu}_{\text{des}}$ to denote the desired control moments and thrust. By replacing $\dot{\boldsymbol{\omega}}^B$ with $\boldsymbol{\alpha}^B_{\text{des}}$ in (6.4) and omitting $\boldsymbol{m}_g$ and $\boldsymbol{m}_a$, we have

$$\boldsymbol{\mu}_{\text{des}} = \begin{bmatrix} \boldsymbol{m}^B_{c,\text{des}} \\ T_{\text{des}} \end{bmatrix} = \begin{bmatrix} \boldsymbol{I}^B_v \boldsymbol{\alpha}^B_{\text{des}} + \boldsymbol{\omega}^B \times \boldsymbol{I}^B_v \boldsymbol{\omega}^B \\ T_{\text{des}} \end{bmatrix} \tag{6.21}$$

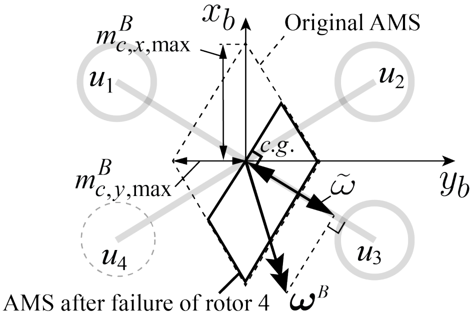

Figure 6.4: Projection of the attainable moment set (AMS) on the $x_b - y_b$ plane before and after the failure of rotor 4. The projection of current angular velocity $\boldsymbol{\omega}^B$ perpendicular to the boundary of AMS is unable to be reduced by the control moment. The magnitude of this component is denoted by $\tilde{\omega}$.

The thrusts generated by rotors need to cooperatively fulfil the reference represented by $\boldsymbol{\mu}_{\text{des}}$. As the thrust produced by a rotor is limited, we establish a constrained Quadratic Programming (QP) problem to solve $\boldsymbol{u}$:

$$\begin{aligned} \text{P1}: \qquad & \min_{\boldsymbol{u}} \quad \left(\boldsymbol{\mu}_{\text{des}} - \boldsymbol{G}\boldsymbol{u}\right)^T \boldsymbol{W} \left(\boldsymbol{\mu}_{\text{des}} - \boldsymbol{G}\boldsymbol{u}\right) + \lambda \boldsymbol{u}^T \boldsymbol{u} \\ & \text{s.t.} \qquad \boldsymbol{u}_{\min} \le \boldsymbol{u} \le \boldsymbol{u}_{\max} \end{aligned} \tag{6.22}$$

where $\boldsymbol{G} = [\boldsymbol{G}_m^T, \boldsymbol{G}_t^T]^T$ is a combined control effective matrix; $\boldsymbol{W} = \text{diag}(W_x, W_y, W_z, W_t)$ is a user defined weighting matrix, which determines the weight for each control objective; $\lambda > 0$ is another weight for minimizing the control effort.

P1 is a typical control allocation method for both aircraft and drones [20, 21]. However, for a quadrotor with single rotor failure, we need to add an additional constraint to P1. We hereby define the *Attainable Moment Set* (AMS) as a set of moments that can be generated by the existing rotors. As Fig. 6.4 shows, the area of AMS is reduced after rotor failure occurs. This is due to the fact that the quadrotor with fixed-pitch rotors can not generate negative lift, namely $\boldsymbol{u}_{\min} \ge 0$. In consequence, the angular velocity which cannot be suppressed by the current attainable moment will cause unstoppable rotations. The magnitude of this angular velocity, denoted by $\tilde{\omega}$, must be restrained during upset recovery.

A constraint of $\tilde{\omega}$ after a brief time period t_h is then introduced. Since the maneuverability on pitch/roll direction is much higher than yaw direction, we assume that ω_z in the period t_h is constant. Recall (6.4), and approximate $\boldsymbol{I}_v^B$ by $\text{diag}(I_x, I_y, I_z)$, we have

$$\begin{bmatrix} \dot{\omega}_x \\ \dot{\omega}_x \end{bmatrix} = \begin{bmatrix} 0 & \frac{I_y - I_z}{I_x}\omega_z \\ \frac{I_z - I_x}{I_y}\omega_z & 0 \end{bmatrix} \begin{bmatrix} \omega_x \\ \omega_y \end{bmatrix} + \hat{\boldsymbol{G}}_m \boldsymbol{u} \tag{6.23}$$

where

$$\hat{\boldsymbol{G}}_m = \mathrm{diag}(I_x,\ I_y)^{-1}\begin{bmatrix} 1 & 0 & 0 \\ 0 & 1 & 0 \end{bmatrix}\boldsymbol{G}_m \tag{6.24}$$

Note that (6.23) is a linear ODE, thus the time history of ω_x and ω_y can be explicitly solved with given initial conditions and control inputs. Assume the control input $\boldsymbol{u}$ is constant within t_h, and use the current ω_x and ω_y as initial conditions, then $\tilde{\omega}$ after t_h can be expressed as

$$\tilde{\omega}(t_h) = \boldsymbol{\phi}\begin{bmatrix} \omega_x(t_h) \\ \omega_y(t_h) \end{bmatrix} = \boldsymbol{\phi}\boldsymbol{\Phi}_0(t_h)\begin{bmatrix} \omega_x \\ \omega_y \end{bmatrix} + \boldsymbol{\phi}\boldsymbol{\Phi}_1(t_h)\hat{\boldsymbol{G}}_m\boldsymbol{u} \tag{6.25}$$

where $\boldsymbol{\phi} \in \mathbb{R}^{1\times 2}$ is a row vector converting ω_x and ω_y to $\tilde{\omega}$, and we have

$$\boldsymbol{\Phi}_0 = \begin{bmatrix} \cos(ct_h) & -\frac{c}{b}\sin(ct_h) \\ \frac{b}{c}\sin(ct_h) & \cos(ct_h) \end{bmatrix} \tag{6.26}$$

$$\boldsymbol{\Phi}_1 = \begin{bmatrix} \frac{1}{c}\sin(ct_h) & \frac{1}{b}\cos(ct_h) - \frac{1}{b} \\ \frac{b}{c^2} - \frac{b}{c^2}\cos(ct_h) & \frac{1}{c}\sin(ct_h) \end{bmatrix} \tag{6.27}$$

where

$$b = \frac{I_z - I_x}{I_y}\omega_z,\quad c = \sqrt{\frac{|(I_z - I_x)(I_y - I_z)|}{I_x I_y}}|\omega_z| \tag{6.28}$$

Note that the detail expression of $\boldsymbol{\phi}$ varies with the quadrotor geometric property and the location of the failure rotor in the body frame.

From (6.25), it is clear that $\tilde{\omega}$ is not only affected by the rotor generated moments, but also coupling moment (term $\boldsymbol{\omega}^B \times \boldsymbol{I}_v^B\boldsymbol{\omega}^B$ in (6.4)) as the function of initial angular velocity. Therefore, reducing $\tilde{\omega}$ is possible by leveraging these coupling moments after complete failure of rotors.

Consequently, the control allocation method constraining $\tilde{\omega}$ can be constructed as

$$\begin{aligned} \mathrm{P2:}\quad \min_{\boldsymbol{u},d}\quad & \left(\boldsymbol{\mu}_{\mathrm{des}} - \boldsymbol{G}\boldsymbol{u}\right)^T \boldsymbol{W}\left(\boldsymbol{\mu}_{\mathrm{des}} - \boldsymbol{G}\boldsymbol{u}\right) + \lambda\boldsymbol{u}^T\boldsymbol{u} + \gamma d^2 \\ \mathrm{s.t.}\quad & \boldsymbol{\phi}\boldsymbol{\Phi}_1\hat{\boldsymbol{G}}_m\boldsymbol{u} \le -\boldsymbol{\phi}\boldsymbol{\Phi}_0[\omega_x,\ \omega_y]^T + \tilde{\omega}_{\max} + d \\ & -d \le 0 \\ & \boldsymbol{u}_{\min} \le \boldsymbol{u} \le \boldsymbol{u}_{\max} \end{aligned} \tag{6.29}$$

where the first constraint stems from (6.25), which sets limitations to the $\tilde{\omega}$ after t_h by $\tilde{\omega}_{\max}$. The slack variable d is added to guarantee the solution of above optimization problem; $\gamma > 0$ is a weight added to the slack variable thereof. Note that the recovery performance is affected by three parameters: t_h, $\tilde{\omega}_{\max}$ and γ. In general, the constraint of $\tilde{\omega}$ is more strict with a larger t_h, γ and a smaller $\tilde{\omega}_{\max}$. P2 is a constrained quadratic programming problem which can be efficiently solved on-line using, for instance, the Active-set Algorithm [20] and the Interior Point Method [22].

After obtaining the reference thrust of each rotor by solving the quadratic programming problem P2, the RPM command or PWM command can be subsequently

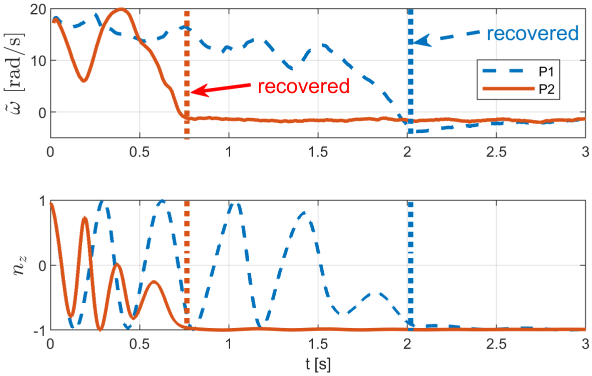

Figure 6.5: Two trajectories initialized from the same condition while using different allocation methods. The upper plot shows the angular rates about the unrecoverable axis $\tilde{\omega}$. The method P2 can more effectively suppress $\tilde{\omega}$ than P1. The lower plot shows the vertical component of the thrust direction $\boldsymbol{n}$, namely n_z, which should converge to -1 when the vehicle thrust vector points upward. It is clear the method P2 results in much faster recovery speed than P1.

calculated using a model obtained by propeller static thrust tests, which is omitted in this chapter for readability.

4. SIMULATION VALIDATION

4.1. CASE STUDY: COMPARISON BETWEEN P1 AND P2 ALLOCATION

The proposed controller is first of all validated in a 6-DoF simulation. The simulation platform uses the quadrotor model developed in [23], which takes complex aerodynamic effects into account. The quadrotor inertial and geometric parameters are given in Table. 6.1. One of the innovations proposed in this article is utilizing P2 from (6.29) to replace P1 in (6.22), such that the undesirable angular rate $\tilde{\omega}$ can be suppressed. Fig. 6.5 shows $\tilde{\omega}$ and n_z of two recovery maneuvers using P1 and P2 as allocation methods respectively. In both simulations, the failure of rotor 4 occurs when $\boldsymbol{n} = [-0.2,\ 0.2,\ 0.98]^T$ and $\boldsymbol{\omega}^B = [-15,\ 15,\ 0]$. At this moment, the drone is almost upside down with a large $\tilde{\omega}$ at 17.3 rad/s. The target thrust orientation of both are set as $\boldsymbol{n}_{\text{des}} = [0,\ 0,\ -1]^T$, namely vertically upwards. It is clear that the trajectory with P2 allocation can effectively suppress $\tilde{\omega}$. Thereby the drone could recover its attitude within around 0.7 s, whereas the same problem without restraining $\tilde{\omega}$ recovers at around 2 s.

4.2. MONTE-CARLO SIMULATION

A set of Monte-Carlo simulations are conducted to validate the proposed method. Another two methods are compared in these simulations: the method with P1 allo-

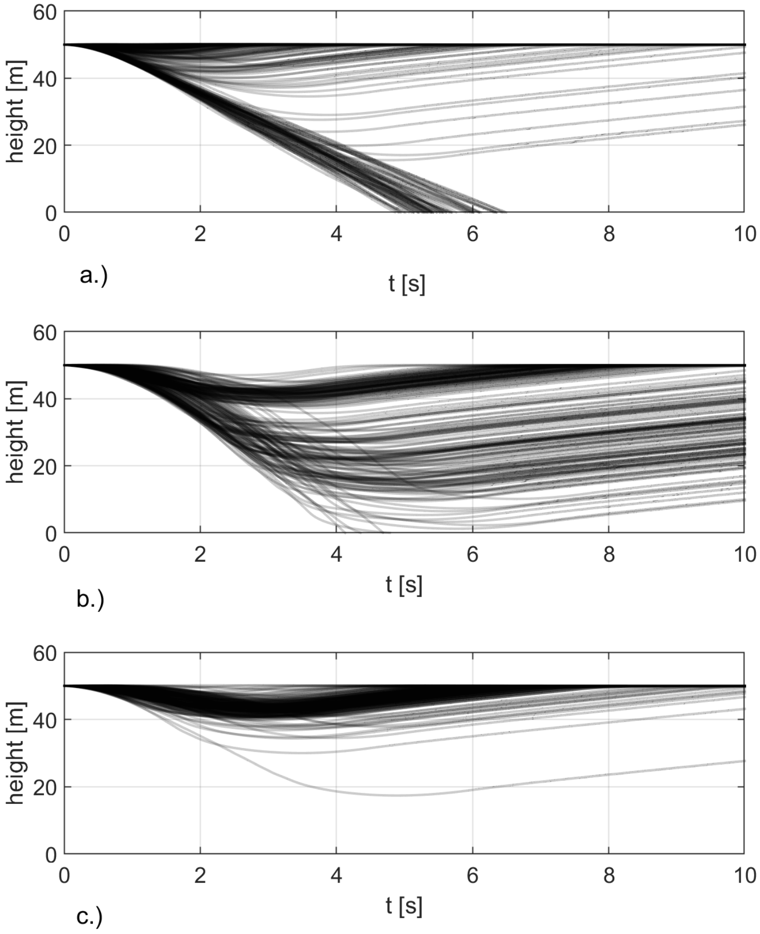

Figure 6.6: Altitude time series of a set of Monte-Carlo simulation including 200 flights initialized from random attitude and angular velocities with different flight control methods. a.) The benchmark method. b.) The proposed method but using P1 allocation. c.) The proposed method.

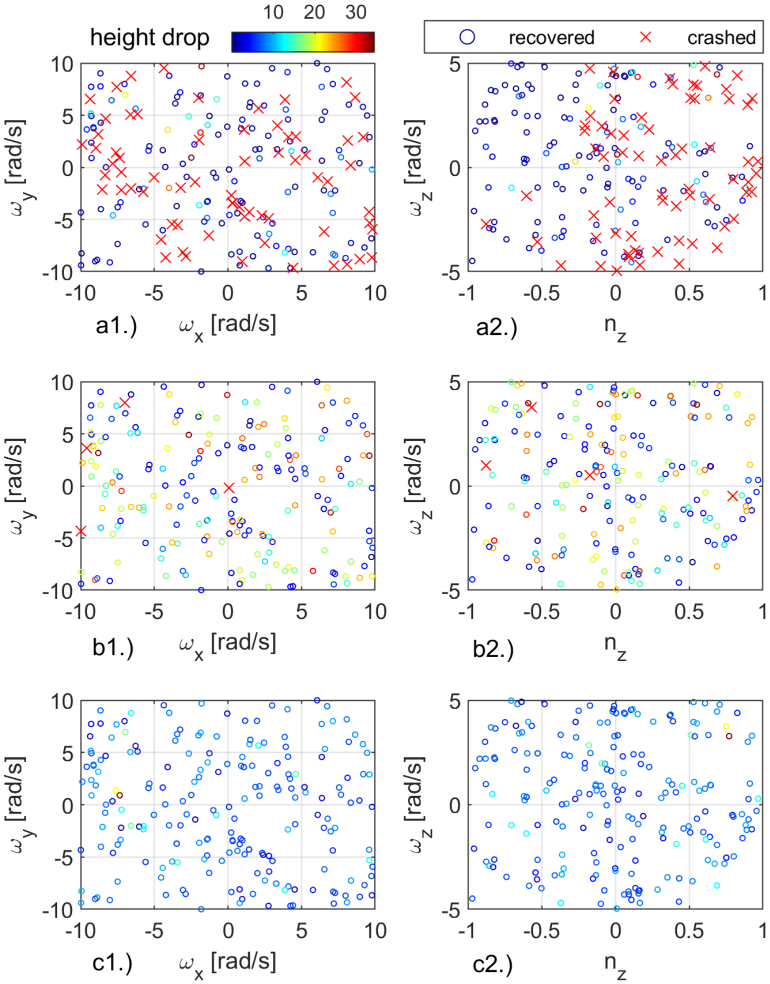

Figure 6.7: Scatter plot of the initial conditions of the Monte-Carlo simulation with colors showing the maximum height drop. The crashed flights are shown in red cross markers. a.) The benchmark method. b.) The proposed method but using P1 allocation. c.) The proposed method.

cation, and the benchmark control method proposed by [12]. For each method, 200 trajectories are simulated from different initial conditions.

We simulate the scenario where the failure of rotor 4 happens during the forward flight at speed. The initial position and velocity of these flights are set as $\boldsymbol{\xi}_0 = [0,\ 0, -50]^T$ m, $\boldsymbol{v}_0 = [10,\ 0,\ 0]^T$ m/s. The initial attitude is randomly selected in the entire SO(3), and the initial angular velocity $\boldsymbol{\omega}_0^B \sim U(-\boldsymbol{\omega}_{0,\max},\ \boldsymbol{\omega}_{0,\max})$ where $\boldsymbol{\omega}_{0,\max} = [10,\ 10,\ 5]^T$ rad/s.

The altitude time series of different methods are plotted in Fig. 6.6. And Fig. 6.7 shows the scatter plot of the initial conditions of these three methods with color showing the maximum height drop. For the benchmark method, there are 67 out of 200 flights crashed. Most of these crashed flights marked in red crosses concentrate in the area with positive initial n_z which indicate downward pointing initial thrust orientations (Fig. 6.7-a2). On the other hand, the initial angular rates seem no special effect on the recovery performance. For method using P1 allocation shown in Fig. 6.6-b and Fig. 6.7-b, there are 4 crashes but many of the rest recover after dropping for a large amount of altitude. There are two crashes concentrate on the top-left ω_x-ω_y plane of Fig. 6.7-b1 meaning that these flights are initialized with large $\tilde{\omega}$. In comparison, the proposed controller using P2 allocation method recovers the damaged drone in all of the 200 flights. 95% of these flights could recover with a height drop of less than 10 m while only 1 flight recovers after dropping over 30 m, as is shown in Fig. 6.6-c and Fig. 6.7-c.

5. EXPERIMENTAL VALIDATION

The proposed method is also validated in the real flight environment. The tested platform is a modified Parrot Bebop 2 quadrotor, as Fig. 6.8 shows. The parameters of this quadrotor are given in Table. 6.1. The flight was conducted in the Cyberzoo, TU Delft where 12 cameras from the motion capturing system (Optitrack) measured the position of 6 reflective markers attached to the drone in 120 Hz. The position information was then transmitted to the drone via WiFi, and the controller was run on-board in 500 Hz. The processor of the drone is a Parrot P7 dual-core CPU Cortex 9, and the IMU is MPU6050 for angular rate and specific force measurements.

To create the arbitrary initial condition, we threw the quadrotor with failure of rotor 4 into the air as Fig. 6.8 shows. After reaching an altitude of 2 meters, the drone started recovering. Fig. 6.9 shows the reduced attitude $\boldsymbol{n}$, the angular rates, height and the rotor RPM in the recovery process. The drone was finally recovered and stayed at 3 m over the ground with a fast yaw rate. The controller parameters of this set of the test are listed in Table. 6.2.

Since the motion capturing system is unable to measure the position of the drone with large attitude deviations from the hovering condition, an Extended Kalman Filter (EKF) is applied to fuse the camera measurements with the IMU measurements to obtain the position, velocity and attitude estimations. The 3rd subplot of

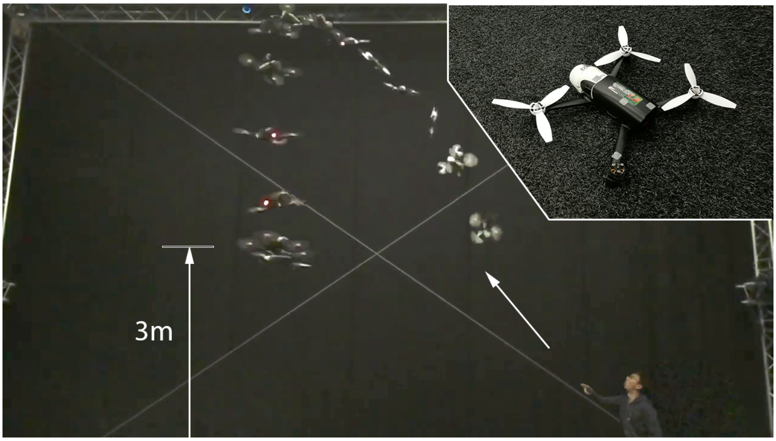

Figure 6.8: Snapshots of the quadrotor recovery maneuver after being tossed into the air. The drone was finally stabilized at 3m above the ground. Right top corner shows the photo of the tested quadrotor of which the left-back rotor was removed.

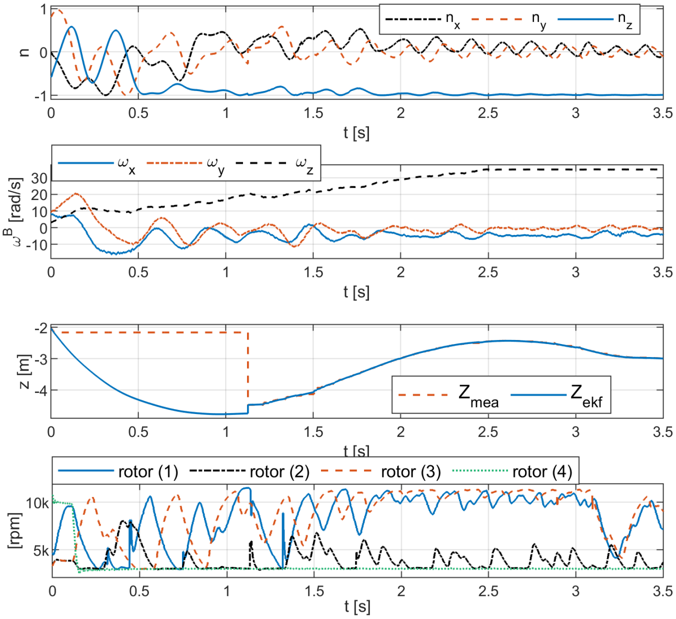

Figure 6.9: Time history of the recovery maneuver. Subfigures from top to bottom present the thrust orientation $\boldsymbol{n}$, angular rates ω^B, altitude z and rotor speeds respectively.

Table 6.1: Inertial and geometric properties of the tested quadrotor.

parameter	value	unit
$\boldsymbol{I}_v^B$	diag(1.45, 1.26, 2.52)$\times 10^{-3}$	kgm^2
m, l, β	0.41, 0.145, 52.6	kg, m, deg
s, σ	1, 0.01	-

Table 6.2: Control parameters of the real-life flight test.

par.	value	par.	value
$\boldsymbol{K}_{p,\mathrm{pos}}$	diag(1, 1, 15)	$\boldsymbol{K}_{p,\mathrm{vel}}$	diag(2, 2, 25)
$\boldsymbol{K}_{i,\mathrm{vel}}$	diag(1, 1, 5)	$(\theta_1,\ \theta_2)$	(30, 70) deg
$k_{p,\mathrm{att}}$	8	$\boldsymbol{K}_{p,\mathrm{rate}}$	diag(15, 15, 1)
$\boldsymbol{W}$	diag(10^4, 10^4, 10^2, 4)	$(\lambda, \gamma, t_h, \tilde{\omega}_{\mathrm{max}})$	(0.1, 10^5, 0.1, 5)

Fig. 6.9 also shows EKF estimated altitude compared with the raw measurements and the latter keeps constant before $t = 1.3$ s due to loss of tracking of the reflective markers.

The in-door tests have a success rate of 71% (46 out of 65 throws). However, those initialized from upside-down orientations and large $\tilde{\omega}$ is rather hard to recover before touching the ground. This is because of the height limitation of the laboratory (6 meters effective height) while it requires about 10 meters to completely recover from the upset condition. Therefore, out-door flight tests will be performed in future research, together with improved state estimation methods.

6. CONCLUSIONS

An upset recovery control method for a quadrotor with one rotor failure has been proposed and tested in this research. The controller can stabilize the quadrotor from arbitrary initial orientations and a wide range of angular velocities to the relaxed hovering condition. A novel control allocation approach is developed to suppress the undesirable angular velocities, which is important to the recovery performance. To demonstrate the reliability of the method, we have conducted Monte-Carlo simulations from random initial conditions. It has shown that the proposed method can timely recover the quadrotor with a height drop of less than 10 m in over 95% flights. In the real-flight test, the controller can recover the damaged quadrotor after being randomly tossed into the air. Further tests in outdoor environments, with onboard state estimation, are suggested for future research.

REFERENCES

[1] J. K. Stolaroff, C. Samaras, E. R. O'Neill, A. Lubers, A. S. Mitchell, and D. Ceperley, *Energy use and life cycle greenhouse gas emissions of drones for commercial package delivery,* Nature Communications **9**, 409 (2018).

[2] T. Li, Y. Zhang, and B. W. Gordon, *Passive and active nonlinear fault-tolerant control of a quadrotor unmanned aerial vehicle based on the sliding mode control technique,* Proceedings of the Institution of Mechanical Engineers, Part I: Journal of Systems and Control Engineering **227**, 12 (2013).

[3] X. Wang, S. Sun, E.-J. van Kampen, and Q. Chu, *Quadrotor fault tolerant incremental sliding mode control driven by sliding mode disturbance observers,* Aerospace Science and Technology **87**, 417 (2019).

[4] A. Lanzon, A. Freddi, and S. Longhi, *Flight control of a quadrotor vehicle subsequent to a rotor failure,* Journal of Guidance, Control, and Dynamics **37**, 580 (2014).

[5] M. W. Mueller and R. D'Andrea, *Stability and control of a quadrocopter despite the complete loss of one, two, or three propellers,* in *2014 IEEE international conference on robotics and automation (ICRA)* (IEEE, 2014) pp. 45–52.

[6] M. W. Mueller and R. D'Andrea, *Relaxed hover solutions for multicopters: Application to algorithmic redundancy and novel vehicles,* The International Journal of Robotics Research **35**, 873 (2016).

[7] V. Lippiello, F. Ruggiero, and D. Serra, *Emergency landing for a quadrotor in case of a propeller failure: A backstepping approach,* in *2014 IEEE/RSJ International Conference on Intelligent Robots and Systems* (IEEE, 2014) pp. 4782–4788.

[8] V. Lippiello, F. Ruggiero, and D. Serra, *Emergency landing for a quadrotor in case of a propeller failure: A pid based approach,* in *2014 IEEE International Symposium on Safety, Security, and Rescue Robotics (2014)* (IEEE, 2014) pp. 1–7.

[9] P. Lu and E.-J. van Kampen, *Active fault-tolerant control for quadrotors subjected to a complete rotor failure,* in *2015 IEEE/RSJ International Conference on Intelligent Robots and Systems (IROS)* (IEEE, 2015) pp. 4698–4703.

[10] Z. Hou, P. Lu, and Z. Tu, *Nonsingular terminal sliding mode control for a quadrotor uav with a total rotor failure,* Aerospace Science and Technology **98**, 105716 (2020).

[11] J. Stephan, L. Schmitt, and W. Fichter, *Linear parameter-varying control for quadrotors in case of complete actuator loss,* Journal of Guidance, Control, and Dynamics **41**, 2232 (2018).

[12] S. Sun, L. Sijbers, X. Wang, and C. de Visser, *High-speed flight of quadrotor despite loss of single rotor,* IEEE Robotics and Automation Letters **3**, 3201 (2018).

[13] L. Crespo, S. Kenny, D. Cox, and D. Murri, *Analysis of control strategies for aircraft flight upset recovery,* in *AIAA Guidance, Navigation, and Control Conference* (2012) p. 5026.

[14] J. A. Engelbrecht, S. J. Pauck, and I. K. Peddle, *A multi-mode upset recovery flight control system for large transport aircraft,* in *AIAA Guidance, Navigation, and Control (GNC) Conference* (2013) p. 5172.

[15] C. M. Belcastro, *Aircraft loss of control: Analysis and requirements for future safety-critical systems and their validation,* in *2011 8th Asian Control Conference (ASCC)* (IEEE, 2011) pp. 399–406.

[16] A. Lambregts, G. Nesemeier, R. Newman, and J. Wilborn, *Airplane upsets: Old problem, new issues,* in *AIAA Modeling and Simulation Technologies Conference and Exhibit* (2008) p. 6867.

[17] M. Faessler, F. Fontana, C. Forster, and D. Scaramuzza, *Automatic re-initialization and failure recovery for aggressive flight with a monocular vision-based quadrotor,* in *2015 IEEE International Conference on Robotics and Automation (ICRA)* (IEEE, 2015) pp. 1722–1729.

[18] R. Mahony, V. Kumar, and P. Corke, *Multirotor aerial vehicles: Modeling, estimation, and control of quadrotor,* IEEE Robotics and Automation magazine **19**, 20 (2012).

[19] N. A. Chaturvedi, A. K. Sanyal, and N. H. McClamroch, *Rigid-body attitude control,* IEEE control systems magazine **31**, 30 (2011).

[20] J. Petersen and M. Bodson, *Constrained quadratic programming techniques for control allocation,* IEEE Transactions on Control Systems Technology **14**, 91 (2006).

[21] E. Smeur, D. Höppener, and C. De Wagter, *Prioritized control allocation for quadrotors subject to saturation,* in *International Micro Air Vehicle Conference and Flight Competition* (2017) pp. 37–43.

[22] R. J. Vanderbei, *Loqo: An interior point code for quadratic programming,* Optimization methods and software **11**, 451 (1999).

[23] S. Sun and C. de Visser, *Aerodynamic model identification of a quadrotor subjected to rotor failures in the high-speed flight regime,* IEEE Robotics and Automation Letters **4**, 3868 (2019).

7

CONCLUSION

This chapter will revisit the research questions given in the Introduction in the light of studies carried out in Chapter 2-6. Then, its limitations and an outlook on future work will be provided.

1. ANSWERS TO RESEARCH QUESTIONS

1.1. RESEARCH QUESTION I

The first research question is about aerodynamic modeling of the damaged quadrotor, and has been addressed in Chapter 2 and 3.

> Research Question I
>
> How to establish aerodynamic models of a quadrotor subjected to complete failure of rotors in the high-speed flight regime using an aerodynamic model identification approach?

In **Chapter 2**, a set of gray-box models are identified for a quadrotor in the nominal configuration from the high-speed flight data obtained in a large-scale wind tunnel. In the high-speed flight condition, significant aerodynamic effects not captured by standard hovering model become apparent. This research has provided new observations of aerodynamic effects from practical experiments, such as

- Thrust degradation due to rotor-body interactions.
- Yaw moment variations in different sideslip angles.
- Significant pitch-up moments causing saturatiosn of rear rotors and longitudinal instability of a quadrotor.

These newly discovered phenomena, together with known effects from the literature, are modeled from flight data using a gray-box identification approach. The resultant gray-box model outperforms the benchmark in thrust prediction, particularly at high sideslip angle, and aerodynamic moment predictions in the high-speed flight regime. On validation data, we have seen 20% and 80% reductions of residual errors of force and moment model predictions, in comparison with the benchmark hovering model.

While the above gray-box model focuses on accuracy, the model established in **Chapter 3** highlights model versatility to both nominal and damaged conditions in high-speed regimes. Therefore, flight data of a quadrotor subjected to complete rotor failures, along with the previous nominal data, are used for identification. There are two factors to be emphasised while establishing the model. First, for data processing, the high-speed yawing motion of the damaged quadrotor needs to be considered. It is critical to obtain an accurate local inflow velocity of each rotor, and more importantly, to remove the bias of the accelerometer from centrifugal forces and IMU installation errors. Secondly, a multi-body parametric model is selected for model versatility, because it can separate the rotor and the airframe effects. For each rotor, a 3-axis force and moment model has been established according to the thrust variations and blade-flapping effects. For the airframe, on the other hand, a novel normalized model structure is developed. This model structure is free of angular singularities; it also removes the requirement for extrapolations because normalized velocities are adopted. In the end, a classical weighted least-square (WLS) estimator is used to identify parameters of the aerodynamic model. Compared with benchmark model from the literature, the model has shown near 40% and 70% reduction of normalized root-mean-square error in force and moment predictions respectively. More importantly, the proposed aerodynamic model can be applied to both nominal and rotor-failure configurations.

1.2. RESEARCH QUESTION II

Research question 2 is about designing robust fault-tolerant control of a quadrotor subjected to complete rotor failures. It has been tackled in work presented in Chapter 4-6.

Research Question II

How to devise a fault-tolerant control method for a quadrotor subjected to complete failure of rotors that is robust against significant aerodynamic effects?

Chapter 4 developed a nonlinear flight controller for a quadrotor subjected to single-rotor failure. The controller is comprised of three loops: a position control loop using the PID method, a reduced attitude control loop, and a control allocation loop. Since the control allocation loop is sensitive to model uncertainties due to high-speed induced aerodynamic effects, the incremental nonlinear dynamic inversion (INDI) approach is adopted for control allocation. Apart from the aerodynamic disturbances, the high-speed yawing motion is another major challenge, which is addressed by the reduced attitude control loop based on nonlinear dynamic inversion (NDI). This method converts the desired acceleration in the inertial reference frame to the angular rate commands using rigid-body kinematics.

Chapter 5 generalizes the work in Chapter 4 to the condition with two opposing rotor failures. This under-actuated control problem, therefore, is composed of several internal states to be stabilized. The output-redefinition technique is thus applied to select a proper control variable to combine the two reduced attitudes, which is scheduled by a designated parameter (denoted by χ in the Chapter 5). It has been proved that, by appropriately selecting χ, the internal states can be stabilized. Otherwise, loss-of-control could occur due to unstable internal states. Parameter χ can also attenuate the detrimental effect of actuator dynamics, by determining a control output rendering higher control effectiveness.

For validation, real flights in the wind-tunnel have been conducted using both methods proposed in **Chapter 4** and **Chapter 5**. The tested quadrotor can reach over 8 m/s, which is over half of its nominal maximum flight speed. The proposed controller has been compared with a benchmark LQR approach adopted in the literature, by conducting maximum flight tests and trajectory tracking tasks in the wind-tunnel. These flights have demonstrated higher robustness of the proposed method against aerodynamic disturbances. By applying the novel FTC, the average maximum flight speeds have been improved from around 5m/s to over 8m/s for the tested quadrotor.

To enlarge the region of attraction of the proposed FTC methods, **Chapter. 6** presents an almost-global convergence approach, whereby a quadrotor subjected to a single-rotor-failure can recover from arbitrary initial angular and angular rate to hover. For preventing the damaged quadrotor from entering an unrecoverable state, a flight-envelope protection method is fused into the control allocation loop, yielding a quadratic programming (QP) problem. This proposed method has been compared with a traditional QP based allocation method, and the one developed in Chapter. 4. The comparison is in the form of Monte-Carlo simulations using the aerodynamic model identified in Chapter 3. The results show that the newly proposed method can recover a quadrotor from any initial orientations, and a broad range of initial angular velocities ($\sim$ 10 rad/s). In addition, this control method has been validated in the real flight, where a quadrotor with only three rotors was casually tossed into the air to create arbitrary initial conditions. Because of the spatial limit in the laboratory, some flights failed to recover before hitting the ground. Nonetheless, more than 70% percent of flights were recovered, and the success rate will rise with a greater initial height.

2. LIMITATIONS AND RECOMMENDATIONS

2.1. UNDERSTANDING OF COMPLEX AERODYNAMIC EFFECTS

While this thesis has revealed the existence of complex aerodynamic effects using a phenomenological approach, the underlying mechanism of these effects should be further investigated by systematic studies. Even though the gray-box model in Chapter 2 can accurately capture these effects, the performance of this model can be unsatisfactory in regimes where flight data are scarce. On the other hand, the rigid-body model in Chapter 3 has better extrapolation performance thanks to its relatively simple model structure at the cost of accuracy. The drawbacks of both models can be complemented by providing a physical-based model of these complex aerodynamic effects, such as rotor wake interactions, aerodynamic induced rotor moments, aerodynamic on to airframe, etc.

Therefore, it is recommended to investigate these complex aerodynamic effects of multi-rotor drones systematically. Possible solutions could be, for instance, static wind tunnel tests [1], computational fluent dynamics (CFD)[2] and analytical approaches [3].

2.2. INDI WITH ACTUATOR DYNAMICS

For a high-speed spinning quadrotor, the bandwidth of the actuator dynamics are comparable with that of the quadrotor. Therefore, the actuator dynamics can lead to non-negligible delay to the system. The INDI approach in this thesis, unfortunately, does not take it into account, which may indirectly cause loss-of-control.

Introducing Pseudo-Control-hedging (PCH) [4] may alleviate the adverse effect of actuator dynamics by restraining unattainable commands to the inner-loop. However, this may deteriorate the outer-loop control performance. A comprehensive study combining INDI and PCH technique is thus recommended to carry out, specifically, for this fault-tolerant control problem.

Since system delays have been extensively studied for linear control problems, insight may be gained from classical linear approaches, such as using phase margin as a tool to analyze the system robustness against delays caused by actuator dynamics. Another effective way is augmenting the original system with states representing actuators [5]. The generalization of these methods to the INDI framework might be possible.

2.3. STATE ESTIMATION

The omission of the state estimation problem is one of the major limitations of this study. Throughout the thesis, all the flight tests rely on external motion capturing systems that can provide accurate and timely measurements of the vehicle attitudes and positions. For linear systems, state estimators (or state observers) can be decoupled with the controller design thanks to the principle of separations [6]. But in reality, due to nonlinearities, the controller performance is coupled with the accuracy of state estimators. This is especially critical for this FTC problem where highly nonlinear and fast dynamics are involved. As a preliminary test, flights have been carried out in Chapter 5 with a complementary filter for attitude estimation. The estimator is found to be significantly deteriorated in such high-dynamic flight conditions, which subsequently degraded the performance of the controller.

Therefore, finding reliable state estimation methods in the rotor failure conditions recommended in future research. Without the reliance on an external motion capturing system, out-door flights can be performed. This will further validate the robustness of the proposed controller in a more realistic scenario. In addition, without spatial limitations such as those found in the laboratory environments and wind-tunnel, more systematic tests of upset-recovery maneuvers, high-speed vertical maneuvers, and post-failure high-speed cruising flights can be performed.

REFERENCES

[1] C. R. Russell, J. Jung, G. Willink, and B. Glasner, *Wind tunnel and hover performance test results for multicopter uas vehicles,* (2016).

[2] J. Luo, L. Zhu, and G. Yan, *Novel quadrotor forward-flight model based on wake interference,* AIAA Journal **53**, 3522 (2015).

[3] L. A. Zori and R. G. Rajagopalan, *Navier—stokes calculations of rotor—airframe interaction in forward flight,* Journal of the American Helicopter Society **40**, 57 (1995).

[4] E. N. Johnson and A. J. Calise, *Pseudo-control hedging: A new method for adaptive control,* in *Advances in navigation guidance and control technology workshop* (Citeseer, 2000) pp. 1–2.

[5] M. W. Mueller and R. D’ Andrea, *Relaxed hover solutions for multicopters: Application to algorithmic redundancy and novel vehicles,* The International Journal of Robotics Research **35**, 873 (2016).

[6] T. T. Georgiou and A. Lindquist, *The separation principle in stochastic control, redux,* IEEE Transactions on Automatic Control **58**, 2481 (2013).

ACKNOWLEDGEMENTS

First of all, I would like to thank Prof. Max Mulder and Dr. Qiping Chu for selecting me as the Ph.D. candidate to pursue this exciting project. Also, their high-level suggestions have helped me to avoid many pitfalls. I would also like to extend my deepest gratitude to my promoter and daily supervisor, Dr. Coen de Visser, not only for his supervisions on technical details but also for being an anchor when I lost my orientations. His guidance and encouragement have played a decisive part in the accomplishment of this thesis. I also wish to thank my promotor Prof. Guido de Croon who directs the MAVLab that has provided me irreplaceable supports.

This project involves many real flight tests and wind tunnel experiments, which cannot be accomplished without the help from these individuals: Erik van der Horst, Dr. Matej Karasek, and Nico van Balen. In addition, I want to express my special thank to Bertine Markus for her administrative supports.

I am also grateful to all the master students who participated in my project and whose help cannot be overestimated. They are: Rudi Schilder, Leon Sijbers, Kieran Kersbergen, Bram Strack van Schijndel, Matthias Baert, Anthony van der Pluijm, and Prashant Solanki. I will always remember those precious moments we spent together in the Cyberzoo and the OJF (Open Jet Facility).

The C&S section is a big family for me. I have enjoyed every moment thanks to these lovely colleagues: Mario Coppola, Dirk van Baelen, Sven Pfeiffer, Diana Olejnik, Jelmer Reitsma, Federico Paredes Vallés, Malik Doole, Kimberly McGuire, Kirk Scheper, Sophie Armanini, Jaime Junell, Hann Woei Ho, Ewoud Smeur, Paolo Scaramuzzino, Dyah Jatiningrum, Tommaso Mannucci, Tom van Dijk, Annemarie Landman, Junzi Sun, Daniel Friesen, Jerom Maas, Kasper van der El, Julien Dupeyroux, Jan Smisek, Emanual Sunil, Sjoerd Tijmons, Sarah Barendswaard, Ivan Miletovic, Noor Nabi, Isabel Metz, Nilay Sheth. I also want to thank my Chinese friends and colleagues: Shuo Li, Lei Yang, Yingfu Xu, Bo Sun, Ye Zhang, Yingzhi Huang, Shushuai Li, Zhou Nie, Ying Yu, Ye Zhou, Peng Lu, Zhi Hong, Hao Yu, Wei Fu, Gehua Wen, Cheng Liu, Lan Yang, Ding Ding, Riming Wang, for our unforgettable happy moments. Special thanks to Junzi for organizing parties for every Chinese New Year.

In addition, I am extremely grateful to Prof. Davide Scaramuzza from the University of Zurich / ETH, for inviting me to visit Robotics and Perception Group (RPG) and conducting such an exciting piece of research. Special thanks to Tammy, and all the colleages in RPG for their backing during this unforgettable period before the end of my Ph.D. project.

I would like to thank the China Scholarship Council (CSC) for their four-year funding support. Also thank SEMP (Erasmus) for funding my 8 months visiting in the Switzerland.

Finally, I want to express my deepest gratitude towards my parents for your unconditional love and supports. And to Xuerui Wang, my beloved wife, also the most reliable research mate. Thank you for your accompany, encouragement, and inspirations during this wonderful period in our lifelong adventure.

Curriculum Vitæ

Sihao Sun (孙思昊)

06-04-1992	Born in Harbin, China.

Education

2007–2010	High School Attached to Northeast Normal University
2010–2014	B.Sc. Aerospace Engineering Beihang University
2014-2017	M.Sc. Aerospace Engineering Beihang University
Since 2016	Ph.D. candidate in Aerospace Engineering Delft University of Technology.

Awards

2016	Chinese Scholarship Council (CSC) Scholarship
2014	Outstanding Graduate Award of Beijing
2013	First price of Embraer scholarship
2013	Champion of Chinese Aeromodeling Competitions
2012-2013	Beihang Science and Technology Innovation Scholarship

LIST OF PUBLICATIONS

JOURNAL PUBLICATIONS

6. **S. Sun**, G. Cioffi, C. de Visser, and D. Scaramuzza, *Autonomous quadrotor flight despite rotor failure with onboard sensors*, IEEE Robotics and Automation Letters. (2021) (submitted).
5. **S. Sun**, X. Wang, Q. Chu, and C. de Visser, *Incremental nonlinear fault-tolerant control of a quadrotor with complete loss of two opposing rotors*, IEEE Transactions on Robotics (2020).
4. **S. Sun,** , L. Sijbers, X. Wang, and C. de Visser, *High-speed flight of quadrotor despite loss of single rotor*, IEEE Robotics and Automation Letters. vol. 3, no. 4, 3201-3207 (2018).
3. **S. Sun**, and C. de Visser *Aerodynamic model identification of a quadrotor subjected to rotor failures in the high-speed flight regime*, IEEE Robotics and Automation Letters. vol.4, no.4, 3868-3875 (2019).
2. **S. Sun**, Q. Chu, and C. de Visser, *Quadrotor gray-box model identification from high-speed flight data*, Journal of Aircraft. vol.56, no.2, 645-661 (2019).
1. X. Wang, **S. Sun**, E. van Kampen, and Q. Chu, *Quadrotor fault tolerant incremental sliding mode control driven by sliding mode disturbance observers*, Aerospace Science and Technology vol. 87, 417-430 (2019).

PEER-REVIEWED CONFERENCE PROCEEDINGS

5. **S. Sun**, M. Baert, B. A. S. van Schijndel, and C. de Visser, *Upset recovery control for quadrotors subjected to a complete rotor failure from large initial disturbances*, in 2020 IEEE International Conference on Robotics and Automation (ICRA), 2020, pp. 4273-4279.
4. **S. Sun** and C. C. de Visser, *Quadrotor safe flight envelope prediction in the high-speed regime: a Monte-Carlo approach*, in AIAA Scitech 2019 Forum, 2019, no. January, pp. 1–12.
3. **S. Sun**, R. Schilder, and C. C. de Visser, *Identification of quadrotor aerodynamic model from high-speed flight data*, in 2018 AIAA Atmospheric Flight Mechanics Conference, 2018, no. January, pp. 1–23.
2. K.Kersbergen, **S. Sun**, C. de Visser, *Quantifying loss-of-control of quadrotors*, in 5th CEAS Conference on Guidance, Navigation and Control, 2019.
1. W. Li, **S. Sun**, and Z. Shen, *An adaptive predictor-corrector entry guidance law based on online parameter estimation*, in CGNCC 2016 - 2016 IEEE Chinese Guidance, Navigation and Control Conference, 2016.